



HAL
open science

Identification des sources printanières de méthylmercure dans le manteau neigeux arctique

Alexandre Renard

► **To cite this version:**

Alexandre Renard. Identification des sources printanières de méthylmercure dans le manteau neigeux arctique. Sciences de la Terre. Université de Grenoble, 2013. Français. NNT : 2013GRENU033 . tel-01065074

HAL Id: tel-01065074

<https://theses.hal.science/tel-01065074>

Submitted on 19 Sep 2014

HAL is a multi-disciplinary open access archive for the deposit and dissemination of scientific research documents, whether they are published or not. The documents may come from teaching and research institutions in France or abroad, or from public or private research centers.

L'archive ouverte pluridisciplinaire **HAL**, est destinée au dépôt et à la diffusion de documents scientifiques de niveau recherche, publiés ou non, émanant des établissements d'enseignement et de recherche français ou étrangers, des laboratoires publics ou privés.



THÈSE

Pour obtenir le grade de

DOCTEUR DE L'UNIVERSITÉ DE GRENOBLE

Spécialité : **Sciences de la Terre et Univers, Environnement**

Arrêté ministériel : 7 août 2006

Présentée par **Alexandre RENARD**

Thèse dirigée par **Christophe FERRARI**
co-dirigée par **Aurélien DOMMERGUE**

préparée au sein du **Laboratoire de Glaciologie et de
Géophysique de l'Environnement**
dans l'**École Doctorale Terre Univers Environnement**

Identification des sources printanières de méthylmercure dans le manteau neigeux arctique

Thèse soutenue publiquement le **4 novembre 2013**,
devant le jury composé de :

Daniel COSSA

Directeur de recherche (IFREMER), rapporteur

Katarina GARDFELDT

Professeur associé (Göteborg Universitet/Chalmers), rapporteur

Laurent MARON

Professeur (Université Paul Sabatier, Toulouse), examinateur

Frédéric MINASSIAN

Maître de conférences (Université de Grenoble), examinateur

Aurélien DOMMERGUE

Maître de conférences (Université de Grenoble), co-directeur de thèse

Christophe FERRARI

Professeur (Université de Grenoble), directeur de thèse



Remerciements

Je voudrais tout d'abord remercier les membres du jury d'avoir accepté de prendre le temps d'évaluer mon travail, en particulier les rapporteurs Katarina Gårdfeldt et Daniel Cossa.

Je remercie également tout le personnel du LGGE pour leur accueil et la facilité qu'il m'a fallu pour m'intégrer. Une pensée spéciale pour tous les doctorants que j'ai eu le plaisir de côtoyer, pour leurs conseils, les discussions (parfois animées !) et leur soutien. Parmi eux, il serait injuste de ne pas citer les quelques-uns qui ont même dû me supporter quotidiennement : Flo, Guillaume, Adina, Julie et Ruben. Ma thèse a été une grande expérience humaine en grande partie grâce à eux tous. Merci.

Je tiens également à remercier ceux sans qui rien n'aurait été possible, ceux qui ont donné leur confiance à un chimiste organicien béotien en problématiques environnementales, ceux qui ont su m'accompagner au cours de cette thèse. Merci de m'avoir donné les moyens de mener ce projet à terme et d'avoir su être là dans certains moments difficiles, toujours à l'écoute tout en gardant certaines exigences. Merci à Aurélien d'avoir très rapidement permis une alternative pour la mesure de nos échantillons lorsqu'il s'est avéré que notre dispositif ne serait pas prêt à temps. Merci à Christophe pour son écoute et son soutien quand le moral était au plus bas, ainsi que pour sa capacité à envisager les problématiques (quelles qu'elles soient) avec un recul pertinent.

J'ai eu la chance de côtoyer un grand nombre de personnes tout au long de ma thèse, qui ont à un moment participé à mon effort et/ou ma réflexion. Qu'ils soient du LGGE (Florent D., Olivier M., Manu B., Stef H., Didier V., Julien G., Aude W., Guillaume S., Maxime H. et Gaëtan P.) ou d'ailleurs (Seb V., Thomas B., Christophe B., Jeroen S., Lars-Eric H., Christelle L., Jérémy M.), merci à eux. Je souhaite également associer à mon travail la personne qui m'a formé au travail de terrain et contribué à la collecte de très nombreux échantillons. Cath, merci d'avoir partagé ta très grande expérience. Merci pour la collaboration scientifique, mais surtout pour tous les délires sans lesquels cette campagne n'aurait pas eu la même saveur. Passe le bonjour à Carl Carmoni !

Une pensée amicale pour Fred Minassian et Nadia Pelloux-Léon qui m'ont inculqué la rigueur et l'exigence scientifique dans la décontraction et la bonne humeur. Je leur en suis immensément reconnaissant.

Pour terminer, mes pensées vont vers ma famille et ma belle-famille, qui m'ont toujours soutenu et remonté le moral. Merci à mes parents, qui ont permis à la vie de faire de moi ce que je suis.

Enfin, merci à Sarah pour la nouvelle dimension qu'elle a apporté à ma vie.

Résumé

Depuis plusieurs décennies, l'environnement arctique est en proie à de nombreux changements notamment dus à l'activité humaine. L'Arctique est en effet très sensible aux espèces polluantes issues de l'industrie de masse ainsi qu'au réchauffement global accéléré par les émissions anthropogéniques. Leurs impacts sur les écosystèmes boréaux, visibles dès les années 1970, (Schindler et Smol, 2006) ont motivé de nombreuses études. Ainsi a été démontrée l'importance des sources ponctuelles et du transport atmosphérique longue distance sur la pollution des zones arctiques.

Un des composants clés de l'écosystème arctique est le manteau neigeux saisonnier, car en directe interaction avec l'atmosphère, le sol et les systèmes aquatiques. La neige contient de nombreuses espèces chimiques, microorganismes, particules et impuretés qui en font un milieu chimiquement et biologiquement dynamique, siège de réactions et d'interactions diverses. L'importante interface atmosphère – neige (milieu poreux) donne notamment lieu à de nombreuses réactions d'oxydoréduction photo-induites impliquées dans des cycles chimiques complexes. Néanmoins, peu de choses sont connues sur l'interaction entre les différentes espèces contenues dans le manteau neigeux, et si on sait désormais que les microorganismes y ont une activité significative, on ignore tout ou presque des interactions chimiques éventuelles. Lors de la fonte du manteau neigeux, ce sont toutes les espèces qui y ont été stockées et formées *in situ* qui seront libérées dans l'écosystème aquatique. Ainsi le manteau neigeux saisonnier constitue un réservoir et réacteur crucial d'espèces chimiques, biologiques et contaminantes pour l'environnement arctique.

Le cycle du mercure est dominé par deux systèmes de réactions majeurs : 1) l'oxydo-réduction ($\text{Hg}^0 \leftrightarrow \text{Hg}^{2+}$) ; et 2) la méthylation-déméthylation ($\text{Hg}^{2+} \leftrightarrow \text{CH}_3\text{Hg}^+ \leftrightarrow \text{CH}_3\text{HgCH}_3$). Les espèces formées par méthylation sont le monométhylmercure CH_3Hg^+ (aussi appelé méthylmercure, noté MMHg) et le diméthylmercure CH_3HgCH_3 (noté DMHg). Dans les régions polaires, le mercure élémentaire gazeux atmosphérique est rapidement oxydé et déposé en très grande quantité lors d'épisodes appelés AMDEs (Atmospheric Mercury Depletion Events) survenant au printemps polaire (Schroeder et al., 1998; Steffen et al., 2008). Durant ces épisodes, la neige se comporte comme une « éponge » à mercure et retient des concentrations en mercure très élevées (de l'ordre de la centaine de ng/L). Plusieurs campagnes de terrain ont montré que le mercure pouvait être soit oxydé soit réduit dans le manteau neigeux (Lalonde et al., 2002; Dommergue et al., 2003; Poulain et al., 2004) bien qu'il soit admis que la plus grande partie du mercure divalent déposé dans le manteau neigeux est réduit puis réémis dans l'atmosphère (Poulain et al., 2004; Kirk et al., 2006). Le mercure

stocké par le manteau neigeux est libéré dans les eaux de fontes en période de réchauffement, en partie sous forme monométhylée (MMHg) (Loseto et al., 2004; St. Louis et al., 2005). Un récapitulatif de la chimie du mercure ainsi que de sa réactivité en arctique et dans le manteau neigeux est présenté en chapitre introductif de cette thèse.

L'objectif des travaux présentés dans ce manuscrit est de clarifier l'influence de la chimie du manteau neigeux saisonnier arctique sur la réactivité du mercure qu'il contient, en particulier celle de sa forme méthylmercure. Comment s'y retrouve-t-il ? Est-il transporté dans la neige ou s'y forme-t-il à partir d'autres espèces mercurielles ? Quel rôle joue le manteau neigeux sur la boucle méthylée du cycle du mercure ? Les résultats présentés ci-après exploitent les données d'échantillons de neige saisonnière, collectés entre avril et juin 2011 autour du site côtier de Ny-Ålesund, dans la région du Kongsfjorden (Svalbard).

La thèse est divisée en six parties, subdivisées en chapitres. La première partie présente les connaissances de la biogéochimie du mercure ainsi que de la physico-chimie du manteau neigeux nécessaires à la compréhension des parties de développement qui suivent.

La deuxième partie présente les différentes méthodes analytiques utilisées pour obtenir notre jeu de données à partir des échantillons de terrain. Il comprend aussi la description d'un dispositif de dosage d'ultra-traces de MMHg que nous avons développé au laboratoire, bien qu'il n'ait pas eu l'aboutissement nécessaire pour analyser nos échantillons. Ce travail de développement analytique fait partie intégrante du travail de thèse et a mobilisé beaucoup de temps et de moyens ; il permet aujourd'hui un dispositif fonctionnel dont les performances doivent encore être précisées. La mise en place de ce dispositif est décrite de manière très complète en abordant un point de vue très pratique sur problèmes rencontrés et leurs solutions. Suit un court mais indispensable chapitre de description du site d'étude, de la méthodologie de terrain et des conditions géochimiques et météorologiques du milieu étudié.

Dans la troisième partie, dédiée à l'étude de la chimie de la neige, nous commencerons par quelques observations sur la dynamique du mercure dans le manteau neigeux avant d'aborder dans un deuxième chapitre la chimie du manteau neigeux saisonnier avec une méthodologie nouvelle dans ce domaine, impliquant des rapports de concentrations d'espèces chimiques (Robinson et al., 2006). Cette approche a permis d'identifier les principales sources d'espèces chimiques dans le manteau neigeux côtier, et notamment d'y identifier les principales sources de MMHg. Le troisième chapitre de cette partie s'appuie sur les résultats sur la chimie de la neige pour discuter de la nature de la source principale de MMHg, en raisonnant sur la chimie globale de la neige et des traceurs de source. Nous y développons une nouvelle explication de l'apport de MMHg dans la neige étudiée – basée sur

nos résultats et étayée par une littérature fournie – clarifiant ainsi le faisceau d’hypothèses habituellement évoqué pour expliquer la présence de MMHg dans le manteau neigeux. Nous n’identifions pas de formation de MMHg *in situ* dans le manteau neigeux côtier étudié.

En réponse et en complément à la partie précédente, la quatrième partie traite de la dynamique du MMHg dans la neige et l’eau de fonte. Dans un premier chapitre sont présentés les résultats d’une étude d’un puits de neige sur le glacier Kongsvegen (une année d’accumulation), un site éloigné de la côte du Kongsfjorden. En utilisant la même méthodologie que précédemment, nous observons un processus chimique reliant le MMHg à d’autres espèces chimiques, qui est certainement identifiable uniquement en raison des faibles concentrations et de la stabilité de ce manteau neigeux dans le temps. En se basant sur les résultats d’une étude de laboratoire sur la formation de MMHg (Gårdfeldt et al., 2003), nous attribuons les relations entre ces espèces chimiques à une réaction de méthylation du mercure *in situ*. L’importance de cette réaction dans le budget de MMHg du manteau neigeux ainsi que les implications potentielles de cette observation préliminaire y sont évaluées et discutées. Un dernier chapitre présentera les observations concernant le méthylmercure dans l’eau de fonte, en complément des résultats présentés plus tôt.

Les cinquième et sixième parties sont constituées respectivement d’une discussion conclusive et des annexes.

Table of contents

I. Introduction	1
i. The mercury element	3
ii. An overview of the global mercury cycle	5
iii. The chemical properties of mercury: the consequences on its cycle	8
iv. The problematic of methylmercury in arctic snow	18
II. Experimental section	35
i. Material and methods	39
ii. Field conditions and methodology	75
III. Identification of the primary sources of methylmercury in a coastal arctic snowpack	83
i. Consideration of the input of THg in arctic snow	87
ii. Assessing the sources of major ions using ratio/ratio plots	95
iii. Discussion on the methylmercury sources	127
IV. Processes involving methylmercury in snow and snowmelt water	141
i. Evidences of Hg ^{II} methylation by acetates: a case study	145
ii. Elution of methylmercury from a melting snowpack	159
V. Conclusion & perspectives	167
VI. Appendix	179

I. Introduction

i. The mercury element

-

ii. An overview of the global mercury cycle

-

iii. The chemical properties of mercury and
the consequences on its cycle

-

iv. The problematic of methylmercury in arctic
snow

i. The mercury element

Mercury is a chemical element with the symbol Hg and atomic number 80. It is commonly known as quicksilver and was formerly named hydrargyrum (from Greek "hydr-" water and "argyros" silver). Mercury belongs to the IIb group (or group 12 in the modern IUPAC numbering) of the periodic table, together with zinc and cadmium. Group 12 elements are all soft divalent metals, and have the lowest melting points among all transition metals.

Elemental mercury Hg^0 is the only metal to be liquid at room temperature (melting point: $-38.8\text{ }^\circ\text{C}$, see Figure 1a). Indeed, because of relativistic effects lowering the energy of its valence 6s orbital (Hg: $[\text{Xe}]4f^{14}5d^{10}6s^2$), elemental mercury is less ionizable (thus oxidizable) than other transition metals. Moreover, its non-polar characteristic prevents all Coulombian interactions; it is therefore almost never associated with polar chemical species. Elemental mercury has also little solubility in polar liquids (including water) and no interactions with the usual complexing agents of transition metals. However, ligands showing great affinity with divalent mercury (Hg^{II}) can favor Hg^0 oxidation to Hg^{II} to form the $[\text{Hg}^{\text{II}}\text{L}_n]^{2-n}$ complex (Yamamoto, 1995). Generally, Hg^0 behaves as a noble gas and mainly establishes weak Van der Waals type interactions; it is incidentally the only element (excepting the noble gases) to exist in the form of monoatomic vapors. This weak reactivity of Hg^0 explains its very low boiling point, its volatility and its estimated residence time in the atmosphere (6-18 months). The great majority of atmospheric mercury is Hg^0 .

Mercury in the oxidation degree I is very rare in the environment, it was proposed as intermediate of photolytic oxidations of Hg^0 into Hg^{I} (Zhang, 2006). Because of its electronic structure, Hg^{I} only exists as mercurous ion Hg_2^{2+} .

Divalent mercury Hg^{II} (oxidation degree II) is the main form of mercury in the environment, excluding the atmosphere (see example in Figure 1b). Unlike Hg^0 , Hg^{II} reactivity is similar to the one of oxidized forms of other transition metals. Considered as a soft acid considering the HSAB (Hard and Soft Acids and Basis) theory, it interacts preferentially with soft nucleophiles, such as thiols— often called “mercaptans” because of their affinity with Hg^{II} – or (thio/dithio)carboxylic acids (Dong et al., 2011; Ravichandran, 2004). The “inorganic” term can be wrong, as the range of Hg^{II} species in aqueous systems includes more than the pH-predicted $[\text{HgCl}_n(\text{OH})_m]^{2-n-m}$ ($n+m < 5$) inorganic mercuric complexes (Morel et al., 1998), such as organic complexes or organomercuric species (containing one

or two $\text{Hg}^{\text{II}} - \text{C}$ bonds)(Dong et al., 2010). Organic mercuric complexes can have a stabilizing effect on Hg^{II} , but can also be the precursors to chemical reactions:

- The photoinduced reduction (solar radiations), mainly studied in aqueous systems (water, snow), produces Hg^0 that can evade to the atmosphere (Dommergue et al., 2003; Lalonde et al., 2002). Divalent mercury can also be reduced *via* a microbial pathway when it is bioavailable (Barkay et al., 1997).
- The formation of very toxic organomercuric species, such as (mono)methylmercury ($\text{CH}_3\text{Hg}^+, \text{X}^-$; noted MMHg or MeHg), generated either *via* biotic or abiotic processes, and that biomagnifies along the trophic food chain. The formation and the toxicity of MMHg are further detailed in the following.

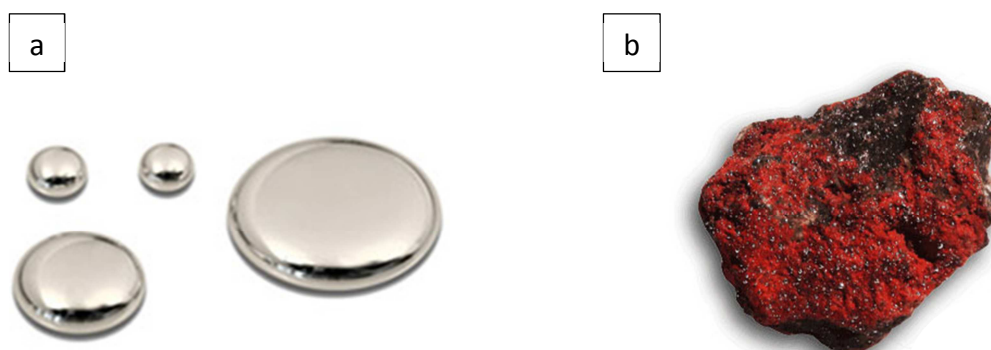


Figure 1. Picture of elemental mercury (a) and cinnabar HgS (b).

Whereas group 11 (or Ib group in the old IUPAC numbering) elements (Cu, Ag, Au) can lose one or two d electrons resulting in ions or complexes in the oxidation degree +II and +III, this is not possible for group 12 elements, which oxidation degree cannot overpass +II. Indeed, the $5d$ orbitals of the mercury atom do not play any role in the $\text{Hg} - \text{X}$ bonds formation; consequently mercury is not really considered as a transition metal, although it has some analogies with them, particularly the ability to form various coordination complexes.

ii. An overview of the global mercury cycle

1. Atmospheric emissions

The industrial and urban activity causes atmospheric emissions of 2320 t/year of mercury (Pirrone et al., 2010). In 2005, the principal processes involved in these anthropogenic emissions were: fossil fuel combustion (40%), artisanal and industrial gold production (17%), non-ferrous metal production (13%), cement industry (10%), waste combustion (8%) and caustic soda production (7%). The relative importance of each source varies widely according to the regions, but fossil fuels are generally the major contributors all around the globe. Only the emissions of Indonesia, Colombia and Brazil are in majority due to gold mining (Pirrone et al., 2010). However, recent estimations assess gold production as the first source of mercury emission even at global scale (UNEP, Global Mercury Assessment, 2013). The geographical distribution of anthropogenic atmospheric mercury emissions is presented in Figure 2.

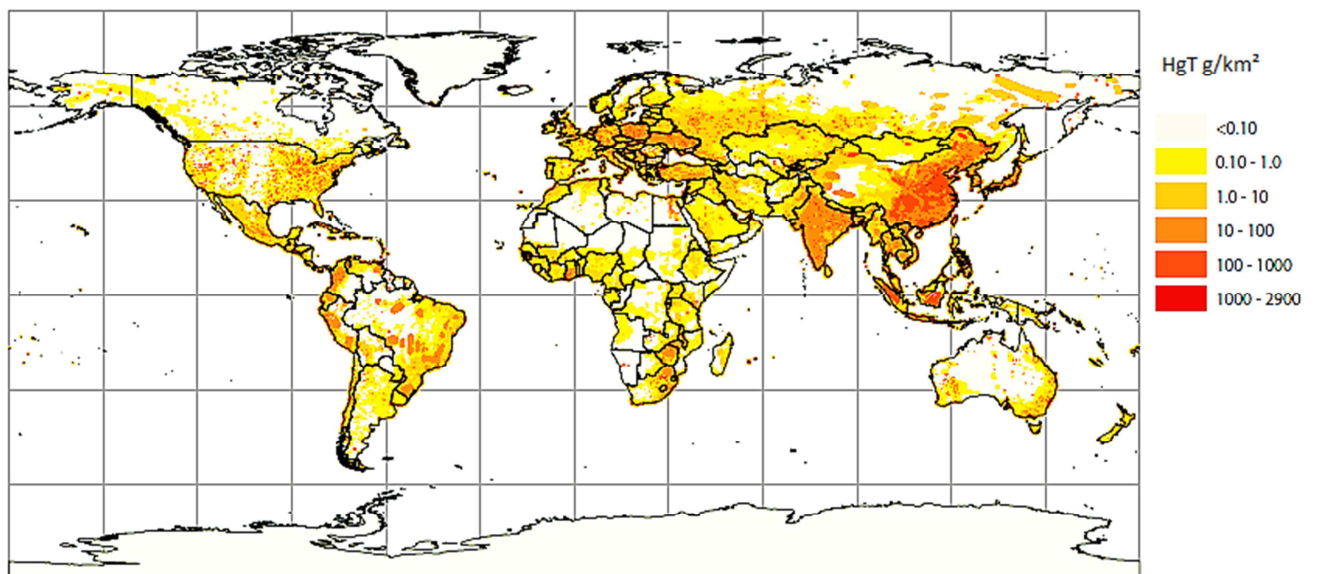


Figure 2. Distribution of anthropogenic atmospheric mercury emissions on a latitude/longitude 0.5° x 0.5° grid. Modified from the Arctic Monitoring and Assessment Programme, 2011.

Annual mercury emissions diminished between 1990 and 2005 (Figure 3), with a substantial decrease in developed countries (European Union, North America and Russia), a strong increasing trend in

Asia, and a slight increase in developing countries (Africa, South America) and Oceania (Arctic Monitoring and Assessment Programme, 2011). In 2005, the main contributors to mercury emissions were Asia (60%, 40% from China only) followed by North America (8.3%), European Union (7.9%), South America (7.3%), Africa (5.5%), Russia (3.9%) and Oceania (2.1%). Beyond demographic and economic concerns, the decrease of anthropogenic mercury emissions is a matter of political will (UNEP, Global Mercury Assessment, 2013).

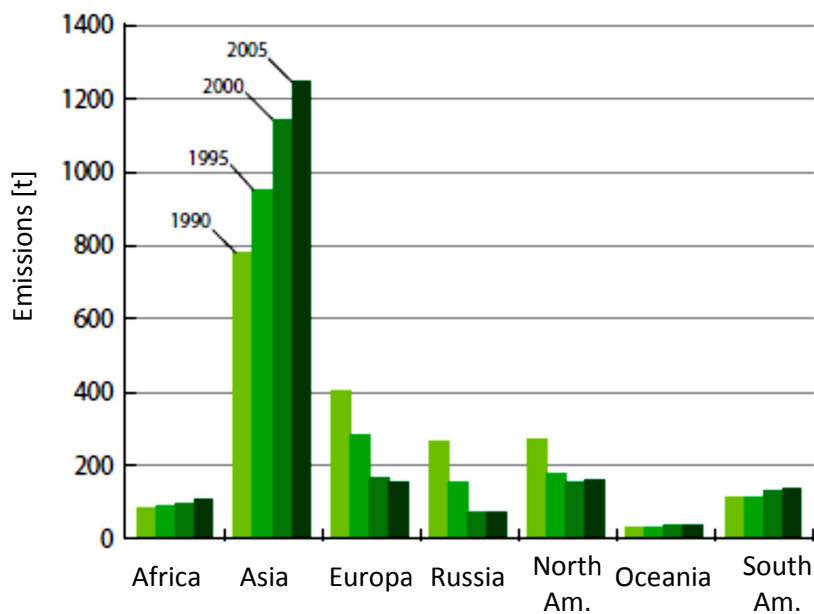


Figure 3. Estimations of anthropogenic atmospheric mercury emissions from different continents/subcontinents. Modified from the Arctic Monitoring and Assessment Programme, 2011.

Natural mercury emissions are nowadays estimated to be around 5200 t/year, which represents around 70% of total emissions (Pirrone et al., 2010). Mercury is present in the terrestrial crust, mainly in the cinnabar form ($\text{Hg}^{\text{II}}\text{S}$), it is delivered to the environment by wet and dry deposition following erosion and volcanic and geothermic activities, which are the primary sources of mercury. In addition to these sources, mercury can be reduced to Hg^0 by photochemical or biological processes and reemitted back to the atmosphere. These reemissions occur from soil and vegetation as well as from oceans, and are considered as secondary sources of mercury (Pirrone et al., 2010).

The oceans are the major contributors to the total mercury emissions (36%), followed by Hg remobilization by biomass burning (9%), erosion of desert and non-wooded metal-bearing regions (7%), and tundras and grasslands (6%). The relative contribution of terrestrial areas to the total mercury emissions is 47%, versus 53% for aquatic areas, and compared to their respective surface

(respectively 3.49 and 1.46×10^8 km² for oceans and continents), the emission rate of terrestrial surfaces is roughly 2.7 times higher than the one of oceans. Biomass burning represents 28% of terrestrial mercury emissions, while 23% are due to deserts and non-wooded metal-bearing regions, 18% to tundras and grasslands and 14% to forests. Primary sources of mercury account for only 4% of terrestrial mercury emissions (Pirrone et al., 2010).

2. Long-range transport

The long distance transportation of mercury mainly occurs in the atmosphere, where mercury is mainly in the Hg⁰ form ($\approx 98\%$) but also in minority in the Hg^{II} form, either in a reactive free phase or in a particulate one (Particulate Mercury, PM). Atmospheric mercury background level in the northern hemisphere – mean concentration in remote area – was estimated to be 1.4 ng/m³ in 2009 (Ebinghaus et al., 2011). This background level is considered as uniform and is constantly diminishing after a peak in the 70's, at a rate of 1.6 - 2.0% per year between 1996 and 2009 (Ebinghaus et al., 2011; Fain et al., 2009; Lindberg et al., 2007). This moderate diminution is the result of the conjugate effects of both absorption of mercury by the oceans (Soerensen et al., 2012) and the drastic mercury emission reductions from the European Union and North America (Wängberg et al., 2007). However, these are almost totally offset by a sharp increase of these emissions in the developing countries (Pacyna et al., 2010) and . As explained previously, Hg⁰ has a relatively long residence time in the atmosphere (6 - 18 months) that allows a long-range transport (at the hemispheric level) within a few days (Arctic Monitoring and Assessment Programme, 2011).

iii. The chemical properties of mercury: the consequences on its cycle

1. Reactivity

a. Methylation

Methylmercury can be formed according to two different kinds of process (Celo et al., 2006): microbial metabolisms (biotic processes) and chemical methylation (abiotic processes). Microbial methylation is the only methylation process recognized in the environment, although abiotic processes cannot be excluded.

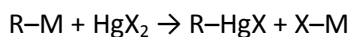
Biotic mercury methylation in the environment is an anaerobic process occurring in sediments and anoxic water columns (Pongratz and Heumann, 1999, 1998). The sulfate reducing bacteria (SRB) and iron reducing bacteria (IRB) are known to show a mercury methylation potential in such media (Fleming et al., 2006; Kerin et al., 2006). The methylation rate depends on the microbial concentration and activity, as well as mercury bioavailability, both depending on several environmental parameters such as temperature, pH, redox potential and the concentrations of organic ligands for mercury (Barkay and Wagner-Döbler, 2005; Barkay et al., 2003, 1997; Golding et al., 2007). Bacteria are also able to form dimethylmercury (DMHg), a volatile compound susceptible to decompose into MMHg (Barkay and Wagner-Döbler, 2005; Pongratz and Heumann, 1999). It has been shown that biotic mercury methylation was possible via methylation of mercuric monocysteine by methyltransferase, following the same reaction than the methylation of cysteine to methionine (Siciliano and Lean, 2002) or by a mechanism involving a ferredoxin as the methyl donor (Parks et al., 2013). Mercury methylation by methylcobalamine (B₁₂ vitamin derivative) has also been evidenced and could be involved in methylmercury formation in the environment, given the importance of the B₁₂ vitamin in the biota (Chen et al., 2007; Choi et al., 1994). However, this reaction could take place *in cellulo* (and be considered as biotic) or *ex cellulo* (and be considered as abiotic).

Abiotic methylation in the environment is photo-mediated and requires the presence of suitable methyl donors, which include small organic molecules such as acetic acid or dimethylsulfoxide, as well as macromolecules such as cobalamines or humic acids (Gårdfeldt et al., 2003; Siciliano et al.,

2005; Yin et al., 2012). Even if some of the potential methyl donors are of biological origin, the methylation is considered as abiotic as soon as the reaction occurs outside any living organism. In the field of molecular chemistry, the reactivity and the chemical properties of mercury are well described, and whereas it tends to be replaced by less toxic species, it has been widely used in organic synthesis (Larock, 1978). The known mechanisms of reactions between mercury and organic compounds (and that are environmentally consistent) are described in the following; all of them lead to the formation of a C – Hg^{II} bond from an inorganic Hg^{II} salt.

The most trivial known reaction allowing the formation of a C – Hg^{II} bond is transmetallation, used in synthesis chemistry to access various organomercurials (Larock, 1978), and suspected to be responsible for some mercury methylation in the environment (Celo et al., 2006; Minganti et al., 2007).

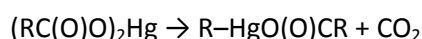
Equation 1



This reaction is favored by the reactivity of the organometallic species R – M (e.g. M = Li, MgX...) and by the created M – X bond strength.

Divalent mercury alkylation or arylation can also occur by decarboxylation of mercuric carboxylate complexes (Pesci reaction).

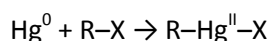
Equation 2



This mechanism is mentioned to explain the formation of MMHg in the environment, notably in rain waters (Gårdfeldt et al., 2003).

The oxidative addition reaction of Hg⁰ with alkyl halides (insertion into the carbon – halogen bond) has been studied from both the theoretical and experimental point of view (Maynard, 1932; Castro et al., personal communication).

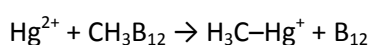
Equation 3



Both approaches agree on the big activation energy necessary for this reaction to proceed, hence leading to a kinetically disfavored reaction. This oxidative addition reaction is therefore unlikely to form MMHg in environmental conditions.

Methylcobalamine (B₁₂ vitamine) is a known methylating agent for Hg^{II} (Chen et al., 2007). The associated mechanism involves a methylide (CH₃⁻ carbanion) transfer from the methylcobalamine to the mercuric ion. Sulfate reducing bacteria use this reaction to methylate mercury (Choi et al., 1994), but as the reaction can take place *ex cellulo*, it could also be the source of abiotic formation in the environment.

Equation 4



The previous examples emphasize that mercury methylation often involves the principle of a nucleophilic addition of CH₃⁻ on Hg^{II} as electrophile. The CH₃⁻ moiety never exists formally as a free carbanion, but in chemical species containing C – X bond where the electronic density is rather lying on the carbon, thus allowing the C – X bond heterolytic cleavage in favor of a nucleophile carbon. Such species need therefore to be identified and preferentially studied in environmental contexts. In addition, several studies mentioned a second mechanism involving radicals, which is nonetheless likely in very minority (Gårdfeldt et al., 2003; Yin et al., 2012). Radical species are often produced by light, and even if the importance of radical mechanism is modest, the UV radiations still have a complex impact on mercury methylation (Malinovsky and Vanhaecke, 2011; Whalin et al., 2007).

- Positive impact: by providing the activation energy necessary for the reaction, or by inducing homolytic cleavages (formation of radicals);
- Negative impact: photodegradation of the produced MMHg and photoreduction of the substrate Hg^{II}.

The reaction of Hg^{II} with acetates – which is the most studied reaction between Hg^{II} and a small organic molecule – is not favored by UV light radiation (which rather favors MMHg decomposition) and does not show evidences of radical mechanism (Gårdfeldt et al., 2003; Yin et al., 2012). Larger molecules, such as humic and fulvic acids (30 to 300 kDa) have also showed a methylation potential in the environment (Hammerschmidt et al., 2007; Siciliano et al., 2005), although the implied mechanisms remain unknown at the molecular scale. Given their omnipresence in aquatic and terrestrial environments (Coble, 1996) as well as their intrinsic nature – mixture of organic molecules

with lots of complexing chemical functions – fulvic and humic acids are of a great interest for mercury biogeochemistry. Their role is however complex – methylation, complexation, reduction (Bartels-Rausch et al., 2011; Dong et al., 2010; Gu et al., 2011; Ravichandran, 2004; Siciliano et al., 2005) – and often related to photochemistry (Black et al., 2012).

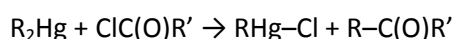
Although the majority of the studies have been led in aqueous media in function of pH and salinity, they often do not take into account neither the very important dilution in the environment, nor the whole complexity of environmental chemistry, which could be susceptible to change mercury complexation (thus availability). Indeed, as mentioned earlier, mercury tends to bind preferentially to organic matter (Dong et al., 2010; Ravichandran, 2004), which is not fully taken into account in studies on the speciation of mercury. This complexation and its effect on reactivity and bioavailability of mercury are still widely unknown given the wide variety and complexity of natural organic matter. However, the complexation of Hg^{II} with methyl donors is considered to be the first step of Hg^{II} methylation (Gårdfeldt et al., 2003). Generally, one should be very cautious before extrapolating the mechanisms presented above to environmental contexts.

b. Demethylation

Two microbial mechanisms lead to MMHg demethylation: oxidative and reductive demethylations. Oxidative demethylation is characterized by a production of Hg^{II} together with CO_2 (and traces of CH_4), whereas reductive demethylation produces Hg^0 and CH_4 only (Barkay and Poulain, 2007; Barkay and Wagner-Döbler, 2005). Organisms possessing the *mer* operon (mercury resistance gene) proceed via reductive demethylation, while the oxidative one occurs according to various biochemical processes (Oremland et al., 1991). The predominance of each mechanism depends on the redox potential of the medium, mercury concentration and speciation; reductive demethylation is however favored in oxic media and at high mercury concentrations (and inversely for oxidative demethylation). Previous studies suggest that the *mer* expression is inhibited in arctic waters (Poulain et al., 2004a; Schaefer et al., 2004). Thus reductive demethylation would not be expected to be dominant in Arctic snow. Oxidative demethylation is also responsible for degradation of small methyl-containing molecules – acetates or methylbromide (Hines et al., 1998) – which is rarely observed in arctic soils (Hines et al., 2001). Hence the likelihood of MMHg degradation in arctic environments is low. However, the occurrence of such biotic demethylating processes in snow and in the Arctic needs to be further addressed (Barkay and Poulain, 2007).

Abiotic mercury demethylation can be promoted by UV light and is responsible for the Hg^{II} reduction to Hg^0 and its subsequent evasion in the atmosphere (Bartels-Rausch et al., 2011; Chen et al., 2003). This reduction reaction is further detailed in the next paragraph. An interesting case of desalkylation(-arylation, -allylation) of organomercuric species in presence of acyl chloride has been observed (Larock and Bernhardt, 1976).

Equation 5



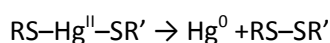
This reaction highlights the “carbanion donor” character of organomercuric species. However the stability of acyl chlorides in the environment and particularly in aqueous media is likely poor, thus the mechanism proposed above is probably not environmentally relevant. Photodegradation of Hg^{II} is the dominant mercury reduction pathway in aquatic environments (Barkay and Poulain, 2007), and has even been shown to be the sole mechanism involved in mercury evasion from an arctic highly oligotrophic freshwater lake (Hammerschmidt and Fitzgerald, 2006).

c. Reduction

Several biotic mercury reduction mechanisms have been discovered. Bacteria possessing the mercury resistance *mer* operon are able to reduce Hg^{II} into Hg^0 , while the other showed mercury reduction by a process depending on Fe^{II} and the cytochrome oxidase enzyme (Barkay et al., 2003; Iwahori et al., 2000; Sugio et al., 2003).

Abiotic mercury reduction is generally photo-mediated and proceeds via organic radicals produced by photolysis of organic molecules (Zhang, 2006). This reaction can take place as well with small organic molecules (benzophenone, $\text{C}_2 - \text{C}_4$ carboxylic diacids...etc.) as in complex organic mixtures (fulvic and humic acids) (Bartels-Rausch et al., 2011; He et al., 2012; Si and Ariya, 2008). Thiols – as excellent ligands for Hg^{II} and inclined to form disulfide bridges – favor Hg^{II} reduction according to the following mechanism (Gu et al., 2011; Si and Ariya, 2011):

Equation 6



Reaction products analysis showed that a radical mechanism can also be responsible for MMHg demethylation (Chen et al., 2003; Si and Ariya, 2008). An example illustrating the diversity and complexity of involved reactions is shown in Figure 4. The reaction constants depend on the temperature, salinity of the medium (Cl^- ions being able to compete with organic ligands for Hg^{II} complexation), pH (influences ligands protonation) and the presence of oxygen, which react with formed radicals and slower the reaction (Gu et al., 2011; Si and Ariya, 2008).

In the snowpack, photo-induced chemical reactions can also lead to Hg^{II} reduction (Dommergue et al., 2007). Photoreduction results in the evasion of almost all the Hg^{II} (in the form of volatile Hg^0) deposited on snow, hence the snow can punctually be a source of Hg^0 for the atmosphere (Kirk et al., 2006; Poulain et al., 2004b). It has been recently suggested that the quasi-liquid-layer surrounding snow grains (more about this in the next I.iv section) could be the priority area where redox reactions of mercury occur (Ferrari et al., 2005), highlighting the potential role of snow physics on mercury chemistry in snow.

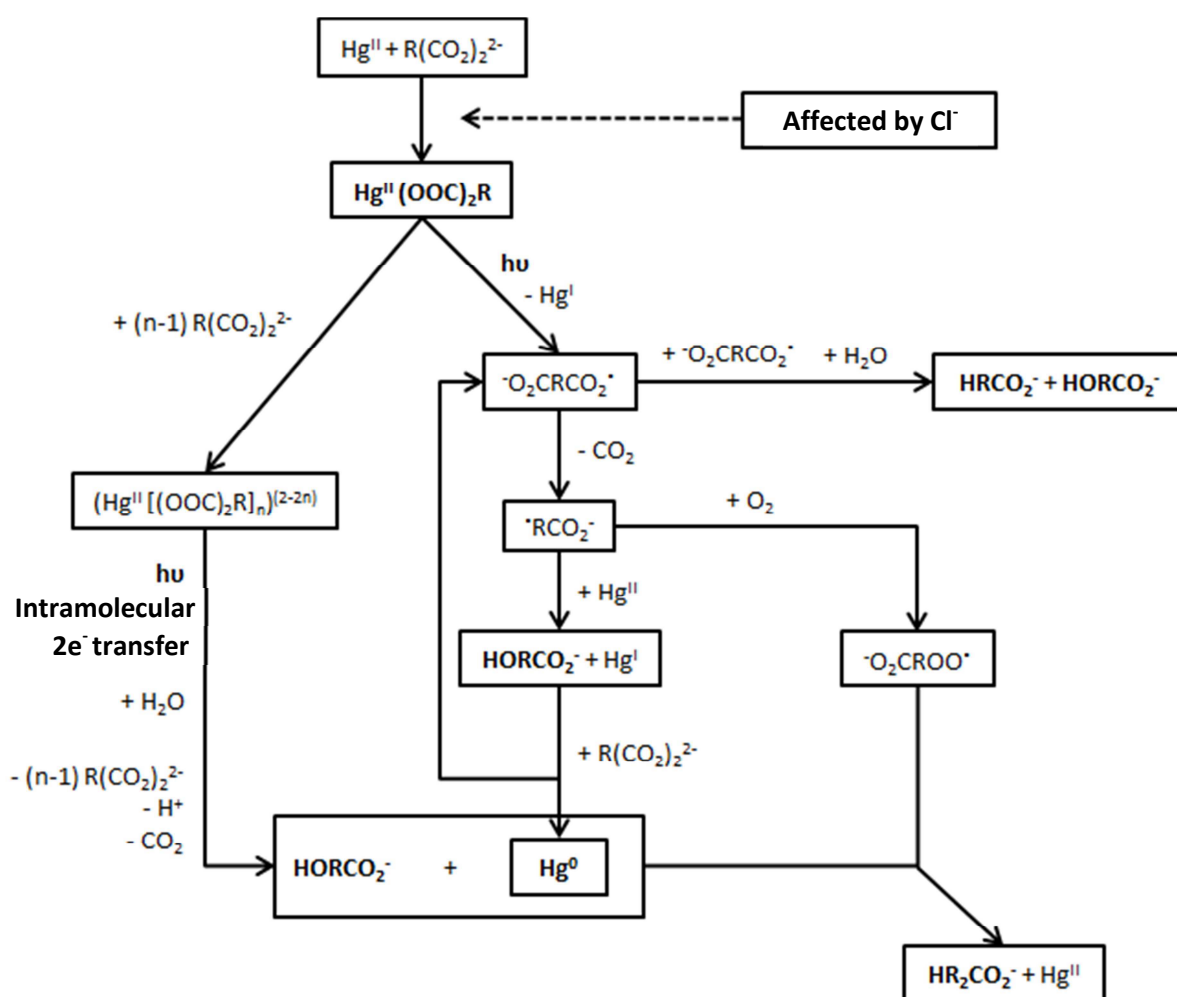


Figure 4. Schematic representation of the reaction mechanism between Hg^{II} and $\text{C}_2 - \text{C}_4$ dicarboxylic acids. Compounds in bold have been identified. Adapted from Si and Ariya, 2008.

2. Health and environmental issues

Mercury is present in the environment in three main key forms: elemental mercury Hg^0 , divalent mercury Hg^{II} and the main organomercuric species: (mono)methylmercury MMHg. The latter is of the utmost importance, as it is highly neurotoxic, even at low doses (Ullrich et al., 2001; Yee and Choi, 1994). It can cause neurological troubles (sense altering, balance disorders...), muscular weaknesses, growth and fertility disorders as well as fetal and cerebral lesions, eventually leading to death in case of prolonged exposure (Castoldi et al., 2001; Harada, 1995; Weiss et al., 2002; Yokoo et al., 2003).

Methylmercury is highly toxic for the ecosystem, as it biomagnifies along aquatic food chains (Campbell et al., 2005; Wren, 1986). The most exposed species are therefore high trophic level ones, for which MMHg represents up to the totality of the mercury accumulated (Schultz and Newman, 1997; Wagemann et al., 1996). It should yet be noted that the mercury concentration (as well as the MMHg proportion of it) can vary according to the species, the size and the age of the considered individual (Dietz et al., 2009).

The mercury concentration in the human body is mainly due to food consumption, notably sea-food (Castoldi et al., 2001; Ratcliffe et al., 1996). Human exposure is limited by a strict legislation, imposing threshold concentrations in the majority of consumed fishes: the World Health Organization (WHO) imposes a mercury concentration below $1 \mu\text{g/g}$ in the dorsal muscle of predatory fishes ($0.5 \mu\text{g/g}$ in non-predatory ones) destined to the food market (Joint FAO/WHO Expert Committee on Food Additives, 2007). Some populations of the Arctic are big fish and high trophic level mammals (seal, beluga, polar bear...) consumers (e.g. Inuits) and can overpass by far the threshold concentration fixed by the WHO ($300 \mu\text{g/week}$, including a maximum of 200 as MMHg)(Arctic Monitoring and Assessment Programme, 2011).

The Arctic is very sensitive to contaminants and pollutants originating from mid-latitudes, and particularly to mercury. The presence of MMHg has been well observed and documented, but although many hypothesis exist to explain it (further description below), it remains undefined (see review by Barkay and Poulain, 2007). The analysis of different biological tissues (teeth, liver, brain, hair...) of many arctic species (marine birds, polar bears, belugas...) shows a steep increase of the mercury concentrations in the arctic wildlife since the beginning of the industrial era (Figure 5). During this time, the mercury concentration in the hair of Greenland inhabitants increased from 3 to 6 times (Dietz et al., 2009).

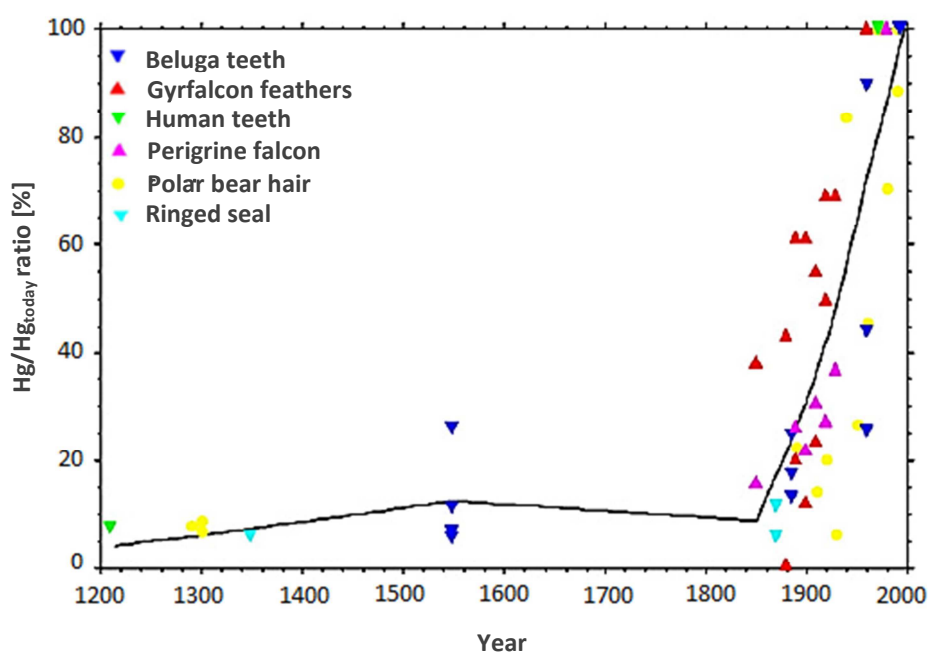


Figure 5. Historical trend of Hg concentrations in different species of the Arctic biota, expressed as a percentage of today values. Adapted from Dietz et al., 2009.

3. Mercury deposition in the Arctic

Mercury deposition in the environment is due to its oxidation from atmospheric Hg^0 to Hg^{II} – as *Reactive Gaseous Mercury* (RGM) and *Particulate Mercury* (PM) – and its subsequent removal from the atmosphere by precipitations, while dry deposition of mercury can also occur (Mowat, 2010; Rutter et al., 2011). Given the cyclic nature of mercury transformation (emission – transportation – deposition – reemission), it can be deposited then reemitted several times before reaching remote regions such as the Arctic (Ariya et al., 2004). In the Arctic, the high surface specific area of snow

could play an important role in RGM adsorption, while PM is suspected to help the nucleation of snow grains (Douglas, 2005).

During arctic springtime (between March and May), events of massive atmospheric Hg^0 oxidation called AMDEs (Atmospheric Mercury Depletion Events) occur simultaneously with ozone depletion events (Schroeder et al., 1998; Steffen et al., 2008). These oxidation events involve mainly Br^\cdot and BrO^\cdot radicals, which result from the photodegradation of marine halogenated species (Br_2 , $\text{BrCl}\dots$) and their subsequent reaction with ozone (Stephens et al., 2012). These punctual AMDEs are characterized by the almost-total loss of atmospheric Hg^0 together with formation and massive deposition of Hg^{II} (RGM and PM) onto the snow, soil and sea surface (Figure 6).

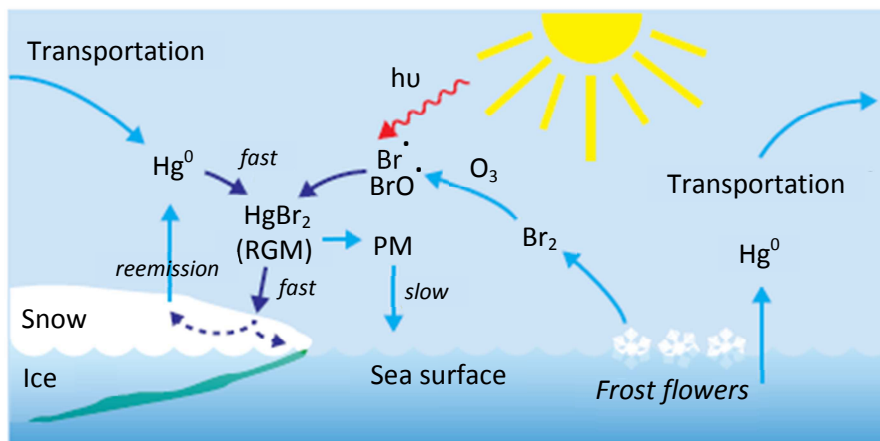


Figure 6. Schematic representation of the mechanisms involved in the mercury cycling in arctic, including Hg^{II} deposition during photo-mediated AMDEs, and Hg^0 evasion from open surfaces.

A recent study showed that the tropospheric layer affected by AMDEs could be up to 1 km thick, with a substantial difference between terrestrial and marine surfaces (Mao et al., 2011). Although it is commonly accepted that most of the Hg^{II} deposited onto snow is rapidly reduced and reemitted back to the atmosphere (Kirk et al., 2006; Poulain et al., 2004b), the remaining fraction can potentially undergo various transformations. The average mercury reemission at Alert (Canadian Arctic) over a 14-days long period of time offsets 59% of deposited mercury during the same time lapse (Brooks et al., 2006), versus more than 75% following a strong deposition event (St. Louis et al., 2005). The mercury stored in seasonal snow is delivered to the aquatic ecosystem during the snowmelt, partially as MMHg (Loseto et al., 2004; St. Louis et al., 2005). This whole process contributes to the MMHg pool that biomagnifies in aquatic food chains, leading to significant mercury concentrations measured in the arctic wildlife, although the Arctic is remote from any mercury emission area (Arctic Monitoring and Assessment Programme, 2011).

As MMHg is of great concern regarding environmental and health issues in the Arctic, the objective of the present manuscript is to clarify the mercury cycle in arctic snow, and particularly regarding the presence of MMHg. The following section presents an overview of the knowledge needed for this purpose. A solid knowledge of the known aspects of the biogeochemistry of mercury – such as its sources and reactivity – is indispensable but not sufficient. In order to fully consider the potential reactivity of mercury in snow, one shall be aware of the intrinsic properties of snow, which appears more and more to be a dynamic reactor for many chemical reactions, including those involving mercury. The next section starts with a global picture of what is a snowpack. The characteristics of snow are not reported fully and with every detail, as this is not the purpose here; however, it should provide sufficient knowledge on how a snowpack behaves and how its characteristics affect or could affect its chemical content and reactivity. Current knowledge of the arctic MMHg biogeochemical cycle will then be presented.

iv. The problematic of methylmercury in arctic snow

1. Physic-chemistry of the snowpack

The formation of the snowpack is mainly due to discontinuous precipitations resulting in a structure of horizontal layers superposition (Colbeck, 1991). Other processes are involved, such as rain events (rain water freezes once in the snowpack) and condensation of atmospheric water vapor on surface snow, forming surface hoar (Cabanes et al., 2002). Moreover, the snow cover perpetually experiences physical changes, as the structure of the snow grains changes according to the atmospheric conditions. These changes – called snow metamorphism – are due to moisture transfers between bottom and surface snow (sublimation – condensation) as well as mechanical compaction and erosion phenomena, mainly due to wind (Colbeck, 1983). These phenomena vary with the temperature profile of the snowpack, and are responsible for significant changes in the different physical parameters of the snowpack, among which:

- The density, representing the air/ice ratio of the snowpack, and which varies typically between 0.2 and 0.4 g/cm³. The compaction phenomena, for instance, tend to increase the density. The typical density values indicate that apart from potential ice layers, snowpacks are mainly made of air (Domine et al., 2008).
- The surface specific area (SSA), representing the surface of the air – ice interface per unit of mass. Typical values can vary widely according to the snow type, from 80 cm²/g for depth hoar to 1600 cm²/g for fresh snow (Domine et al., 2008).

Snow metamorphism leads to a constant evolution of snow crystals shape, depending on their location in the snowpack and the temperature gradient in it. As a consequence, the snowpack shall be divided in layers differing from each other by the morphological properties of the snow grains (see examples in Figure 7). The moisture transfer processes also impact chemistry in the snowpack: sublimation or melting of the surface of a grain can uncover species previously located deeper in the grain, whereas water vapor condensation can inversely trap species previously located at the surface of the grain.

Despite that the snowpack is often integrally porous, the 50 to 100 top centimeters are considered as the most important regarding snow chemistry, as exchanges with the atmosphere are more important there, notably because of wind-forced convection (Albert et al., 2002; Domine, 2002). The 10 to 20 top centimeters constitute the photic area, where the incoming solar radiations are the most important, favoring therefore photo-induced chemical reactions (Simpson et al., 2002; Perovich, 2007). Many redox reactions are observed in this photic area: nitrate photolysis, for instance, plays an important role in the nitrogen species (NO_x) cycle (Domine, 2002; Honrath et al., 2000; Moller et al., 2010; Simpson et al., 2002a, 2002b). At a smaller scale, the surface of snow crystals shows a more disordered molecular H_2O network than the one of their inside, with properties between those of ice and liquid water. This disordered surface layer, called the quasi-liquid layer (QLL), is possibly the privileged area for multiphasic reactions, as it marks the snow – air interface (Ferrari et al., 2005; Jacobi and Hilker, 2007; Thomas et al., 2011).

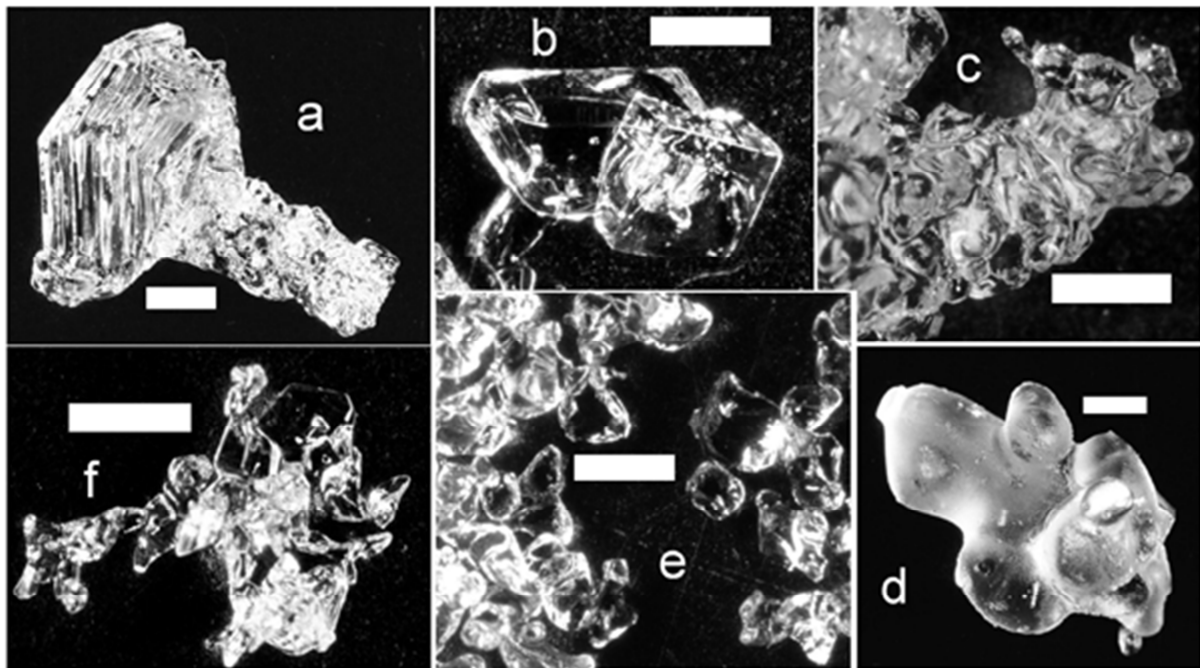


Figure 7. Photochromatographs of metamorphic crystals commonly encountered in snowpacks: (a) depth hoar; (b) faceted crystals; (c) dense melt-refreeze crust; (d) melt-refreeze polycrystal originated from a low density melt-refreeze crust (0.11 g/cm^3); (e) mid-sized grains originated from a quasi-basal layer (density = 0.35 g/cm^3); (f) mixt crystal with rounded shapes and facets. White bars represent 1 mm (reproduction from Domine et al., 2008).

The chemical species contained in a snowpack originate either from the atmosphere or from other sources relatively close to the snowpack. During the formation of ice crystals in the troposphere by water condensation (Kuhn, 2001), many gaseous species are co-condensed and trapped in snowflakes; aerosols and various particles participating to the grains nucleation are additional sources of chemicals (Andreae and Rosenfeld, 2008)(Toom-Saunty and Barrie, 2002; Douglas and Sturm, 2004; De Caritat et al., 2005; Krnavek et al., 2012). Hence fresh snow already has a complex

chemical composition by the time of its deposition. Other sources can participate – as for example marine surface at coastal sites, geological erosion or anthropogenic activity – and be susceptible to alter the chemistry of the snowpack (de Caritat et al., 2005; Douglas and Sturm, 2004; Krnavek et al., 2011; Toom-Sauntry and Barrie, 2002). In addition, the snow is constantly exchanging with the atmosphere through adsorption, desorption and diffusion of 1) air streams into the snowpack (wind convection); and 2) chemical species into the ice material. The presence in snow of aerosols and particles containing microorganisms – 200 - 5000 cells/mL (Alfreider et al., 1996; Carpenter et al., 2000; Segawa et al., 2005) – suggest that biological activity may be possible, producing bioorganic (macro)molecules that participate to the chemical diversity of snow (Alfreider et al., 1996; Carpenter et al., 2000). The current state of analytical techniques allows for an overview of the whole chemical content of a snowpack, but a discrete, detailed and complete chemical composition remains illusory. Indeed, the chemical content of snow is too rich and varied, and analytical methods are sometimes not sensitive enough and/or allow access to values corresponding to mixtures of different species, e.g. total organic carbon (TOC, see the “Materials and Methods” chapter), or humic-like substances (HULIS). Finally, the chemical characterization of snow always requires a melting, which can change the concentrations of volatile species (by addition or removal) and which excludes any spatial resolution of the chemicals repartition at the grain scale. A recent comparison of the pH of ice before and after melting (and inversely before and after freezing) confirmed that the act of melting can induce analytical discrepancies (Wren and Donaldson, 2012).

2. The snowmelt: a transfer of contaminants to the arctic ecosystem

The snowmelt is a metamorphic process due to positive temperatures and intense solar radiations, that occurs sometimes at negative temperatures (Kuhn, 1987). Superficial layers of snow grains melt first and the resulting meltwater percolates down to the basis of the snowpack through melt – refreeze cycles. In moderate melting conditions, liquid water is retained in concave cavities of snow crystals and in interstitial gaps; the refreeze of these liquid pockets is responsible of the changes in snow grains shape. Water can fill between 5 and 10% of the total interstitial space before percolating deeper (Colbeck, 1981, 1979). The meltwater runoff at the surface of snow grains – in addition to the metamorphic consequences – leads to the dissolution and mobilization of chemical species. As a result, these species are eluted away from both the melting snow grains and the surface of the snow grains crossed by meltwater streams. Simultaneously and consequently, the meltwater stream gets richer in eluted chemical species when percolating toward the bottom of the snowpack. If the

atmospheric conditions allow it, snowmelt water can refreeze in the middle of the snowpack and form high density layers (close to ice), but in strong melting conditions, meltwater reaches the ground before refreezing as an ice layer (Kuhn, 2001).

As they follow the path of meltwater streams, chemical compounds are re-concentrated in interstitial spaces and cavities of the snow grains first, then in the ice layer formed by meltwater refreezing at the bottom of the snowpack. The chemicals are eluted according to their solubility in water: inorganic ions first and the most hydrophobic organic molecules at last (Eichler et al., 2001; Meyer et al., 2009, 2006), while particles usually remain trapped in snow until the last step of the snowmelt (Berry Lyons et al., 2003; Meyer et al., 2006). The rain events, whether they happen during or before the melting periods, favor the elution process the same way that percolating meltwater does (Daly and Wania, 2004). Chemical species are rapidly removed from the snowpack, as roughly 80% of them are eluted by the first third of meltwater, with variations according to the snow type (Kuhn, 2001). The meltwater streams hence deliver as a pulse the majority of the chemical species contained in the snowpack to the tributary ecosystems: soils, swamps, fjords. The shorter the melting season, the more concentrated the pulse is; in the Arctic, the melting season is usually very short (around 2 weeks), which exposes the arctic ecosystems to a very strong chemical pulse at the end of arctic spring (Daly and Wania, 2004).

3. The sources of MMHg in arctic snow

As described above, the snowpack is a dynamic, heterogeneous and complex medium. Its physical properties and chemical composition are not yet fully understood. Mercury is in constant exchange between snow and atmosphere, *via* redox cycling. Once in the interstitial air of the snowpack, Hg^0 can be oxidized to Hg^{II} (Maron et al., 2008; O'Concubhair et al., 2012) and deposited in snow but also reemitted back following Hg^{II} reduction (see the I.iii section). However, in this manuscript, our main focus is the dynamics of MMHg in the snowpack, which require knowledge of the previous studies on this topic, presented in the following.

Methylmercury is present in snow at the tenth of picogram per liter (of melted snow) range. Given its high neurotoxicity and ability to biomagnify in the trophic chain, it constitutes a danger when delivered to aquatic ecosystems during the snowmelt (Loseto et al., 2004). A few phenomena are suspected to explain the presence of MMHg in snow:

- An atmospheric source for MMHg, suspected to be due to the evasion of dimethylmercury from leads and polynyas where it may be formed by phytoplankton in

the water column (Pongratz and Heumann, 1999, 1998), and its subsequent atmospheric photodegradation to monomethylmercury chloride (Niki et al., 1983; Waring and Pellin, 1967) and deposition.

- Biotic or abiotic *in situ* methylation. Once in snow, Hg^{II} is likely mainly bound to organic molecules, despite the presence in majority of competing inorganic ligands (Cl^- , HO^- ...etc.)(Dong et al., 2011; Ravichandran, 2004). Microorganisms present in snow – and which show evidences of biological activity (Alfreider et al., 1996; Carpenter et al., 2000) – can also metabolize or incorporate by diffusion the deposited Hg^{II} , according to its bioavailability. The biotic and abiotic complexes formed can favor the methylation by methyl transfer from the ligand -or a third methyl-donating species) to Hg^{II} . Biochemical reactions involved in the sulfur cycle have been recently suspected to lead to *in situ* methylation of bioavailable mercury (Larose et al., 2011, 2010). For more information about the possible mechanisms, refer to the “Methylation” paragraph of the I.iii section.
- Mercury methylation in the atmosphere at the surface of aerosols, which showed a potential as biochemical reactors (Ariya and Amyot, 2004; Ariya, 2002). Particles participating to the snow nucleation or adsorbed at the surface of the snow crystals will contribute to the chemical content of the snowpack after deposition.

The current overview of the MMHg input pathways in snow is presented in Figure 8. All the mechanisms proposed in Figure 8 have been observed and described in other contexts (Bartels-Rausch et al., 2011; Black et al., 2012; Chen et al., 2003; Gårdfeldt et al., 2003; Larose et al., 2010; Malinovsky and Vanhaecke, 2011; Maron et al., 2008; O’Concubhair et al., 2012; Stephens et al., 2012; Whalin et al., 2007; Yamamoto, 1995) and all are susceptible to occur in snow. The biotic and abiotic contributions to these mechanisms remain undefined. Based on the knowledge presented in this last introductory section, the following chapters propose a new insight on the origin of MMHg in snow using a novel analytical approached of snow chemistry.

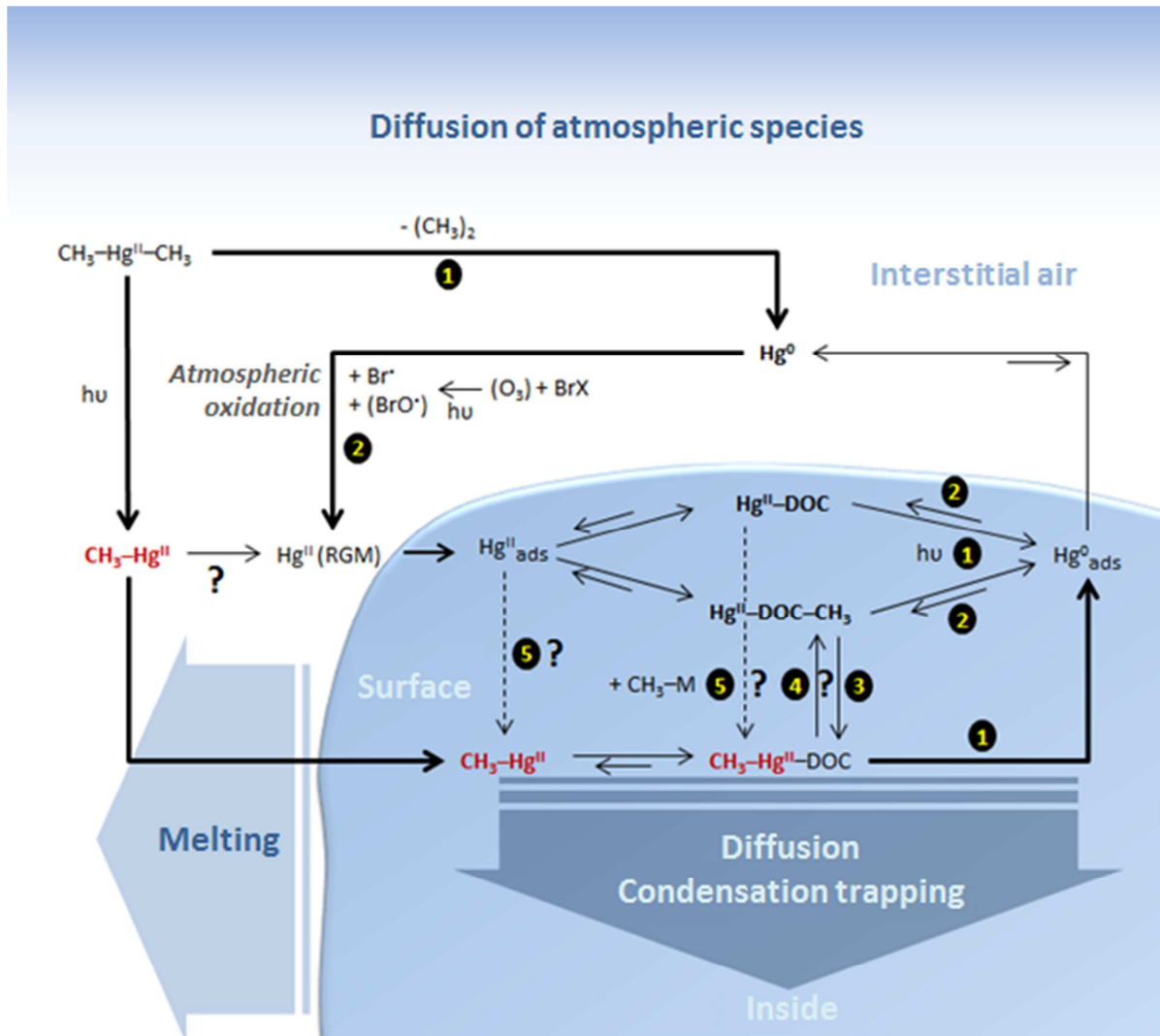


Figure 8. Summary of the mechanisms possibly involved in the MMHg (in red) cycling in snow: (1) reductive elimination; (2) oxidative addition; (3) transmethylation from a methyl donor to Hg^{II} ; (4) transmethylation from MMHg (demethylation of Hg^{II}) and (5) transmetallation (methyltransfer from a metal to Hg^{II} , $\text{M} = \text{Sn}, \text{Pb} \dots$).

References

- Albert, M.R., Grannas, A.M., Bottenheim, J., Shepson, P.B., Perron, F.E., 2002. Processes and properties of snow–air transfer in the high Arctic with application to interstitial ozone at Alert, Canada. *Atmos. Environ.* 36, 2779–2787.
- Alfreider, A., Pernthaler, J., Amann, R., Sattler, B., Glockner, F., Wille, A., Psenner, R., 1996. Community analysis of the bacterial assemblages in the winter cover and pelagic layers of a high mountain lake by in situ hybridization. *Appl. Environ. Microbiol.* 62, 2138–2144.
- Andreae, M.O., Rosenfeld, D., 2008. Aerosol–cloud–precipitation interactions. Part 1. The nature and sources of cloud-active aerosols. *Earth-Sci. Rev.* 89, 13–41.
- Arctic Monitoring and Assessment Programme, 2011. AMAP assessment 2011. Arctic Monitoring and Assessment Programme, Oslo, Norway.
- Ariya, P.A., 2002. Microbiological degradation of atmospheric organic compounds. *Geophys. Res. Lett.* 29.
- Ariya, P.A., Amyot, M., 2004. New Directions: The role of bioaerosols in atmospheric chemistry and physics. *Atmos. Environ.* 38, 1231–1232.
- Ariya, P.A., Dastoor, A.P., Amyot, M., Schroeder, W.H., Barrie, L., Anlauf, K., Raofie, F., Ryzhkov, A., Davignon, D., Lalonde, J., Steffen, A., 2004. The Arctic: a sink for mercury. *Tellus B* 56, 397–403.
- Barkay, T., Gillman, M., Turner, R.R., 1997. Effects of dissolved organic carbon and salinity on bioavailability of mercury. *Appl. Environ. Microbiol.* 63, 4267–4271.
- Barkay, T., Miller, S.M., Summers, A.O., 2003. Bacterial mercury resistance from atoms to ecosystems. *FEMS Microbiol. Rev.* 27, 355–384.
- Barkay, T., Poulain, A.J., 2007. Mercury (micro)biogeochemistry in polar environments. *FEMS Microbiol. Ecol.* 59, 232–241.
- Barkay, T., Wagner-Döbler, I., 2005. Microbial Transformations of Mercury: Potentials, Challenges, and Achievements in Controlling Mercury Toxicity in the Environment, in: *Advances in Applied Microbiology*. Elsevier, pp. 1–52.
- Bartels-Rausch, T., Krysztofiak, G., Bernhard, A., Schläppi, M., Schwikowski, M., Ammann, M., 2011. Photoinduced reduction of divalent mercury in ice by organic matter. *Chemosphere* 82, 199–203.
- Berry Lyons, W., Welch, K.A., Fountain, A.G., Dana, G.L., Vaughn, B.H., McKnight, D.M., 2003. Surface glaciochemistry of Taylor Valley, southern Victoria Land, Antarctica and its relationship to stream chemistry. *Hydrol. Process.* 17, 115–130.

- Black, F.J., Poulin, B.A., Russell Flegal, A., 2012. Factors controlling the abiotic photo-degradation of monomethylmercury in surface waters. *Geochim. Cosmochim. Acta*.
- Brooks, S.B., Saiz-Lopez, A., Skov, H., Lindberg, S.E., Plane, J.M.C., Goodsite, M.E., 2006. The mass balance of mercury in the springtime arctic environment. *Geophys. Res. Lett.* 33.
- Cabanes, A., Legagneux, L., Dominé, F., 2002. Evolution of the specific surface area and of crystal morphology of Arctic fresh snow during the ALERT 2000 campaign. *Atmos. Environ.* 36, 2767–2777.
- Campbell, L.M., Norstrom, R.J., Hobson, K.A., Muir, D.C.G., Backus, S., Fisk, A.T., 2005. Mercury and other trace elements in a pelagic Arctic marine food web (Northwater Polynya, Baffin Bay). *Sci. Total Environ.* 351-352, 247–263.
- Carpenter, E.J., Lin, S., Capone, D.G., 2000. Bacterial Activity in South Pole Snow. *Appl. Environ. Microbiol.* 66, 4514–4517.
- Castoldi, A.F., Coccini, T., Ceccatelli, S., Manzo, L., 2001. Neurotoxicity and molecular effects of methylmercury. *Brain Res. Bull.* 55, 197–203.
- Celo, V., Lean, D., Scott, S., 2006. Abiotic methylation of mercury in the aquatic environment☆. *Sci. Total Environ.* 368, 126–137.
- Chen, B., Wang, T., Yin, Y., He, B., Jiang, G., 2007. Methylation of inorganic mercury by methylcobalamin in aquatic systems. *Appl. Organomet. Chem.* 21, 462–467.
- Chen, J., Pehkonen, S.O., Lin, C.-J., 2003. Degradation of monomethylmercury chloride by hydroxyl radicals in simulated natural waters. *Water Res.* 37, 2496–2504.
- Choi, S.C., Chase, T., Jr, Bartha, R., 1994. Enzymatic catalysis of mercury methylation by *Desulfovibrio desulfuricans* LS. *Appl. Environ. Microbiol.* 60, 1342–1346.
- Coble, P.G., 1996. Characterization of marine and terrestrial DOM in seawater using excitation-emission matrix spectroscopy. *Mar. Chem.* 51, 325–346.
- Colbeck, S.C., 1979. Water flow through heterogeneous snow. *Cold Reg. Sci. Technol.* 1, 37–45.
- Colbeck, S.C., 1981. A simulation of the enrichment of atmospheric pollutants in snow cover runoff. *Water Resour. Res.* 17, 1383.
- Colbeck, S.C., 1983. Snow Particle Morphology in the Seasonal Snow Cover. *Bull. Am. Meteorol. Soc.* 64, 602–609.
- Colbeck, S.C., 1991. The layered character of snow covers. *Rev. Geophys.* 29, 81.
- Daly, G.L., Wania, F., 2004. Simulating the Influence of Snow on the Fate of Organic Compounds. *Environ. Sci. Technol.* 38, 4176–4186.
- De Caritat, P., Hall, G., Gislason, S., Belsey, W., Braun, M., Goloubeva, N.I., Olsen, H.K., Scheie, J.O., Vaive, J.E., 2005. Chemical composition of arctic snow: concentration levels and regional distribution of major elements. *Sci. Total Environ.* 336, 183–199.

- Dietz, R., Outridge, P.M., Hobson, K.A., 2009. Anthropogenic contributions to mercury levels in present-day Arctic animals—A review. *Sci. Total Environ.* 407, 6120–6131.
- Domine, F., 2002. Air-Snow Interactions and Atmospheric Chemistry. *Science* 297, 1506–1510.
- Domine, F., Albert, M., Huthwelker, T., Jacobi, H.-W., Kokhanovsky, A.A., Lehning, M., Picard, G., Simpson, W.R., 2008. Snow physics as relevant to snow photochemistry. *Atmospheric Chem. Phys.* 8, 171–208.
- Dommergue, A., Bahlmann, E., Ebinghaus, R., Ferrari, C., Boutron, C., 2007. Laboratory simulation of Hg⁰ emissions from a snowpack. *Anal. Bioanal. Chem.* 388, 319–327.
- Dommergue, A., Ferrari, C.P., Poissant, L., Gauchard, P.-A., Boutron, C.F., 2003. Diurnal Cycles of Gaseous Mercury within the Snowpack at Kuujuarapik/Whapmagoostui, Québec, Canada. *Environ. Sci. Technol.* 37, 3289–3297.
- Dong, W., Bian, Y., Liang, L., Gu, B., 2011. Binding Constants of Mercury and Dissolved Organic Matter Determined by a Modified Ion Exchange Technique. *Environ. Sci. Technol.*
- Dong, W., Liang, L., Brooks, S., Southworth, G., Gu, B., 2010. Roles of dissolved organic matter in the speciation of mercury and methylmercury in a contaminated ecosystem in Oak Ridge, Tennessee. *Environ. Chem.* 7, 94.
- Douglas, T.A., 2005. Elevated mercury measured in snow and frost flowers near Arctic sea ice leads. *Geophys. Res. Lett.* 32.
- Douglas, T.A., Sturm, M., 2004. Arctic haze, mercury and the chemical composition of snow across northwestern Alaska. *Atmos. Environ.* 38, 805–820.
- Ebinghaus, R., Jennings, S.G., Kock, H.H., Derwent, R.G., Manning, A.J., Spain, T.G., 2011. Decreasing trends in total gaseous mercury observations in baseline air at Mace Head, Ireland from 1996 to 2009. *Atmos. Environ.* 45, 3475–3480.
- Eichler, A., Schwikowski, M., Gaggeler, H.W., 2001. Meltwater-induced relocation of chemical species in Alpine firn. *Tellus B* 53, 192–203.
- Fain, X., Ferrari, C.P., Dommergue, A., Albert, M.R., Battle, M., Severinghaus, J., Arnaud, L., Barnola, J.-M., Cairns, W., Barbante, C., Boutron, C., 2009. Polar firn air reveals large-scale impact of anthropogenic mercury emissions during the 1970s. *Proc. Natl. Acad. Sci.* 106, 16114–16119.
- Ferrari, C., Gauchard, P., Aspö, K., Dommergue, A., Magand, O., Bahlmann, E., Nagorski, S., Temme, C., Ebinghaus, R., Steffen, A., 2005. Snow-to-air exchanges of mercury in an Arctic seasonal snow pack in Ny-Ålesund, Svalbard. *Atmos. Environ.* 39, 7633–7645.
- Fleming, E.J., Mack, E.E., Green, P.G., Nelson, D.C., 2006. Mercury Methylation from Unexpected Sources: Molybdate-Inhibited Freshwater Sediments and an Iron-Reducing Bacterium. *Appl. Environ. Microbiol.* 72, 457–464.

- Gårdfeldt, K., Munthe, J., Strömberg, D., Lindqvist, O., 2003. A kinetic study on the abiotic methylation of divalent mercury in the aqueous phase. *Sci. Total Environ.* 304, 127–136.
- Golding, G.R., Kelly, C.A., Sparling, R., Loewen, P.C., Barkay, T., 2007. Evaluation of Mercury Toxicity as a Predictor of Mercury Bioavailability. *Environ. Sci. Technol.* 41, 5685–5692.
- Gu, B., Bian, Y., Miller, C.L., Dong, W., Jiang, X., Liang, L., 2011. Mercury reduction and complexation by natural organic matter in anoxic environments. *Proc. Natl. Acad. Sci.* 108, 1479–1483.
- Hammerschmidt, C.R., Fitzgerald, W.F., 2006. Photodecomposition of Methylmercury in an Arctic Alaskan Lake. *Environ. Sci. Technol.* 40, 1212–1216.
- Hammerschmidt, C.R., Lamborg, C.H., Fitzgerald, W.F., 2007. Aqueous phase methylation as a potential source of methylmercury in wet deposition. *Atmos. Environ.* 41, 1663–1668.
- Harada, M., 1995. Minamata Disease: Methylmercury Poisoning in Japan Caused by Environmental Pollution. *Crit. Rev. Toxicol.* 25, 1–24.
- He, F., Zheng, W., Liang, L., Gu, B., 2012. Mercury photolytic transformation affected by low-molecular-weight natural organics in water. *Sci. Total Environ.*
- Hines, M.E., Crill, P.M., Varner, R.K., Talbot, R.W., Shorter, J.H., Kolb, C.E., Harriss, R.C., 1998. Rapid consumption of low concentrations of methyl bromide by soil bacteria. *Appl. Environ. Microbiol.* 64, 1864–1870.
- Hines, M.E., Duddleston, K.N., Kiene, R.P., 2001. Carbon flow to acetate and C₁ compounds in northern wetlands. *Geophys. Res. Lett.* 28, 4251–4254.
- Honrath, R.E., Guo, S., Peterson, M.C., Dziobak, M.P., Dibb, J.E., Arsenault, M.A., 2000. Photochemical production of gas phase NO_x from ice crystal NO₃⁻. *J. Geophys. Res.* 105, 24183.
- Iwahori, K., Takeuchi, F., Kamimura, K., Sugio, T., 2000. Ferrous Iron-Dependent Volatilization of Mercury by the Plasma Membrane of *Thiobacillus ferrooxidans*. *Appl. Environ. Microbiol.* 66, 3823–3827.
- Jacobi, H.-W., Hilker, B., 2007. A mechanism for the photochemical transformation of nitrate in snow. *J. Photochem. Photobiol. Chem.* 185, 371–382.
- Joint FAO/WHO Expert Committee on Food Additives, Meeting, W.H.O., Food and Agriculture Organization of the United Nations, 2007. Evaluation of certain food additives and contaminants sixty-seventh report of the Joint FAO/WHO Expert Committee on Food Additives. World Health Organization, Geneva, Switzerland.
- Kerin, E.J., Gilmour, C.C., Roden, E., Suzuki, M.T., Coates, J.D., Mason, R.P., 2006. Mercury Methylation by Dissimilatory Iron-Reducing Bacteria. *Appl. Environ. Microbiol.* 72, 7919–7921.

- Kirk, J.L., St. Louis, V.L., Sharp, M.J., 2006. Rapid Reduction and Reemission of Mercury Deposited into Snowpacks during Atmospheric Mercury Depletion Events at Churchill, Manitoba, Canada. *Environ. Sci. Technol.* 40, 7590–7596.
- Krnavek, L., Simpson, W.R., Carlson, D., Domine, F., Douglas, T.A., Sturm, M., 2011. The chemical composition of surface snow in the Arctic: Examining marine, terrestrial, and atmospheric influences. *Atmos. Environ.*
- Kuhn, M., 1987. Micro-meteorological conditions for snow melt. *J. Glaciol.* 33, 24–26.
- Kuhn, M., 2001. The nutrient cycle through snow and ice, a review. *Aquat. Sci.* 63, 150–167.
- Lalonde, J.D., Poulain, A.J., Amyot, M., 2002. The Role of Mercury Redox Reactions in Snow on Snow-to-Air Mercury Transfer. *Environ. Sci. Technol.* 36, 174–178.
- Larock, R.C., 1978. Organomercury Compounds in Organic Synthesis. *Angew. Chem. Int. Ed. Engl.* 17, 27–37.
- Larock, R.C., Bernhardt, J.C., 1976. Mercury in organic chemistry VIII. A convenient synthesis of α,β -unsaturated ketones. *Tetrahedron Lett.* 17, 3097–3100.
- Larose, C., Dommergue, A., De Angelis, M., Cossa, D., Averty, B., Maruszczak, N., Soumis, N., Schneider, D., Ferrari, C., 2010. Springtime changes in snow chemistry lead to new insights into mercury methylation in the Arctic. *Geochim. Cosmochim. Acta* 74, 6263–6275.
- Larose, C., Dommergue, A., Maruszczak, N., Coves, J., Ferrari, C.P., Schneider, D., 2011. Bioavailable Mercury Cycling in Polar Snowpacks. *Environ. Sci. Technol.*
- Lindberg, S., Bullock, R., Ebinghaus, R., Engstrom, D., Feng, X., Fitzgerald, W., Pirrone, N., Prestbo, E., Seigneur, C., 2007. A synthesis of progress and uncertainties in attributing the sources of mercury in deposition. *Ambio* 36, 19–32.
- Loseto, L.L., Lean, D.R.S., Siciliano, S.D., 2004. Snowmelt Sources of Methylmercury to High Arctic Ecosystems. *Environ. Sci. Technol.* 38, 3004–3010.
- Malinovsky, D., Vanhaecke, F., 2011. Mercury isotope fractionation during abiotic transmethylation reactions. *Int. J. Mass Spectrom.*
- Mao, H., Talbot, R.W., Sive, B.C., Youn Kim, S., Blake, D.R., Weinheimer, A.J., 2011. Arctic mercury depletion and its quantitative link with halogens. *J. Atmospheric Chem.* 65, 145–170.
- Maron, L., Dommergue, A., Ferrari, C., Delacour-Larose, M., Faïn, X., 2008. How Elementary Mercury Reacts in the Presence of Halogen Radicals and/or Halogen Anions: A DFT Investigation. *Chem. - Eur. J.* 14, 8322–8329.
- Maynard, J.L., 1932. The action of mercury on organic iodides. I. The formation of methylmercuric iodide and benzylmercuric iodide. *J Am Chem Soc* 54, 2108–2112.
- Meyer, T., Lei, Y.D., Muradi, I., Wania, F., 2009. Organic Contaminant Release from Melting Snow. 1. Influence of Chemical Partitioning. *Environ. Sci. Technol.* 43, 657–662.

- Meyer, T., Lei, Y.D., Wania, F., 2006. Measuring the Release of Organic Contaminants from Melting Snow under Controlled Conditions. *Environ. Sci. Technol.* 40, 3320–3326.
- Minganti, V., Capelli, R., Drava, G., De Pellegrini, R., 2007. Solubilization and methylation of HgS, PbS, and SnS by iodomethane, a model experiment for the aquatic environment. *Chemosphere* 67, 1018–1024.
- Moller, S.J., Lee, J.D., Commane, R., Edwards, P., Heard, D.E., Hopkins, J., Ingham, T., Mahajan, A.S., Oetjen, H., Plane, J., Roscoe, H., Lewis, A.C., Carpenter, L.J., 2010. Measurements of nitrogen oxides from Hudson Bay: Implications for NO_x release from snow and ice covered surfaces. *Atmos. Environ.* 44, 2971–2979.
- Morel, F.M.M., Kraepiel, A.M.L., Amyot, M., 1998. The chemical cycle and bioaccumulation of mercury. *Annu. Rev. Ecol. Syst.* 29, 543–566.
- Mowat, L., 2010. Influence of forest canopies on the deposition of methylmercury to boreal ecosystem watersheds.
- Niki, H., Maker, P.S., Savage, C.M., Breitenbach, L.P., 1983. A Fourier-transform infrared study of the kinetics and mechanism of the reaction of atomic chlorine with dimethylmercury. *J. Phys. Chem.* 87, 3722–3724.
- O'Concubhair, R., O'Sullivan, D., Sodeau, J.R., 2012. Dark Oxidation of Dissolved Gaseous Mercury in Polar Ice Mimics. *Environ. Sci. Technol.* 46, 4829–4836.
- Oremland, R.S., Culbertson, C.W., Winfrey, M.R., 1991. Methylmercury decomposition in sediments and bacterial cultures: involvement of methanogens and sulfate reducers in oxidative demethylation. *Appl. Environ. Microbiol.* 57, 130–137.
- Pacyna, E.G., Pacyna, J.M., Sundseth, K., Munthe, J., Kindbom, K., Wilson, S., Steenhuisen, F., Maxson, P., 2010. Global emission of mercury to the atmosphere from anthropogenic sources in 2005 and projections to 2020. *Atmos. Environ.* 44, 2487–2499.
- Parks, J.M., Johs, A., Podar, M., Bridou, R., Hurt, R.A., Smith, S.D., Tomanicek, S.J., Qian, Y., Brown, S.D., Brandt, C.C., Palumbo, A.V., Smith, J.C., Wall, J.D., Elias, D.A., Liang, L., 2013. The Genetic Basis for Bacterial Mercury Methylation. *Science* 339, 1332–1335.
- Perovich, D.K., 2007. Light reflection and transmission by a temperate snow cover. *J. Glaciol.* 53, 201–210.
- Pirrone, N., Cinnirella, S., Feng, X., Finkelman, R.B., Friedli, H.R., Leaner, J., Mason, R., Mukherjee, A.B., Stracher, G.B., Streets, D.G., Telmer, K., 2010. Global mercury emissions to the atmosphere from anthropogenic and natural sources. *Atmospheric Chem. Phys.* 10, 5951–5964.

- Pongratz, R., Heumann, K.G., 1998. Production of methylated mercury and lead by polar macroalgae — A significant natural source for atmospheric heavy metals in clean room compartments. *Chemosphere* 36, 1935–1946.
- Pongratz, R., Heumann, K.G., 1999. Production of methylated mercury, lead, and cadmium by marine bacteria as a significant natural source for atmospheric heavy metals in polar regions. *Chemosphere* 39, 89–102.
- Poulain, A.J., Amyot, M., Findlay, D., Telor, S., Barkay, T., Hintelmann, H., 2004a. Biological and photochemical production of dissolved gaseous mercury in a boreal lake. *Limnol. Oceanogr.* 49, 2265–2275.
- Poulain, A.J., Lalonde, J.D., Amyot, M., Shead, J.A., Raofie, F., Ariya, P.A., 2004b. Redox transformations of mercury in an Arctic snowpack at springtime. *Atmos. Environ.* 38, 6763–6774.
- Ratcliffe, H.E., Swanson, G.M., Fischer, L.J., 1996. Human exposure to mercury: a critical assessment of the evidence of adverse health effects. *J. Toxicol. Environ. Health* 49, 221–270.
- Ravichandran, M., 2004. Interactions between mercury and dissolved organic matter—a review. *Chemosphere* 55, 319–331.
- Rutter, A.P., Schauer, J.J., Shafer, M.M., Creswell, J.E., Olson, M.R., Robinson, M., Collins, R.M., Parman, A.M., Katzman, T.L., Mallek, J.L., 2011. Dry deposition of gaseous elemental mercury to plants and soils using mercury stable isotopes in a controlled environment. *Atmos. Environ.* 45, 848–855.
- Schaefer, J.K., Yagi, J., Reinfelder, J.R., Cardona, T., Ellickson, K.M., Tel-Or, S., Barkay, T., 2004. Role of the Bacterial Organomercury Lyase (MerB) in Controlling Methylmercury Accumulation in Mercury-Contaminated Natural Waters. *Environ. Sci. Technol.* 38, 4304–4311.
- Schroeder, W.H., Anlauf, K.G., Barrie, L.A., Lu, J.Y., Steffen, A., Schneeberger, D.R., Berg, T., 1998. Arctic springtime depletion of mercury. *Nature* 394, 331–332.
- Schultz, I.R., Newman, M.C., 1997. Methylmercury toxicokinetics in channel catfish (*Ictalurus punctatus*) and largemouth bass (*Micropterus salmoides*) after intravascular administration. *Environ. Toxicol. Chem.* 16, 990.
- Segawa, T., Miyamoto, K., Ushida, K., Agata, K., Okada, N., Kohshima, S., 2005. Seasonal Change in Bacterial Flora and Biomass in Mountain Snow from the Tateyama Mountains, Japan, Analyzed by 16S rRNA Gene Sequencing and Real-Time PCR. *Appl. Environ. Microbiol.* 71, 123–130.
- Si, L., Ariya, P.A., 2008. Reduction of Oxidized Mercury Species by Dicarboxylic Acids (C₂–C₄): Kinetic and Product Studies. *Environ. Sci. Technol.* 42, 5150–5155.

- Si, L., Ariya, P.A., 2011. Aqueous photoreduction of oxidized mercury species in presence of selected alkanethiols. *Chemosphere*.
- Siciliano, S.D., Lean, D.R.S., 2002. Methyltransferase: an enzyme assay for microbial methylmercury formation in acidic soils and sediments. *Environ. Toxicol. Chem.* 21, 1184.
- Siciliano, S.D., O'Driscoll, N.J., Tordon, R., Hill, J., Beauchamp, S., Lean, D.R.S., 2005. Abiotic Production of Methylmercury by Solar Radiation. *Environ. Sci. Technol.* 39, 1071–1077.
- Simpson, W.R., King, M.D., Beine, H.J., Honrath, R.E., Peterson, M.C., 2002a. Atmospheric photolysis rate coefficients during the Polar Sunrise Experiment ALERT2000. *Atmos. Environ.* 36, 2471–2480.
- Simpson, W.R., King, M.D., Beine, H.J., Honrath, R.E., Zhou, X., 2002b. Radiation-transfer modeling of snow-pack photochemical processes during ALERT 2000. *Atmos. Environ.* 36, 2663–2670.
- Soerensen, A.L., Jacob, D.J., Streets, D.G., Witt, M.L.I., Ebinghaus, R., Mason, R.P., Andersson, M., Sunderland, E.M., 2012. Multi-decadal decline of mercury in the North Atlantic atmosphere explained by changing subsurface seawater concentrations: Hg trends in the Atlantic atmosphere. *Geophys. Res. Lett.* 39.
- St. Louis, V.L., Sharp, M.J., Steffen, A., May, A., Barker, J., Kirk, J.L., Kelly, D.J.A., Arnott, S.E., Keatley, B., Smol, J.P., 2005. Some Sources and Sinks of Monomethyl and Inorganic Mercury on Ellesmere Island in the Canadian High Arctic. *Environ. Sci. Technol.* 39, 2686–2701.
- Steffen, A., Douglas, T., Amyot, M., Ariya, P., Aspö, K., Berg, T., Bottenheim, J., Brooks, S., Cobbett, F., Dastoor, A., Dommergue, A., Ebinghaus, R., Ferrari, C., Gardfeldt, K., Goodsite, M.E., Lean, D., Poulain, A.J., Scherz, C., Skov, H., Sommar, J., Temme, C., 2008. A synthesis of atmospheric mercury depletion event chemistry in the atmosphere and snow. *Atmospheric Chem. Phys.* 8, 1445–1482.
- Stephens, C.R., Shepson, P.B., Steffen, A., Bottenheim, J.W., Liao, J., Huey, L.G., Apel, E., Weinheimer, A., Hall, S.R., Cantrell, C., Sive, B.C., Knapp, D.J., Montzka, D.D., Hornbrook, R.S., 2012. The relative importance of chlorine and bromine radicals in the oxidation of atmospheric mercury at Barrow, Alaska. *J. Geophys. Res.* 117.
- Sugio, T., Fujii, M., Takeuchi, F., Negishi, A., Maeda, T., Kamimura, K., 2003. Volatilization of Mercury by an Iron Oxidation Enzyme System in a Highly Mercury-resistant *Acidithiobacillus ferrooxidans* Strain MON-1. *Biosci. Biotechnol. Biochem.* 67, 1537–1544.
- Thomas, J.L., Stutz, J., Lefer, B., Huey, L.G., Toyota, K., Dibb, J.E., von Glasow, R., 2011. Modeling chemistry in and above snow at Summit, Greenland – Part 1: Model description and results. *Atmospheric Chem. Phys.* 11, 4899–4914.
- Toom-Sauntry, D., Barrie, L.A., 2002. Chemical composition of snowfall in the high Arctic: 1990-1994. *Atmos. Environ.* 36, 2683–2693.

- Ullrich, S.M., Tanton, T.W., Abdrashitova, S.A., 2001. Mercury in the Aquatic Environment: A Review of Factors Affecting Methylation. *Crit. Rev. Environ. Sci. Technol.* 31, 241–293.
- UNEP, Global Mercury Assessment, 2013. UNEP, 2013. Global Mercury Assessment 2013: Sources, Emissions, Releases and Environmental Transport. UNEP Chemicals Branch, Geneva, Switzerland.
- Wagemann, R., Innes, S., Richard, P.R., 1996. Overview and regional and temporal differences of heavy metals in Arctic whales and ringed seals in the Canadian Arctic. *Sci. Total Environ.* 186, 41–66.
- Wängberg, I., Munthe, J., Berg, T., Ebinghaus, R., Kock, H.H., Temme, C., Bieber, E., Spain, T.G., Stolk, A., 2007. Trends in air concentration and deposition of mercury in the coastal environment of the North Sea Area. *Atmos. Environ.* 41, 2612–2619.
- Waring, C., Pellin, R., 1967. Kinetics and mechanism of thermal decomposition of dimethylmercury. *J. Phys. Chem.* 71, 2044–&.
- Weiss, B., Clarkson, T.W., Simon, W., 2002. Silent latency periods in methylmercury poisoning and in neurodegenerative disease. *Environ. Health Perspect.* 110 Suppl 5, 851–854.
- Whalin, L., Kim, E., Mason, R., 2007. Factors influencing the oxidation, reduction, methylation and demethylation of mercury species in coastal waters. *Mar. Chem.* 107, 278–294.
- Wren, C.D., 1986. A review of metal accumulation and toxicity in wild mammals. *Environ. Res.* 40, 210–244.
- Wren, S.N., Donaldson, D.J., 2012. How does deposition of gas phase species affect pH at frozen salty interfaces? *Atmospheric Chem. Phys.* 12, 10065–10073.
- Yamamoto, M., 1995. Possible mechanism of elemental mercury oxidation in the presence of sulfur compounds in aqueous solution. *Chemosphere* 31, 2791–2798.
- Yee, S., Choi, B.H., 1994. Methylmercury Poisoning Induces Oxidative Stress in the Mouse Brain. *Exp. Mol. Pathol.* 60, 188–196.
- Yin, Y., Chen, B., Mao, Y., Wang, T., Liu, J., Cai, Y., Jiang, G., 2012. Possible alkylation of inorganic Hg(II) by photochemical processes in the environment. *Chemosphere*.
- Yokoo, E., Valente, J., Grattan, L., Schmidt, S., Platt, I., Silbergeld, E., 2003. Low level methylmercury exposure affects neuropsychological function in adults. *Environ. Health Glob. Access Sci. Source* 2, 8.
- Zhang, H., 2006. Photochemical Redox Reactions of Mercury, in: Atwood, D.A. (Ed.), *Recent Developments in Mercury Science*. Springer-Verlag, Berlin/Heidelberg, pp. 37–79.

II. Experimental section

i. Material and methods

-

ii. Field conditions and methodology

Résumé

Dans un premier chapitre, cette partie a pour but de décrire la totalité de l'instrumentation manipulée lors de ce travail de thèse. Tout d'abord, une présentation très détaillée et exhaustive du travail de développement analytique d'un dispositif de mesure du MMHg par hydruration-GC-CVAFS est faite, incluant autant de détails que possible sur les problèmes pratiques rencontrés. Le but de cette description poussée est de favoriser à l'extrême la reconstruction par le lecteur en l'informant de tous les écueils susceptibles de le ralentir. Les performances analytiques de ce dispositif n'étant pas encore pleinement définies, ces informations seront certainement d'un grand secours à son futur opérateur.

En continuant sur la description de l'instrumentation utilisée, nous décrivons les dispositifs opérationnels auxquels nous avons eu recours pour acquérir notre jeu de données, notamment la méthode de mesure du MMHg par double dilution isotopique, grâce à un couplage GC-ICP-MS. Les méthodes de mesure de la chromatographie ionique, du carbone organique total, des particules ainsi que du mercure total sont aussi décrites. Toutes ces analyses et leurs préparations, sans exception, font partie intégrante du travail de cette thèse.

Le deuxième chapitre présente les conditions de la campagne de terrain. Le but de ce chapitre est non-seulement de décrire le site d'étude et la méthodologie d'échantillonnage appliquée, mais aussi les conditions géochimiques et météorologiques durant les 9 semaines de la campagne. En effet, nous listons les épisodes de précipitations, qui (de par piégeage des contaminants atmosphériques) ont un effet potentiel sur la chimie du manteau neigeux. Un épisode de tempête induisant des dépôts de sprays marins sur le manteau neigeux côtier est aussi recensé et décrit, ainsi qu'une brève description préliminaire des AMDEs.

Le régime venteux est aussi d'un grand intérêt considérant la chimie du manteau neigeux, car de nombreux contaminants, notamment Hg^0 , peuvent être transportés sur de longues distances avant leur dépôt. Les retro-trajectoires sur 24h des masses d'air arrivant au site d'étude sont présentées pour chaque jour de la campagne, et montrent une grande variabilité dans leurs origines. Le régime venteux à l'échelle du Kongsfjorden, au contraire, est très marqué par des vents dirigés entre ses deux extrémités (le glacier Kongsvegen et l'ouverture sur le large), le plus souvent depuis le glacier Kongsvegen. Les vents issus du large sont associés aux épisodes d'AMDE.

Un épisode d'apport massif de particules a été enregistré dans le manteau neigeux côtier dans le dernier mois de la campagne. Il ne semble relié à aucune origine de masse d'air particulière, à aucun changement de direction du vent à l'échelle locale, ni à aucun autre événement recensé (AMDE,

précipitation ou tempête). Le déclin de cet événement (diminution du nombre de particules dans la neige) semble cependant corrélé avec la fonte du manteau neigeux. La source de ces particules et leur impact sur la chimie de la neige côtière sont discutés dans un chapitre suivant.

En plus de tous ces événements géochimiques et météorologiques, une hausse de température anticipée a été observée et son impact sur le manteau neigeux est décrit brièvement. Les résultats montrent une forte hausse de la température à 2 m dans la première moitié de la campagne, avant un retour à des conditions de température plus conservatives pour le manteau neigeux, puis finalement la fonte saisonnière attendue. En conséquence, le manteau neigeux est fortement modifié dès les premières semaines de la campagne et montre notamment des signes visibles de fonte dès la fin avril. L'impact de cette fonte prématurée sur la chimie de la neige est discuté dans un chapitre suivant.

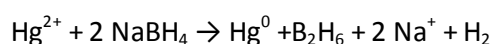
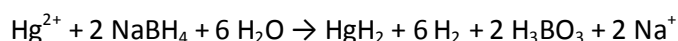
Outre un intérêt purement descriptif de la méthodologie et des événements géochimiques et météorologiques, cette partie permet d'identifier les processus qui s'avèrent (dans la suite de la thèse) être critiques concernant la chimie du manteau neigeux. En particulier, les résultats présentés dans ce chapitre permettront l'identification des sources principales des différentes espèces chimiques du manteau neigeux, incluant le MMHg.

i. Material and methods

1. Toward a reliable and mobile system for MMHg measurement

Various MMHg titration methods have been reviewed (Berzas Nevado et al., 2011) among which a few are sensitive enough to allow for the measurement of MMHg at the pg/L level in melted snow. These methods are developed for sea-water samples, which contain MMHg concentrations in the same range than melted snow samples. The first step is always a derivatization of MMHg to a volatile species. Most of the methods use ethyl group donors to transform MMHg into the volatile methylethylmercury, while the most sensitive ones proceed via hydride generation to obtain the volatile methylmercury hydride. The latest allow very low detection limits (< 5 pg/L) in aqueous samples with low DOC content, which made it our reference method for the development of our own MMHg measuring device.

Hydride generation occurs via addition of a mild reactive hydride donor (sodium borohydride NaBH₄) in the sample. Once NaBH₄ added, hydrides react with Hg species, yielding as follows:



The generated Hg⁰ HgH₂ and MeHgH are volatile species and can be purged out by helium flux into a chromatographic column immersed in liquid nitrogen (-196 °C), where they are trapped by adsorption. Emerging the column and subsequent warming to room temperature in appropriate helium flux allow for the trapped species to 1) undergo thermal desorption; 2) be pulled by the helium flux and 3) be separated along the column. Once separated, the Hg species are converted to Hg⁰ to be detectable by a cold vapor atomic fluorescence spectrometer (CVAFS). This process allows for the quantitative detection of generated Hg hydrides, in roughly 10-12 min per sample.

In summary, the four critical steps of the method are 1) the Hg hydride generation; 2) their adsorption onto the cold trap; 3) their thermal desorption/elution and 4) their measurement by CVAFS. The major advantages of using this method are critical regarding environmental MMHg

monitoring in Arctic snow. It is the suitable compromise between sensitivity, cost-effectiveness and handling ability. Particularly, the derivatization-purge-and-trap methods are the only one that can be brought on the field and thus allow real-time monitoring with every deriving advantage. Other methods can be as sensitive as the one presented here but often require heavy sample preparation/extraction and extremely expensive devices (e.g. the double spike method in the part 2 of the present section).

For the development of our own apparatus, we chose to start from the existing procedure described in (Tseng et al., 1998) using parameters from Cossa and coworkers (personal communication), who use the purge and trap method for years on a daily basis. However, the optimal setting of each parameter happens to vary from one assembly to another, as well as overtime. This is mainly due to the differences (even the tiniest) existing between two different assemblies, but also to some changes happening to a given assembly over use. Although we were aware of many analytical parameters and suspected a few more, time and experimentation made us discover empirical issues that can affect the quality of the result. Hence, while it is quite easy to obtain a working apparatus, the optimization necessary to the sensitivity and the reproducibility of the result is a lot more time consuming and uncertain. The following is a description of the issues we encountered during the optimization process.

a. System description

A schematic overview of the assembly is presented in Figure 1. It consists in a helium line made of Teflon (PFA) passing successively through:

- A golded sand trap, for helium purification of possible Hg^0 traces;
- A four-way pinch electrovalve, allowing the helium to flow either to the sample reactor (60 mL braun borosilicate glass, coated with DMCS $(\text{CH}_3)_2\text{SiCl}_2$) or directly to the rest of the assembly;
- A U-shaped silanised (coated with DMCS $(\text{CH}_3)_2\text{SiCl}_2$) borosilicate glass column (6 mm ext. \varnothing , 4 mm int. \varnothing , Verre Labo Mula, France) filled with WAW-DMCS (60/80 mesh impregnated with 15% OV-3, Interchim, France) and wrapped in a Ni-Cr resistor (5 Ω /m, Conrad, France) ;
- A 25 cm long quartz tube (Verre Labo Mula, France) heated to 800 °C in a tubular-cavity oven (Carbolite, Switzerland).

- A three-way pinch electrovalve, allowing the helium to flow either to the atmosphere via a ball flowmeter A (Aalborg, USA), or to the following ;
- A Tekran 2500 CVAFS mercury analyzer (Tekran Inc., Canada);
- A ball flowmeter B (Aalborg, USA).

The sample reactor is a brown borosilicate glass unique bottle in which the sample is transferred at the beginning of the analyzing procedure. The reactor has a gas input (from the gold trap), a NaBH_4 (VWR SAS, France) solution input and a gas output (to the column). A peristaltic pump designs the NaBH_4 throughput to the sample. All the tubing between the different parts is made of Teflon (PFA), or food-processing silicone tubing (at the pinch valves). The assembly is built so that the line is as short as possible. All chemical and equipment, if not specified, were purchased from Fischer Scientific SAS, France.

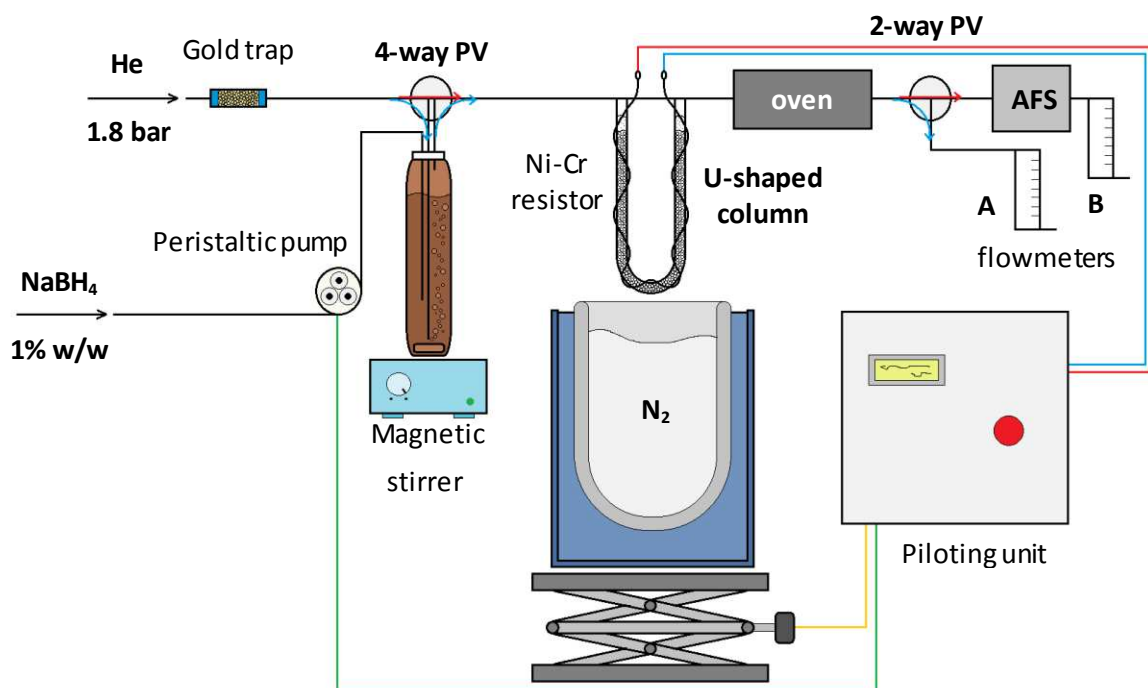


Figure 1. Schematic representation of the derivatization-purge-and-trap-GC-CVAFS assembly.

The analysis of one sample proceeds as follows:

- 1) **Trap cooling:** the liquid nitrogen bath is lifted up to immerse the column. The helium flows directly to the column and is released to the atmosphere after the oven (without passing through the CVAFS). The efficient trapping of Hg derivative depends on the temperature of the column after this cooling step. If this step is too short, the trapping is

not quantitative. The optimal time required for a complete cooling is 90 s (Tseng et al., 1998; Cossa, personal communication).

2) Hydride generation

a) The 40 mL sample is stirred while adding a 1% w/w aqueous solution of NaBH_4 (prepared daily) at 0.4 mL/min for 3 min. As NaBH_4 readily reacts with H_2O , a slow addition of a large excess of NaBH_4 (with respect to Hg species) is preferred. This step allows the reactions described above, and strongly depends on the pH of the sample, Tseng et al. suggesting an optimal pH of 1-2 (Tseng et al., 1998). We determined empirically the optimal volume of Suprapur HCl necessary to yield the largest MMHg peak (in synthetic samples, matrix: milliQ water, pH around 6)(Figure 2). As this method was originally designed for sea-water samples, we tried the effect of salinity on the MMHg peak area, with visible improving results up to 2 g of NaCl (no visible effect for larger additions). The addition of NaCl and NaBH_4 often induces Hg^{II} contamination at significant levels regarding the sensitivity of the method. This means that Hg^{II} cannot rigorously be determined with this method, and also that a too large excess of NaBH_4 as well as too much NaCl can induce an overwhelming Hg^{II} peak and therefore deteriorate the MMHg peak detection.

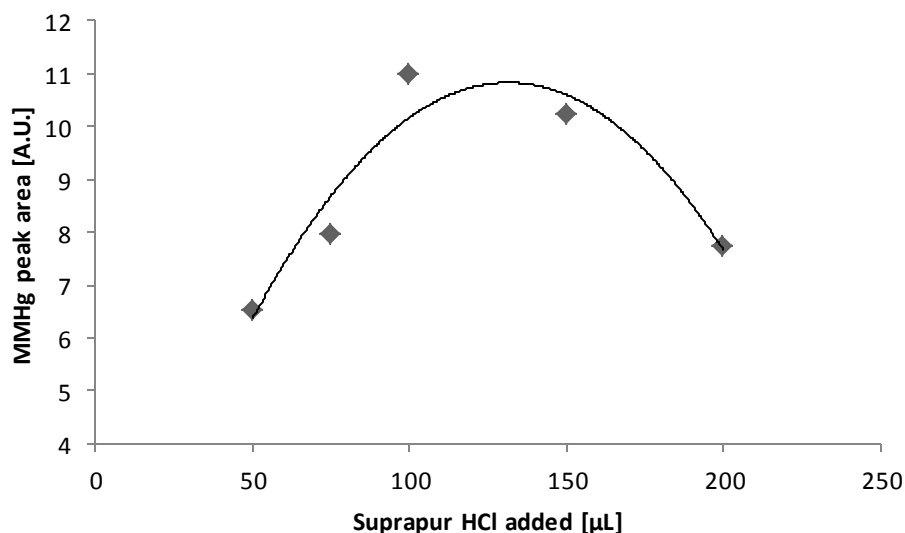


Figure 2. Effect of HCl addition during the hydride generation step on the final MMHg peak area.

- b) Simultaneously to NaBH_4 addition, the helium flux is redirected to purge the sample before going to the column, aiming to withdraw all the volatile Hg species (and particularly MeHgH) from the sample via water-gas exchanges at the wall of the helium bubbles. This step requires a homogeneous purging of the total volume of the sample, as well as optimal water-helium exchange conditions. This can be achieved by using a borosilicate glass frit (pore size: 16-40 μm) and by stirring the sample. The porosity of the gas delivering glass frit is important regarding the water-helium exchanges: the smaller the bubbles, the higher the water-helium interface, and then the more effective the water-helium exchanges. However, if the glass frit porosity is too small, the hindrance to the helium flux (2 bar) is too strong, hence the system is too pressurized, eventually leading to explosions at the different junction points of the assembly. The other important parameter regarding the Hg hydride purge efficiency is the helium flow rate, as it determines the bubble speed in the sample: the lower the speed of the bubble, the longer its residence time in the sample, the longer (thus more effective) the water-helium exchange window. This also explains the slender shape of the reactor, helping maximizing the residence time of the bubbles between the bottom (gas delivery) and the surface of the water sample (bubble evasion). Purged species are trapped by adsorption in the column immersed in liquid nitrogen.
- 3) **Additional purge** with helium in the conditions of 2)b) but without NaBH_4 input 2)a) anymore. A quantitative purge of all the generated Hg hydrides is achieved for a total helium/sample volume ratio of 15:1. Our observations on the factors determining the purge efficiency (see paragraph 2)b) above) would suggest a very long purge time with very low helium flow rate as the optimal purge. However the simultaneous purge of water vapor and its subsequent condensation upstream of the column – as both liquid and ice – can form an obstructing plug to the helium stream, leading to overpressures and possible subsequent explosions. In addition, this water can be caught by the helium flux during the following elution step, enter the detector and deteriorate the chromatogram quality: baseline lift, fluorescence scattering. The optical cell of the CVAFS detector, once contaminated with water condensation, is hard and tricky to clean. Therefore, to avoid water condensation as much as we can, some restrictions should be applied to the overall purge time (reminding the 15:1 helium/sample ratio): not too long but with moderate helium stream. The optimal conditions were empirically found to be a 7.5 min purge (steps 2) and 3)) with a 350 mL/min helium flow (flowmeter A). However,

it is not possible to completely avoid water condensation, which remains the main issue of the method.

- 4) **Thermal desorption and elution** step: the liquid nitrogen container is pulled down, allowing the column to warm gradually to room temperature, under a continuous helium flux directed toward the CVAFS spectrometer inlet. Each Hg species is desorbed from the column at a given temperature (depending on its volatility and affinity with the static phase) and carried by the helium flux. The Hg species are then separated while flowing out of the column (Hg^0 being less retained than MeHgH) and converted to Hg^0 at 800 °C to allow detection by the CVAFS spectrometer (Figure 3). The main parameters influencing the optimization of this step are the helium flow rate and the column warming gradient. The higher helium throughput, the thinner the peaks; however the helium throughput also defines the residence time of Hg species in both the oven and the detector optical cell. A too short residence time in the oven would mean non-quantitative conversion of Hg species into Hg^0 , while a too short residence time in the optical cell would mean a non-quantitative detection of Hg^0 . The latter happens to be the most limiting factor to the helium flux and does not allow higher throughputs than 125 mL/min (flowmeter B). Lower throughputs induce rapidly very large peaks and deteriorate therefore the chromatogram quality, hence an helium flux of 125 mL/min is considered as optimal during the elution step. The column warming is also crucial, as a quicker warming would result in closer desorption instants, thus in smaller peak separations. As shown on Figure 3, peaks corresponding to Hg^{II} and MMHg are well separated, and one could expect a quicker warming to be much more time-effective while still allowing a very good peak separation. This is true, however the problem here comes once again from the water condensate upstream of the column, which liberates water vapors as the column is warmed. If the warming is only induced by the air temperature, this water remobilization can be controlled, but for any quicker warming it can happen before MeHgH is desorbed. As water vapor enters the optical cell of the CVAFS, it can scatter both emitted and reemitted UV light, thus lead to a non-quantitative Hg^0 detection and to a baseline shift. If oversaturation allows water to condensate in the optical cell, the analysis shall be stopped and the cell cleaned.

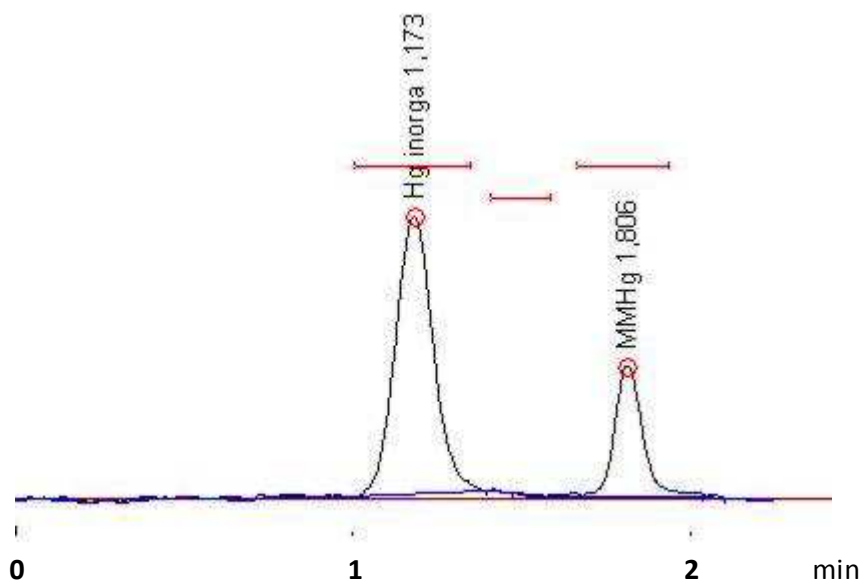


Figure 3. Typical chromatogram obtained for 10 pg of MMHg.

- 5) **Drying of the column:** the Ni-Cr resistor wrapped around the column is fed with 24 V power, up to 145 °C for a 20 Ω resistor (4 m long). This step aims to vaporize the ice and water formed upstream of the column (and possibly in the column itself) and to reject it in the atmosphere (via flowmeter A). The helium throughput – for obvious practical reasons – is set to the same value as during the sample purge, and allows a total drying of the assembly after 6 min.

b. Empirical issues

The care brought to the building of the assembly itself is at least as important as the parameter optimization described above. Indeed, these parameters are rather fine tuning and are worth optimizing only once several key building features are respected to allow the assembly to physically work properly. This is of course the trickiest part of the development, as a lot of key-factors for the building of the assembly are often non-obvious and unexpected. What follows is a list of these key-factors, identified through troubleshooting of all the dysfunctions encountered during the daily work on the assembly.

- A. **The tubing:** its nature and its length are of great importance in order to have a working assembly. The longer the analytical line, the higher the risk of condensation spots (“cold spots”). This is the main concern in our case: at the current knowledge of the assembly and given the number of parameters to test, we cannot afford to be uncertain about “cold spots”. Hence we removed all the superfluous tubing downstream the 4-way pinch valve and upstream the 2-way one, and connected directly the different parts together. The silicone tubing of the 4-way pinch valve is connected to the column, which is connected directly to the quartz tube passing through the oven. All the tubing upstream of the 4-way pinch valve, downstream the 2-way one and in the reactor is made of 1/16 inches Teflon tubing.
- B. **The connections:** this parameter is commonly considered by analytical chemists. Indeed, connections are the location where most of the leaks occur. For the purpose of an extremely short line, industrial connections are not the best solution in our case. The connections between the reactor and the AFS detector need to be flexible to avoid tensions on the glass/quartz parts, and to allow the angles of the connection to be other than 90° or 180°. In addition, connections up- and downstream of the column should not allow rapid and important heat transfer, as we want the temperature to be as steady as possible at a given point of the analytical line (except the column of course). Finally, we do not exclude to use heating strips on some parts of the line to have a better control on the temperature, and this requires thin easy-to-heat connections. All these conditions are best filled by simple food-processing silicone tubing, despite the regular change of a silicone connection exposed to thermal stretches is sometimes needed. Besides, up- and downstream the pinch valves, small T- or Y-shaped polyethylene connections are used to split or to reunify the line. As the assembly can require many manipulations for trouble-shooting or maintenance reasons, connections shall be thought to be easy to plug/unplug. The connections between 1/8 Teflon tubing and 1/8 silicone tubing are therefore made with linear polyethylene connections, as shown on Figure 4. This might seem just like a complication of the direct connection, but it is actually much easier to plug/unplug without any stretch or tension. Such connections can be used in all the assembly but not directly downstream of the column, as the strong heating during the drying step would cause the polyethylene part to melt. Silicone connections shall be changed when becoming opaque – which is a sign of thermal degradation – otherwise they risk a rupture. At the pinch valves, the required silicone tubing shall be checked on a regular basis for pinch persistence. This is particularly true for the tube directed to the atmosphere in the 2-way valve, which experiences strong humidity during the drying step

and tends rapidly to remain pinched. If no care is taken, the water expelled during the next drying step will be forced to the AFS detector and cause severe harm to the optical cell.

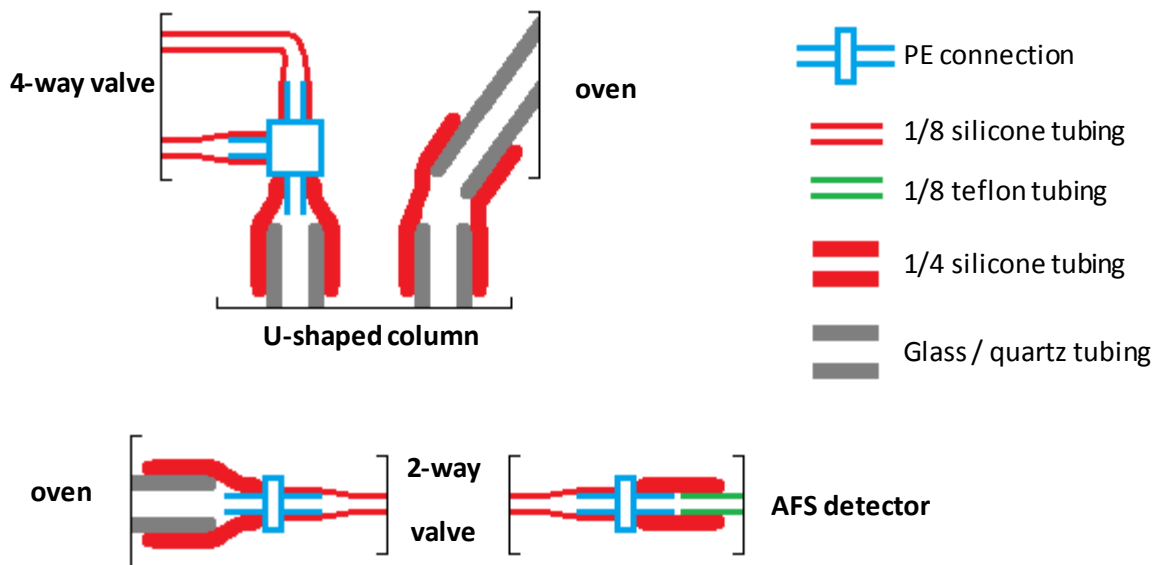


Figure 4. Schematic view of the different connections used.

- C. **Leakproof qualities of the cap of the reactor:** it seems obvious that any leak from the reactor will possibly lead to a loss of MeHgH during the purging step. However, there is to our knowledge no 3-way transfer cap available on the market for the thin reactor we use. Waterproof caps made of Teflon and with Teflon tubing passing through are an option. The Teflon tubing requires an external silicone coating – actually the Teflon tube is plugged into a silicone one and forced through a tiny hole in the Teflon cap. Another option was to use a septum on the cap and to force Teflon tubing through, however this does not allow full waterproof qualities for larger tubing than 1/32 inches (we use 1/8), and the ageing of the septum can induce hole stretching and porosity over time. For long term use, as we want the most reliable cap, we decided not to use septum-equipped caps, and for practical reasons, we decided to use the caps provided with the reactor as a working basis (24-400 Teflon-coated polyphenol caps). Although polyphenol is much more rigid than Teflon, it was possible to force Teflon tubing with silicone coating through a tapped polyphenol cap; however this causes too much stretching constraint to the silicone coating and eventually a rupture over time and use. The best solution was achieved by forcing Teflon tubing directly through a polyphenol cap and by using silicon at the external junction to ensure the

waterproof qualities. The internal side of the cap shall remain untouched, and the Teflon tubing should be forced through the cap from the internal to the external side, to avoid the internal Teflon coating removal. The obtained 3-way transfer cap (Figure 5) offers the best performances in our case.

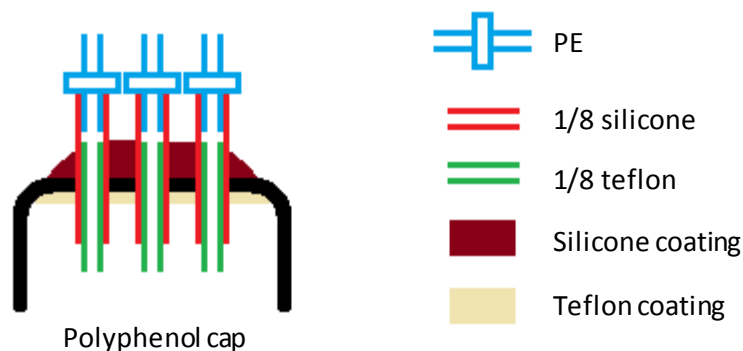


Figure 5. Schematic view of the 3-way transfer cap

- D. **The column** is glass-made as it shall support wide thermal stretches and must be neutral regarding Hg species (which could not be the case for metallic columns). It is filled with WAW-DMCS (60/80 mesh impregnated with 15% OV-3) up to 2 cm below the inlet of the tube and up to the top at the outlet. Quartz wool plugs are used to prevent the WAW-DMCS phase to be pushed out of the columns by the gas fluxes: one is placed after the phase and the other one before the phase (the brutal flux decrease during the elution step often causes the phase to flux backward) in order to hold it tight. It is advised to let 2 cm free of any filling before the phase, as this is where water condensation during the purging step usually occurs, and any filling would increase the risk of obstruction. Both the glass column and the quartz wool are silanized with DMCS ($(\text{CH}_3)_2\text{SiCl}_2$) prior assembling to provide a uniform $\text{Si}(\text{CH}_3)_2$ coating corresponding to the WAW-DMCS phase – the oxygen of the glass/quartz surface replace the Cl on the Si. With time and use, the phase gets tighter as it gets pushed by successive runs, and the quartz wool plug is forced out of the column. Although this plug usually stays stuck in the silicone connection downstream of the column (thus preventing the phase to be expelled from the column) the use of a glass column with a tightening at the outlet gives better results. Indeed, this offers a better control on the packing of the phase by

immobilizing the quartz wool plug at the outlet of the column, as well as easy conditions for changing the silicone connection downstream of the column.

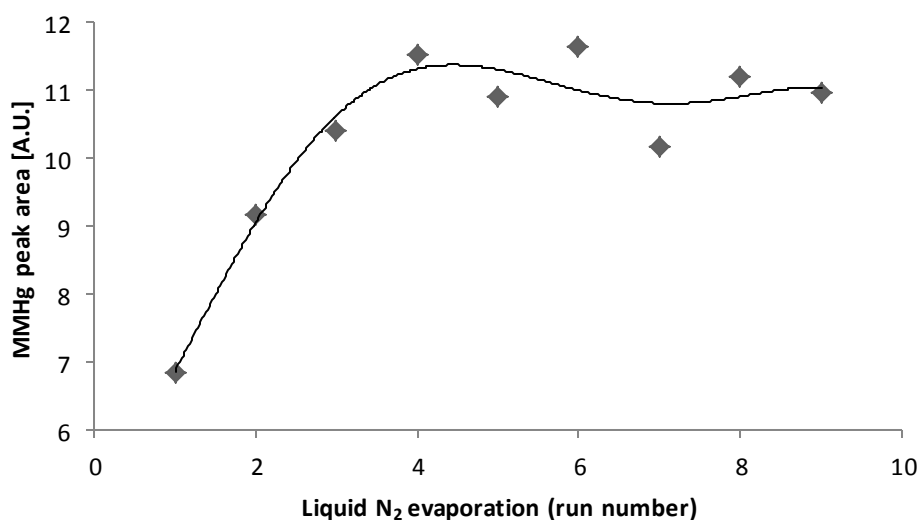


Figure 6. Effect of the liquid nitrogen immersion level on the final MMHg peak area.

Another critical factor regarding the column is its immersion in liquid nitrogen. For some reasons the MMHg peak area is larger when the column is only immersed up to half-height. Data presented in Figure 6 is the result of several successive analysis of 10 pg of MMHg without adjusting the level of liquid nitrogen to keep it constant from one run to the next. It shows that the peak area increases when the liquid nitrogen level decreases, down to half-height of the column, where this effect stops. This could be because the portion of the column downstream the immersed part stays warmer and hence retains less MMHgH during the elution step. In other words, only a small portion of the phase would act as the cold trap (and should thus be immersed), while the part downstream would act as the separating part, and would be more efficient when not too cold (so would take advantage of not being immersed in liquid nitrogen).

- E. **The quartz tube passing through the oven.** This is where the Hg species are reduced to Hg⁰ by pyrolysis at 800 °C. The use of a quartz wool filling is suggested (Cossa, personal communication) to have a more efficient warming of the helium flux, but this did not result in any improvement in our case. From one batch to another, the quartz wool does not always resist to the very high temperature very well, and partial to total melting of the wool can occur, eventually leading to the obstruction of the tube. In addition, we suspect that the quartz wool is subject to slow degradation at 800°C, as a yellow brown deposit appears over

use at the exit of the tube when filled with quartz wool. Finally, the use of quartz wool causes the evasion of barely visible quartz wool fragments in the helium flux that can adsorb on the walls of the analytical line, and to the optical cell of the AFS detector. As such quartz dust is very difficult to clean away, we finally chose not to fill our tube with quartz wool, which did not induce any change in the chromatogram. The tube should be long enough to allow its end to be cold enough for connections, depending on the oven radiations. In our case, 3 cm upstream of the oven and 5 cm downstream were enough to prevent the connections from any rupture (silicone) or melting (polyethylene). The oven cavity is 17 cm long, which allows (given the helium flow rate) a residence time of the Hg species long enough for quantitative reduction to Hg^0 (Cossa et al., internal IFREMER file).

- F. **The chromatography interface hardware settings** need to be optimized in order to enhance the quality of the chromatograms. Using our method, the peaks are rather broad compared to common gas chromatography techniques (they can last 20 seconds), thus a low acquisition rate of the chromatography interface hardware would result in low baseline noise while still allowing very good peak definition. The acquisition frequency of 1 sec^{-1} allows for a perfect peak shape while reducing the baseline noise to undetectable levels.
- G. **The Tekran 2500 CVAFS detector settings.** One should be careful while installing one from the mid 2000's, as Tekran changed the main circuit board and sometimes provided with new generation detectors the notice for the old one. Both versions look almost the same but require very different settings, which can induce very bad performances in case of confusion. The global functioning of the detector depends on the UV intensity reaching the optical cell, which is set constant by a photodiode (fed with a D_{out} voltage) adjusting the lamp voltage. This UV intensity depends on 1) the orientation of the lamp, which should be oriented perfectly toward the optical cell; and 2) the ageing of the lamp. Once the lamp correctly oriented, its ageing should be the only parameter changing the intensity it delivers: the older the lamp, the lower the intensity and – in response from the photodiode – the higher the lamp voltage. The two critical parameters are the UV lamp voltage and the D_{out} voltage. The detector is run in “auto” mode, which means that the lamp voltage is adjusted automatically to deliver a constant intensity to the optical cell, measured by the photodiode, fed with D_{out} negative voltage. This parameter varies with the lamp orientation and should be set in “fixed” mode, where no auto adjustment of the lamp voltage will compensate the rotation of the lamp to a less effective position. We remarked that D_{out} affects the sensitivity of the detector, in a way presented in Figure 7: the higher $|D_{\text{out}}|$, the larger the peak area. Despite

the UV lamp voltage is subject to slow increase overtime (as explained previously), it should be set to 8.0 V for a new lamp, and higher if 1) the lamp is old and/or 2) the user wants to boost the signal over lamp longevity. Because the MMHg levels we want to measure are in the lower detection range of the Tekran 2500 detector, we chose to boost the signal by setting the lamp voltage at 9.6 V.

- H. **The Tekran 2500 optical system (cell and filter):** as this is the part that restitutes to the photomultiplier the fluorescence radiations emitted by Hg^0 deexcitation, it should be kept in perfect working conditions. This first means that both the optical cell and the filter should be perfectly clean of any dust or deposition. The filter is not meant to be manipulated and should thus remain clean, but the optical cell can be exposed to water condensation or to particulate impurities carried by the helium flux. Although the optical cell is obviously hidden of any light pollution (hence not visible), its alterations are easily visible in real time on the chromatograms. If any harm is suspected, the optical cell should be removed and cleaned to recover its transparency. The manipulation of the quartz-made optical cell requires care, as it is easily breakable while moving it from- or to its tight cavity. We tried to change the optical system of the detector for a more efficient one, including a mirror-equipped optical cell and a new filter, resulting in a 30-fold increase of the signal with signal/noise reduction.

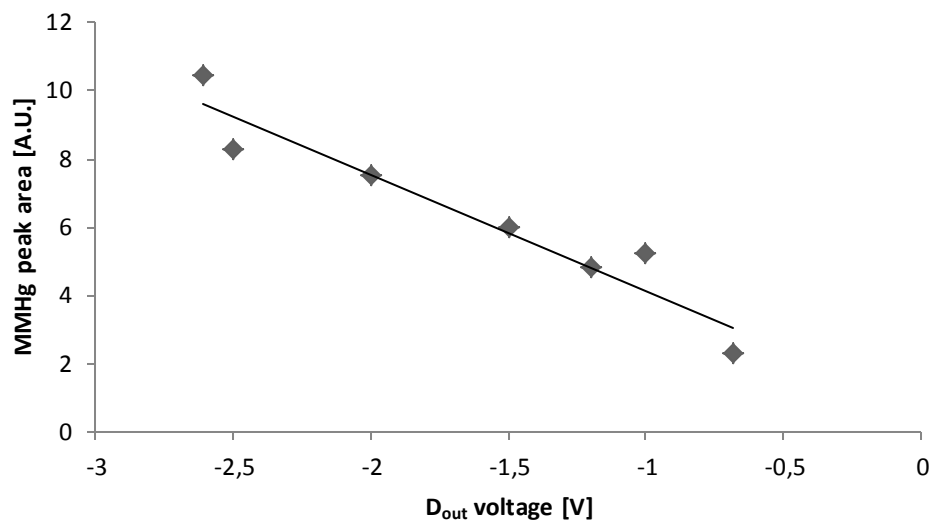


Figure 7. Effect of the D_{out} voltage setting on the final MMHg peak area.

- I. **The quality of the stationary phase.** Given the artisanal nature of the assembly, the user might logically attribute bad performances to variations of any of the parameters described above, before blaming the quality of the industrial WAW-DMCS phase. However, our

experience attests that the features of the peaks (height and retention time) mainly result from the stationary phase. If the assembly is set as described all along this chapter, the chromatogram should qualitatively look like the one presented in Figure 3. If any major change occurs – like disappearance of a peak or incomplete peak separation – it is probably due to the WAW-DMCS phase. Sometimes, when working on the assembly optimization, such change can occur simultaneously with the (sometimes involuntary) change of one or several parameters and confuse the user. In our case, we changed the phase batch (because of the exhaustion of the previous batch) a few days after the addition of a soda lime trap to the assembly, and imputed the very bad performances to the ageing of the soda lime first, then to conjugate effects of many parameters, while they simply resulted of bad phase quality. It is therefore useful to be aware that despite the stationary WAW-DMCS phase is industrially manufactured and checked, some batches can have a very poor quality for any analytical use. This can save the user from heavy time consuming tests and manipulations, which can sometimes be counterproductive given the fragility of some parts of the assembly. We were advised (Cossa, personal communication) to change the stationary phase in the column every 250-300 runs. Doing so, we never noticed any change imputable to the phase ageing over use.

- J. **Potential water removal solutions.** As previously mentioned, the water and ice condensation upstream of the column is one of the main issues concerning the assembly, as it is sometimes important enough to obstruct the helium flux and to cause overpressures and subsequent explosions. In addition, it has to be removed by a strong heating of the column which damages the silicone connections and possibly the stationary phase. During this drying step, accidental redirection of the helium flux to the optical cell of the detector sometimes occur due to silicone tubing degradation, leading to water condensation in the optical cell. It would therefore be a significant step forward to be able to suppress this water condensation. We tried two different common desiccants used in chemical analysis that are supposed to be inert to Hg species: soda lime and 3 Å molecular sieves. The modification to the assembly consisted in the addition of a roughly 10 cm³ desiccant-containing trap (1/2 inches glass or Teflon tubing) between the 4-way valve and the column. Molecular sieves consist in inert porous ceramic balls that absorb (in a reversible way) the chemical species of the same size than the pore. The 3 Å molecular sieves are designed to trap the water molecule. It is difficult to assess *a priori* whether MeHgH should be adsorbed or not (as its size should be in the range of 3 Å), but Hg⁰ having a smaller radius than the pore size (1.3 vs 3 Å) it should not be absorbed. Indeed, Hg⁰ is not adsorbed but MeHgH and water are quantitatively trapped. The

second option was soda lime, which we already use for the same purpose (water removal from the gas stream) in THg analysis. Soda lime is alkaline, and therefore would be expected to be inert with respect to any Hg hydride while reactive with water and acids. As the helium stream may purge acidic species (we add HCl in the sample), soda lime would be twice as interesting as molecular sieves. However it acts in an irreversible way and is therefore subject to ageing. The first tests lead to a small increase in baseline stability with soda lime, but with performances rapidly decreasing with time, as the soda lime gets hydrated over use (within 15-20 runs). We chose to avoid soda lime use as the benefit was minimal for a substantial consumption of desiccant (almost 1 trap/day). We did not consider any additional option, as the other common desiccants would either be expected to interact with Hg hydrides, or are not compatible with gas purification. In the literature, soda lime traps are sometimes used for similar MMHg measurements (not with Hg hydrides though), but for much larger samples, hence much larger quantities of water condensates (Bowman and Hammerschmidt, 2011).

c. Conclusion and perspectives

During this thesis work, we managed to build an assembly for MMHg measurement at the ultra-trace level (< 100 pg/L). This process took months of tests and issues identification to result in an operating device and a wide self-taught knowledge of the assembly. Although this consists in the biggest part of the development of a routine MMHg analysis, further work is needed to validate and characterize the method. By comparison with one of the only similar setup with low volume samples (30-40 mL) based at the IFREMER laboratory in Nantes, we know that we are in the same detection limit range (10-20 pg/L), although we still have to confirm it. However, there is a more urging need for a more reliable and performing assembly, which we think can be accomplished through better control on the purge and trap system.

The actual system consists in a simple U-shaped column acting as both cold trap and chromatographic column. The drawback of this system is that it is not possible to uncouple thermic conditions for the trap and the column, which are always decoupled in performing analytical devices. On one hand, this would allow the column temperature to be controlled separately and therefore a much better control on the peak separation and shape. On the other hand, this would allow a better control on the trap and particularly the possibility to try other materials than the WAW-DMCS phase as adsorbing surface. For this purpose, we designed new borosilicate glass pieces to allow this trap-

column uncoupling (see Figure 8). The first one (A) is a small J-shaped column, which shorter side is the downstream side and should be totally immersed in liquid nitrogen; the second piece is a regular straight glass tube (B). Both have a shrinking at the downstream as a stop for the quartz wool plugs. A third piece is designed as a junction between the two others (C), and is relevant for two main reasons:

- The column (B) needs to be a bit away from the trap to be isothermal. Indeed the cold helium stream coming from the trap (A) freezes the two first centimeters downstream while warming up. This warming should occur as much as possible before the stream enters the column, to avoid any strong uncontrolled thermic gradient during the elution. In order to maximize this effect, the (C) part is warmed by a heating strip.
- An insert into the upstream end of the column (B) is required to pack its content and prevent it from unpacking when the helium flow sharply decreases for the elution step. This phenomenon causes the packing of the stationary phase to change from one run to the next. As the packing changes, the porosity of the column changes too, therefore its retention and separation properties. A satisfying control of these parameters is achieved through the (C) junction piece and the downstream shrinking of (B). The whole (A-C-B) assembly could have been simplified to two pieces by merging (A) and (C), but the (A-C-B) option is physically more flexible. This is crucial in this case, as this part of the system often requires maintenance, or is exposed to physical stretching due to handling of other parts.

By building the trap-column assembly this way, we verified the two assumptions made above. We were allowed to heat the (B) and (C) parts constantly event when the trap (A) was immersed in liquid nitrogen, and controlled perfectly the packing of the stationary phase. Although a better control of the trap-column settings was visible, we were unable to assess the analytical performances of this system, as the WAW-DMCS phase used during the tests was of very poor quality. However, no change was observed on the chromatogram between the U-shaped column solution and the (A-C-B) one, using the same poor stationary phase batch for both. Further tests are needed with a good quality WAW-DMCS phase to acquire a full picture of the benefits (if any) of this (A-C-B) system. For now, the preliminary results and observations suggest that this solution should be at least as performing as the previous one.

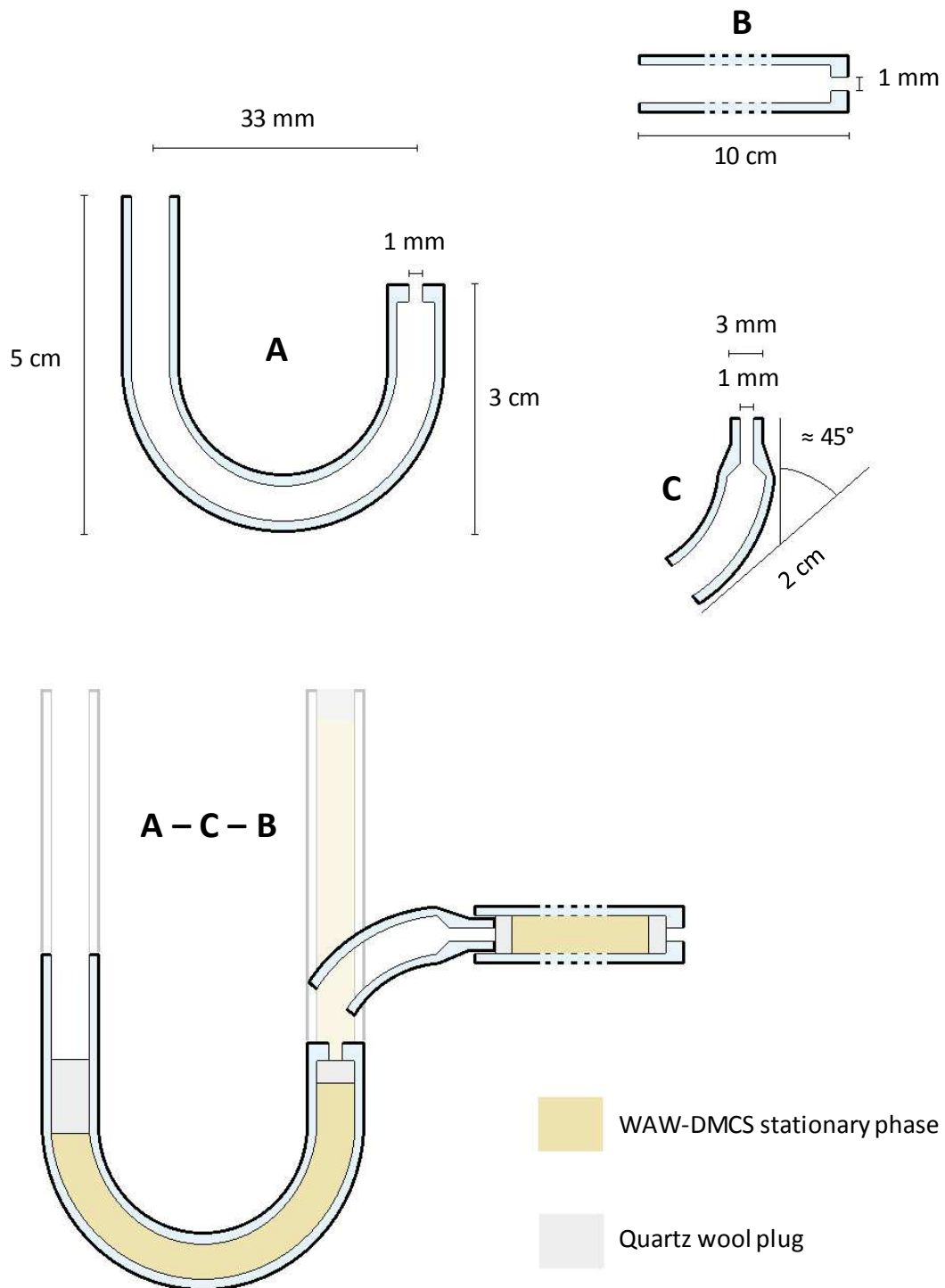


Figure 8. Scheme of the three-pieces solution designed for a better control of the trap-column settings.

In order to obtain MMHg data for our samples, as the present method was not ready, we collaborated with GET Toulouse on a highly sensitive MMHg measurement method involving GC-ICPMS.

2. Methylmercury measurement by species-specific isotope-dilution analysis

a. Material and reagents

The sample preparation is processed in 120 mL narrow-necked glass bottles dedicated to this use. After each use, they are triple-rinsed with ultra-pure water and scorched at 500 °C overnight to purge away organic and Hg adducts. Solutions of $^{199}\text{HgCl}_2$ (91.7% abundance, ISC-Science®, Spain) and $\text{MM}^{201}\text{HgCl}$ (96.5% abundance, ISC-Science®, Spain) were used as isotopic spikes. Other reagents necessary to sample preparation include ultra-grade glacial acetic acid (CH_3COOH , 99%, Avantor™, The Netherlands), hexane and ammonia, which was stored at 4 °C. Sodium tetra-*n*-propylborate (98%, packed under argon, Merseburger Spezialchemikalien®, Germany) solutions were prepared daily and stored at -18 °C.

b. Sample preparation

A known volume of melted snow (ideally between 110 and 115 mL) is added to the 120 mL bottle and spiked with the speciated isotopic standard solutions – $^{199}\text{HgCl}_2$ (10 ppb) and $\text{MM}^{201}\text{HgCl}$ (0.1 ppb). The concentration of MMHg in the sample can be calculated from the observed isotope ratios when the natural and enriched isotope ratios and the masses of both sample and spike are known. The spike volume of $\text{MM}^{201}\text{HgCl}$ solution to add is determined using the following calculation:

$R_e = 0.87$ is the natural 201/202 isotopic ratio

$R_s = 40.85$ is the spike 201/202 isotopic ratio

$R_m = (R_e \times R_s)^{1/2}$ is the 201/202 ratio in the sample + spike mixture

Considering $M = R_m(R_s - R_e) / [(R_m - R_e)(R_s - R_m)]$ in function of R_m , the method is accurate and valid for R_m values determined for M close to its minimum (Figure 9).

$R = 1/R_m$ correspond to the 202/201 isotopic ratio in the sample once the spike is added, and shall be in the range allowed by the R_m validity. This is a value of interest to validate or discard single measurements. The spike volume is chosen to fit the R validity range (which is

intrinsically a bit flexible), which requires to anticipate to some extent the MMHg content of the samples.

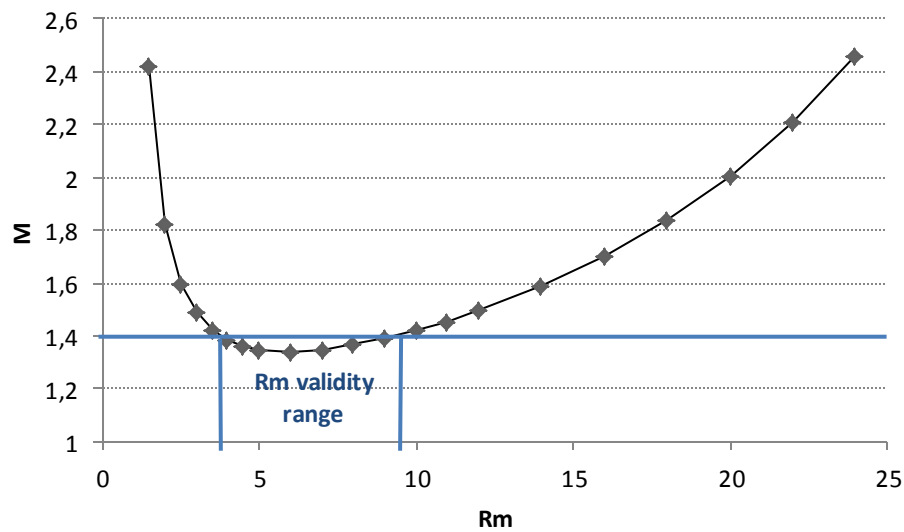


Figure 9. Graphical representation of M in function of Rm, displaying a visual estimation of the Rm validity range.

In our case, the method is valid for R ranging from 0.20 to 0.70, allowing us to estimate the MMHg content of our sample with roughly a factor 3 (0.70/0.20) maximum difference. This would have been arbitrary (and way too much time-consuming) to make this estimation on each sample, so we chose to differentiate samples using their physical type (coastal snow, glacier snow, sea-water, meltwater...etc.) and the previous results of our team. As MMHg in Arctic springtime snow can vary over wider ranges than a factor 3 (Larose et al., 2010), the risk was to misestimate the MMHg content of some of our samples before analysis hence to finally discard too many outlier pieces of data. The volume of $^{199}\text{HgCl}_2$ spike is chosen using the same method (with $R = 202/199$), and as we chose to focus on MMHg, the HgCl_2 spike was set to 100 μL per 100-115 mL for all the samples.

After spike addition, the samples are stirred for homogenization and let 1 hour at least for equilibration. Isotope dilution is based on the addition of a known amount of the enriched isotope to a sample. Equilibration of the spiked isotope with the natural element/species (MMHg in our case) in the sample alters the isotope ratio that is measured and used for calculation. At the end of the equilibration, spiked and natural MMHg should be integrated in the sample matrix in the same way and in the same proportions. In practice, the achievement of effective equilibrium of the enriched spike and the sample is not easy to obtain, but it is critical for the accuracy of the results. In our case, in samples containing low DOC, the equilibration was achieved quite rapidly (within 1 hour).

After the equilibration step, the samples were buffered with 5 mL of a 0.1 M acetic acid-sodium acetate buffer (pH = 3.9) and adjusted, if needed, to pH = 3.9 with ammonia. Then, 500 μL of 0.5% w/w sodium tetrapropylborate and 200 μL of hexane were added to derivatize and extract the dialkylated compounds formed (MeHgPr and HgPr_2). This derivatization step is strongly pH dependent (Monperrus et al., 2003, 2004), hence one should not forget to adjust the pH before adding tetrapropylborate to the sample. After 10 min of manual shaking, the organic layer was manually collected and transferred to a glass vial capped with septum-equipped caps and stored at $-18\text{ }^\circ\text{C}$ until analysis.

c. Analytical system and operating conditions

The analytical system consists in a coupling between a gas chromatography device (or GC, Thermo Scientific® Trace Ultra) and a high-resolution inductively coupled plasma mass spectrometer (or HR-ICPMS, Thermo Scientific® Element-XR) in the Geoscience Environment Toulouse (GET) laboratory (Toulouse, France). These two elements are linked by a 0.5 m heated transfer line. A picture of the coupled system is presented in Figure 10 (courtesy of J. Sonke).



Figure 10. Picture of the GC-HR-ICPMS equipment at GET. *Courtesy of J. Sonke.*

The glass vials containing the samples (dialkylated Hg derivatives in hexane) are placed on the autosampler rack. The autosampler syringe rinses three times with hexane, three times with 2 μL of the sample and injects 10 μL of the sample into the GC. This procedure is repeated three times for each sample (analytical triplicates). As the GC-ICPMS coupling is just physical, the operating conditions of the GC and the ICPMS can only be set up separately. These operating conditions are described below in Table 2.

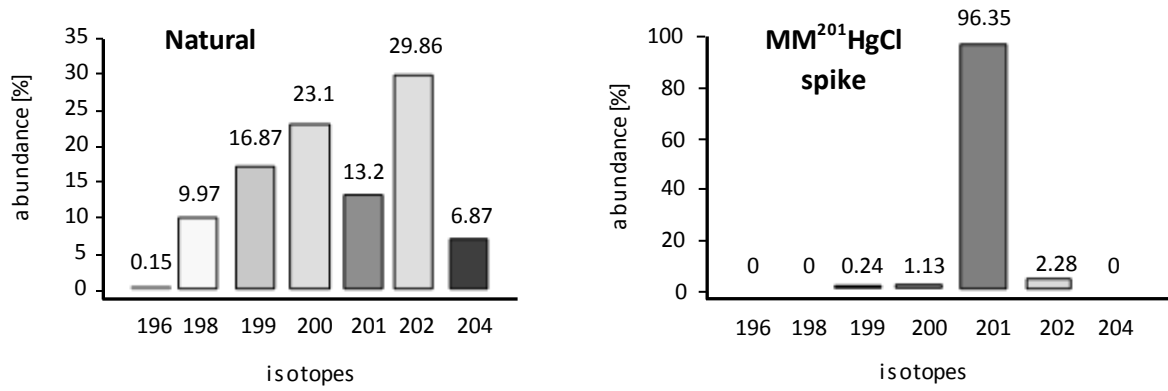
Table 1. GC and ICPMS parameters used in isotopic-dilution-GC-ICPMS analytical method

GC conditions	ID-GC-ICPMS
<i>Column</i>	RTX [®] -5MS fused silica 30 m id 0.25 mm, D.f. 0.25 μm
<i>Injection port</i>	PTV Splitless
Injection port temperature	250 °C
Injection volume	2 μL
Carrier gas flow	He 0.8 mL/min
Make-up gas flow	Ar 0.7 L/min
<i>Oven program</i>	
Initial temperature	40 °C
Initial time	1.5 min
Ramp rate	50 °C/min
Final temperature	250 °C
Hold time	1.5 min
<i>Transfer line</i>	
Temperature	250 °C
Length	0.5 m
ICPMS conditions	
Rf power	1200 W
Gas flow	
Cool	16 L/min
Auxiliary	0.8 L/min

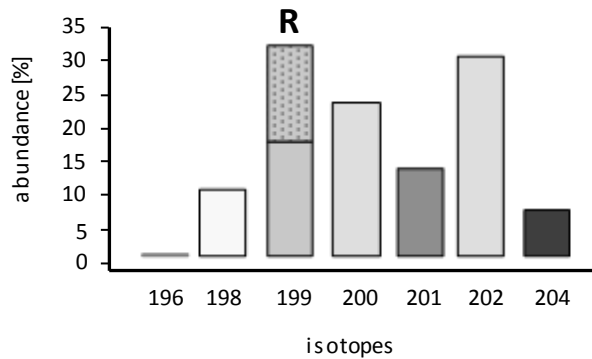
Nebulizer	0.45 L/min
Isotopes/dwelltimes	Hg : 196, 198, 199, 200, 201, 202, 204 (40ms) Tl : 203, 205 (30ms)

Each run produces four chromatograms for Hg species: for the 199, 200, 201 and 202 isotopes (198 interacts with Pt, 204 with Pb). Each chromatogram shows one first peak for MeHgPr (or MMHg in the sample) and a second one for HgPr₂ (or Hg²⁺ in the sample). First, the samples for which MMHg peaks are too small (compared to the baseline noise) and do not allow peak integration are discarded. Then, as mentioned previously, samples where R (202/201 isotopic ratio) outranges its validity range (Figure 9) are discarded too.

The MMHg concentration can be calculated for the remaining samples, knowing for both the sample and the spike 1) their mass; 2) the 202 and 201 isotopic abundances; and 3) the relative mercury atomic mass. The R ratio in the [sample + spike] mixture is also needed for MMHg determination and is calculated by comparing MM²⁰²Hg and MM²⁰¹Hg peak areas on the chromatogram. A brief description of the isotopic dilution principle and the equation providing the MMHg concentration in the sample are presented in Figure 11.



Natural + spike



$$c = \frac{c'w'A_r(RY' - X')}{wA'_r(X - RY)}$$

where

- w** : sample mass
- w'** : spike mass
- c** : sample concentration
- c'** : spike concentration
- A_r** : relative atomic mass of natural mercury
- A'_r** : relative atomic mass of enriched mercury
- X** : natural abundance of the 201 isotope
- X'** : abundance of the 201 isotope in the spike
- Y** : natural abundance of the 202 isotope
- Y'** : abundance of the 202 isotope in the spike
- R** = 201/202 isotopic ratio

Figure 11. Principle of the isotopic dilution for MMHg measurement in natural samples

3. Ion chromatography

a. Sample preparation

Samples for ion chromatography were directly sampled in Coulter polycarbonate Accuvettes[®] sealed with polyethylene caps and melted in a class 100 clean room at LGGE-CNRS laboratory (Grenoble, France). They were then transferred into Dionex glass vials previously rinsed with ultra-pure Millipore water (conductivity > 18.2 mΩ, TOC < 10 ng/g) and analyzed less than 24 hours after melting. Analyses were performed by conductivity-suppressed ion chromatography using a Dionex ICS 3000[®] apparatus and a Dionex AS40[®] autosampler placed in the clean room facilities.

b. Analytical conditions

The Dionex ICS3000[®] equipment allows for the simultaneous analysis of anions and cations by injecting an aliquot of the same sample into the injection loop of each chromatographic module. The remnant was left in the cuvette, refrozen and stored as a reserve for complementary analyses. Due to the large number of samples, the analyses were run 24 hours per day with stops only during weekends. The operating conditions are presented in Table 1.

Table 2. Operating conditions for the ion chromatograph Dionex ICS 3000[®] for the analyses of Arctic snow and water samples.

Conditions	Anions	Cations
Injection system	Autosampler	Autosampler
Separation column	AS11-HC 2 mm	CS16 2 mm
Guard column	AG11-HC 2 mm	CG16 2 mm
Suppressor	ASRS-300 2 mm	CSRS-300 2 mm
Injected volume [μL]	300	300
Eluent	KOH	MSA
Eluent flow rate [mL/min]	0.38	0.50

Eluent concentration [mM]	Gradient from 3 to 30	Isocratic, first 30 and later diminished to 24
Regenerant	H ₂ O	H ₂ O
Temperature [°C]	37	37
Run time [min]	23	15 but increased to fit the anions run time

c. Control and validation

Calibration

The detector signal (conductivity in S) is proportional to the ionic concentration in the sample. To determine the relationship between conductivity and ion concentrations, we established daily calibration curves using mixed solutions of known concentrations, called standard solutions. The standard solutions were prepared in two steps: a first dilution was made from concentrated solutions (500-1000 mg/g) to prepare intermediate solutions (0.4-20 mg/g), and then a second dilution from the intermediate solutions was made to prepare the final standard solutions used for calibration (0.2-20 ng/g for minor ions 1-100 ng/g for major ions).

While intermediate solutions are renewed twice or three times per month for inorganic ions, they are weekly renewed for organic ions, the latter to prevent losses by bacterial contamination or gaseous exchanges. Standard solutions were prepared daily. The uncertainty related to the preparation of standard solutions is in average less than 1%. Uncertainty ranges corresponding to highest and lowest concentrations in standard solutions are [0.7-3.0%] for F⁻ and Br⁻; [0.8-3.6%] for oxalate, succinate, pyruvate, lactate, propionate and glutarate; [0.4-1.8%] for acetate and formate; [0.4-0.6%] for MS and Mg²⁺; [0.7-0.9%] for K⁺ and NH₄⁺; and [0.3-0.4%] for Na⁺, Cl⁻, Ca²⁺, NO₃⁻ and SO₄²⁻. Intermediate solutions were monitored at the beginning and at the end of daily set of analysis to verify that no losses took place during storage and also allowed to test the stability of the column.

Each calibration curve consisted of 6 points and was fitted by a linear function (for Na⁺, F⁻, Cl⁻, Br⁻, NO₃⁻, SO₄²⁻, lactate, acetate, formate, oxalate) or quadratic (for other ions), passing or not through the origin. Some calibration curves showed a positive Y-intercept at the origin (F⁻, Ca²⁺, acetate, formate, oxalate). The concentration to be added to the theoretical values of the standards to compensate this intercept was determined graphically and the calibration curve offset was then

forced to zero (dashed line in Figure 12). This initial offset value is generally very close to the value of the procedure blanks. It corresponds either to contamination related to standard preparation or to contamination produced inside the autosampler or the analytical equipment. It was deduced from final concentrations only in this last case.

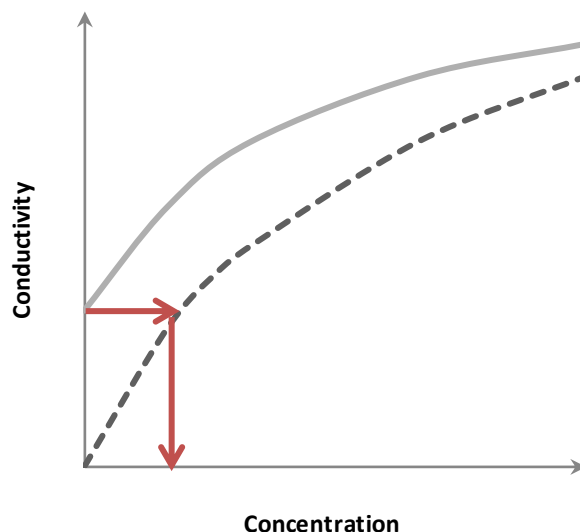


Figure 12. Schematic representation of a calibration curve with a Y-intercept (continuous grey line). After adding the graphically determined concentration, the offset is forced to be zero (dashed line). The graphically-determined concentrations were close to the procedure blank values obtained by injecting ultrapure water in the chromatograph.

Procedure blanks

Every day, various procedure blanks consisting in a few milliliters of ultra-pure Millipore water were prepared and analyzed in exactly the same way as the samples. This procedure accounts for the influence on measurements of water impurity content, and contamination occurring during sample transfer and analysis. Blank concentrations usually fit Y-intercept of calibration curves (Figure 12).

A significant decrease of procedure blanks are observed for F^- , acetate, formate and Ca^{2+} when the injection is done manually (i.e., when samples are directly injected with a syringe into the injection port without using the autosampler). Acetate, oxalate and Ca^{2+} blank values tended to decrease gradually the longer the equipment was used mostly due to the progressive rinsing of autosampler loops and injection lines leading to significantly lower desorption from plastic tubings. For instance, Ca^{2+} contamination was higher for the first 10-12 samples analyzed after a weekend off and also in samples analyzed just after more concentrated samples. The origin of the F^- blank is uncertain: it is

probably due to an interference with an organic ion desorbed by PEEK (polyetheretherketone) Dionex connections. It remained constant during all our measurements.

Blanks of formate and acetate are due to gaseous contamination. Once placed on the autosampler rack, samples remained between a few minutes and more than 12 hours within the autosampler enclosure before the injection into the chromatograph lines. Contamination is higher for samples stored for longer time in the autosampler, very likely due to slow air penetration through the pre-pierced septa of the Dionex vials. A slight gaseous contamination may also occur when water microdroplets remain in vials once rinsed. Based on all these observations, blanks are minimized by improving the techniques of vial rinsing (in particular by avoiding inner wet residues), by renewing the vials and septa after every four to five uses and by analyzing the anions before the cations (so the septum will be pierced first for the gaseous contamination sensible samples). Contamination for formate is thus significantly reduced, but it is not possible to avoid acetate increase during one batch duration. However, considering that values were close to the detection limit, acetate concentrations were not corrected for this progressive increase in the dataset produced, as major peaks of these species would be noticeable, if any.

In conclusion, to correct daily measurements of formate, acetate, oxalate and Ca^{2+} , we subtracted the corresponding values daily measured for procedure blanks from sample concentrations.

Instrument Detection Limit

The instrument detection limit (DL) is the lowest concentration of a species that is just distinguishable from zero. It was calculated from the equation:

$$DL = 3s \times b$$

where b is the value of background noise and s is the standard deviation of a system blank. A system blank corresponds to the passage of the eluent alone, without injection of water or sample. Both b and s are determined between the start and the end time where the peak of a given analyte must be located. Missing data and unexplainable outliers were replaced by DL values, as they are indicators of the uncertainty of the measurements.

4. Dust concentration and size distribution measurement

a. Sample preparation

We use the same samples than for the ionic chromatography, which have been originally sampled in accuvettes© then melted and subsampled in a class 100 clean room at LGGE for ion analysis. We added pure formaldehyde (1 mL) to the accuvettes© just after subsampling for ion chromatography to avoid any microorganism growth (which would induce particle contamination). The samples were all prepared, stored and analyzed in the same class 100 clean room.

The laboratory blanks were carefully checked before and during each series of measurements and represented always <1 ppb of total dust. They consist of MilliQ water and the dust content of the accuvettes.

b. The measurement: principle, handling and limitations

The measurements of dust concentration and size distribution were performed using a Coulter Counter (CC) Multisizer IIe© set up in a class 100 clean room. The instrument works on the basis of the detection of the electric signal generated by the particles that are forced to flow through a small aperture tube (50 μm in diameter). The melted snow sample is made conductive by addition of a pre-filtered 20% NaCl electrolyte solution giving a 1% concentration in the final solution. Melted samples were continuously stirred (mechanically) before the analysis in order to prevent dust sedimentation in the accuvettes©. At least three consecutive measurements were performed on each sample. After each sample a blank solution (ultra-pure water added with the electrolyte) was measured for cleaning the orifice tube, and checked through a single measurement.

The instrument was set for measurements of particles with diameters from 0.7 to 20 μm in 256 channels on a logarithmic scale. The particle size is expressed by the diameter of a sphere of equivalent volume, and the mass was calculated from the measured volume assuming an average crustal density for particles of 2.5 g/cm^3 . These two assumptions constitute the main limit of the method. Actually, the particles present in Arctic snow are not always regular and isometric. The

density is also adopted arbitrarily, considering that clays and quartz are the most abundant mineral phases of long-range transported particles.

5. Total organic carbon (TOC) measurement

a. Sample preparation

Samples for TOC measurement were collected in 100 mL acid washed glass bottles and melted in the dark at +4 °C prior to analysis. The samples are filtrated on an ultra-pure water washed Acrodisc® 0.2 µm filter. The resulting filtrate is transferred in a 50 mL glass bottle and injected in the input capillary of a 700 TOC (OI Analytical) equipment. The analyzer has up to 8 input capillaries and can therefore autosample up to 8 samples. Every manipulation is handled wearing clean nitrile protection gloves under a laminar flux hood.

b. The measurement

The method used is based on the conversion of the total dissolved carbon into CO₂ and its subsequent detection by infrared detection. In order to discriminate the total inorganic- and organic carbon (TIC and TOC), the TIC is first transformed in CO₂ by acidification (pH = 2.2) at 100 °C (addition of 200 µL of a 5% phosphoric acid solution) purged out of the sample and analyzed. While the TIC is being analyzed, an excess of sodium persulfate (1 mL of a 100 g/L solution) is added to the sample to oxidize the TOC to CO₂. The following TOC analysis proceeds as for the TIC by infrared detection, giving the carbon content of 2 mL of sample. The whole process is automated.

In our case, as air-sample CO₂ exchanges probably occurred (and altered the TIC content) during both melting and storage of the sample, we discarded the TIC data. Each sample was analyzed in triplicate.

c. Control and validation

Calibration

The area of the peak provided by the detector is proportional to the carbon concentration of the sample. The determination of TOC concentration in our samples requires a daily external calibration, to test the repeatability of the sample preparation. The calibration consists in the analysis of 362 µL

of 5 standard solutions of known concentrations, from the less to the more concentrated. The standards are prepared daily from a concentrated sucrose solution (4.20 mgC/mL) and range from 75 to 1125 $\mu\text{gC/mL}$. The calibration curve equation allows for the determination of the the carbon content of a 2 mL sample. Figure 13 shows the calibration curve constructed from all the values measured during our daily calibrations. The positive Y-intercept at the origin is due to small sample contamination during the exposure to the atmosphere of the laboratory. The low variance of the results assess for the good repeatability of the operator manipulation.

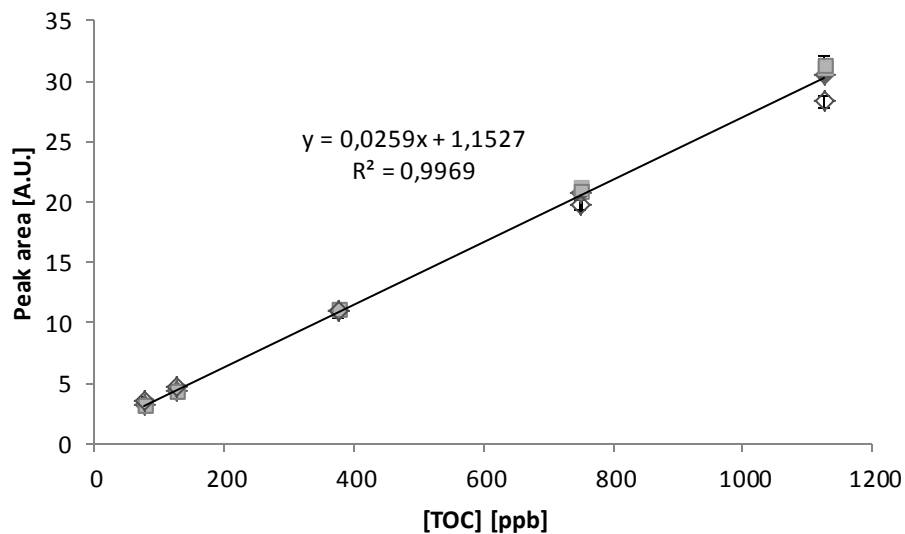


Figure 13. Representation of the four different calibration curves obtained during the TOC analysis.

Blanks

Every day, ultra-pure water was directly analyzed to determine its carbon content as for regular samples (2 mL collection). In addition, filtrated ultra-pure water—following the conditions of sample preparation—was also analyzed. The difference between filtrated and unfiltrated blanks corresponds to the carbon residue of the Acrodisc filters, which was usually very low. As our samples are filtrated, it is more consistent to consider the filtrated blanks as procedure blanks. The blank values are presented in Figure 14.

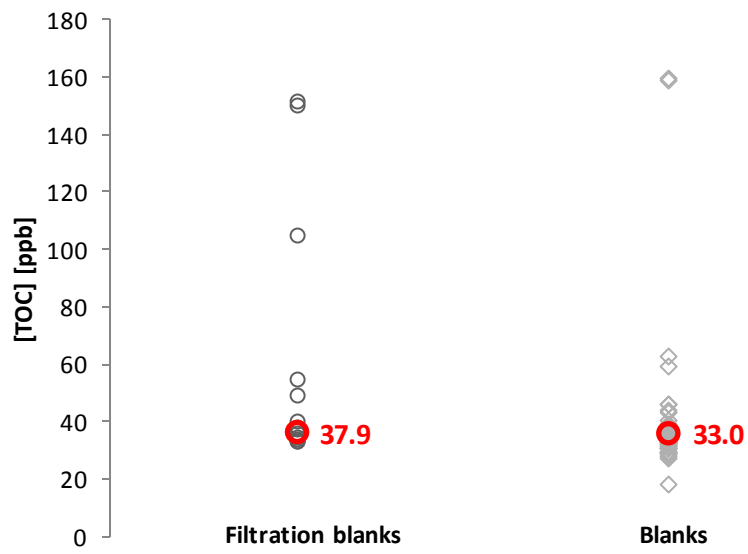


Figure 14. Repartition of the blank (open diamonds) and filtration blank (open squares) values around their median value (displayed in red).

6. Total mercury measurement

a. Sample preparation

The samples were melted in the dark and spiked with BrCl (see US EPA method 1631 reagent preparation, 5 mL per liter of sample) and let to react overnight. During this time, all the mercury species contained in the sample are converted to Hg^{2+} (de-alkylation and/or oxidation). Just before the analysis, hydroxylammonium chloride is added to the sample (see US EPA method 1631 reagent preparation, 5 mL per liter of sample) to neutralize the BrCl excess, and roughly 50 mL of the resulting sample are put in a disposable falcon on the autosampler rack of a Tekran® 2600 analyzer (Tekran® Inc., Canada). Once in the autosampler rack, a sample is analyzed within 3 hours.

b. The measurement

The Tekran® 2600 analyzer allows for the determination of THg concentration by coupling Hg^0 -preconcentration, thermal desorption and Hg^0 measurement by cold vapor atomic fluorescence spectroscopy (CVAFS). In our case, the US EPA 1631 method is used for reagent preparation and sample analysis. The samples are directly injected in the instrument tubing together with a SnCl_2 solution (see US EPA method 1631 reagent preparation), which reduces the Hg^{2+} of the sample into volatile Hg^0 . The resulting mixture passes through a phase separator where the Hg^0 is removed from the aqueous phase by a continuous ultra-pure argon flux. Two gold traps are mounted in series on the gas line downstream of the phase separator to trap Hg^0 by metallic amalgamation. The heating of these traps to 600 °C under ultra-pure argon stream allows Hg^0 thermal desorption and subsequent transportation through an optical cell. Mercury atoms are excited by UV radiations to produce fluorescence emissions ($\lambda = 253.7 \text{ nm}$) measured by a photomultiplier.

The autosampler settings are driven via software interface and do not need daily reset. The instrumental settings (i.e. argon, sample and SnCl_2 throughputs) are reset daily directly on the Tekran® 2600 equipment. As some of the instrumental settings can barely be exactly reproduced every day, a daily external calibration is required. A daily work schedule always includes:

- i. A cleaning run, to purge the instrument from the Hg contamination overnight;

- ii. Several (usually 3) “wash station” blanks: runs with ultra-pure water as analyte (see below). This step is repeated as soon as the results are stable.
- iii. Several (usually 3) reagent blanks (see below): 50 mL of ultra-pure water added with 250 μL of BrCl and $\text{NH}_2\text{OH.HCl}$ solutions.
- iv. A calibration followed by one or two “wash station” blanks;
- v. Sample analysis in triplicate. Each triplicate is separated from the next one by one or two “wash station” blanks. A NIST certified standard solution is analyzed every 5 samples.
- vi. A cleaning run;
- vii. Several rinsing runs: “wash station” blanks or acidified ultra-pure water.

The analyzer is very sensitive to constant Hg contamination (continuous Hg^0 diffusion from the ambient air inside the tubing). In addition, the samples – once on the autosampler rack – are susceptible to be contaminated by deposition of Hg-containing particles (Hg^0 solvation from the ambient air is negligible). To avoid these contaminations as much as possible, the Tekran 2600[®] analyzer is operated under a laminar flux hood (in the field facilities), or in a class 10000 clean room at the LGGE.

c. Control and validation

Calibration

The Hg content of the sample is proportional to the area of the peak detected by the photomultiplier. A daily calibration was run by analyzing Hg^{II} NIST SRM-3133 standards between 0.5 and 100 ng/L, and showed always a very strong linearity ($0.99985 < r^2 < 0.99999$). The standards are prepared by spiking the adequate amount of Hg^{II} working solution ($[\text{Hg}^{\text{II}}] = 4.60 \mu\text{g/L}$, prepared monthly) in exactly 50 mL of ultra-pure water previously spiked with 250 μL of BrCl solution and the same amount of $\text{NH}_2\text{OH.HCl}$ solution. The BrCl and $\text{NH}_2\text{OH.HCl}$ shall be added in the same proportion than in the real samples during their preparation step. An example of calibration curve is displayed in Figure 15.

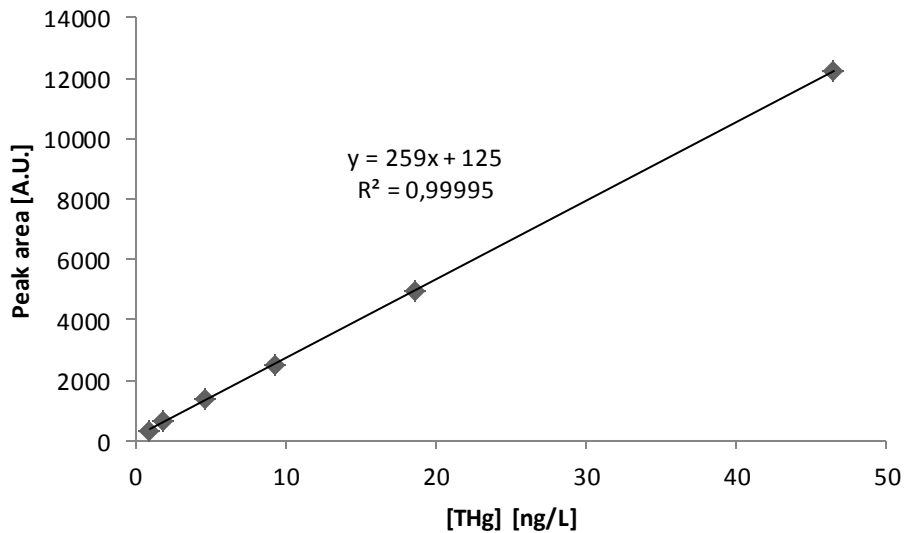


Figure 15. Example of a calibration curve of the Tekran® 2600 analyzer (method 1631).

Blanks

The “wash station” term refers to a part of the autosampler where the autosampling tube is rinsed in a continuous ultra-pure water stream. The “wash station” blanks therefore refer to runs where only ultra-pure water from the wash station is analyzed. They indicate the cleanness of the tubing and shall be as low and as stable as possible, thus their stabilization (step ii in the 6.b paragraph) indicates that the equipment is as clean as possible. “Wash station” blanks are also required to rinse the system after samples or standards (once or twice depending on the concentration), or at the end of the analysis schedule.

The reagent blanks are prepared as the calibration standards but without any Hg^{II} addition. They indicate the bias on the peak area due to the addition of the reagents (BrCl and NH₂OH.HCl), in other words the THg contained in these reagents. The value of the reagent blanks is therefore subtracted to the one of the samples analyzed during the same day.

Detection limit

The instrument detection limit was calculated from the equation:

$$DL = 3.33s$$

where s is the standard deviation of a reagent blank, determined daily and before any sample analysis. Missing data and unexplainable outliers were replaced by DL values, which never exceeded 0.1 ng/L.

References

- Berzas Nevado, J.J., Rodríguez Martín-Doimeadios, R.C., Krupp, E.M., Guzmán Bernardo, F.J., Rodríguez Fariñas, N., Jiménez Moreno, M., Wallace, D., Patiño Roper, M.J., 2011. Comparison of gas chromatographic hyphenated techniques for mercury speciation analysis. *Journal of Chromatography A*.
- Bowman, K.L., Hammerschmidt, C.R., 2011. Extraction of monomethylmercury from seawater for low-femtomolar determination. *Limnology and Oceanography: Methods* 9, 121–128.
- Larose, C., Dommergue, A., De Angelis, M., Cossa, D., Averty, B., Maruszczak, N., Soumis, N., Schneider, D., Ferrari, C., 2010. Springtime changes in snow chemistry lead to new insights into mercury methylation in the Arctic. *Geochimica et Cosmochimica Acta* 74, 6263–6275.
- Monperrus, M., Rodríguez Martín-Doimeadios, R.C., Scancar, J., Amouroux, D., Donard, O.F.X., 2003. Simultaneous Sample Preparation and Species-Specific Isotope Dilution Mass Spectrometry Analysis of Monomethylmercury and Tributyltin in a Certified Oyster Tissue. *Analytical Chemistry* 75, 4095–4102.
- Monperrus, M., Tessier, E., Veschambre, S., Amouroux, D., Donard, O., 2004. Simultaneous speciation of mercury and butyltin compounds in natural waters and snow by propylation and species-specific isotope dilution mass spectrometry analysis. *Analytical and Bioanalytical Chemistry* 381, 854–862.
- Tseng, C.M., De Diego, A., Pinaly, H., Amouroux, D., Donard, O.F.X., 1998. Cryofocusing coupled to atomic absorption spectrometry for rapid and simple mercury speciation in environmental matrices. *J. Anal. At. Spectrom.* 13, 755–764.

ii. Field conditions and methodology

1. Description

a. Study site

The research campaign was held between April 13th and May 7th, 2011 at Ny-Ålesund in the Spitsbergen island of Svalbard archipelago, Norway (76°56'N, 11°52'E). The sampling site is a 200 m² area with restricted access to limit human induced contaminations. It is located on the south coast of the Kongsfjorden, which is SE-NW oriented and opened on the sea on its west side (Figure 1). This fjord was free of persistent sea-ice during the field campaign, but experienced several punctual refluxes of floating ice due to tide streams.

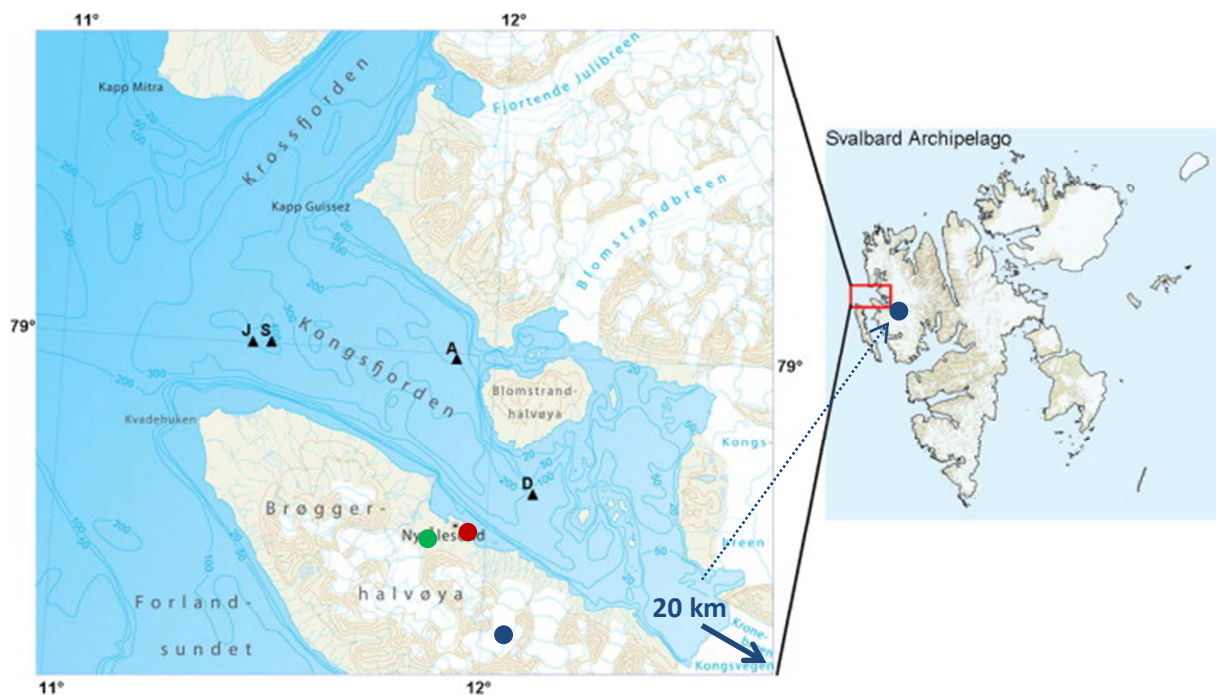


Figure 1. Svalbard and Kongsfjorden map. Sampling sites are displayed in red (coastal snow), blue (glacier snow) and green (meltwater).

b. Snow and meltwater sampling

Snow was collected daily on the study site for surface samples, and every three days from pits. Snow samples were also collected from pits dug in two surrounding glaciers: Kongsvegen (78°45'N, 13°20'E, 670 m) and Midre Lovénbren. Meltwater was collected continuously on a secondary site located between Ny-Ålesund and the Zeppelin station, because of a much thicker snow cover. The sampling apparatus consisted in six half-tubes of acid-washed black PVC disposed with a slight angle at three different depths through a 1 x 1 m (height x horizontal thickness) snow wall (Figure 2). An acid-washed 1 L borosilicate glass bottle with aluminum external coating (to avoid photo-induced reactions) was placed open at the lower end of each channel, and daily sampled (if enough material collected). Samples for MMHg and THg were collected in acid-washed 250 mL borosilicate glass or Teflon FEP bottles. Samples for major ions and particles were collected in 30 mL sterile acuvettes. Samples for DOC and aldehydes were collected in acid-washed glass bottles of different volumes. All samples were stored frozen (-20 °C) and in the dark until analysis.

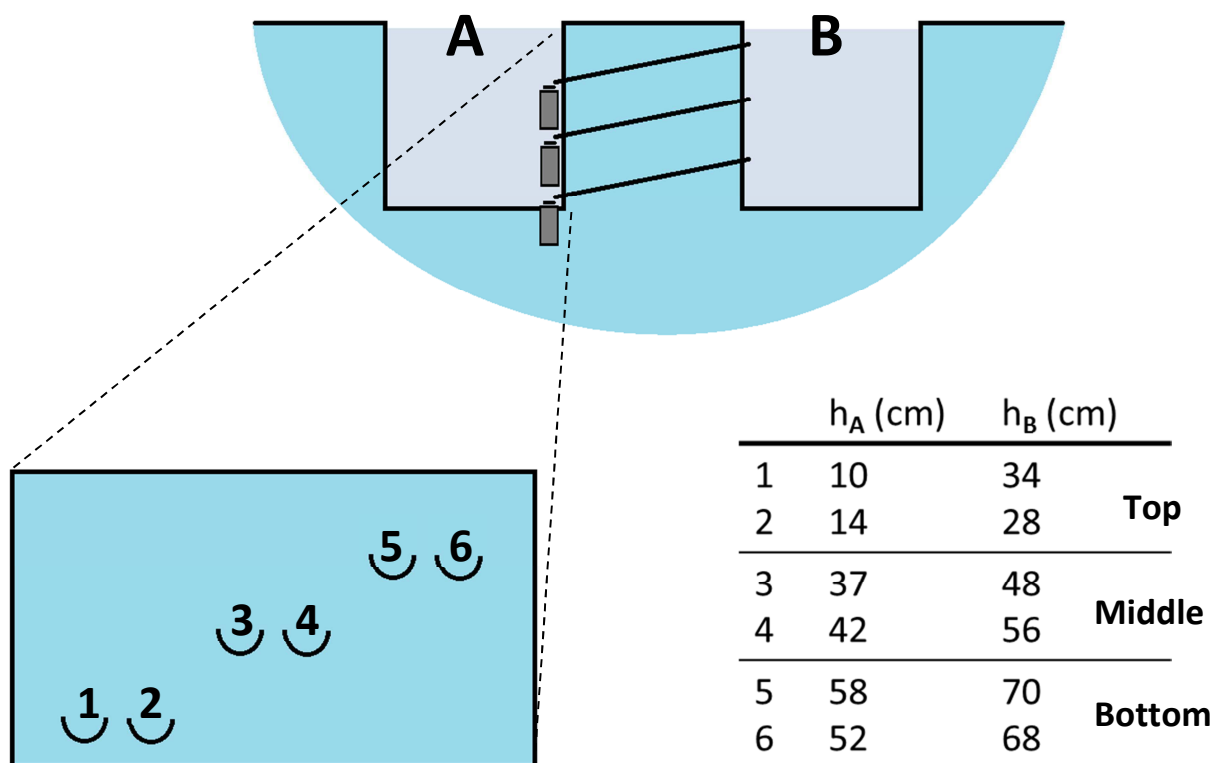


Figure 2. Scheme of the meltwater sampling system. The bottles are coated with aluminum sheet on their external side.

c. Sea water sampling

Surface sea water was collected every 5 days at both 100 and ca. 1000 m offshore. Sea water was also collected on several transects (perpendicular to the south coast) along the fjord, between the front of Kongsvegen glacier (east end of the fjord) and Ny-Ålesund. Samples for MMHg were collected in acid-washed FLPE bottles and frozen before analysis. Samples for THg were collected in disposable falcons previously triple-rinsed with MQ water ($\rho = 18.18 \text{ M}\Omega\cdot\text{cm}$) and stored in the cold (4 °C) before analysis (usually in the following day).

2. Geochemical and meteorological data

Figure 3 outlines the main geochemical and meteorological event during the field campaign. This allows differentiating several sample groups:

- Strong wind occurred punctually several times from April 15th until a strong windstorm on April 20th (Figure 3), leading to an important deposition of sea water and visible organic materials (algae). Snow sampled during this event and in the following days hence shows a strong marine chemical signature (Figure 4). This period is referred to as “storm event” in the text below, and includes the storm event.
- From the end of April until mid-May, the snowpack encounters several strong melts due to warm temperatures, affecting both the physical (thickness, stratigraphy) and measured chemical parameters. Samples from this period may show chemical signatures of preferential elution (of a species over another) and therefore may not be representative of chemical inputs to the snowpack (Figure 4).
- Between mid-May until early June, we observe a massive particle input to the surface snow. Particle number reaches a plateau on May 23th and starts to decrease as of May 26th, when snow starts to melt with increasingly positive temperature. During this event, surface snow shows a specific chemical signature (Figure 4). This period is referred to as “particle event” in the following.

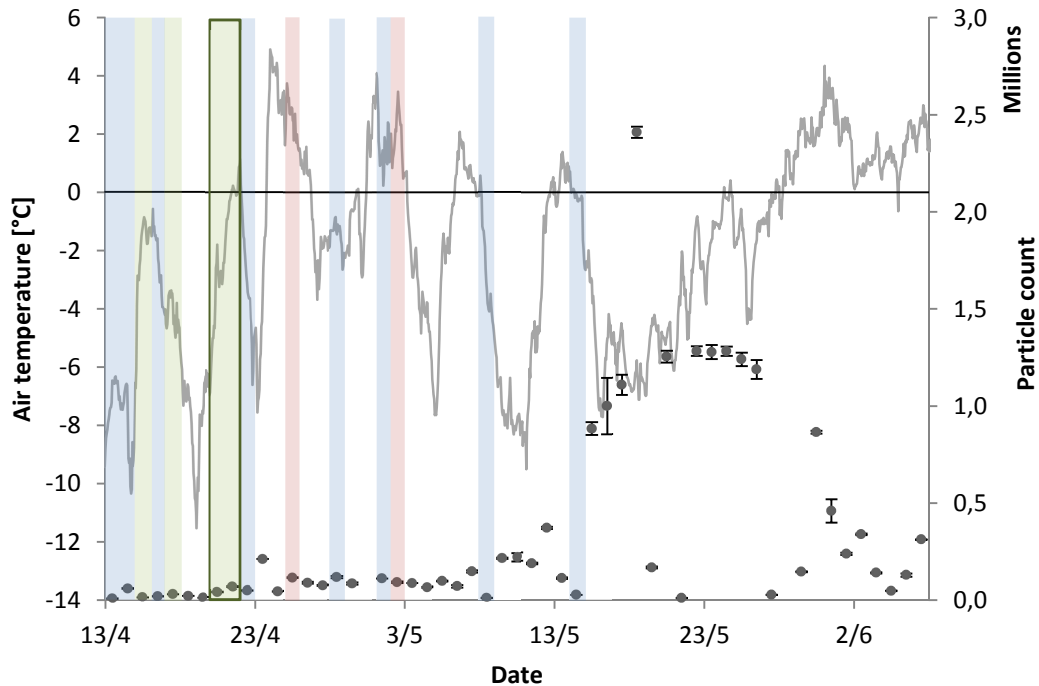


Figure 3. Outline of the main geochemical and meteorological events of the field campaign. Air temperature is displayed as a grey line, particle number in grey dots with error bars, fresh snow precipitations in blue, rainfall in red, and periods of interrupted strong winds (speed > 20 m/s) in green. The boxed green area represents the strongest wind experienced (wind storm).

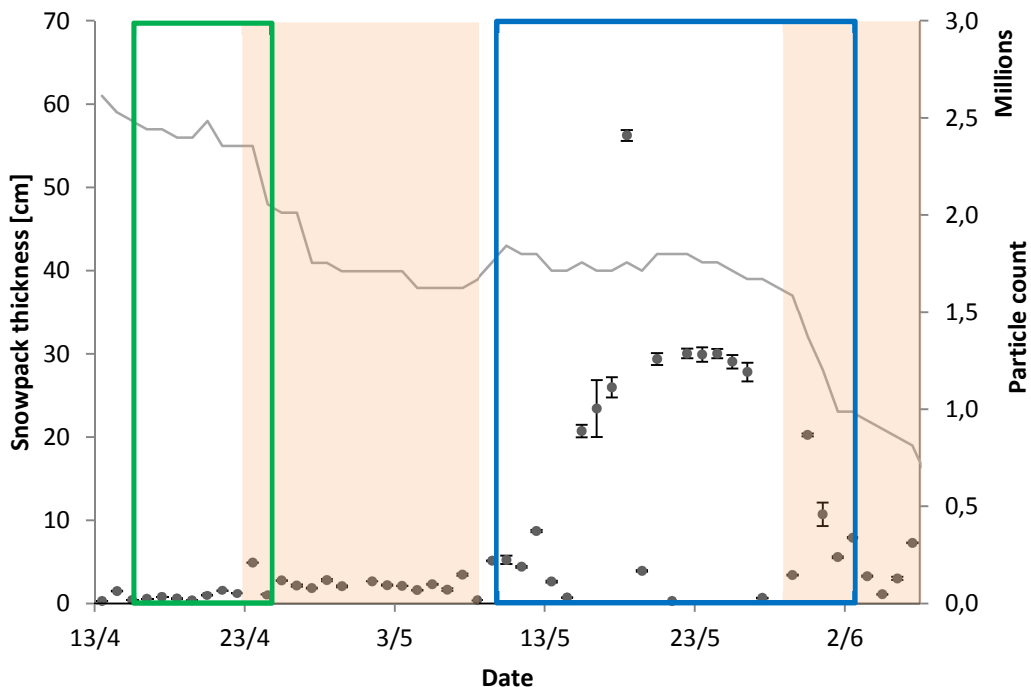


Figure 4. Classification of surface snow samples based on empirical observations. The green box represents samples with strong sea-sprays influence (called in the following “storm event”), the blue box samples under the chemical influence of particles input, and orange areas the samples chemically impacted by snowmelt. The thickness of the snowpack is indicated as a grey line.

a. Wind regime

The local wind regime in the Kongsfjorden is driven by its SE-NW orientation: the wind comes either from the open ocean (NW) or the Kongsvegen glacier (SE). This pattern is observable during our field campaign for winds of moderate speed and above (> 7 m/s) as displayed on Figure 5. Below this threshold value of 7 m/s, this SE-NW directional pattern becomes unclear, while it disappears completely for low speed winds (< 4 m/s). Interestingly winds with speed > 7 m/s coming from the open ocean are not observed, except during an AMDE event on May 8th and 9th. This is in agreement with the current knowledge of AMDEs, initiated by reactive bromine species (such as BrO or Br₂), thus related to marine bromine explosions. It is however clear that winds arriving to Ny-Ålesund – except during AMDEs – originate locally from the Kongsvegen glacier direction.

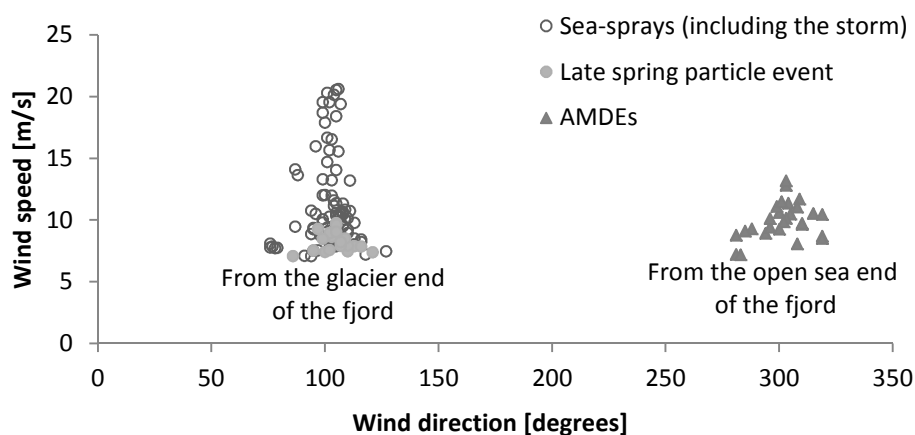


Figure 5. Local wind regime in Ny-Ålesund during the field campaign, above the threshold value of 7 m/s. Each data point represents one-hour average of wind speed and direction.

The large scale wind regime, as shown on the backward trajectory of air masses (Figure 6) doesn't show any trend. The only observable trend is a global clockwise rotation of the origin of air masses from week to week during the field campaign, from S (mid-April) gradually to NW (mid-May) and finally to N-NE (early June). There is no correlation between the origin of air masses and any observable singular event, such as the storm or the particle event in the second half of May. However, as an exception, the aforementioned AMDE event (on May 8th and 9th) is clearly due to air masses from the high Arctic Ocean (north of Greenland) having probably travelled over sea-ice-covered areas.

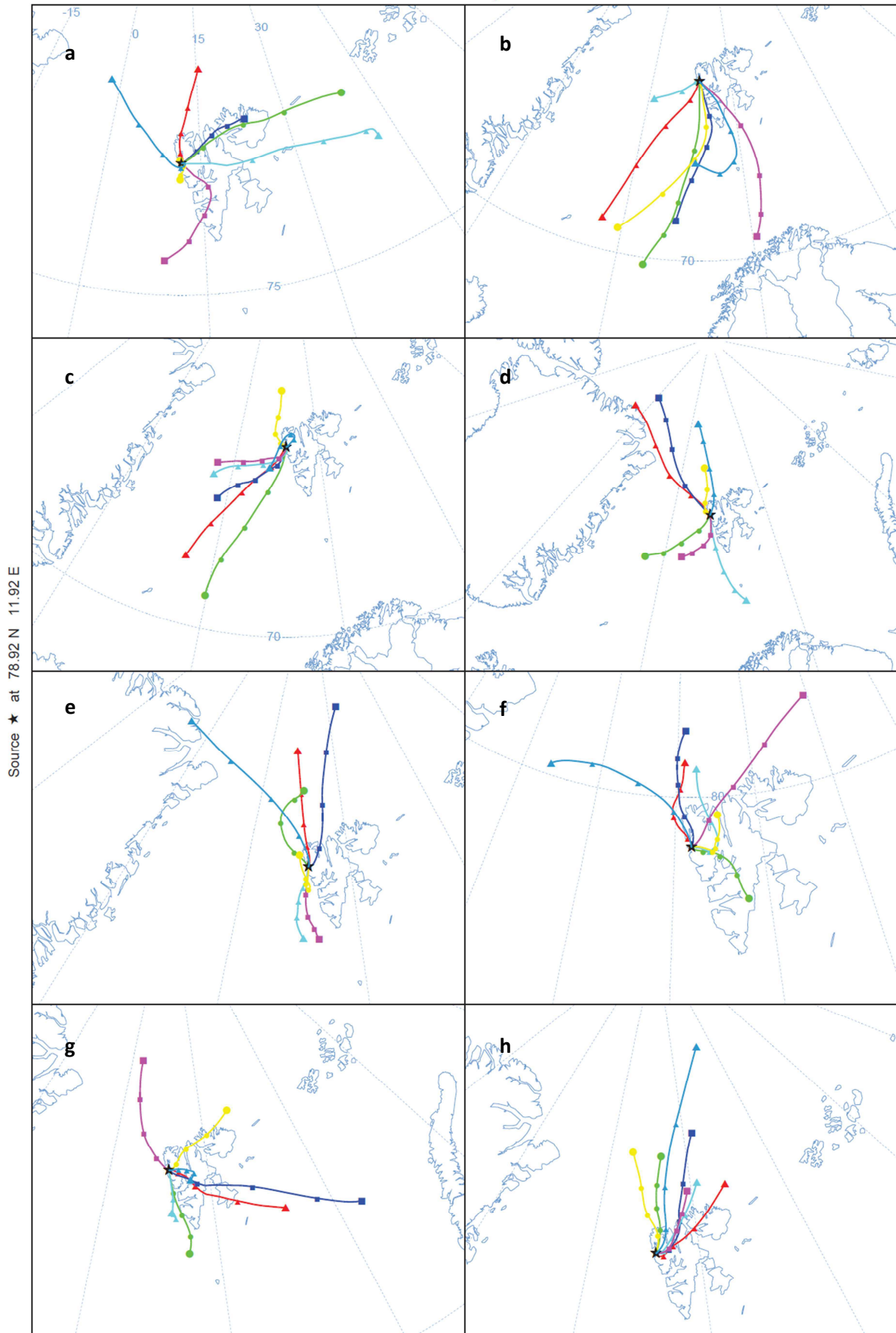
NOAA HYSPLIT MODEL
GDAS Meteorological Data

Figure 6. Backward trajectories (24 h) of air-masses ending at Ny-Ålesund. Excerpt (a) for the first week, (b) for the second week, etc... For each week, backward trajectory for day 1 is displayed in blue, day 2 in yellow, day 3 in purple, day 4 in light blue, day 5 in green, day 6 in dark blue and day 7 in red.

b. Snowpack dynamics

The whole snowpack was very dynamic during the field campaign, as the warming in late April caused its anticipated melting and important thinning (Figure 4). In addition, because of spatial variability, the snowpack was twice deeper at the place we measured its thickness as it was on the adjacent sampling field, and mainly consisted in a 20-30 cm thick porous and homogeneous melted snow layer. In consequence, we have very few samples of non-surface snow, and considered surface snow only when estimating external input of chemical species to the snowpack.

III. Identification of the primary sources of MMHg in a coastal arctic snowpack

i. Consideration of the input of THg in arctic snow

-

ii. Assessing the sources of major ions using ratio/ratio plots

-

iii. Discussion on the MMHg sources

Résumé

Cette partie présente les données de neige de surface acquises sur le site côtier tout au long de la campagne. Un premier chapitre présente les données de mercure total dans la neige côtière. Bien qu'elle contienne une brève discussion, le but essentiel de ce chapitre est de présenter les données acquises, sans revendiquer un quelconque impact sur les implications scientifiques du présent manuscrit.

Dans un deuxième chapitre, nos données sont analysées en utilisant des rapports de concentrations molaires plutôt que les concentrations directes, afin d'accéder à plus d'information (Robinson et al., 2006). Ce faisant, nous identifions pour la quasi-totalité deux sources majeures pour expliquer la chimie de la neige côtière. Si la première – les sprays marins – était attendue, la deuxième est reliée à un événement particulier observé dans la neige et décrit dans la section II.ii. Avant même de discuter de ces sources, nous évaluons leur contribution à la chimie de la neige pour chaque espèce mesurée, reliant les sprays marins aux principaux ions marins, et la deuxième source à un apport accru en calcium, magnésium, petites molécules organiques et en MMHg.

En troisième chapitre (distingué du premier pour des raisons de confort de lecture uniquement), nous discutons de la nature de cette seconde source. Les apports additionnels en calcium suggèrent en premier lieu un apport terrigène, en cohérence avec le début de la fonte sur les zones rocheuses. Cependant, cette hypothèse est jugée incompatible avec la présence accrue de petites molécules organiques et de MMHg ainsi qu'avec la grande stabilité de la composition chimique de la source (pas de variations visibles sur 3 semaines).

Une hypothèse alternative est développée, impliquant des aérosols organiques d'origine marine, qui sont décrits dans la littérature et contiennent habituellement des fragments calcaires et des dérivés biochimiques et biologiques maintenus en cohésion par un gel bio-organique. Cette composition est davantage en accord avec les caractéristiques chimiques de cette seconde source que nous observons : du calcium et du magnésium (le premier dû aux fragments calcaires, les deux servant de coagulants aux gels organiques), des petites molécules organiques et du MMHg, en tant que (sous)produits d'activité biologique marine. Cette théorie suggère une source constante et proche du site d'étude (situé à 10-20 m du fjord).

L'origine de l'événement important de dépôt de ces aérosols dans la neige de surface côtière est aussi discutée. Nous suggérons que le bloom marin printanier – un épisode de densification biologique des eaux des fjords arctiques – et la sénescence qui s'en suit sont une source abondante des composants élémentaires des aérosols organiques marins. En effet, l'explosion de l'activité

biologique ainsi que son déclin peuvent générer d'importantes quantités de produits et débris bio-organiques, ainsi que des squelettes calcaires planctoniques. En raison de l'absence de données disponibles sur le bloom du Kongsfjorden, son timing et ses implications sur la biologie marine au printemps de notre campagne, il reste impossible de confirmer cette théorie.

Finalement, nous replaçons ces résultats dans le contexte bibliographique en les comparant aux travaux existants. Bien que la question des sources de MMHg dans la cryosphère arctique soit posée depuis une dizaine d'années, elle reste ouverte depuis. Plusieurs assertions sont cependant communément acceptées, impliquant une source marine, une source atmosphérique et la méthylation *in situ*, théories qui trouvent un écho, un soutien et des explications dans cette partie (cependant nous reconnaissons la méthylation *in situ* comme négligeable dans notre manteau neigeux côtier). En effet, notre théorie n'est pas seulement compatible avec les hypothèses avancées jusque-là, mais elle détaille et identifie des processus qui n'avaient pour lors été qu'évoqués. La raison en est sans doute, au-delà de toute autre considération, l'utilisation d'une méthodologie d'analyse des données encore embryonnaire dans le monde de la chimie environnementale, mais qui permet un accès à des informations supplémentaires sur la chimie du milieu étudié.

Nous espérons qu'au-delà des résultats propres de cette étude, le lecteur retiendra la méthodologie appliquée et l'envisagera pour enrichir ses futurs travaux.

i. Considerations of the input of THg in arctic snow

The net input of Hg in snow is generally much smaller than the deposition fluxes, as a large majority is reemitted back to the atmosphere. As potential precursors to MMHg – which is the main focus of the present manuscript – the dynamics of both Hg^{II} and Hg^0 shall be considered. For this purpose, we measured THg daily on our coastal study site as a temporal record of Hg reactivity. In snow, THg is expected to be mainly (>98%) in its stable oxidized form Hg^{II} (not methylated), but a negligible proportion of volatile Hg^0 may be present as well as MMHg (Arctic Monitoring and Assessment Programme, 2011). Methylmercury barely exceeds a few percent of Hg^{II} , and often represents less than 1% in snow. Hence THg concentrations are assimilated to those of Hg^{II} in our snow samples in the following section and for the rest of the present study.

1. THg deposition on snow

The evolution of THg concentrations in surface snow is presented in Figure 1. The THg background concentration decreases during the field campaign with important noise due to small temporal and spatial variations. Total Hg concentrations decrease down to around 2 ng/L and less between the 24th and the 29th of April and at the end of the campaign (after the 1st of June), when strong melting of the snowpack occurs (see “Field condition and methodology” section). The main deposition events are distinguishable on the 14th of April, on the 10th of May and on the 14th of May. The first one corresponds to a snowing event, the second one is dry deposition during a strong AMDE event with clear sky, and the last one is a snowing event during an AMDE (for more information about AMDEs, refer to the “Introduction” part, or to Schroeder et al., 1998; Steffen et al., 2008). As low atmospheric Hg^0 can result of the arrival of already Hg-depleted air-masses, the AMDE events are identified by simultaneous atmospheric Hg^0 decrease and snow THg increase. However, as observed in previous studies (Dommergue et al., 2007; Kirk et al., 2006; Poulain et al., 2004; St. Louis et al., 2005) all these deposition events are immediately offset by following reemission events – owing to Hg^{II} photoreduction – resulting in negligible net input of THg in snow.

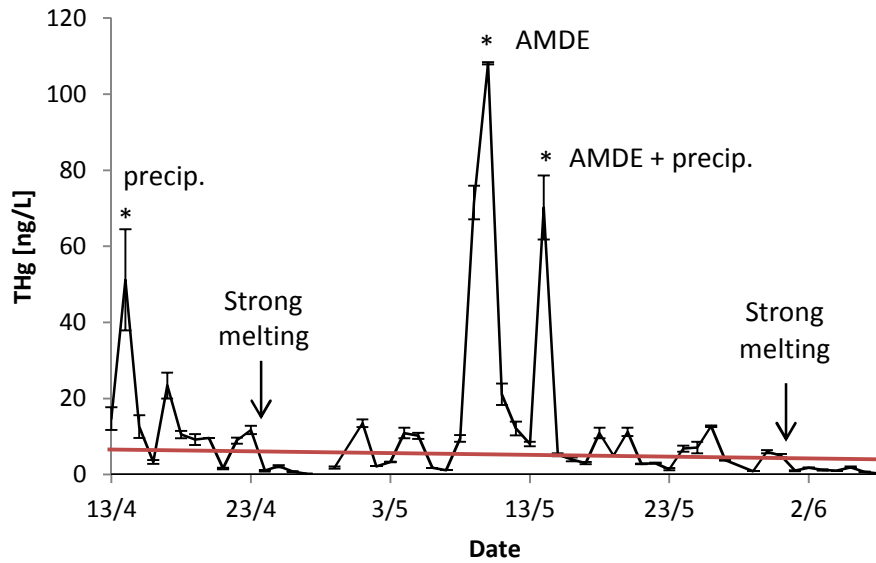


Figure 1. Evolution of THg concentration in surface coastal snow. Stars represent the main deposition events and arrows point the first day of strong melting periods (see “Field Campaign” section for more details). The red line shows the background [THg] trend (excluding the deposition peaks).

2. THg dynamics in the snowpack

Figure 2 displays the THg concentrations in both surface and basal (snow layer directly lying on the ground) snow, put in the same timescale (pits were dug every 3 or 4 days). Basal THg concentrations are very low until the 22th of April and unrelated to surface THg concentrations until the 2nd of May. This period corresponds to the early strong melting of the snowpack, during which a thin melt-refreeze ice layer (\approx 1-2 cm) separating the basal snow from upper layer completely melted. As depicted in the “Field condition and methodology” section, the snowpack resulting from this melting event was around 30% thinner (up to 50% in some cases) and consisted of a porous and almost uniform snowpack (2 layers). As a result, surface and basal snow were no longer isolated from each other and both show similar trends in THg concentrations until the end of the campaign. Interestingly, except samples from the two melting events, THg is always lower in basal snow than in surface one.

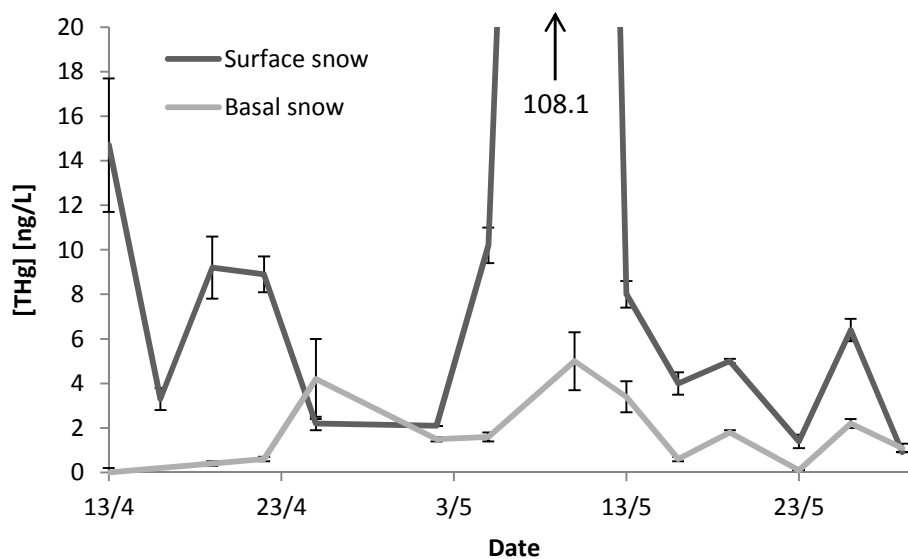


Figure 2. Evolution of THg concentration in surface (black line) and basal (grey line) coastal snow.

Our observations show that Hg transfers occur in the snowpack, from surface to basal snow and inversely. As Hg^0 in the interstitial air is greatly linked with Hg in snow by redox transformations (Dommergue et al., 2003; Fain et al., 2006; Lalonde et al., 2002; Poulain et al., 2004), we suggest that the difference between Hg concentrations in basal and surface snow can be due to Hg adsorptive diffusion in the snowpack (Domine et al., 2008). This diffusion probably affects mainly gaseous Hg^0 , as the Hg^{II} depositing during the AMDE on the 10th of May mainly affected surface snow (50 fold increase in Hg concentration) while only moderately basal snow (3 to 4 fold increase in Hg concentration). We suggest that small increases in Hg concentrations are probably due to changes in atmospheric conditions (temperature, chemical concentrations...), allowing for more oxidation of Hg^0 in the interstitial air of snow, and eventually for adsorption of the produced Hg^{II} on ice grains. The decreases in Hg concentrations would inversely be due to changes in atmospheric conditions favoring Hg^{II} reduction and the evasion of the produced Hg^0 to the interstitial air and eventually to the atmosphere. These photoinduced mercury redox reactions are not expected to be as effective in deep snow as in the very first centimeters of snow (Poulain et al., 2004), as the light flux in snow is divided by e every 20 cm roughly, depending on snow physics (Domine et al., 2008; Simpson et al., 2002). Moreover, the redox transformations of Hg imply other reactants (see the “Chemical properties of mercury” section of the “Introduction” chapter) that are probably also subject to adsorptive diffusion and which concentration might depend on the chemical content of snow. In addition, if the redox transformations of mercury occur at the snow-air interface (as suggested by Ferrari et al., 2005), the physical properties of snow (and particularly its SSA) could also affect the reaction rates. Finally, the metamorphism of snow should affect the fate of Hg adsorbed on the

surface of snow grains, thus induce Hg transfers between the different layers of a snowpack (Domine et al., 2008; Larose et al., 2010; Mann et al., 2011). All these parameters could possibly explain that Hg redox reactions are less efficient in depth snow, leading to lower Hg concentrations in basal snow than in surface one. As snow physics and chemistry as well as Hg transformations in snow are only partially known, the picture of Hg dynamic in snow remains unclear. However, although the reasons of such Hg transfer through the snowpack remain undefined, it is clearly observed in our snowpack (Figure 2).

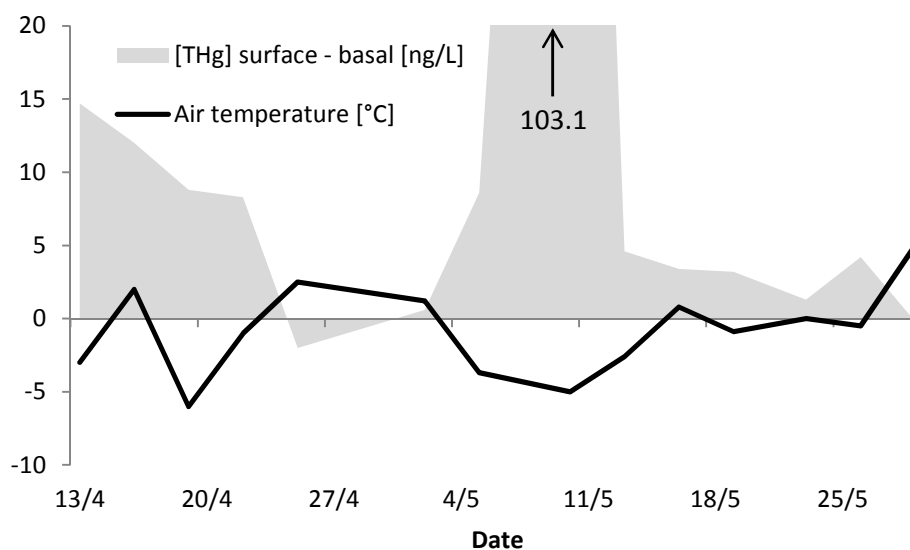


Figure 3. Evolution of the surface - basal [THg] difference (grey area) in comparison with the 2 m air temperature (black line).

Figure 3 shows the difference of THg concentration between the surface and the bottom snow layers (surface-bottom) and the 2m air temperature along the whole field campaign. The difference is always positive (for negative temperatures), except during the melting events where air temperature is above 0 °C. This highlights the transfer of Hg to lower layers of the snowpack during melting events, likely *via* mobilization by percolating meltwater and partial re-adsorption onto deeper snow grains (Mann et al., 2011; Meyer et al., 2009). This is an example of Hg remobilization by snow metamorphism, regarding melting as a strong metamorphic process.

The results briefly presented in the present section allow us to emphasize a few features of THg dynamics in snow at our coastal sampling site:

- Hg background concentrations in surface snow fluctuate between 5 and 20 ng/L roughly, with both spatial and temporal variations, in agreement with other studies (Arctic Monitoring and Assessment Programme, 2011);
- Strong Hg deposition event (AMDEs) do not affect the long term THg background level;

- Hg concentrations are lower in basal snow but follow the trends observed in surface snow. We suggest it can be due to Hg diffusion in the snowpack and/or to decreasing rates of Hg redox transformations with increasing depth;
- The influence of snow metamorphism on Hg dynamics in the snowpack is unknown. As a clue, melting induces a downward flux of Hg.

These observations are useful for our knowledge of the study site, but shall be applied to other snowpack with great caution. There is to our knowledge only one other study about Hg dynamics in an arctic snowpack over a two month time period, and the authors do not identify any link between Hg concentrations in basal and surface snow (Larose et al., 2010). In the present study, the studied snowpack rapidly collapsed to a thin partially melted snow cover on which we made our assumptions, and which could be representative of this particular case only. Future research on Hg dynamics in snow should focus on more stable snowpacks overtime and include depth profiles of gaseous Hg as well as snow grain characterization (in relation to metamorphic processes).

References

- Arctic Monitoring and Assessment Programme, 2011. AMAP assessment 2011. Arctic Monitoring and Assessment Programme, Oslo, Norway.
- Domine, F., Albert, M., Huthwelker, T., Jacobi, H.-W., Kokhanovsky, A.A., Lehning, M., Picard, G., Simpson, W.R., 2008. Snow physics as relevant to snow photochemistry. *Atmospheric Chem. Phys.* 8, 171–208.
- Dommergue, A., Bahlmann, E., Ebinghaus, R., Ferrari, C., Boutron, C., 2007. Laboratory simulation of Hg⁰ emissions from a snowpack. *Anal. Bioanal. Chem.* 388, 319–327.
- Dommergue, A., Ferrari, C.P., Poissant, L., Gauchard, P.-A., Boutron, C.F., 2003. Diurnal Cycles of Gaseous Mercury within the Snowpack at Kuujjuarapik/Whapmagoostui, Québec, Canada. *Environ. Sci. Technol.* 37, 3289–3297.
- Fain, X., Ferrari, C.P., Gauchard, P.-A., Magand, O., Boutron, C., 2006. Fast depletion of gaseous elemental mercury in the Kongsvegen Glacier snowpack in Svalbard. *Geophys. Res. Lett.* 33.
- Ferrari, C., Gauchard, P., Aspö, K., Dommergue, A., Magand, O., Bahlmann, E., Nagorski, S., Temme, C., Ebinghaus, R., Steffen, A., 2005. Snow-to-air exchanges of mercury in an Arctic seasonal snow pack in Ny-Ålesund, Svalbard. *Atmos. Environ.* 39, 7633–7645.
- Kirk, J.L., St. Louis, V.L., Sharp, M.J., 2006. Rapid Reduction and Reemission of Mercury Deposited into Snowpacks during Atmospheric Mercury Depletion Events at Churchill, Manitoba, Canada. *Environ. Sci. Technol.* 40, 7590–7596.
- Lalonde, J.D., Poulain, A.J., Amyot, M., 2002. The Role of Mercury Redox Reactions in Snow on Snow-to-Air Mercury Transfer. *Environ. Sci. Technol.* 36, 174–178.
- Larose, C., Dommergue, A., De Angelis, M., Cossa, D., Averty, B., Maruszczak, N., Soumis, N., Schneider, D., Ferrari, C., 2010. Springtime changes in snow chemistry lead to new insights into mercury methylation in the Arctic. *Geochim. Cosmochim. Acta* 74, 6263–6275.
- Mann, E., Meyer, T., Mitchell, C.P.J., Wania, F., 2011. Mercury fate in ageing and melting snow: Development and testing of a controlled laboratory system. *J. Environ. Monit.* 13, 2695.
- Meyer, T., Lei, Y.D., Muradi, I., Wania, F., 2009. Organic Contaminant Release from Melting Snow. 1. Influence of Chemical Partitioning. *Environ. Sci. Technol.* 43, 657–662.
- Poulain, A.J., Lalonde, J.D., Amyot, M., Sheard, J.A., Raofie, F., Ariya, P.A., 2004. Redox transformations of mercury in an Arctic snowpack at springtime. *Atmos. Environ.* 38, 6763–6774.
- Schroeder, W.H., Anlauf, K.G., Barrie, L.A., Lu, J.Y., Steffen, A., Schneeberger, D.R., Berg, T., 1998. Arctic springtime depletion of mercury. *Nature* 394, 331–332.

- Simpson, W.R., King, M.D., Beine, H.J., Honrath, R.E., Zhou, X., 2002. Radiation-transfer modeling of snow-pack photochemical processes during ALERT 2000. *Atmos. Environ.* 36, 2663–2670.
- St. Louis, V.L., Sharp, M.J., Steffen, A., May, A., Barker, J., Kirk, J.L., Kelly, D.J.A., Arnott, S.E., Keatley, B., Smol, J.P., 2005. Some Sources and Sinks of Monomethyl and Inorganic Mercury on Ellesmere Island in the Canadian High Arctic. *Environ. Sci. Technol.* 39, 2686–2701.
- Steffen, A., Douglas, T., Amyot, M., Ariya, P., Aspö, K., Berg, T., Bottenheim, J., Brooks, S., Cobbett, F., Dastoor, A., Dommergue, A., Ebinghaus, R., Ferrari, C., Gardfeldt, K., Goodsite, M.E., Lean, D., Poulain, A.J., Scherz, C., Skov, H., Sommar, J., Temme, C., 2008. A synthesis of atmospheric mercury depletion event chemistry in the atmosphere and snow. *Atmospheric Chem. Phys.* 8, 1445–1482.

ii. Assessing the sources of major ions using ratio/ratio plots

The goal of this section is to determine the sources of major ions and Hg species in the surface snowpack (as mentioned previously, surface snow collected daily is considered). For this purpose, we propose a general methodology that will be applied to all the measured chemical species.

1. Methodology

a. Sea-salt tracers: Na and Cl

Sodium and chloride are known to be good tracers of sea-salt in snow, despite they can be subjects to post-deposition processes, such as precipitation of mirabilite (Na_2SO_4) or HCl condensation (Krnavek et al., 2011). In our samples, these processes are not discernible and Na and Cl correlate at the sea-salt stoichiometry: $[\text{Na}]/[\text{Cl}] = 0.9$, $r^2 > 0.99$, $n = 50$ (Figure 1). In the following, Na and Cl will then be used as sea-salt tracer, respectively for cations and anions.

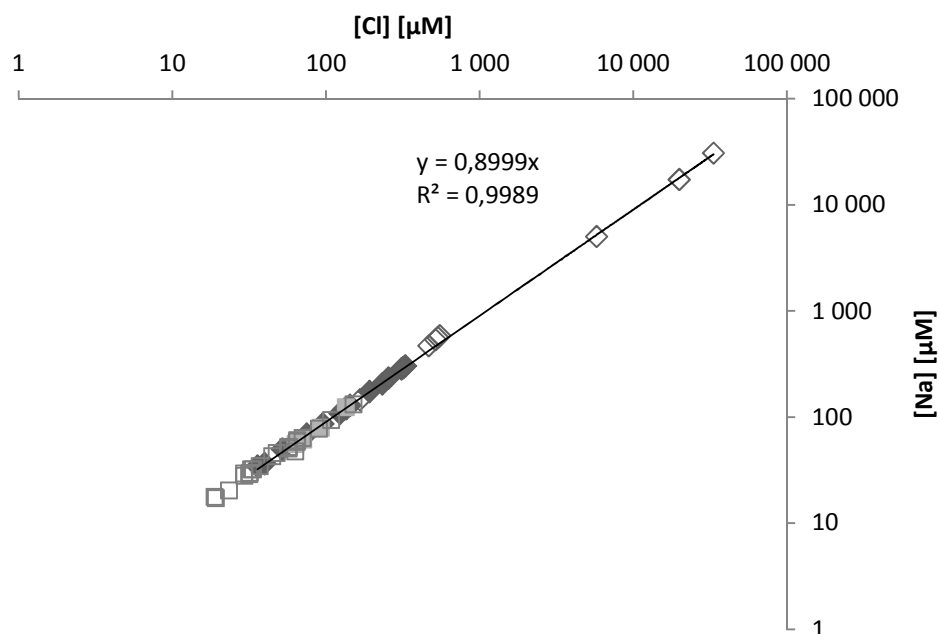


Figure 1. Correlation plot of Na with respect to Cl. Black diamonds represent the particle input event, open diamonds represent samples with strong sea-spray influence (including the strong storm event), grey squares represent fresh snow samples and open squares samples possibly chemically impacted by the snowmelt. The solid line represents empirical sea-salt dilution.

b. Calcium as a multiple source tracer

Among the major cations present in snow (Na, Mg, Ca, K, Li), all are known to be related to sea water chemistry. However, Ca can originate from non-marine sources (likely terrestrial mineral dust) to a non-negligible extent (Fischer et al., 2007; Jacobi et al., 2012; Kang et al., 2001; Krnavek et al., 2011; Ruth et al., 2008; Ström et al., 2003).

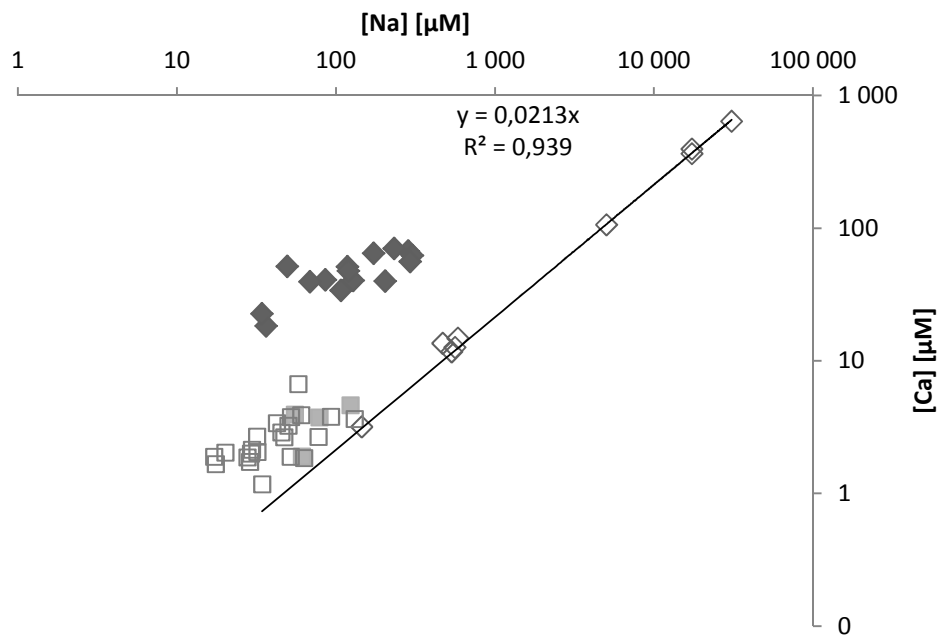


Figure 2. Correlation plot of Ca with respect to Na (as a sea-salt tracer). Black diamonds represent the particle input event, open diamonds represent samples with strong sea-spray influence (including the strong storm event), grey squares represent fresh snow samples and open squares represent samples possibly chemically impacted by the snowmelt. The solid line represents empirical sea-salt dilution.

Figure 2 shows the correlation plot of Ca with respect to Na in our samples. Only the samples from the sea-spray event fit the sea-salt dilution line, while systematic Ca enrichment is observed in other samples. The highest enrichment is observed in samples collected during the particle event. The highest concentrations of Ca in surface snow (except the outlier storm event) are due to this particle input. Non-sea-spray Ca (nss-Ca) is graphically represented on Figure 2 by the distance from the empirical sea-salt dilution line and is calculated as follows:

$nss-Ca = Ca_{measured} - [Na \times (Ca_{sea-sprays}/Na_{sea-sprays})]$, the sea-spray sample with the lowest $[Ca]/[Na]$ is chosen as reference.

In the following, the proportion of non-sea-spray Ca (nss-Ca) will be considered as the relative contribution of non-sea-spray sources to the snow chemistry, and will be calculated as follows:

$$\text{non-sea-spray contribution: } K_d = \text{nss-Ca}/\text{Ca}_{\text{measured}}$$

Interestingly, the time evolution of nss-Ca in surface snow is strongly correlated with several atmospheric events (Figure 3). Indeed snow surface experienced important nss-Ca inputs during 1) the storm event in late April; and 2) the input of particles during the second half of May. Table 1 shows the features of surface snow regarding Ca and particles during these event. Results presented in Table 1 and Figure 3 suggest that the particle input of May brings additional Ca than sea-sprays and becomes the main source for Ca in samples from the particle input event.

Table 1. Chemical signature of Ca and particles in surface snow during the storm event and the particle input event. The [nss-Ca]/[Ca] molar ratio is calculated from data presented in Figure 2.

	n	Median particle count [mL ⁻¹] (min ; max)	Median [μM] (min ; max)	nss-Ca	Median [%] (min ; max)	[nss-Ca]/[Ca]
Sea-spray event	9	57 756 (15 161 ; 215 090)	1.4 (0 ^a ; 35.0)		4.7 (0 ^a ; 27.9)	
Particle event	15	1 109 789 (458 861 ; 2 409 240)	45.0 (31.6 ; 65.3)		95.2 (93.1 ; 98.0)	

^a reference sample for nss-Ca calculation

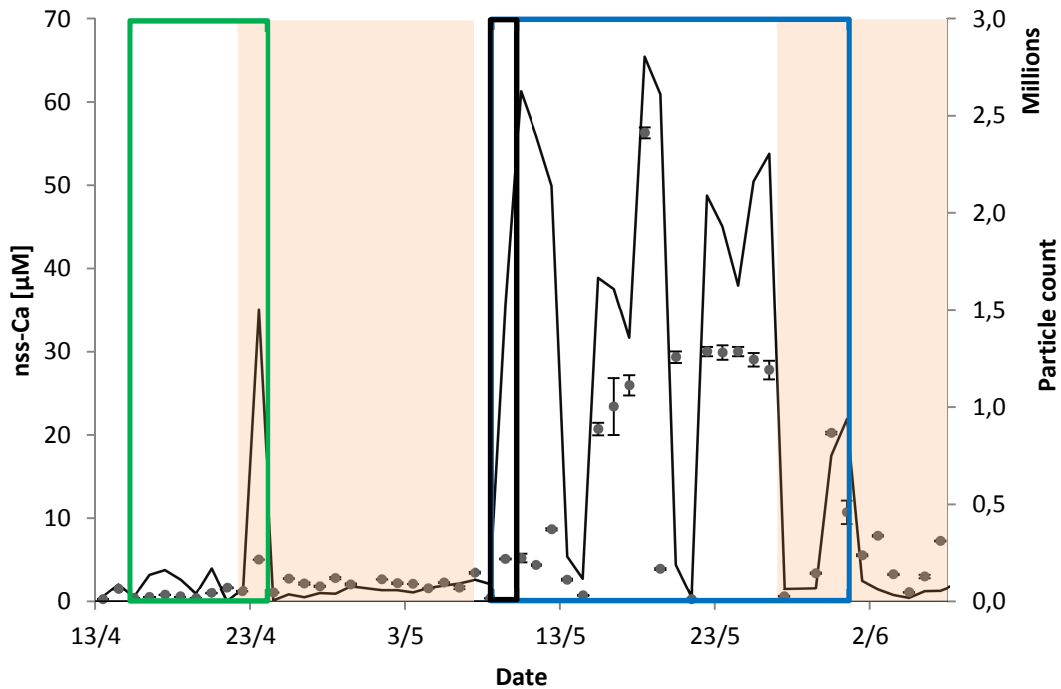


Figure 3. Particle number (dots) and nss-Ca (line) evolution during the field campaign. The black box represents the AMDE event, the green box samples with strong sea-sprays influence storms? and the blue box samples under the chemical influence of particles input.

As being present in sea-sprays as well as in other sources, Ca is a relevant species to estimate the different sources contributions in surface snow. Indeed, the $[\text{nss-Ca}]/[\text{Ca}]$ ratio is a good proxy for estimating the contribution of non-sea-sprays sources of chemicals in snow.

c. Tracking of multiple sources

For a given species X, its concentration $[X]$ is plotted versus the concentration of the appropriate sea-salt tracer; if sea-sprays (source A on Figure 4) are the major source for X in the samples, data points will be depicted by a straight line representing the ideal dilution of the sea-salt source ($y = x$ in Figure 4). If a second source B exists for X, some of the data points will move away from this straight line towards the ideal dilution straight line of the source B (Figure 4). Because of multiple source contribution and/or chemical altering of snow (i.e. melting), most of the samples will be located in-between all dilution lines. However, when one source is in great majority (often for high concentrations), every chemical species is expected to fit its dilution (source A in Figure 4).

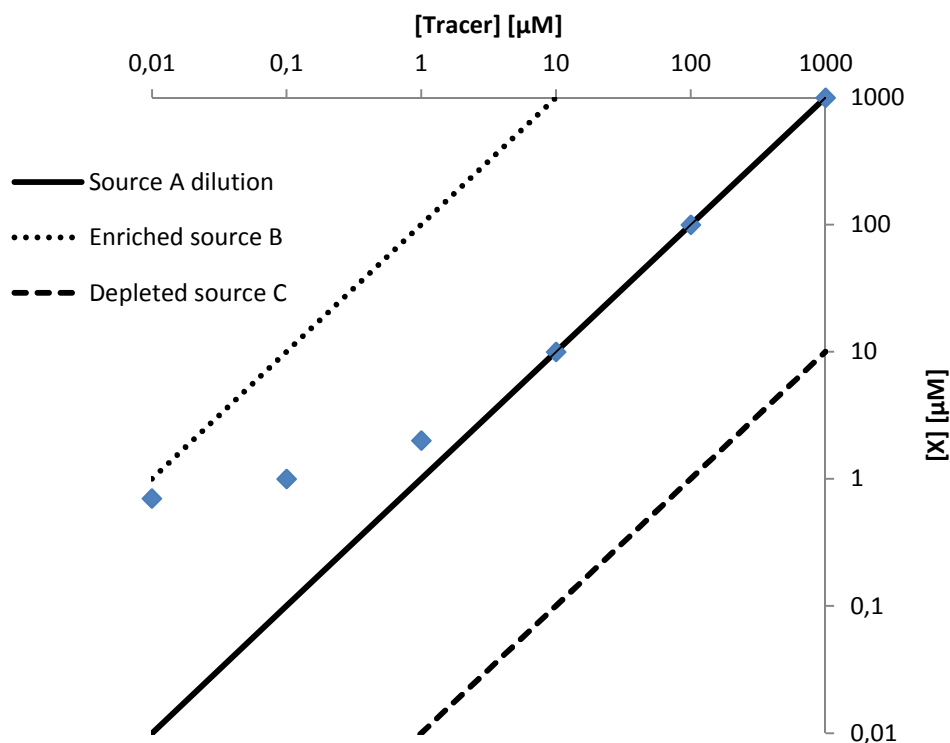


Figure 4. Display of different sources on a [X] versus [Tracer] plot. Source A is defined by the $y=x$ line (solid line), and examples of enriched and depleted sources (respectively B and C) are represented respectively as small and large dash line. Blue diamonds are an example of distribution for X having A as a main source and B as a secondary one.

Using this approach, we can have an overview at the different sources contributions to the chemical content of snow. Some chemical species can have other sources or sinks, which might be unobservable on dilutions graphs such as Figure 4. In this case, the use of a second graphical tool is needed to further describe this third source.

Figure 5 is a plot displaying the variations of $[X]/[Z]$ and $[Y]/[Z]$ molar ratios, X, Y and Z being different chemical species. Each source of these cations is plotted as a defined dot A, B or C, which are defined either because their content in X, Y and Z is known, or because of data points with clear signatures. In the latter case, the location of each source on the graph is determined empirically by using a particular sample or cluster of samples. Straight lines between all the sources define either a line (if two sources) or a polygon (if three or more sources) containing all the sample plots, in which side AB represents the mixing line between source A and source B. The math and mechanics under ratio/ratio plots have been well described elsewhere (Robinson et al., 2006). The representation of a given sample is determined by 1) the contribution of each source to its $[X]/[Z]$ and $[Y]/[Z]$ ratios; 2) possible enrichment or loss processes, which may shift its position following linear ways (Figure 5). A detailed description of ratio/ratio plots is available elsewhere (Robinson et al., 2006).

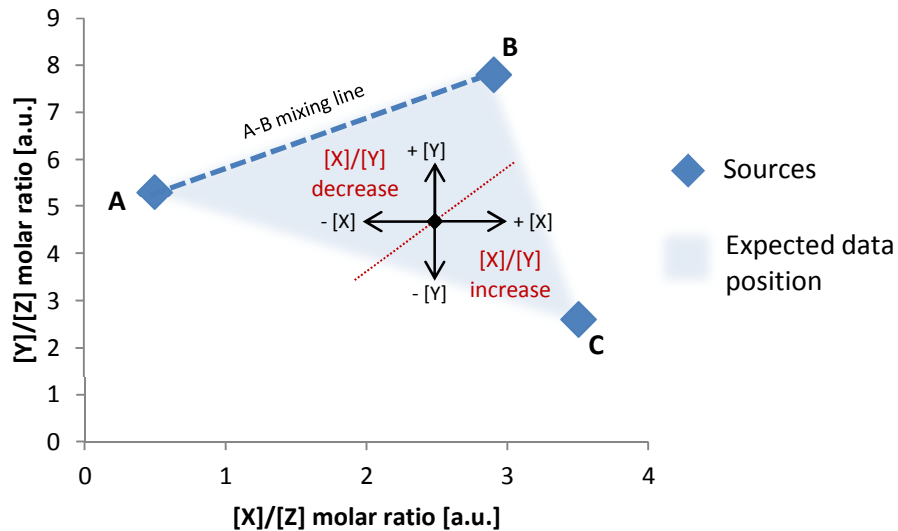


Figure 5. Ratio/ratio plot of $[X]/[Z]$ versus $[Y]/[Z]$. Sources are represented by fixed point (diamonds on the graph) as having fixed $[X]/[Z]$ and $[Y]/[Z]$. Data points of snow having inputs from sources A and/or B and/or C are expected to be located in the blue triangle area, defined by the position of sources A, B and C. Any point can be shifted by various enrichment or depletion processes, as shown by the arrows.

In the following section, $[Ca]$ – as a multiple source tracer – will always be chosen as denominator, and abscissa will always be the $[nss-Ca]/[Ca]$ molar ratio. This way, the horizontal axis of the plot will represent the nss-Ca source contribution expressed in %. As a consequence, the ordinate at 0% will represent the $[X]/[Ca]$ in sea-sprays, while the ordinate at 100% will represent $[X]/[Ca]$ in the pure nss-Ca source. The storm event samples – which contain very high concentrations of all the measured chemical species that decreased rapidly (within a few days) to expected normal values (based on empirical observation) (in green on Figure 6) – will be displayed as part of the “samples with strong sea-spray influence” (see legend of Figure 2) to help the design of the sea-salt dilution line (on $[X]$ versus $[Tracer]$ plots) or of the sources mixing line (on ratio/ratio plots). The latter will be

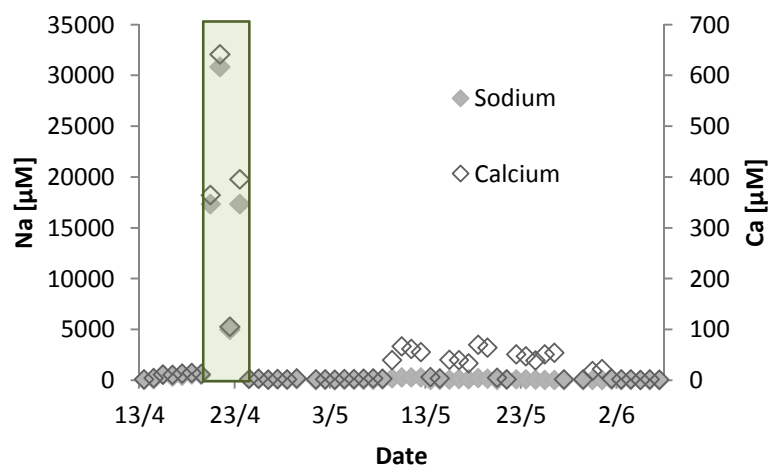


Figure 6. Time series of Na and Ca during the field campaign. Snow samples impacted by the storm event are displayed in a green box, and the concentration values for all the species will be considered as outliers.

drawn as linear regressions of samples from the storm event (open diamonds on all ratio/ratio plots) together with samples from the particle event (full diamonds on all ratio/ratio plots).

In summary, the two steps described above will allow determining (for each species) the number of sources and their importance in terms of input to snow. Depletion processes (or sinks, in opposition to sources) can possibly be identified if they are substantial enough to induce anomalies on the graphs. Preferential melting processes (of X versus Y, or particulate versus non-particulate species for example) can alter snow chemistry, thus one could expect melting snow to be sometimes unrepresentative of all external quantitative inputs it encountered. It is therefore crucial to consider the timing of geochemical and meteorological events for an extended comprehension of our dataset, as both can have a great impact on the concentrations of chemicals in snow (Figure 6).

2. Magnesium

Figure 7 shows the correlation plot of Mg with respect to Na. Magnesium and Na are linearly correlated and their molar ratio follows the sea-salt composition ($[Mg]/[Na] = 0.113$). However, substantial enrichments and depletions are seen for concentrations below $60 \mu\text{M}$. Samples from the particle input event are enriched in Mg, while samples from melting snow are systematically depleted. The majority of the samples (94%) contain Mg at concentrations below $65 \mu\text{M}$, while higher concentrations (up to $3488.7 \mu\text{M}$) are observed in samples from the sea-spray storm only (three samples among the sea-spray event), outlining this storm as an outlier event, as explained in paragraph 1.c of this section. These observations are the same that the ones drawn from the Ca versus Na plot (Figure 2).

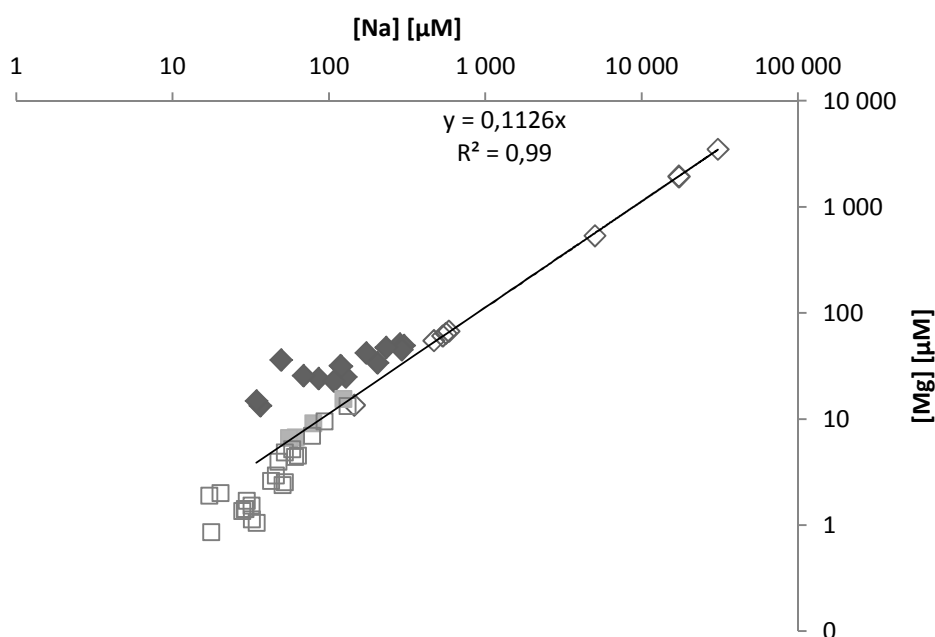


Figure 7. Correlation plot of Mg with respect to Na (as a sea-salt tracer). Black diamond represent the particle input event, open diamonds represent samples with strong sea-spray influence (including the strong storm event), grey squares represent fresh snow samples and open squares samples possibly chemically impacted by the snowmelt. The solid line represents empirical sea-salt dilution.

Figure 8 shows the molar ratio/ratio plot of $[Mg]/[Ca]$ with respect to $[nss-Ca]/[Ca]$. A mixing line (linear regression) is drawn for each cation, between the nss-Ca source (samples from the particles event) and the sea-spray source (samples from the sea-sprays event). All the samples fit this mixing line except the melting snow samples, which are systematically located below. The estimated $[Mg]/[Ca]$ ratio in the nss-Ca source is estimated to be 0.403.

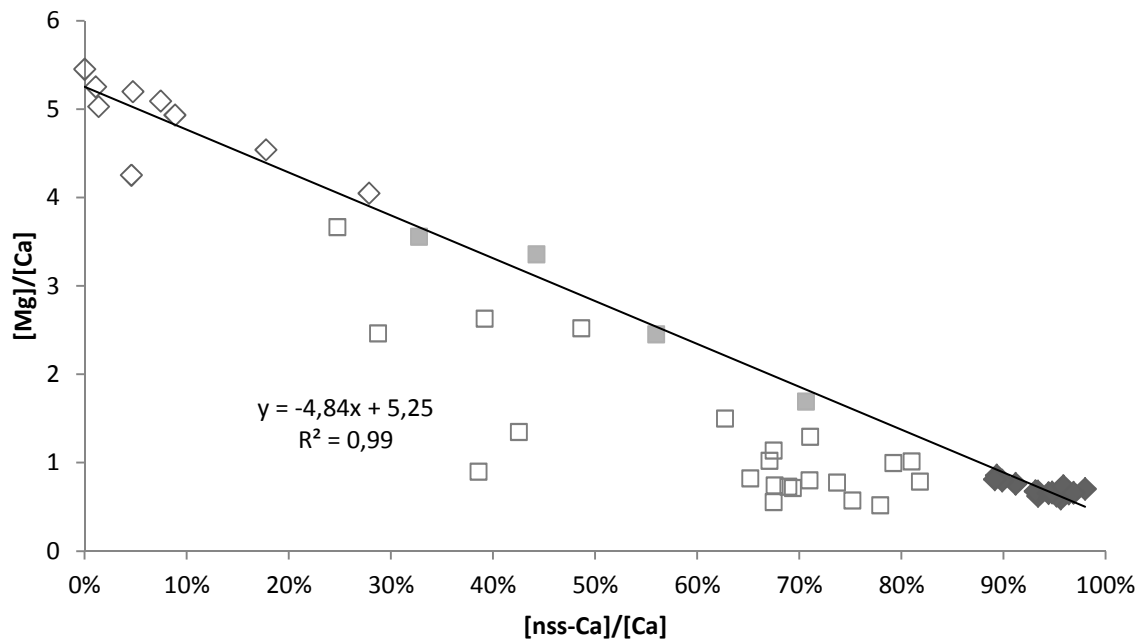


Figure 8. Ratio/ratio plot of $[Mg]/[Ca]$ with respect to $[nss-Ca]/[Ca]$ (as contribution of the nss-Ca source to total Ca). Black diamond represent the particle input event, open diamonds represent samples with strong sea-spray influence (including the strong storm event), grey squares represent fresh snow samples and open squares samples possibly chemically impacted by the snowmelt. The solid line represents the mixing line between sea-sprays and the nss-Ca source. The ordinate for $x = 0\%$ represents $[Mg]/[Ca]$ ratio in sea-sprays, for $x = 100\%$ $[Mg]/[Ca]$ in the nss-Ca source.

Magnesium behaves like a sea-salt compound but is however substantially enriched compared to sea-salt during the particle event. The same trend was observed for Ca, but with a higher enrichment. Similarly to Ca, Mg is a major ion which is present in both sea-salt and late spring particles, considering both the Mg enrichment (Figure 7) and the $[Mg]/[Ca]$ ratio estimated in late spring particles (0.403, see Figure 8). In melting snow samples, the systematical Mg exhaustion (open squares on Figure 7) together with the low $[Mg]/[Ca]$ anomaly (open squares on Figure 8) suggest a preferential elution of Mg over Ca at the beginning of the snowmelt. This assessment is however hard to explain considering the chemical properties of Mg and Ca, which are very close.

3. Species related to sea-sprays chemistry: K and Li

Figure 9 shows the correlation plot of K with respect to Na. Potassium versus K follows the sea-salt composition ($[K]/[Na] = 0.021$) with small scatter for low concentrations, corresponding to melting snow samples (open squares on Figure 9). Such scattering is probably due to small source fractionation (minor contribution of another source), visible only for low concentrations of K ($< 2 \mu\text{M}$). The majority of the samples (84%) show a K concentration of less than $7 \mu\text{M}$, while higher concentrations (up to $651.9 \mu\text{M}$) are all encountered in the samples from the sea-spray event only.

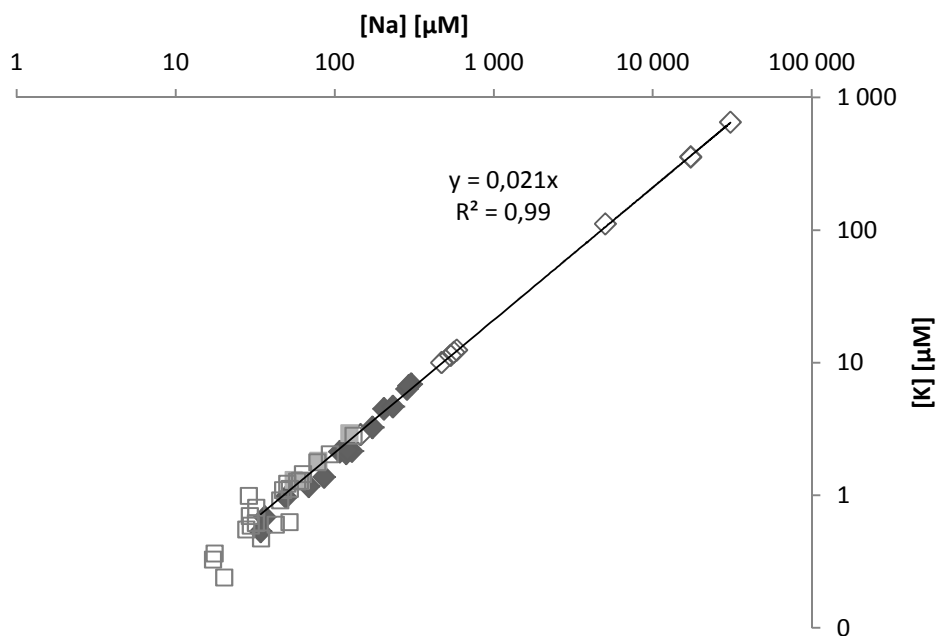


Figure 9. Correlation plot of K with respect to Na (as a sea-salt tracer). Black diamond represent the particle input event, open diamonds represent samples with strong sea-spray influence (including the strong storm event), grey squares represent fresh snow samples and open squares samples possibly chemically impacted by the snowmelt. The solid line represents empirical sea-salt dilution.

Figure 10 shows the correlation plot of Li with respect to Na. Similarly to K, Li is correlated with sea-salt with scattering for concentrations below 20 nM. The majority of the samples (83%) contain Li at 20 nM or less, while higher concentrations (up to 1627.9 nM) are measured in samples from the sea-spray event only. The scattering observed occurs only toward Li enrichment compared to sea-salt, with no regards to sample type. The molar ratio $[Li]/[Na]$ in sea-salt is $4.97 \cdot 10^{-5}$.

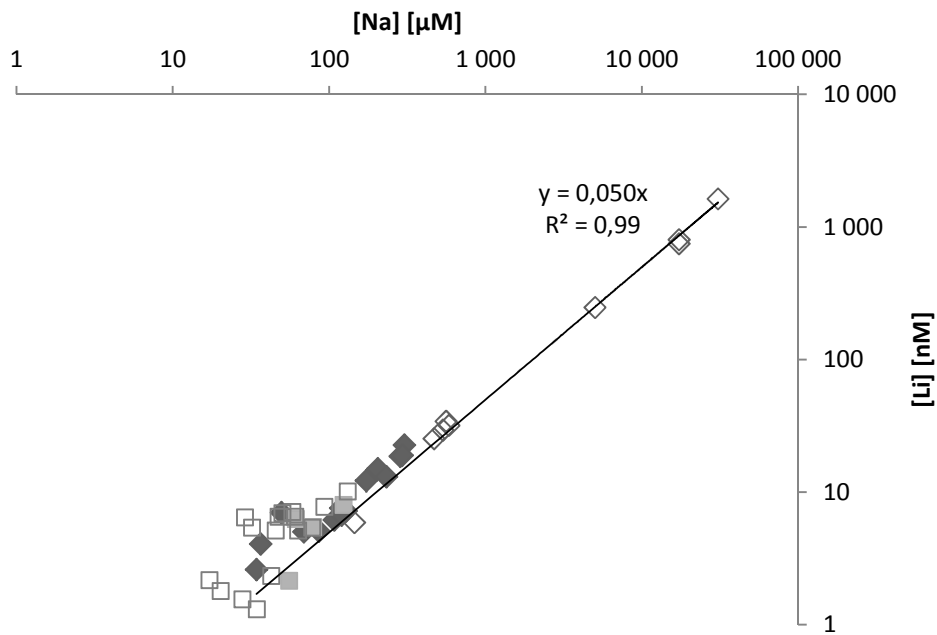


Figure 10. Correlation plot of Li with respect to Na (as a sea-salt tracer). Black diamond represent the particle input event, open diamonds represent samples with strong sea-spray influence (including the strong storm event), grey squares represent fresh snow samples and open squares represent samples possibly chemically impacted by the snowmelt. The solid line represents empirical sea-salt dilution.

Figure 11 shows the molar ratio/ratio plot of $[K]/[Ca]$ with respect to $[nss-Ca]/[Ca]$. A mixing line is drawn for each cation, between the nss-Ca source (samples from the particles event) and the sea-spray source (samples from the sea-sprays event). All the samples fit this mixing line, with small scattering for samples with the lower concentrations (melting snow). The estimated $[K]/[Ca]$ in the nss-Ca source is 0 (calculation from Figure 11 gives a negative value).

Figure 12 shows the molar ratio/ratio plot of $[Li]/[Ca]$ with respect to $[nss-Ca]/[Ca]$. All the melting snow samples show a $[Li]/[Ca]$ increase compared to the mixing line, confirming the Li enrichment observed on Figure 10 for samples with the lowest concentrations. Estimated $[Li]/[Ca]$ ratio in the nss-Ca source is 0.

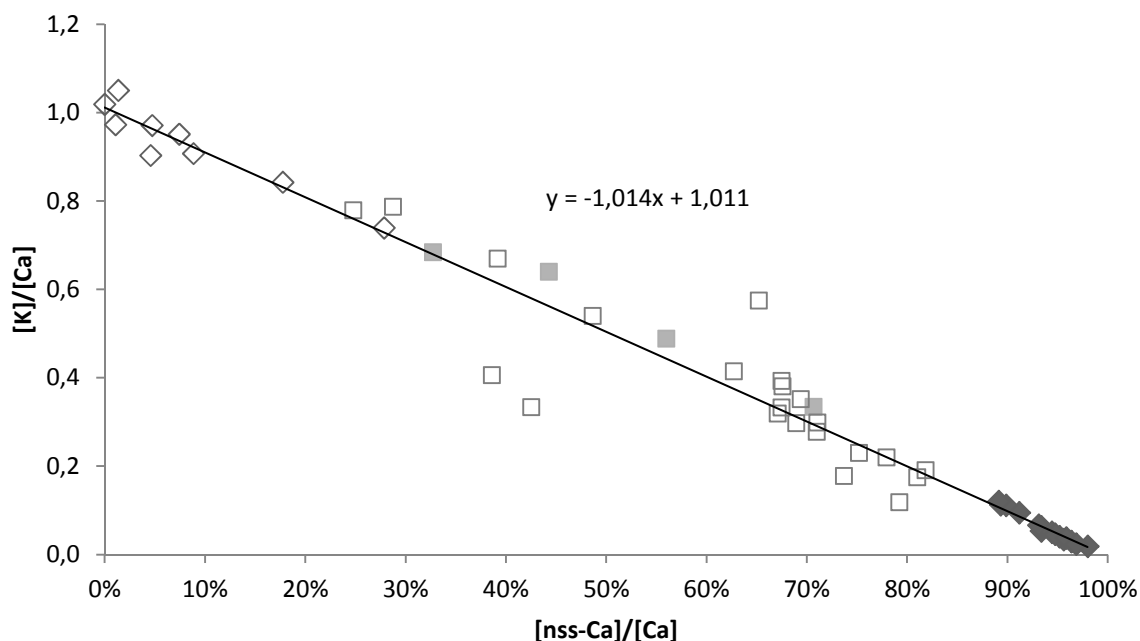


Figure 11. Ratio/ratio plot of $[K]/[Ca]$ with respect to $[nss-Ca]/[Ca]$ (as contribution of the nss-Ca source to total Ca). Black diamond represent the particle input event, open diamonds represent samples with strong sea-spray influence (including the strong storm event), grey squares represent fresh snow samples and open squares samples possibly chemically impacted by the snowmelt. The solid line represents the mixing line between sea-sprays and the nss-Ca source, as the linear regression of the (sea-spray + late spring particle event) sample ensemble. The ordinate for $x = 0\%$ represents $[K]/[Ca]$ ratio in sea-sprays, for $x = 100\%$ $[K]/[Ca]$ in the nss-Ca source.

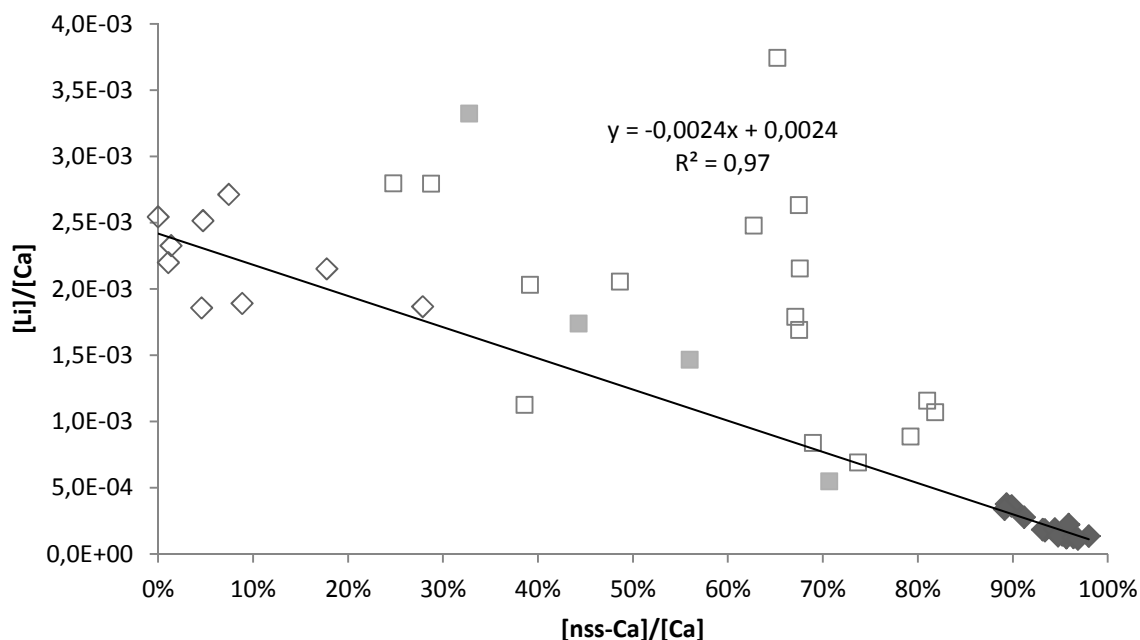


Figure 12. Ratio/ratio plot of $[Li]/[Ca]$ with respect to $[nss-Ca]/[Ca]$ (as contribution of the nss-Ca source to total Ca). Black diamond represent the particle input event, open diamonds represent samples with strong sea-spray influence (including the strong storm event), grey squares represent fresh snow samples and open squares samples possibly chemically impacted by the snowmelt. The solid line represents the mixing line between sea-sprays and the nss-Ca source, as the linear regression of the (sea-spray + late spring particle event) sample ensemble. The ordinate for $x = 0\%$ represents $[Li]/[Ca]$ ratio in sea-sprays, for $x = 100\%$ $[Li]/[Ca]$ in the nss-Ca source.

The source fractionation observed at lower concentrations for both K and Li are mainly observed in melting snow samples. In the case of Li, the fractionation suggests that when snow melts, both Na and Ca are primarily removed from snow by percolating water (positive Li anomaly in Figure 10 and Figure 12 for samples of melting snow). For K, the fractionation is smaller and do not show any obvious trend: it can be attributed to minor processes such as small inputs of dust (different from the late spring particles) or small removal by snow melting. As a summary, both Li and K strongly correlate with sea-salt tracer and $[K]/[Ca]$ and $[Li]/[Ca]$ ratio are close to zero in the nss-Ca source (estimated from Figure 11 and Figure 12). It clearly suggests that these species are mainly due to sea-sprays deposited onto surface snow.

4. Species related to sea-sprays and atmospheric chemistry: sulfates and Br

Figure 13 shows the correlation plot of sulfates with respect to Cl. Sulfate is correlated with sea-salt ($[\text{Sulfates}]/[\text{Cl}] = 0.051$), with a visible enrichment for concentration below $50 \mu\text{M}$ (which is more visible in fresh snow). Some data scattering occur for melting snow samples, at concentrations below $4 \mu\text{M}$. As for sea-related species described above, 82% of the samples contain sulfates at a concentration below $25 \mu\text{M}$, while higher concentrations (up to $1764.8 \mu\text{M}$) are measured in the samples from the sea-spray event only.

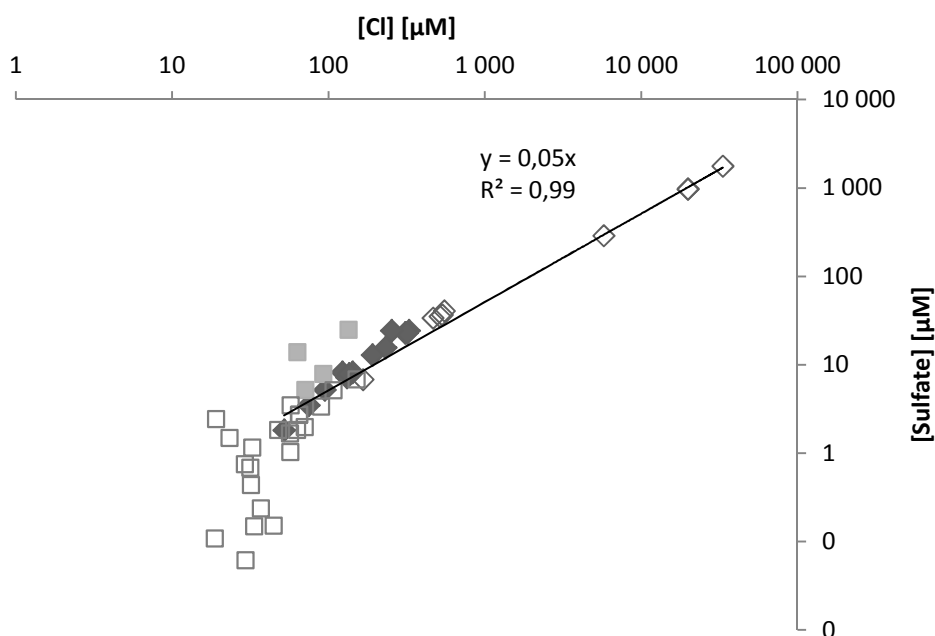


Figure 13. Correlation plot of sulfate with respect to Cl (as a sea-salt tracer). Black diamond represent the particle input event, open diamonds represent samples with strong sea-spray influence (including the strong storm event), grey squares represent fresh snow samples and open squares samples possibly chemically impacted by the snowmelt. The solid line represents empirical sea-salt dilution.

The correlation plot of Br with respect to Cl (Figure 14) is close to sea-salt species such as K (Figure 9). However, fresh snow samples are systematically depleted in Br. The majority of the samples (86%) show Br concentrations below 500 nM , while higher concentrations (up to $50.5 \mu\text{M}$) are observed during the sea-spray event only. The molar ratio $[\text{Br}]/[\text{Cl}]$ in sea-salt is $1.55 \cdot 10^{-3}$.

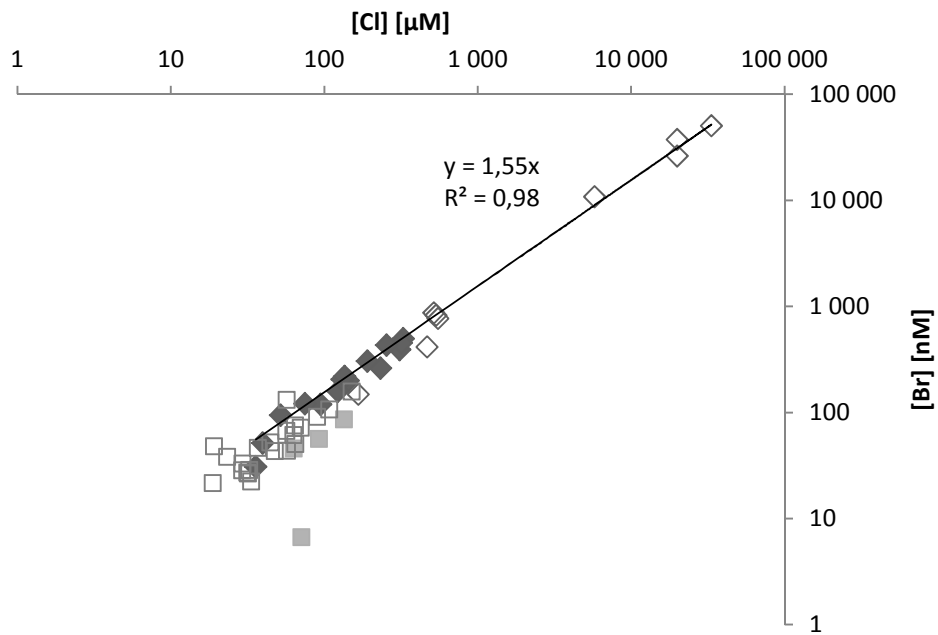


Figure 14. Correlation plot of Br with respect to Cl (as a sea-salt tracer). Black diamond represent the particle input event, open diamonds represent samples with strong sea-spray influence (including the strong storm event), grey squares represent fresh snow samples and open squares samples possibly chemically impacted by the snowmelt. The solid line represents empirical sea-salt dilution.

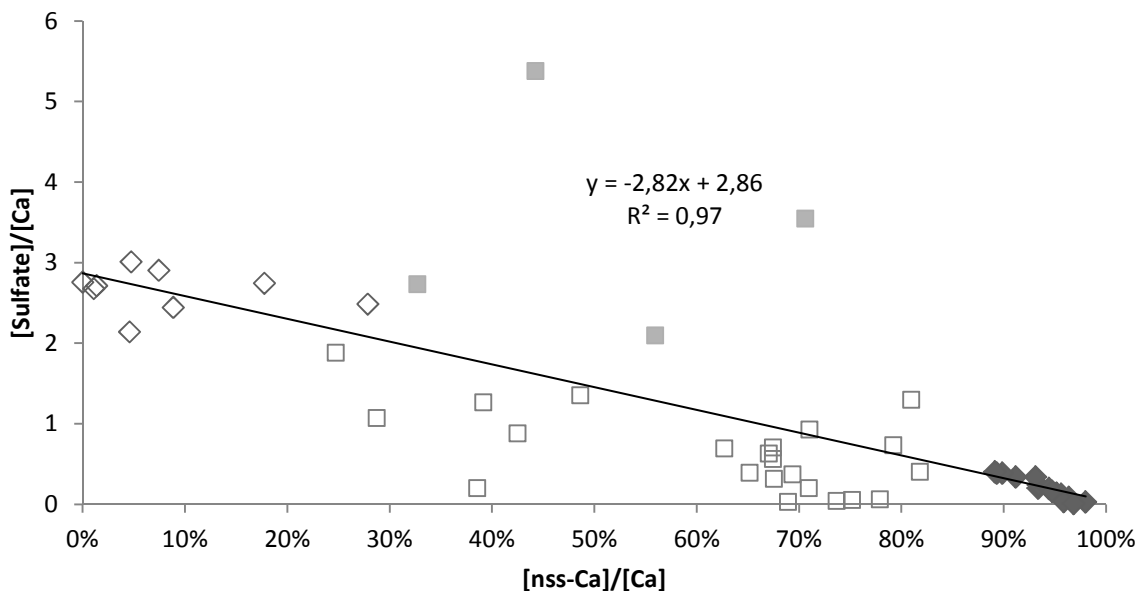


Figure 15. Ratio/ratio plot of $[\text{Sulfate}]/[\text{Ca}]$ with respect to $[\text{nss-Ca}]/[\text{Ca}]$ (as contribution of the nss-Ca source to total Ca). Black diamond represent the particle input event, open diamonds represent samples with strong sea-spray influence (including the strong storm event), grey squares represent fresh snow samples and open squares samples possibly chemically impacted by the snowmelt. The solid line represents the mixing line between sea-sprays and the nss-Ca source, as the linear regression of the (sea-spray + late spring particle event) sample ensemble. The ordinate for $x = 0\%$ represents $[\text{Sulfate}]/[\text{Ca}]$ ratio in sea-sprays, for $x = 100\%$ $[\text{Sulfate}]/[\text{Ca}]$ in the nss-Ca source.

Figure 15 shows the molar ratio/ratio plot of $[\text{Sulfates}]/[\text{Ca}]$ with respect to $[\text{nss-Ca}]/[\text{Ca}]$. A mixing line is drawn for each cation, between the nss-Ca source (samples from the particles event) and the sea-spray source (samples from the sea-sprays event). For sulfates, samples from sea-spray and particles events fit this mixing line, while samples of melting snow globally show higher $[\text{Sulfate}]/[\text{Ca}]$ ratios. Interestingly, fresh snow samples have a distinctly lower $[\text{Sulfate}]/[\text{Ca}]$ ratio than expected on the mixing line. The estimated $[\text{Sulfate}]/[\text{Ca}]$ molar ratio in the nss-Ca source is 0.043.

The molar ratio/ratio plot of $[\text{Br}]/[\text{Ca}]$ with respect to $[\text{nss-Ca}]/[\text{Ca}]$ (Figure 16) has the same pattern than sulfate (Figure 15), nevertheless fresh snow samples have higher $[\text{Br}]/[\text{Ca}]$ ratios and are less distinct from the other samples. The estimated $[\text{Br}]/[\text{Ca}]$ molar ratio in the nss-Ca source is 0.

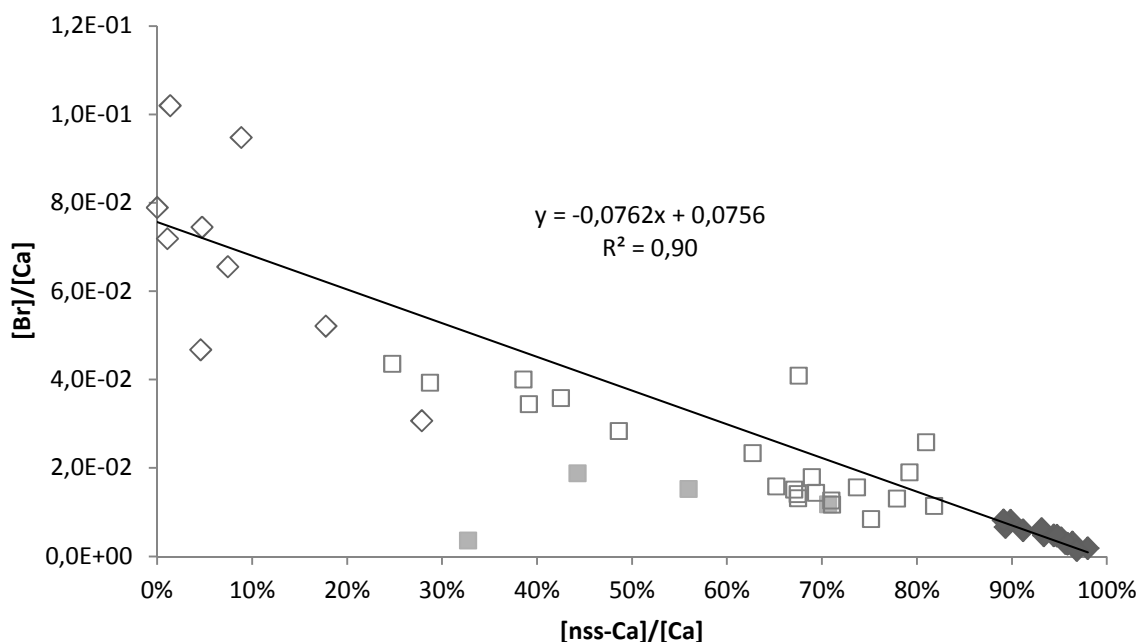


Figure 16. Ratio/ratio plot of $[\text{Br}]/[\text{Ca}]$ with respect to $[\text{nss-Ca}]/[\text{Ca}]$ (as contribution of the nss-Ca source to total Ca). Black diamond represent the particle input event, open diamonds represent samples with strong sea-spray influence (including the strong storm event), grey squares represent fresh snow samples and open squares samples possibly chemically impacted by the snowmelt. The solid line represents the mixing line between sea-sprays and the nss-Ca source, as the linear regression of the (sea-spray + late spring particle event) sample ensemble. The ordinate for $x = 0\%$ represents $[\text{Br}]/[\text{Ca}]$ ratio in sea-sprays, for $x = 100\%$ $[\text{Br}]/[\text{Ca}]$ in the nss-Ca source.

Sulfates and Br behave like sea-salt related species; however both show a particular fractionation in fresh snow samples (Figure 15 and Figure 16). It is clear that $[\text{Sulfate}]/[\text{Ca}]$ is lower in fresh snow, possibly outlining a source fractionation during the atmospheric process of fresh snow formation, or a third source for sulfates in fresh snow (different from sea-sprays or the nss-Ca source). Melting snow samples are enriched in sulfates with regards to Ca, hence do not fit the mixing line. It could be

due to the net effect of preferred elution of Ca over sulfates during snow melting or sulfate enrichment processes by atmospheric deposition of sulfuric acid, ammonium sulfate or mirabilite (Krnavek et al., 2011). In addition, Figure 13 shows a depletion of sulfate with regards to Cl in the same melting snow samples. It could suggest a preferred elution of sulfates over Cl, or degradation/disparition processes (i.e. hypothetical microbial transformations or sulfuric acid volatilization). In summary, sulfate is mainly brought by sea sprays, with additional atmospheric additions, most importantly during precipitations (Figure 13 and Figure 15). The nss-Ca source is only responsible for minor inputs of sulfate to surface snow (no enrichment on Figure 13, very low [Sulfate]/[Ca] on Figure 15).

Bromide can experience both atmospheric removal and inputs in surface snow. Activation of Br by atmospheric oxidation (to BrO^\cdot , Br_2) leads to removal of Br, while the reaction of activated Br species with aldehydes and VOCs generates HBr, which can undergo deposition on snow surfaces. As the same snow probably experiences continuous exchange of Br with the atmosphere via these processes, the global picture of Br in snow is clouded, even for high concentration samples (Figure 14). Fresh snow samples are depleted in Br compared to Cl (full squares in Figure 14), thus, besides not being an additional input media for Br, fresh snow is likely to experience more important Br activation (removal). However, fresh snow samples are not clearly differentiated from the others, hence such assessment shall be taken with caution. Generally, Br is added to surface snow mainly by sea-sprays, and subject to continuous exchange with the atmosphere, with possible dominant removal for fresh snow. The nss-Ca source does not bring any additional Br to the snowpack (no enrichment on Figure 14, $[\text{Br}]/[\text{Ca}] = 0$ on Figure 16).

5. Species weakly related to sea-sprays: small organic acids and F

Figure 17 shows the correlation plots of acetates, oxalates, formates and fluorides with respect to Cl. The sea-spray dilution is represented by the black straight line and is empirical (based on sea-spray samples) for all species. However, except the samples from the sea-spray event, the samples do not fit the sea-spray dilution line at all, but rather seem to roughly fit another dilution (red line). Small organic species can undergo dynamic exchanges between the ice and the snow phases (Legrand and De Angelis, 1995), which likely explain their cloudy overall picture. It is noticeable that for all species on Figure 17, samples from different origin are organized with the same pattern along a second dilution line (in red). Samples from the late spring particle event are the “less diluted”, followed by fresh snow samples and melting snow samples.

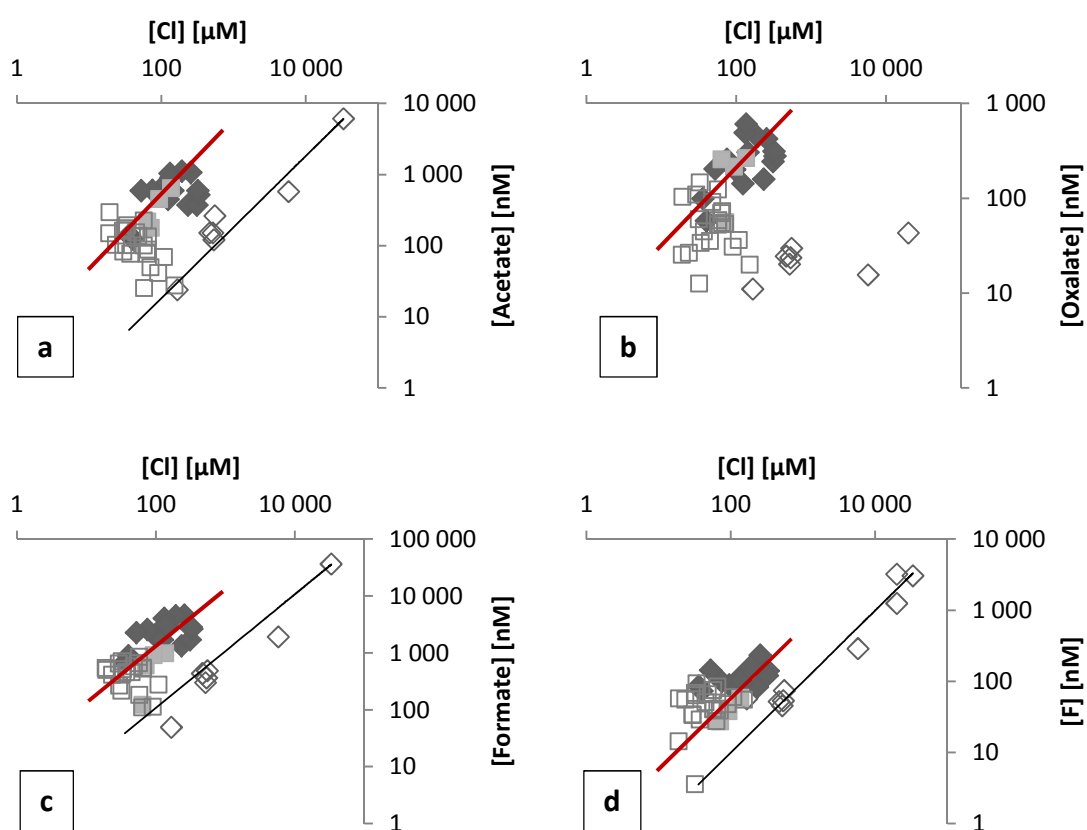


Figure 17. Correlation plot of acetate (a), oxalates (b), formates (c) and F (d) with respect to Cl (as a sea-salt tracer). Black diamond represent the particle input event, open diamonds represent samples with strong sea-spray influence (including the strong storm event), grey squares represent fresh snow samples and open squares represent samples possibly chemically impacted by the snowmelt. The solid line represents empirical sea-salt dilution.

Figure 18 shows the molar ratio/ratio plots of [Acetates]/[Ca], [Formates]/[Ca], [Oxalates]/[Ca] and [F]/[Ca] with respect to [nss-Ca]/[Ca], with the mixing line between the sea-spray and the late spring particle sources. Here again, all the species show the same trend: a similar enrichment ($[X]/[Ca]$) for both sources and a substantial enrichment in fresh snow. For all species, melting induces a fractionation toward higher enrichment, suggesting that melting causes a preferential elution of Ca.

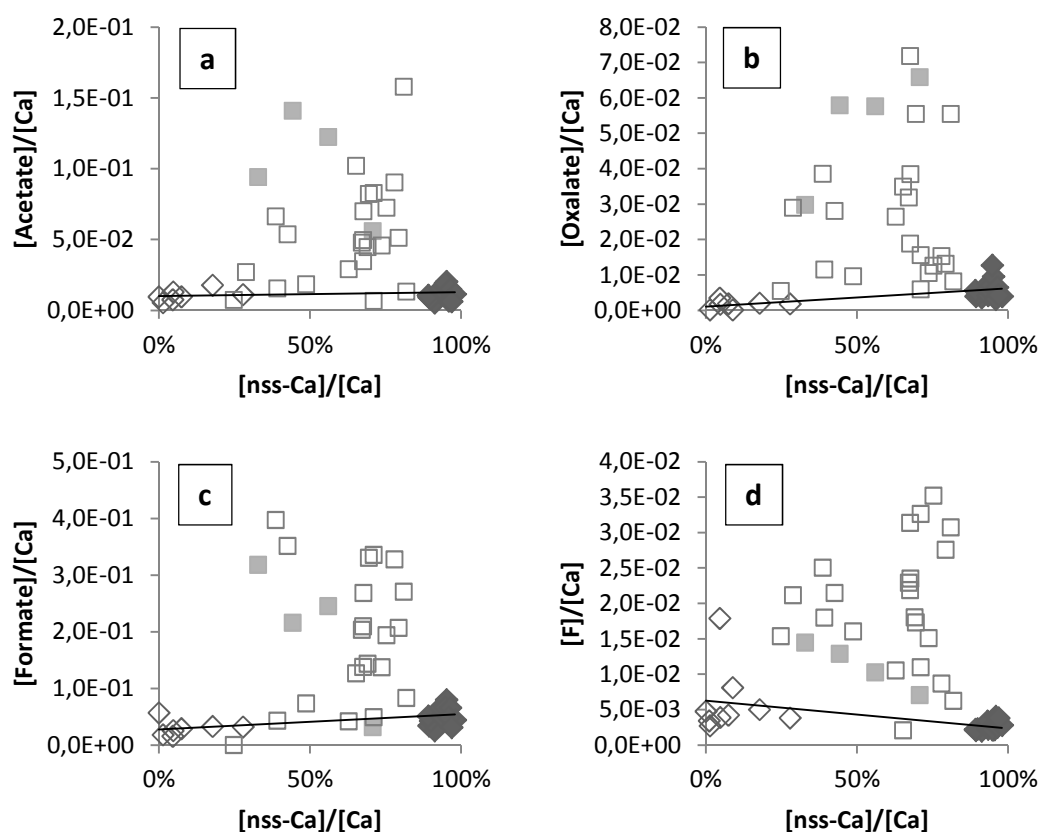


Figure 18. Ratio/ratio plot of [acetates]/[Ca] (a), [oxalates]/[Ca] (b), [formates]/[Ca] (c) and [F]/[Ca] (d) with respect to [nss-Ca]/[Ca] (as contribution of the nss-Ca source to total Ca). Black diamonds represent the particle input event, open diamonds represent samples with strong sea-spray influence (including the strong storm event), grey squares represent fresh snow samples and open squares samples possibly chemically impacted by the snowmelt. The solid line represents the mixing line between sea-sprays and the nss-Ca source, as the linear regression of the (sea-spray + late spring particle event) sample ensemble. The ordinate for $x = 0\%$ represents $[X]/[Ca]$ ratio in sea-sprays, for $x = 100\%$ $[X]/[Ca]$ in the nss-Ca source.

As shown in Figure 19, the alkalinity of snow (= cationic charge – anionic charge) is positively correlated with nss-Ca except for sea-sprays sample. Surface snow becomes more alkaline during the particle event. These changes in the alkalinity of snow will likely alter the stability of dissolved species, chelation equilibrium and exchanges processes at the snow-air interface. In particular, it could affect gas phase equilibrium of small organic monoacids (such as acetic acid and formic acid) (Legrand and De Angelis, 1996, 1995). However, we notice that these processes do not affect our

samples, as data points from both the late spring particle and the sea-spray events organize into narrowed clusters on Figure 18. This indicates that these points are gathered around the source mixing line, because other possibilities (such as processes) would cloud the overall picture, thus unlikely result in such tight clusters (for example, the snowmelt induces a very cloudy picture on Figure 18). We suggest that changes in $[X]/[Ca]$ ratios observed in the late spring particle samples are not due to changes in alkalinity but rather directly result from the contribution of the late spring particles. Finally, Figure 17 suggests that $[X]$ in surface snow is a dilution of highly concentrated material that is initially provided by the late spring particles.

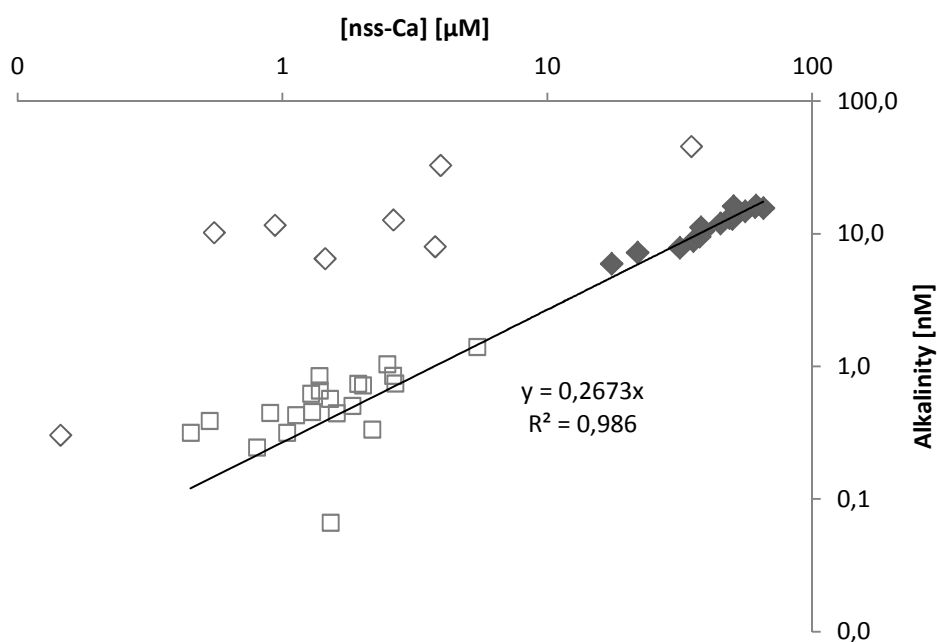


Figure 19. Correlation of alkalinity (net ionic charge of cations – anions) with respect to the nss-Ca concentration. Black diamonds represent the particle input event, open diamonds represent samples with strong sea-spray influence (including the strong storm event) and open squares samples possibly chemically impacted by the snowmelt. The solid line represents the linear regression excluding samples of strong sea-spray influence (open diamonds).

6. Methylmercury

Figure 20 shows the correlation plot of MMHg with respect to Na. Alike small organic acids, the majority of the data points do not fit the sea-spray dilution (assessed by the samples from the sea-spray event, not drawn), but rather fit a second dilution line (black line). On this second dilution line, samples from the late spring particle event are the “less diluted” while samples from melting snow are “more diluted”. The only measured fresh snow sample has the second highest MMHg concentration (after the strong storm sample) and does not fit none of the two dilution straight lines. Generally, the highest concentrations of MMHg are measured during the late spring particle event.

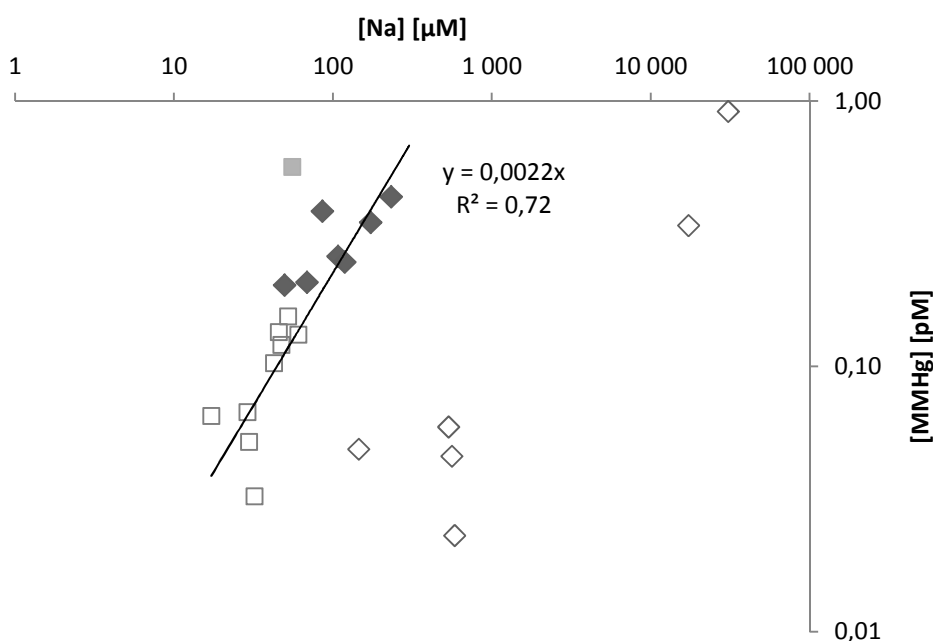


Figure 20. Correlation plot of MMHg with respect to Na (as a sea-salt tracer). Black diamond represent the particle input event, open diamonds represent samples with strong sea-spray influence (including the strong storm event), grey squares represent fresh snow samples and open squares samples possibly chemically impacted by the snowmelt. The solid line represents empirical dilution observed.

Figure 21 shows the molar ratio/ratio plot of $[\text{MMHg}]/[\text{Ca}]$ with respect to $[\text{nss-Ca}]/[\text{Ca}]$. Samples from the sea-spray event and the late spring particle event indicates their respective source fractionation, with similar and very low $[\text{MMHg}]/[\text{Ca}]$ ratio. Interestingly, the only fresh snow sample is clearly enriched in MMHg compared to all other samples, as reported in a previous study (surface snow data from the 21th and 27th of May 2008 in Larose et al., 2010). Melting snow samples are close

to both the late spring particle source and fresh snow (in the triangle between fresh snow and the two sources). It suggests that MMHg in surface snow majorly results from fresh snow and late spring particle inputs and is barely related to sea-sprays inputs. This is consistent with results from Figure 20, suggesting that MMHg in surface snow is a dilution of material brought by the late spring particles (as for the small organic acids).

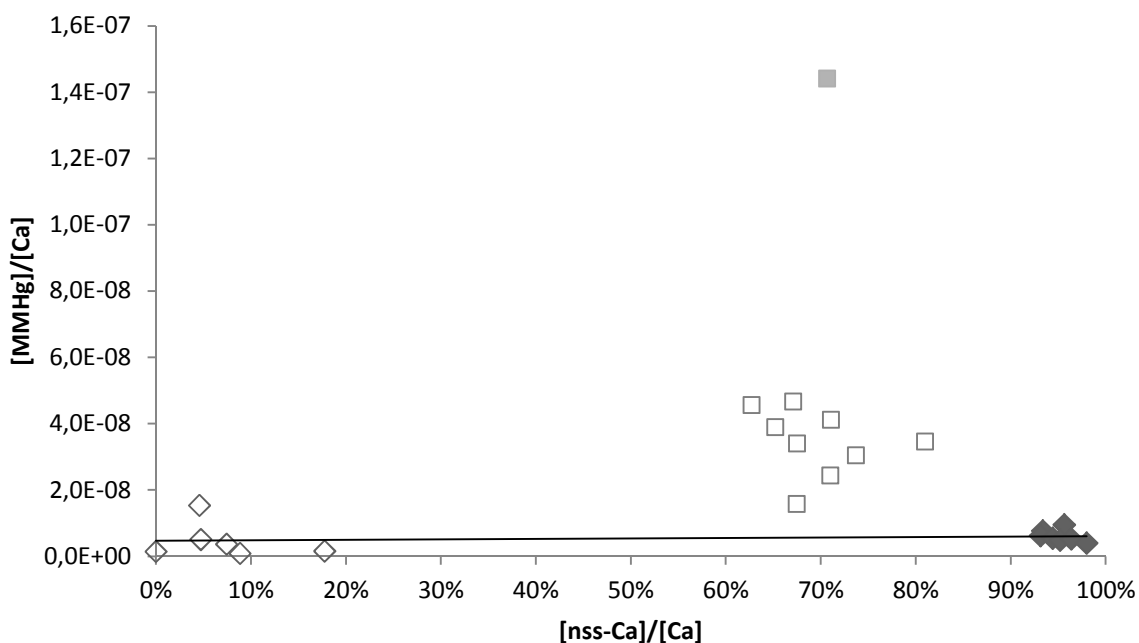


Figure 21. Ratio/ratio plot of $[MMHg]/[Ca]$ with respect to $[nss-Ca]/[Ca]$ (as contribution of the nss-Ca source to total Ca). Black diamond represent the particle input event, open diamonds represent samples with strong sea-spray influence (including the strong storm event), grey squares represent fresh snow samples and open squares samples possibly chemically impacted by the snowmelt. The solid line represents the mixing line between sea-sprays and the nss-Ca source, as the linear regression of the (sea-spray + late spring particle event) sample ensemble. The ordinate for $x = 0\%$ represents $[MMHg]/[Ca]$ ratio in sea-sprays, for $x = 100\%$ $[MMHg]/[Ca]$ in the nss-Ca source.

7. Species related to atmospheric processes: THg, MSA and nitrates

Figure 22 shows the correlation plot of MSA with respect to Cl. As for small organics and MMHg, the data points are not distributed around a sea-salt dilution line. MSA rather follows another dilution line (drawn in black, excluding samples from the sea-spray event), on which several samples from the late spring particle event are the “less diluted” while samples of melting snow are the “more diluted”. In addition, an important MSA enrichment is present in one sample of fresh snow, corresponding to the AMDE + precipitation event.

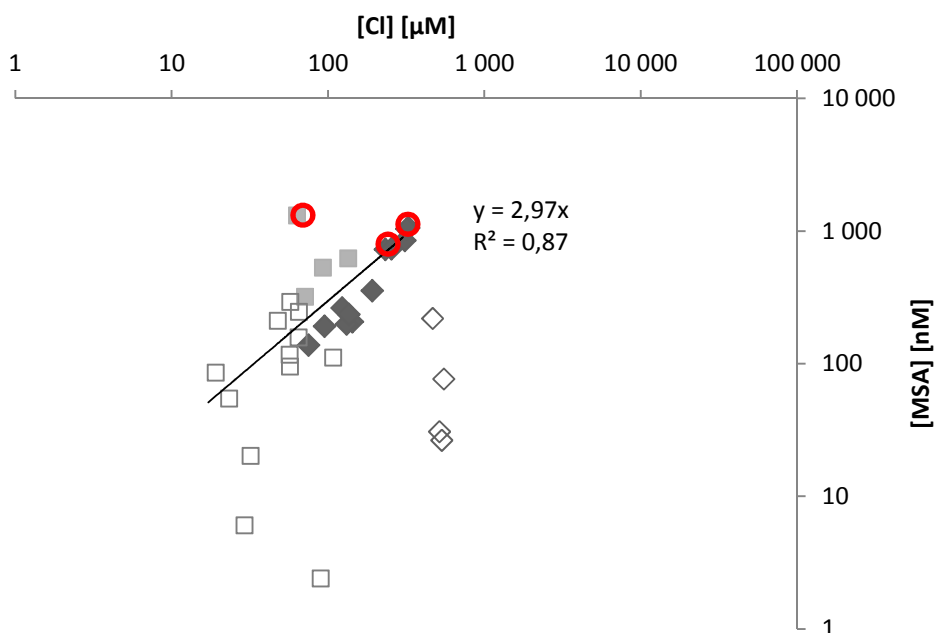


Figure 22. Correlation plot of MSA with respect to Cl (as a sea-salt tracer). Black diamond represent the particle input event, open diamonds represent samples with strong sea-spray influence (including the strong storm event), grey squares represent fresh snow samples and open squares represent samples possibly chemically impacted by the snowmelt. The solid line represents empirical dilution observed. Red circles highlight AMDE events.

Figure 23 shows the correlation plot of THg with respect to Na. The overall picture of THg is too cloudy to be as clearly depicted as for MSA, but four samples are distinct from the others because of their high THg concentration (> 120 ng/L): two precipitation events (one precipitation event and one AMDE + precipitation event, respectively on the 14th of April and the 14th of May) and two samples from the late spring particles, corresponding to the strong AMDE event of the 10th of May.

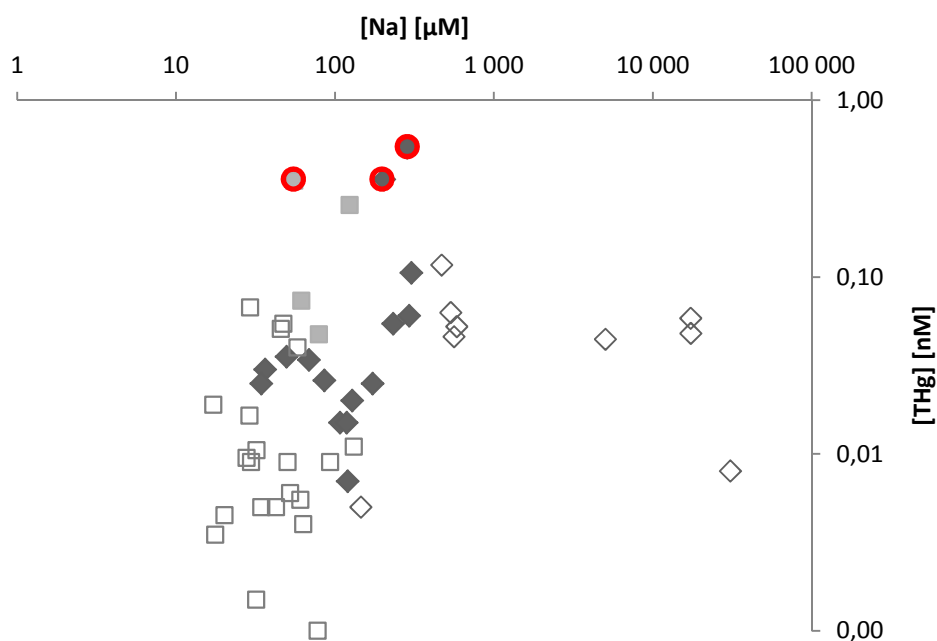


Figure 23. Correlation plot of THg with respect to Na (as a sea-salt tracer). Black diamond represent the particle input event, open diamonds represent samples with strong sea-spray influence (including the strong storm event), grey squares represent fresh snow samples and open squares samples possibly chemically impacted by the snowmelt. Red circles highlight AMDE events.

Figure 24 shows the molar ratio/ratio plot of $[MSA]/[Ca]$ with respect to $[nss-Ca]/[Ca]$. Interestingly, as the data points do not fit a dilution line involving sea-sprays, they can be excluded as significant source of MSA. Fresh snow has not the same MSA fractionation ($[MSA]/[Ca] \approx 0.15$) than in snow from the late spring particle event ($[MSA]/[Ca]$ close to 0). It suggests the existence of two input pathways for MSA in snow: one involving late spring particles, and one involving fresh snow (probably atmospheric scavenging by falling snow). The fresh snow sample from the strong AMDE + precipitation event (14th of May) is highly enriched in MSA (and brings a high MSA concentration in snow, see Figure 22), implying that fresh snow scavenged twice as much as MSA as during precipitations without AMDE. This could be evidence that MSA is formed to a greater extent in the atmosphere during AMDEs. Although MSA concentrations can be high (> 700 nM) in some samples from the particle event (see Figure 22), these samples correspond to snow samples between the 8th and the 13th of May during the strong AMDE event, thus cannot be attributed to the input of particles. Hence we do not consider the particle event as a significant source of MSA in our samples. Actually, as MSA is a product of marine dimethylsulfide atmospheric oxidation, we suggest that the strong oxidative properties of the atmosphere during AMDEs particularly favor MSA formation. Precipitation during an AMDE would enhance the formed MSA deposition by atmospheric washing (scavenging by fresh snow). We do not observe the same trends for sulfates, which are the end

product of dimethylsulfide atmospheric oxidation. The oxidative species responsible for MSA formation during AMDEs is not reactive enough to fully oxidize dimethylsulfide into sulfates.

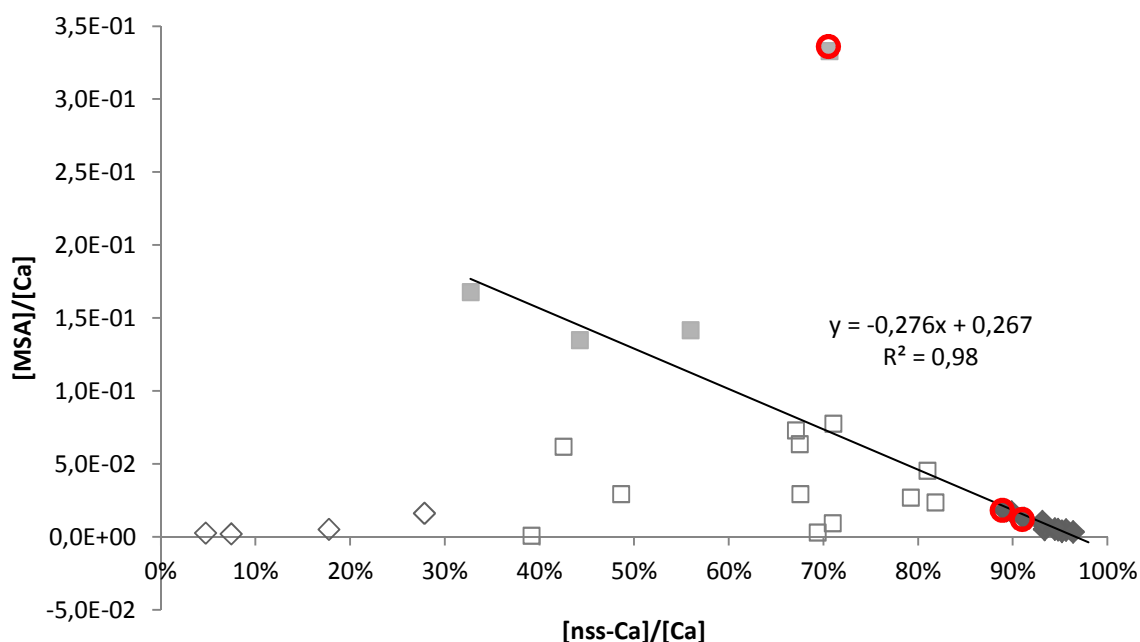


Figure 24. Ratio/ratio plot of $[MSA]/[Ca]$ with respect to $[nss-Ca]/[Ca]$ (as contribution of the nss-Ca source to total Ca). Black diamond represent the particle input event, open diamonds represent samples with strong sea-spray influence (including the strong storm event), grey squares represent fresh snow samples and open squares samples possibly chemically impacted by the snowmelt. The solid line represents the mixing line between fresh snow and the nss-Ca source, as the linear regression of the (fresh snow + late spring particle event) sample ensemble. The ordinate for $x = 0\%$ represents $[MSA]/[Ca]$ ratio in sea-sprays, for $x = 100\%$ $[MSA]/[Ca]$ in the nss-Ca source. Red circles highlight AMDE events.

Figure 25 shows the molar ratio/ratio plot of $[THg]/[Ca]$ with respect to $[nss-Ca]/[Ca]$. Samples from the sea-spray event and the late spring particle event indicates their respective source fractionation, with similar and very low $[THg]/[Ca]$ ratio. However, fresh snow samples and samples from the strong AMDE are enriched in THg, suggesting the contribution of a third source linked to atmospheric processes occurring during snow precipitation, which are not AMDEs (displayed in red on Figure 25). The strong AMDE occurs at the beginning of the particle event and induces a > 10 -fold increase of THg concentration. However, the simultaneous particle event induces an increase in Ca concentration, resulting in a lower $[THg]/[Ca]$ increase (6-fold) than expected from the > 10 -fold increase in THg concentration only. As a result, samples corresponding to AMDEs do not show a clear singular chemical signature. Thus we do not consider AMDEs as a significant source of THg in our snow.

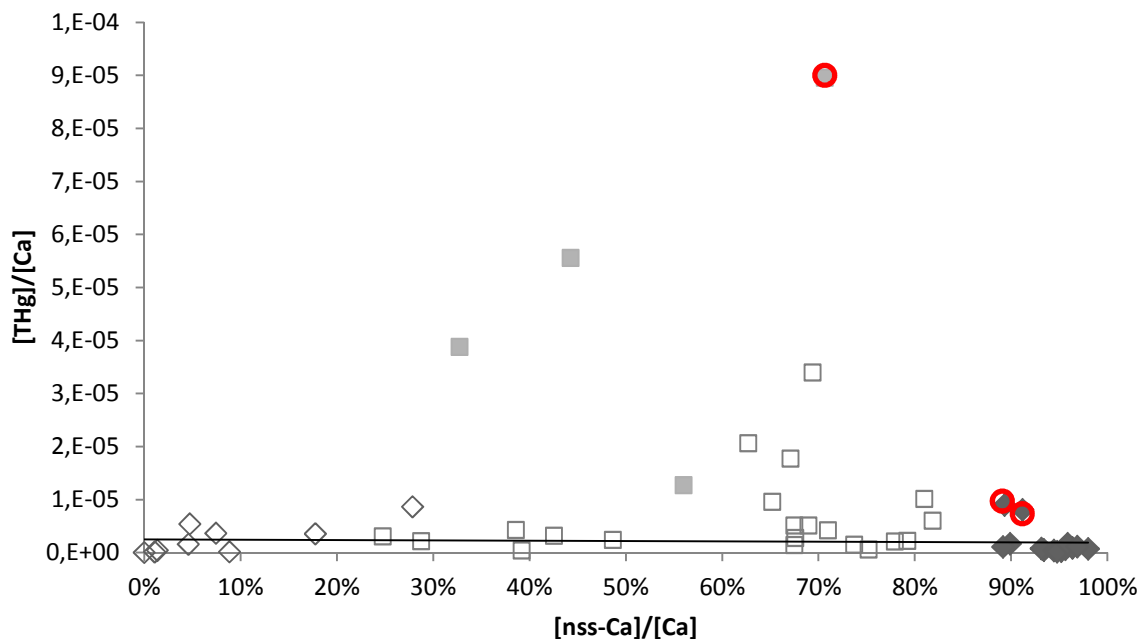


Figure 25. Ratio/ratio plot of $[THg]/[Ca]$ with respect to $[nss-Ca]/[Ca]$ (as contribution of the nss-Ca source to total Ca). Black diamond represent the particle input event, open diamonds represent samples with strong sea-spray influence (including the strong storm event), grey squares represent fresh snow samples and open squares samples possibly chemically impacted by the snowmelt. The solid line represents the mixing line between sea-sprays and the nss-Ca source, as the linear regression of the (sea-spray + late spring particle event) sample ensemble. The ordinate for $x = 0\%$ represents $[THg]/[Ca]$ ratio in sea-sprays, for $x = 100\%$ $[THg]/[Ca]$ in the nss-Ca source. Red circles highlight AMDE events.

In summary, Figure 23 and Figure 25 show that except four measurements, the THg concentration in coastal surface snow is generally below 0.10 nM and do not show any significant difference whether the main source is sea-sprays or late spring particles (which have the same $[THg]/[Ca]$ fractionation). Consequently, we believe that the primary source of THg (which explains the background THg concentration > 0.10 nM) cannot be observed. The absence of clear source suggests that Hg in snow does not originate from defined chemical sources but rather from a thermodynamic equilibrium between snow and the atmosphere. We think that Hg rapidly exchanges with the atmosphere (*via* oxidation and photoreduction cycling) and that the snow-air equilibrium (leading to the THg observed in snow) is driven by a net contribution of both the oxidative properties of the atmosphere and the photoreductive potential (UV radiation, presence of reductive agents... etc). The extreme examples of this theory would be the AMDEs (predominance of the oxidative potential versus the photoreductive one), and inversely the following strong emission events (AMEEs). In other words the Hg background concentration and its small variations could be attributed to the contribution of “micro-AMDEs” and “micro-AMEEs” constantly adjusting the Hg snow-air equilibrium, which slightly varies with atmospheric physical and chemical conditions. The strong AMDE events observed would be due to a brutal change of the snow-air equilibrium (because of strong oxidative properties of the atmosphere), and the following AMEEs would result of the opposite. This is in agreement with the

results discussed in section III.i and the literature pointing the redox transformations of Hg in the interstitial air of the snowpack as critical regarding the Hg concentration in snow (Dommergue et al., 2003; Fain et al., 2006; Lalonde et al., 2002; Poulain et al., 2004).

8. Summary of the results

Considering the results presented and discussed above, the chemistry of our snow samples has three main contributors: 1) sea-sprays; 2) the late spring input of particles; and 3) atmospheric depositions (dry and wet). The ratio/ratio plots allow to estimate the $[X]/[Ca]$ ratios for each species and both sea-sprays and particle sources. The estimated $[X]/[Ca]$ in the sea-sprays and the late spring particles are summarized in Table 2.

Table 2. Chemical features of sea-sprays and late spring particles.

X	Sea-sprays		Late spring particles	
	$[X]/[Ca]$	Mean [X] in snow** (n = 5)	$[X]/[Ca]$	Mean [X] in snow (n = 9)
Na	48.08	537.5 ± 49.6 µM	0 ^a	120.4 ± 55.1 µM
nss-Ca	0 ^b	2.0 ± 1.5 µM	1 ^b	46.3 ± 11.3 µM
Li	0.0024	30.2 ± 3.8 nM	0	7.8 ± 2.9 nM
K	1.011	11.4 ± 1.1 µM	0	2.2 ± 1.1 µM
Mg	5.251	61.7 ± 5.3 µM	0.403	31.9 ± 8.6 µM
Br	0.076	720.4 ± 207.3 nM	0	206.9 ± 106.9 nM
Cl	51.38	517.7 ± 36.2 µM	0	133.5 ± 61.0 µM
F	0.0063	56.1 ± 12.4 nM	0.0024	125.3 ± 48.6 nM
Sulfates	2.87	36.5 ± 3.0 µM	0.043 (≈ 0)	8.8 ± 6.6 µM
Nitrates*	0.076	1.9 ± 0.9 µM	0.035	1.8 ± 1.7 µM
Acetates*	0.010	171.3 ± 62.4 nM	0.013	780.1 ± 256.7 nM
Formates*	0.028	394.9 ± 80.7 nM	0.055	3073.6 ± 1094.0 nM
Oxalates*	0.001	24.4 ± 3.9 nM	0.006	343.1 ± 157.0 nM
THg*	3 10 ⁻⁶	49.0 ± 32.5 pM	2.4 10 ⁻⁶	26.0 ± 14.0 pM
MMHg*	5 10 ⁻⁹	42.5 ± 18.0 fM	6 10 ⁻⁹	298.0 ± 91.5 fM
Particles	-	42 966 ± 61 401 mL ⁻¹	-	1 184 250 ± 580 072 mL ⁻¹

*species with a comparable $[X]/[Ca]$ ratio in both sea-sprays and late spring particles (with overlapping $[X]/[Ca]$ ranges)

**except samples from the storm event

^a as sea-sprays tracer

^b as late spring particles tracer (calculated from [Na], see equation)

Based on data summarized in Table 2 and observations from paragraph 7 of the present section concerning the atmospheric contribution to surface snow chemistry, we address a simplified picture of the chemical composition of each source as presented in Table 3.

Table 3. Qualitative overview of the chemical composition of the different sources types observed in our samples^a.

	Sea-sprays	“Atm. deposit.”	Late spring particles
Primary source for	Na, Li, K, Mg, Cl, Br, Sulfates	Nitrate, MSA	Ca, MMHg, Acetates, Formates, Oxalates, F
Secondary source for	Ca	Br, Sulfates	Mg
Sporadic source for	Everything but THg, Oxalate, Nitrate, MSA	MMHg, THg,	-

^a If a source A induces a significant higher concentration [X] in the selected samples than the other source B (the two concentration ranges should not overlap), source A will be considered as the main source for X. A secondary source for X can be a source inducing visible anomaly on the correlation plot of [X] with respect to [Na] or [Cl] (see above) without inducing the highest absolute concentrations [X]. Every event bringing X for a short period of time or on an exceptional basis (on extrema events such as the sea-spray storm) will be considered as a punctual source for X.

The sea-sprays, as showed by our results summarized in Table 2 and Table 3, induce surface snow chemistry following the sea water dilution. Small sea-water droplets are formed and withdrawn from surface sea waters by the wind and undergo further trapping by surface snow (Domine et al., 2004) which is known to occur only on the first centimeters of the snowpack. Sea-sprays mainly deposit sea-salt species (Na, Li, K, Mg, Ca, Br, Cl, Sulfates). Deposition of traces of small organics and mercury species (THg, MMHg) are exceptionally observable in our samples due to the storm event.

An important feature of the late spring particle event is the particular size-distribution of particles deposited on surface snow. Figure 26 displays the numerical fraction of particles depending on size, for the late spring particle event. The particle profile shows a more important contribution of particles of diameter comprised between 4 and 7 μm , with a Gaussian-like repartition, which is not observable on the other particle profiles. In addition, particles collected in snow from the late spring particle event show a particular fingerprint that is visible for particle size of around 0.8 and 1.9 μm . This is further proof that this late spring particle event consists in an input of the same kind of particles during all its duration.

At this stage, we know about this late spring particle event as much as our analysis allows, with a good knowledge of physical and chemical properties of the particles. The first observation is that these properties are quite stable with time (daily samples on a two-week period have similar properties). Concerning chemistry, these particles directly bring on surface snow (= contain) Ca, Mg, acetates, formates, oxalates, F and MMHg. Interestingly, the $[X]/[Ca]$ molar ratio (X being one of the species mentioned) are close to the one encountered in sea-sprays, except $[Mg]/[Ca]$ which is much lower in the particles. Concerning physical properties, these particles differentiate by a particular size distribution and fingerprint. This represents an additional input compared to the particles observed in the other samples.

The next section of this manuscript aims to discuss the origin of these late spring particles, based on the results presented in the present section. It provides a new insight into arctic coastal snow chemistry, with a particular focus on the origin of MMHg in the arctic coastal snowpack.

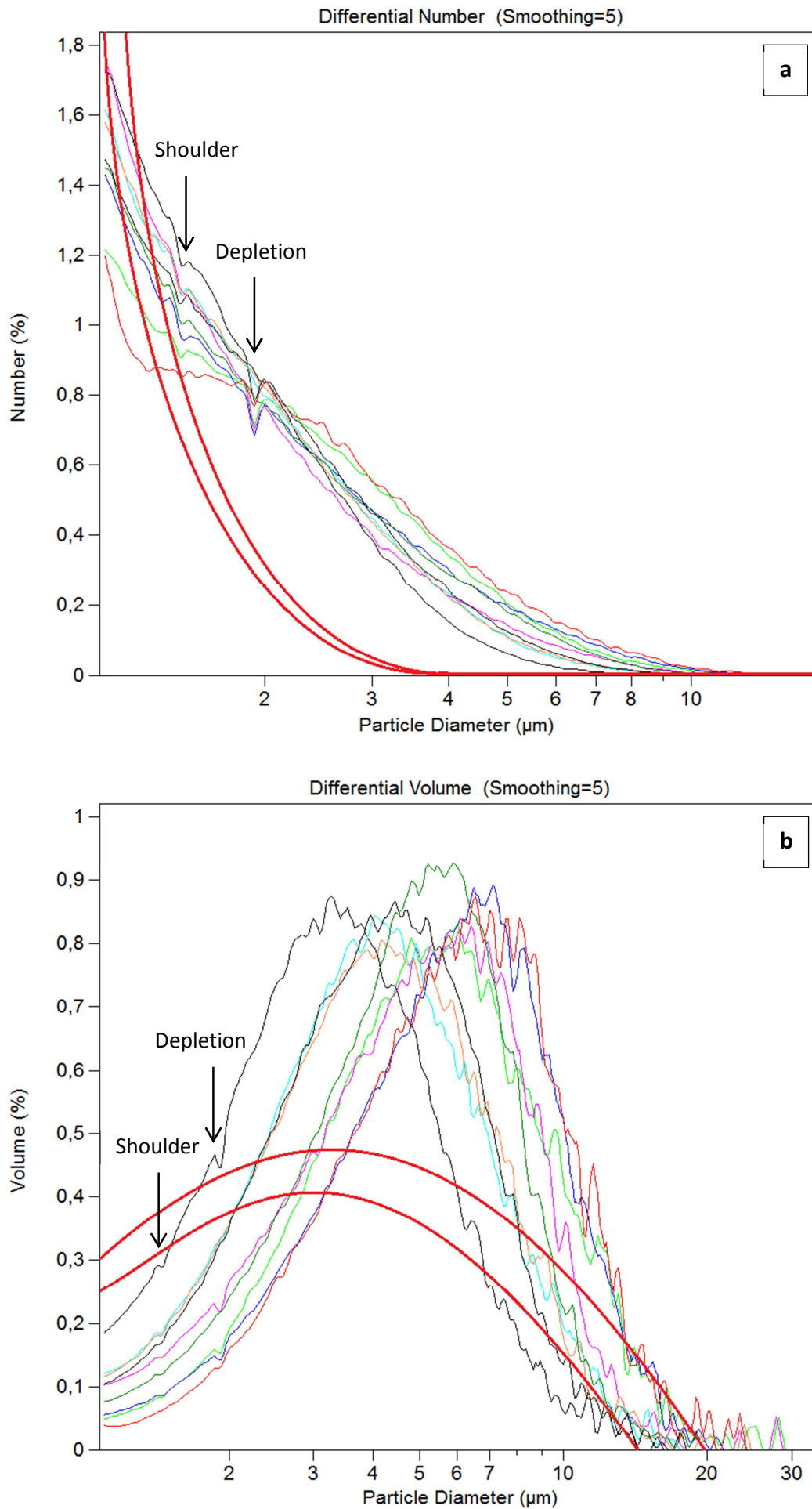


Figure 26. Differential number (a) and differential volume (b) of particles from the late spring particle event, displayed daily. The bold red curve represents the profile range for particles which are not from the late spring particle event.

iii. Discussion on the MMHg sources

Particles from the late spring particle event have been identified as a critical contributor to the surface snow composition including ions, small organics and MMHg. Our results indicate that the snow chemistry resulting from this particle input depicts the chemistry of the particle source rather than *in situ* processes. In addition, the data presented in Figure 4 from section II.ii (showing a parallel diminution of particle number and snowpack thickness at the end of the observation period) suggest that snowmelt causes the decrease of the net particle concentration in snow. The first observation about the late spring particles is that their properties are quite stable with time (daily samples on a two-week period have similar properties). Concerning chemistry, these particles are responsible for additional input of Ca, Mg, acetates, formates, oxalates, F and MMHg in snow. Concerning physical properties, these particles differentiate by a particular size distribution and fingerprint. In fact, their input could remain important even after the snow season, and be a source for MMHg on all open surfaces.

1. A mineral source for nss-Ca ?

In the literature, nss-Ca inputs in snow are often provided by mineral dust particles formed by weathering and erosion (Fischer et al., 2007; Jacobi et al., 2012; Kang et al., 2001; Ruth et al., 2008; Ström et al., 2003). Mineral dust aerosol formation is more efficient in semi-arid regions, where weathering conditions are strong enough and soil moisture sufficiently low to allow for dust mobilization (Fischer et al., 2007). Mineral dust in snow or ice cores can originate from long range transportation in sites where dust mobilization is low (e.g. inland regions of Antarctica and Greenland)(Fischer et al., 2007; Ruth et al., 2008), and/or from regional erosion (e.g. northern Tibetan plateau or the Arctic)(Jacobi et al., 2012; Kang et al., 2001).

The timing of the observed late spring particle event coincides with the snowmelt on the steepest area of the fjord: a significant increase of open rocky surfaces is visible between mid-April and mid-May, as displayed by the photographic comparison on Figure 1. Thus erosion could have taken place gradually from the end of April and released an increasing number of dust particles on the surface snow we sampled.

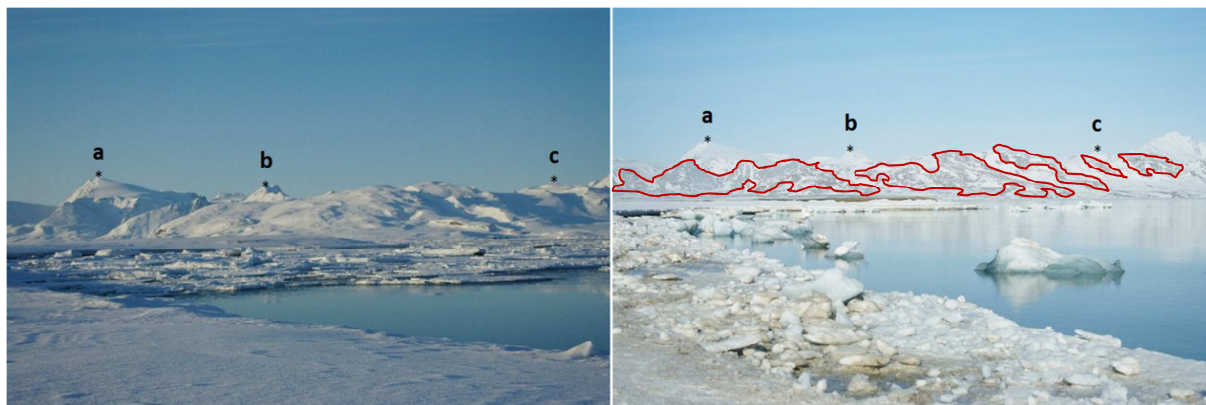


Figure 1. Pictures of a given section of the north coast of Kongsfjorden taken from the study site in mid-April (left) and mid-May (right). Uncovered bedrock area are highlighted in red.

Mineral particles are chemically recognizable, as they contain the main metallic and semi-metallic constituents of the Earth crust – such as silicon (Si) or aluminum (Al) – as well as alkali and alkaline earth metals, such as Ca, Mg, Na or K for instance (Hans Wedepohl, 1995). We were not able to perform Si or Al analysis on our samples, so we cannot include them in the discussion. The late spring particles bring additional Ca and Mg in our samples and the estimated $[Mg]/[Ca]$ in the particle source ratio is 0.403. However, they do not contain any K, as their estimated $[K]/[Ca]$ ratio is 0 (Figure 11 in section III.ii). Despite the lack of knowledge concerning the impact of the eroding processes on mineral dust chemistry (potential fractionation), we compared this $[K]/[Ca]$ ratio to the ones described in the literature. The estimated mean $[K]/[Ca]$ ratio for the continental crust 0.88 (Hans Wedepohl, 1995) might not be relevant considering Svalbard geology (Elvevold et al., 2007; Nejbort et al., 2011). A recent study investigates the chemical composition of dolerites from east and central Svalbard (Nejbort et al., 2011), describing very low $[K]/[Ca]$ ratios (around 0.04), and $[Mg]/[Ca]$ around 0.7-0.9. Nevertheless, our data suggest that the nss-Ca containing particles do not bring additional K, as even small $[K]/[Ca]$ ratios could have been observable given the accuracy of the ratio/ratio plot of $[K]/[Ca]$ with respect to $[nss-Ca]/[Ca]$ used for estimation (Figure 11 in section III.ii). More importantly, all the terrestrial sources contain substantial amount of Na as Na_2O (Hans Wedepohl, 1995; Rudnick et al., 2004), hence deposition of soluble mineral dust on surface snow should result in anomalies on the $[Na]/[Cl]$ ratio, which is not the case here (Figure 1 in section III.ii).

Another crucial result concerning these particles is their organic content. As previously described in section III.ii, small organic acids concentrations in surface snow are increasing with the nss-Ca particle input and our data suggest that this increase is directly due to the particles chemical composition. This is supported by the direct correlation of each organic with nss-Ca during the late spring particle event, as shown on Figure 2. In this case, if considering that these particles are of mineral origin, one should assume that the presence of these organics is due to their adsorption onto

the mineral aerosols – although there is to our knowledge no description of such phenomenon. As one would expect this phenomenon to vary overtime, it would then be very unlikely to observe direct positive correlations between nss-Ca and each small organic acid in samples collected over a two-week long period (Figure 2). In other words, there is no reason to observe very close $[X]/[Ca]$ ratios in all the samples from the late spring particle event if X and Ca in these particles do not have the same source. The chemical composition of these particles is therefore likely to be brought by a single source. The hypothesis of a mineral source would thus be in disagreement with the presence of small organic acids, which are expected to be totally absent from any mineral medium. Consequently, although mineral dust inputs could easily explain the nss-Ca composition of our surface snow samples, there are chemical anomalies strongly suggesting an alternative source for the nss-Ca.

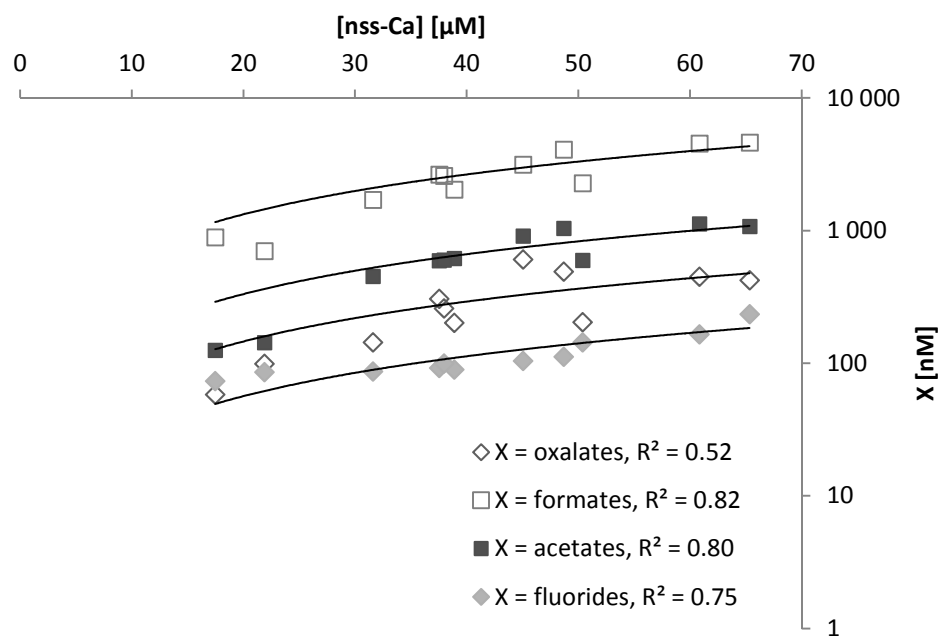


Figure 2. Correlation of [X] (X = oxalates, formates, acetates or F) with respect to [nss-Ca] in snow samples from the late spring particle event. Linear regressions pass through the origin.

2. A (paradoxal) marine source for nss-Ca ?

Previous studies reported the formation of sea-salt depleted aerosols made of biogenic exopolysaccharides (EPS) bound to divalent cations (Ca, Mg...) to form organic gels (Bigg and Leck, 2008; Keith Bigg et al., 2004; Leck, 2005, 2002). These aerosols, formed by bubble bursting above the surface marine layer, withdraw organic and biological species (Bigg and Leck, 2008; Gao et al., 2012).

The process of bubble formation requires EPS as surfactant to allow their stability, and their implosion leads to a separation of saline hydrophilic and hydrophobic species (EPS, organics, insoluble materials...) and therefore to the formation of organic aerosols, whose chemistry can have no apparent correlation with sea-salt (Bigg and Leck, 2008). Their atmospheric lifetime depends on the photo-induced cleavage of EPS into smaller polysaccharides and finally monosaccharides, and barely exceeds a few days (Bigg and Leck, 2008). Other aerosols containing organics without sea-salt have been observed, formed with proteinaceous material or fragments of calcareous phytoplankton (Hawkins and Russell, 2010), the latter containing substantial amount of Ca as well as an organic gel coating. Recently, such aerosols have been proposed to explain Ca enrichment compared to sea-salt in arctic snow (Krnavek et al., 2011). The common factor in all these kinds of marine organic aerosols is the presence of a macro-organic gel coating. The chemical definition of a gel is the formation of a semi-rigid network in a chemical media by polymerization, either by covalent bounding or by other chemical bounds involving complexation with multivalent cations or metals. Polysaccharides and macroorganics in organic aerosols need multivalent cations to assemble into gels via bridge connections between different macromolecules. The formation of such gels from marine dissolved organic matter (DOM) has been observed with Ca and Mg (Chin et al., 1998). The authors suggest that if such gels assemble into Ca-saturated particles, they should contribute to sedimentation and aerosol formation.

We were only able to collect a few samples for dissolved organic carbon (DOC) determination, and we have no data for the late spring particle event. However, the small organics observed in these particles are probably part of a high DOM content which should mainly consist in macromolecules. As explained above, the close $[X]/[Ca]$ in all the samples from the late spring particle event suggests a common source for Ca and the small organics. This would be in agreement with the hypothesis of the formation of non-sea-salt-related marine organic aerosols described above.

The chemical features of such organic marine aerosols are also consistent with our observations of Ca and Mg enrichment in the late spring particles. Magnesium is enriched compared to sea-salt, as observable on the correlation plot of $[Mg]$ with respect to $[Na]$ (Figure 7 in section III.ii), but far less than Ca, as highlighted by the low $[Mg]/[Ca]$ ratio estimated in the particles compared to sea-sprays (0.403 and 5.251 respectively). The enrichment of these two multivalent cations, in parallel with no enrichment of any monovalent cation (such as Na, Li or K) is consistent with the enrichment of Ca and Mg during the process of formation of organic gels (Chin et al., 1998). The difference between the moderate enrichment of Mg and the substantial enrichment of Ca is consistent with the fact that they do not have the same affinity with macromolecules (Ca would then be the preferred substrate for gel formation). A higher enrichment for Ca is also consistent with the fact that marine organic

aerosols can contain calcareous phytoplankton fragments (Hawkins and Russell, 2010). The presence of these pure Ca fragments (as CaCO_3) even in low amounts, are likely to be responsible for the main proportion of Ca in marine organic aerosols. Concerning the Arctic, there is to our knowledge only one study investigating organic marine aerosols, that describes exclusively proteinaceous and polysaccharides particles, with 74% ($n = 47$) of particles larger than $2 \mu\text{m}$, which would correspond to the main size range of particles from the late spring event in our samples (Figure 26 in section III.ii)(Hawkins and Russell, 2010). As previously explained, such aerosols are degraded in the atmosphere by photo-cleavage of the organic macromolecules into smaller units. Because the late spring particles we observe have a large diameter ($> 4 \mu\text{m}$), their residence time in the atmosphere is expected to be short. It would indicate that their formation occurs at a very regional scale (in the fjord for instance). Furthermore, MMHg concentrations in surface snow during the late spring particle event are high and do not diminish within a few hours or days (like high concentrations from fresh snow or sea-sprays do). This could be due to a continuous input of MMHg containing particles and/or to a less effective photo-reduction of MMHg because of its chemical environment. Despite this cannot be determined by our data, organic complexation has been proven to affect MMHg photo-reduction, either favoring or hindering (Hammerschmidt and Fitzgerald, 2006; Oh et al., 2011; Ribeiro Guevara et al., 2008; Siciliano et al., 2005). Anyway, this late spring particle event induces higher and steadier concentrations of MMHg in surface snow.

3. Discussion on MMHg dynamic in the Arctic

At this point, having considered the two possible hypotheses to explain the additional input of Ca by the late spring particle event (either terrestrial mineral dust or marine organic aerosols), the formation of organic aerosols from the marine surface layer (Bigg and Leck, 2008) is the most likely to explain the results from our data. Indeed the organic content of the late spring particles, as well as the Ca and Mg enrichment are in favor of the formation of organic polymers gels able to withdraw organic and biological material from the surface marine layer by bubble bursting (Chin et al., 1998; Gao et al., 2012). The mineral dust particle hypothesis is not likely to explain this organic content, as well as the absence of enrichment for other cations ordinary present in the mineral crust, both at global and regional scale, such as K or Na. It doesn't seem straightforward to explain such a strong terrestrial contribution (up to 93-99% of Ca during the particle event) by mineral dust input on a sampling site located ten meters away from open sea-waters. In addition, the estimated $[X]/[\text{Ca}]$ ratios in the late spring particles (X being any of the measured small organics and MMHg) are close to

the one observed in sea-sprays, which would be in agreement with a primary marine source of particles made of Ca and organic species.

We suggest that the late spring particles in our samples result from the formation of aggregates of hydrophobic chemical and/or biological materials and possibly calcareous fragments, held together by organic polymer gels retaining Ca and Mg. The MMHg in these particles is probably produced in the water column prior to scavenging by DOM and incorporated to the subsequent organic particles. This type of particles is rapidly photo-degraded in the atmosphere; hence the fact that the particles we observe contain a substantial amount of MMHg (which is highly photo-degradable) suggests that they were rapidly deposited after their formation, accounting for a fjord-scale production. The scavenging of these marine organic particles by precipitations can also contribute to the particular fractionation observed in fresh snow for the organic species and MMHg (Figures 18 and 21 in section III.ii). Indeed, a large proportion of the emitted marine organic aerosols can remain and travel in the troposphere, undergo degradation of organic species (by oxidation) and photo-degradable material (including MMHg) and further scavenging by precipitations. It is however insufficient to explain the very high [MMHg]/[Ca] ratio observed in our fresh snow sample.

In summary, MMHg in Arctic seasonal surface snow would be of marine origin, with two different pathways. First, the deposition of small wind-blown sea-water droplets (sea-sprays) on surface snow leads to a snow chemistry following sea-water content dilutions, hence with high concentrations of sea-salt species but low concentrations of organics and MMHg. Storm events can lead to abnormal sea-water deposition, including visible fragments of bio-organic material (algae) thus high concentrations of organics and MMHg, which undergo rapid degradation or volatilization (within a few hours to a few days). A second source of MMHg highlighted by our results is Ca-containing particles. The data invalidate a mineral origin for such big and calcareous particles, but rather suggest a marine particle origin. These particles are made of hydrophobic organic gels (inducing Ca and Mg) and potentially biological material and/or calcareous phytoplankton fragments. Such particles are strongly believed to form in the surface marine layer and to contribute to a large part of the tropospheric aerosols in oceanic regions (such as Svalbard) and provide the suitable chemical conditions for MMHg withdrawal from surface sea-waters and atmospheric transportation. These particles are mainly observed during a strong and gradual particle input between mid-May and early June, and contribute to continuously high concentrations of MMHg over this time period. Algal blooms are known to occur in Kongsfjorden in spring, depending on both sunlight and nutrient content of the sea-water column (Rokkan Iversen and Seuthe, 2010; Seuthe et al., 2010). The consequences of such blooms are not well known, but the biological activity and the following senescence could provide abnormally high amounts of bio-organic molecules and biological

fragments favoring the formation of the aforementioned marine organic particles (Leu et al., 2006). Anyway, assuming that the Ca-, organics- and MMHg-containing particles are of marine origin, their strong input in snow during the late spring event has to be correlated with surge of their marine production.

A commonly mentioned source for MMHg in arctic coastal snow is related to marine production and evasion of MMHg or DMHg (dimethylmercury) prior deposition on snow surfaces (Loseto et al., 2004; Pongratz and Heumann, 1999, 1998; St. Louis et al., 2005). However, if DMHg (as a gaseous species) can readily volatilize from surface sea-waters and undergo subsequent atmospheric degradation to MMHgCl (Niki et al., 1983), the evasion pathway of MMHg is unclear. The MMHg that we measured in snow from the late spring particle event does not derive from atmospheric demethylation of DMHg. It would be inconsistent with the clustered positioning of [MMHg]/[Ca] data points on Figure 21 of the III.ii section.

Internal sources are also proposed for MMHg in arctic snowpacks. Many studies using bioreporters indicate that a substantial proportion of Hg in snow is bioavailable (Larose et al., 2011; Scott, 2001). Furthermore, arctic snow contains 200-5000 cells/mL, some of them being active at *in situ* temperatures (Alfreider et al., 1996; Barkay and Poulain, 2007; Carpenter et al., 2000; Segawa et al., 2005), together with organic species as potential carbon sources. If some of the active microorganisms in snow could methylate Hg (which remains speculative), then an internal biotic source of MMHg in oxic conditions would be possible (Larose et al., 2010). In addition to this, evidences of abiotic Hg methylation by DOC in freshwater systems were found (Ribeiro Guevara et al., 2008; Siciliano et al., 2005). Our results however suggest that such internal mechanisms (if any) do not contribute significantly to the MMHg content of surface snow. We were unable to investigate MMHg dynamics in deeper snow at the same sampling site, as the snowpack experienced strong melting early during the field campaign, resulting in a thin porous uniform snow layer. As optimal conditions for studying internal Hg related process, we recommend a thick and stable snowpack, over space and overtime.

Recent studies reported very high MMHg concentrations in fresh snow and rainwater (Hall et al., 2005; Rose et al., 2013). The authors suggested the scavenging of MMHg-containing aerosols to explain the presence of MMHg in precipitations, without excluding Hg methylation. This question of Hg methylation in the atmosphere remains an open question, as the first abiotic mechanism described in laboratory conditions (Gårdfeldt et al., 2003) was successively considered as a potential source for MMHg (Hammerschmidt et al., 2007) or as not likely to take place (Bittrich, 2011). Despite our results do not identify the source for MMHg in precipitations, the [MMHg]/[Ca] ratio in our fresh

snow sample indicates that the two MMHg source we identified in the **III.ii** section (sea-sprays and late spring particles) cannot be the only contributors to MMHg concentrations in fresh snow. Therefore, our results also suggest the existence of 1) a third source for MMHg in the atmosphere; and/or 2) an atmospheric MMHg generating process.

References

- Alfreider, A., Pernthaler, J., Amann, R., Sattler, B., Glockner, F., Wille, A., Psenner, R., 1996. Community analysis of the bacterial assemblages in the winter cover and pelagic layers of a high mountain lake by in situ hybridization. *Appl. Environ. Microbiol.* 62, 2138–2144.
- Barkay, T., Poulain, A.J., 2007. Mercury (micro)biogeochemistry in polar environments. *FEMS Microbiology Ecology* 59, 232–241.
- Bigg, E.K., Leck, C., 2008. The composition of fragments of bubbles bursting at the ocean surface. *Journal of Geophysical Research* 113.
- Bittrich, D.R., 2011. Speciation of Mercury (II) and Methylmercury in Cloud and Fog Water. *Aerosol and Air Quality Research*.
- Carpenter, E.J., Lin, S., Capone, D.G., 2000. Bacterial Activity in South Pole Snow. *Applied and Environmental Microbiology* 66, 4514–4517.
- Chin, W.C., Orellana, M.V., Verdugo, P., 1998. Spontaneous assembly of marine dissolved organic matter into polymer gels. *Nature* 391, 568–572.
- Elvevold, S., Blomeier, D., Dallmann, W., 2007. *Geology of Svalbard*. Norsk polarinstitutt, Tromsø.
- Fischer, H., Siggaard-Andersen, M.-L., Ruth, U., Röthlisberger, R., Wolff, E., 2007. Glacial/interglacial changes in mineral dust and sea-salt records in polar ice cores: Sources, transport, and deposition. *Reviews of Geophysics* 45.
- Gårdfeldt, K., Munthe, J., Strömberg, D., Lindqvist, O., 2003. A kinetic study on the abiotic methylation of divalent mercury in the aqueous phase. *The Science of the Total Environment* 304, 127–136.
- Gao, Q., Leck, C., Rauschenberg, C., Matrai, P.A., 2012. On the chemical dynamics of extracellular polysaccharides in the high Arctic surface microlayer. *Ocean Science* 8, 401–418.
- Hall, B., Manolopoulos, H., Hurley, J., Schauer, J., StLouis, V., Kenski, D., Graydon, J., Babiarz, C., Cleckner, L., Keeler, G., 2005. Methyl and total mercury in precipitation in the Great Lakes region. *Atmospheric Environment* 39, 7557–7569.
- Hammerschmidt, C.R., Fitzgerald, W.F., 2006. Photodecomposition of Methylmercury in an Arctic Alaskan Lake. *Environ. Sci. Technol.* 40, 1212–1216.
- Hammerschmidt, C.R., Lamborg, C.H., Fitzgerald, W.F., 2007. Aqueous phase methylation as a potential source of methylmercury in wet deposition. *Atmospheric Environment* 41, 1663–1668.
- Hans Wedepohl, K., 1995. The composition of the continental crust. *Geochimica et Cosmochimica Acta* 59, 1217–1232.

- Hawkins, L.N., Russell, L.M., 2010. Polysaccharides, Proteins, and Phytoplankton Fragments: Four Chemically Distinct Types of Marine Primary Organic Aerosol Classified by Single Particle Spectromicroscopy. *Advances in Meteorology* 2010, 1–14.
- Jacobi, H.W., Voisin, D., Jaffrezo, J.L., Cozic, J., Douglas, T.A., 2012. Chemical composition of the snowpack during the OASIS spring campaign 2009 at Barrow, Alaska. *Journal of Geophysical Research* 117.
- Kang, S., Quin, D., Mayewski, P., Gjessing, Y., 2001. Snow chemistry in Svalbard, Arctic. *Bulletin of Glaciological Research* 18, 9–13.
- Keith Bigg, E., Leck, C., Tranvik, L., 2004. Particulates of the surface microlayer of open water in the central Arctic Ocean in summer. *Marine Chemistry* 91, 131–141.
- Krnavek, L., Simpson, W.R., Carlson, D., Domine, F., Douglas, T.A., Sturm, M., 2011. The chemical composition of surface snow in the Arctic: Examining marine, terrestrial, and atmospheric influences. *Atmospheric Environment*.
- Larose, C., Dommergue, A., De Angelis, M., Cossa, D., Averty, B., Maruszczak, N., Soumis, N., Schneider, D., Ferrari, C., 2010. Springtime changes in snow chemistry lead to new insights into mercury methylation in the Arctic. *Geochimica et Cosmochimica Acta* 74, 6263–6275.
- Larose, C., Dommergue, A., Maruszczak, N., Coves, J., Ferrari, C.P., Schneider, D., 2011. Bioavailable Mercury Cycling in Polar Snowpacks. *Environmental science & technology*.
- Leck, C., 2002. Chemical composition and sources of the high Arctic aerosol relevant for cloud formation. *Journal of Geophysical Research* 107.
- Leck, C., 2005. Source and evolution of the marine aerosol—A new perspective. *Geophysical Research Letters* 32.
- Leu, E., Falk-Petersen, S., Kwaśniewski, S., Wulff, A., Edvardsen, K., Hessen, D.O., 2006. Fatty acid dynamics during the spring bloom in a High Arctic fjord: importance of abiotic factors versus community changes. *Canadian Journal of Fisheries and Aquatic Sciences* 63, 2760–2779.
- Loseto, L.L., Lean, D.R.S., Siciliano, S.D., 2004. Snowmelt Sources of Methylmercury to High Arctic Ecosystems. *Environ. Sci. Technol.* 38, 3004–3010.
- Nejbert, K., Krajewski, K.P., Dubinska, E., Pécskay, Z., 2011. Dolerites of Svalbard, north-west Barents Sea Shelf: age, tectonic setting and significance for geotectonic interpretation of the High-Arctic Large Igneous Province. *Polar Research* 30.
- Niki, H., Maker, P.S., Savage, C.M., Breitenbach, L.P., 1983. A Fourier-transform infrared study of the kinetics and mechanism of the reaction of atomic chlorine with dimethylmercury. *The Journal of Physical Chemistry* 87, 3722–3724.
- Oh, S., Kim, M.-K., Lee, Y.-M., Zoh, K.-D., 2011. Effect of Abiotic and Biotic Factors on the Photo-Induced Production of Dissolved Gaseous Mercury. *Water Air Soil Pollut* 220, 353–363.

- Pongratz, R., Heumann, K.G., 1998. Production of methylated mercury and lead by polar macroalgae — A significant natural source for atmospheric heavy metals in clean room compartments. *Chemosphere* 36, 1935–1946.
- Pongratz, R., Heumann, K.G., 1999. Production of methylated mercury, lead, and cadmium by marine bacteria as a significant natural source for atmospheric heavy metals in polar regions. *Chemosphere* 39, 89–102.
- Ribeiro Guevara, S., Queimaliños, C.P., Diéguez, M. del C., Arribére, M., 2008. Methylmercury production in the water column of an ultraoligotrophic lake of Northern Patagonia, Argentina. *Chemosphere* 72, 578–585.
- Rokkan Iversen, K., Seuthe, L., 2010. Seasonal microbial processes in a high-latitude fjord (Kongsfjorden, Svalbard): I. Heterotrophic bacteria, picoplankton and nanoflagellates. *Polar Biology* 34, 731–749.
- Rose, N.L., Munthe, J., McCartney, A., 2013. Winter peaks of methylmercury in deposition to a remote Scottish mountain lake. *Chemosphere* 90, 805–811.
- Rudnick, R.L., Holland, H.D., Turekian, K.K., 2004. *The crust*. Elsevier Pergamon, Amsterdam; Boston.
- Ruth, U., Barbante, C., Bigler, M., Delmonte, B., Fischer, H., Gabrielli, P., Gaspari, V., Kaufmann, P., Lambert, F., Maggi, V., Marino, F., Petit, J.-R., Udisti, R., Wagenbach, D., Wegner, A., Wolff, E.W., 2008. Proxies and Measurement Techniques for Mineral Dust in Antarctic Ice Cores. *Environmental Science & Technology* 42, 5675–5681.
- Scott, K.J., 2001. Bioavailable mercury in arctic snow determined by a light-emitting mer-lux bioreporter. *Arctic* 54, 92–95.
- Segawa, T., Miyamoto, K., Ushida, K., Agata, K., Okada, N., Kohshima, S., 2005. Seasonal Change in Bacterial Flora and Biomass in Mountain Snow from the Tateyama Mountains, Japan, Analyzed by 16S rRNA Gene Sequencing and Real-Time PCR. *Applied and Environmental Microbiology* 71, 123–130.
- Seuthe, L., Rokkan Iversen, K., Narcy, F., 2010. Microbial processes in a high-latitude fjord (Kongsfjorden, Svalbard): II. Ciliates and dinoflagellates. *Polar Biology* 34, 751–766.
- Siciliano, S.D., O’Driscoll, N.J., Tordon, R., Hill, J., Beauchamp, S., Lean, D.R.S., 2005. Abiotic Production of Methylmercury by Solar Radiation. *Environ. Sci. Technol.* 39, 1071–1077.
- St. Louis, V.L., Sharp, M.J., Steffen, A., May, A., Barker, J., Kirk, J.L., Kelly, D.J.A., Arnott, S.E., Keatley, B., Smol, J.P., 2005. Some Sources and Sinks of Monomethyl and Inorganic Mercury on Ellesmere Island in the Canadian High Arctic. *Environ. Sci. Technol.* 39, 2686–2701.
- Ström, J., Umegård, J., Tørseth, K., Tunved, P., Hansson, H.-C., Holmén, K., Wismann, V., Herber, A., König-Langlo, G., 2003. One year of particle size distribution and aerosol chemical

composition measurements at the Zeppelin Station, Svalbard, March 2000–March 2001. *Physics and Chemistry of the Earth, Parts A/B/C* 28, 1181–1190.

IV. Processes involving MMHg in snow and snowmeltwater

i. Evidences of Hg^{II} methylation by acetates

-

ii. Elution of methylmercury from a melting
snowpack

Résumé

La partie précédente a conclu à une contribution négligeable de la méthylation *in situ* dans le budget global de MMHg dans la neige de surface côtière. En complément de ces résultats, la partie qui suit présente en premier lieu une étude menée sur un manteau neigeux éloigné du fjord, représentant une accumulation d'un an proche du sommet du glacier Kongsvegen. Les concentrations en THg et MMHg diminuent avec l'âge de la couche de neige considérée, indiquant la dégradation de MMHg et Hg^{II} en Hg^0 et son évaporation du manteau neigeux avec le temps comme le mécanisme principal affectant la dynamique des espèces mercurielles. En utilisant la même méthodologie que précédemment (Robinson et al., 2006), nous mettons en évidence un mécanisme chimique impliquant MMHg, ammonium et acétates ainsi que le vieillissement du sel marin dissous dans la neige.

Les concentrations en acétate, ammonium et MMHg sont positivement corrélées sur toute l'épaisseur du manteau neigeux, sauf dans une couche (que nous excluons pour cause de contamination en acétates). De plus, nous observons deux anti-corrélations entre la proportion de mercure méthylé (MMHg/THg) et acétates ou ammonium. En outre, moins la couche de neige contient de THg et de MMHg (et d'acétates et d'ammonium), plus le rapport MMHg/THg est élevé. Enfin, plus le sel marin montre des signes de vieillissement atmosphérique (Cl/Na diminue), plus MMHg est enrichi (MMHg/Na très faible dans le sel de mer augmente fortement) dans les couches ayant subi le plus fort vieillissement atmosphérique, MMHg est enrichi entre 1000 et 10000 fois malgré de très faibles concentrations. Les corrélations présentées ci-avant sont fortes ($R^2 > 0,70$ et souvent $R^2 > 0,90$) et visibles dans toutes les couches d'un manteau neigeux qui s'est formé sur une période d'un an, ce qui renforce l'hypothèse d'un procédé chimique commun à toutes les couches.

Ainsi nous émettons l'hypothèse que si la dégradation des espèces mercurielles est le processus dominant dans ce manteau neigeux, une méthylation abiotique minoritaire y a lieu qui affecte le rapport MMHg/THg. Nous pensons que le mécanisme est le même que celui observé dans une étude de laboratoire précédente (Gårdfeldt et al., 2003), impliquant donc un transfert de méthyle d'une molécule d'acétate vers le mercure, après formation d'un complexe mercure – acétates (dont les conditions sont discutées). Cette réaction est dépendante de l'acidité de la neige (que nous montrons dépendre de la concentration en ammonium) et consomme toujours des acétates avec le temps.

Ayant établi notre théorie, nous discutons de l'importance et des implications de cette méthylation abiotique *in situ*. Dans notre cas, la méthylation a un impact très faible sur la concentration en

MMHg : celle-ci diminue jusqu'à des concentrations extrêmement basses (< 5 pg/L). Il est probable que dans des manteaux neigeux plus proches de sources directes ou plus prompts au métamorphisme (comme notre manteau neigeux côtier d'étude), les concentrations en espèces chimiques sont trop hautes et trop fluctuantes pour pouvoir identifier un quelconque processus de méthylation aussi faible que celui que nous observons. Il est donc possible d'affirmer qu'un tel processus de méthylation ne peut vraisemblablement pas être à l'origine d'une proportion importante de MMHg dans une quelconque neige arctique.

Cependant, la corrélation entre l'enrichissement en MMHg (MMHg/Na) et le vieillissement atmosphérique du sel marin contenu dans la neige (Cl/Na) dans toutes les couches observées ne ferme pas les portes à un processus atmosphérique. En effet, nul ne peut s'avancer à déterminer à quel stade du cycle de la neige (stockage, dépôt, formation ou même transport des aérosols servant à sa nucléation) la méthylation abiotique prend place. Il est tout à fait plausible que cette réaction prenne place dès que les conditions de formation de complexes mercure – acétates sont remplies, peut-être même avant la formation des cristaux de neige et leur dépôt. Il est aussi possible que cette réaction soit pour une quelconque raison cinétique accélérée dans les nuages ou lors de la nucléation des grains de neige. Nous émettons cette possibilité pour expliquer les très fortes concentrations en MMHg mesurées dans les précipitations, notamment très récemment dans la neige écossaise (Rose et al., 2013) et dans notre seul échantillon de neige fraîche.

Plus généralement, nous pensons que la méthylation abiotique du mercure par les acétates est désormais à considérer davantage dans les milieux environnementaux remplissant les conditions adéquates de formation de complexes mercure – acétates. Le mercure et les acétates étant deux espèces chimiques très largement présentes dans les écosystèmes, il est très probable que d'autres milieux soient réacteurs pour ces deux espèces. De plus, il est possible que certains de ces milieux favorisent même la méthylation abiotique dans des proportions où sa contribution à la quantité de MMHg ne serait plus négligeable, voire même prépondérante.

Dans un deuxième et dernier chapitre, nous étudierons l'élution du MMHg lors de la fonte du manteau neigeux. Les données suggèrent une élution tardive de MMHg comparée à l'élution des ions majeurs, que nous pensons due à la co-élution du MMHg et des particules organiques marines présentes dans la neige (identifiées en section III.iii). En effet nous retrouvons la signature chimique de ces particules dans l'eau de fonte, même si leur signature de taille n'y est pas visible (voir section III.ii).

i. Evidences of Hg^{II} methylation by acetates: a case study

We have previously identified the sources for MMHg in coastal surface snow, on a site located a few meters away from the open waters of the fjord. We collected snow that accumulated during one season in a pit dug near the summit of Kongsvegen glacier (78°77'N, 13°28'E) on April 18th. Eight layers were identified based on grain morphology and collected integrating the whole thickness of each layer. Samples were analyzed for major ions and Hg species (THg and MMHg). This site is located 27 kilometers away from the open fjord, at an altitude around 700 m and the topology is highway flat. The fact that we sampled early in the season avoided the early melting as well as the organic particle input observed in coastal snow, respectively in late April and between mid-May and early June. Although this sampling site is not totally remote from open sea-waters, it is remote enough to avoid strong marine interferences (important sea-sprays storms) and has a quite steady snowpack over time and space. It is therefore suitable to study the fate of snow, weeks and months after its deposition.

1. Preliminary discussion on the chemistry of the snow pit

The chemical composition of a given snow layer is driven by the initial composition of the precipitation, and post-depositional processes including chemical and microbial transformations as well as metamorphism. The influence of post-depositional processes on snow chemistry is logically expected to be greater with time. Moreover, chemical correlations could be observable along the whole profile, in snow layers of different initial composition, but ageing the same way. If the initial composition of snow is the main factor governing the chemical composition of each layer, any chemical correlation between two different layers would be purely coincidental. This is only true assuming that fresh snow never forms the same way, thus never traps the same chemicals at the same amounts and proportions. In a given snow pit, the composition of surface snow layers would be mainly ruled by initial composition, while the composition of deeper (thus older) snow would show increasing evidences of internal processes (if any).

For these reasons, ratio/ratio plots (as presented in previous section III.ii) are once again useful, as they allow identifying non-obvious chemical correlations. For instance, Figure 1 shows the molar ratio/ratio plots of $[\text{MMHg}]/[\text{Na}]$ with respect to $[\text{Cl}]/[\text{Na}]$ and $[\text{MMHg}]/[\text{Ca}]$ with respect to $[\text{NH}_4^+]/[\text{Ca}]$ for all the layers of the snow pit. Considering the samples with $[\text{Cl}]/[\text{Na}]$ close to the sea-salt value ($[\text{Cl}]/[\text{Na}] \approx 1.17$), the $[\text{MMHg}]/[\text{Ca}]$ ratio is very low, in the same range than the one previously estimated in sea-sprays ($5 \cdot 10^{-9}$, see section III.ii). The $[\text{Cl}]/[\text{Na}]$ ratio is expected to diminish in sea-salt aerosols with Cl displacement by atmospheric chemicals, such as sulfates (Legrand and Delmas, 1988; Toom-Sauntry and Barrie, 2002). Hence $[\text{Cl}]/[\text{Na}]$ can be a proxy of the quantitative impact of atmospheric chemistry on the snow: the lower $[\text{Cl}]/[\text{Na}]$ in snow, the greater the atmospheric ageing. Results from Figure 1 could mean that MMHg enrichment in snow

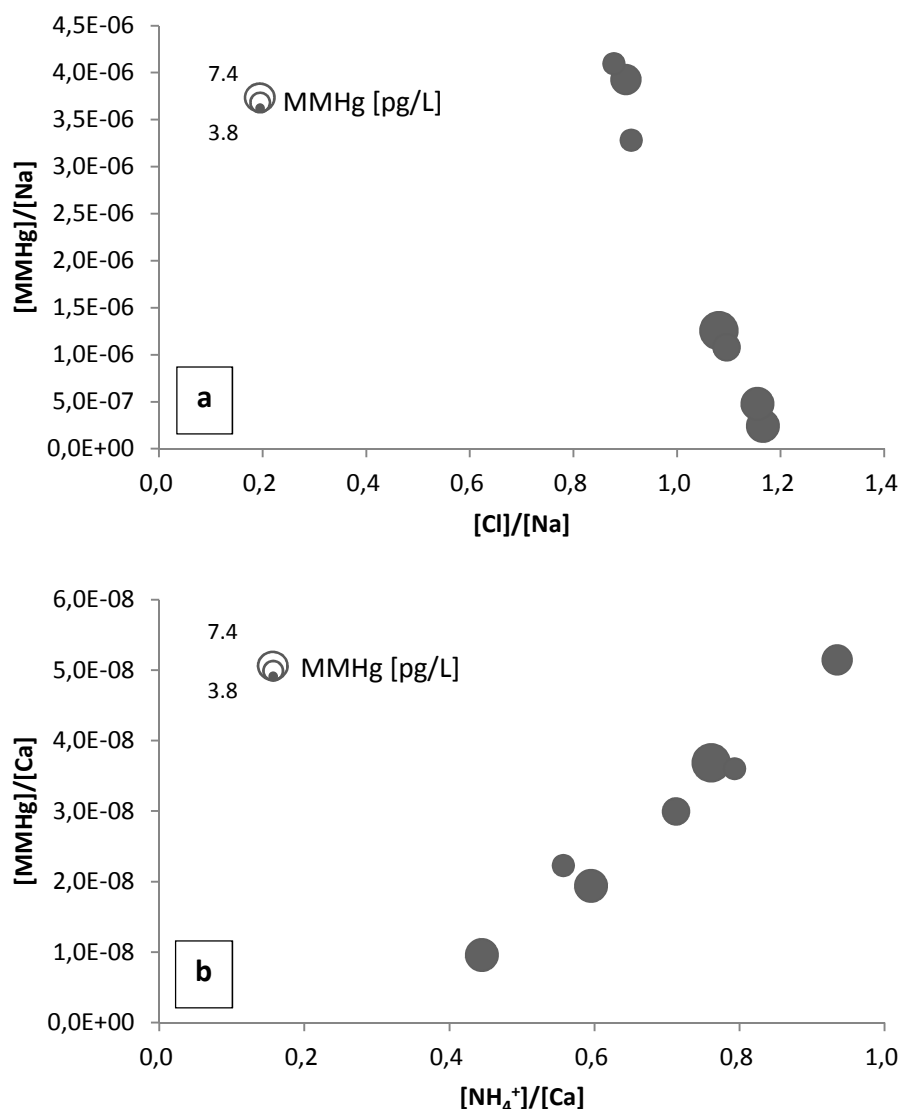


Figure 1. Correlation plot of $[\text{MMHg}]/[\text{Na}]$ with respect to $[\text{Cl}]/[\text{Na}]$ (a) and $[\text{MMHg}]/[\text{Ca}]$ with respect to $[\text{NH}_4^+]/[\text{Ca}]$ in the Kongsvegen pit. The size of the disks represents the MMHg concentration.

([MMHg]/[Na] ratio, assuming Na cannot be observably removed from the snowpack) is positively correlated with atmospheric ageing. The ratio correlations presented here imply different snow layers from a whole year accumulation snowpack, hence snow formed in very various atmospheric conditions. Illustrating what we emphasized in the previous paragraph, chemical correlations between all the different snow layers of a one-year accumulation pit are rather due to processes than to an original uniformity of all the samples, which is clearly unlikely. A further evidence of the implication of processes is that the [MMHg], $[\text{NH}_4^+]$, [Ca], [Cl] or [Na] concentrations are not directly correlated – except [Cl] and [Na], both coming from sea-salt – while their enrichment $[\text{X}]/[\text{Na}]$ are. This means that the snow layers are originally chemically different from each other (as the concentrations do not correlate) and that something else should explain the ratio correlations: 1) chemical processes; or 2) analytical artifacts. Concerning the latter, snow for MMHg determination was sampled in a different bottle than snow for ion chromatography, and MMHg determination by GC-ICP-MS prevents from interferences with non-metallic species. It is therefore very unlikely to explain correlations between MMHg and other species by analytical artifacts. Considering ionic chromatography, the method used is well known and is set up so that analytical interferences between the different ionic species are negligible and controlled. Thus the existence of the ratio correlations presented in Figure 1 testifies the existence of a given process involving MMHg, NH_4^+ and Cl which is the same in all the snow layers of the pit. It is possible to further assess that this process is either quite fast and/or takes place even before deposition, as even the “youngest” snow layers are concerned. In addition, there is no link between the concentration [X] and the enrichment $[\text{X}]/[\text{tracer}]$, suggesting that the quantitative impact of this process is very modest, hence invoking rather a slow process.

2. Mercury dynamics in the snow pit

The snow pit was 2.1 m deep and consisted of 8 different layers. The deepest layer was a 27 cm thick melt-refreeze layer from the last summer that showed high chemical concentrations (up to 3 orders of magnitude higher than the values in overlaying layers). This layer represents the melting of the snow accumulated during and before the summer of 2010, and was therefore discarded. The profiles of MMHg and THg are presented in Figure 2. Both profiles are characterized by their overall shape: a rapidly increasing concentration with depth in the first layers. After a maximum is reached, the concentrations decrease with depth. The major difference between MMHg and THg profiles is that the maximum is reached next to the surface for MMHg, while maximum THg is reached deeper than 20 cm.

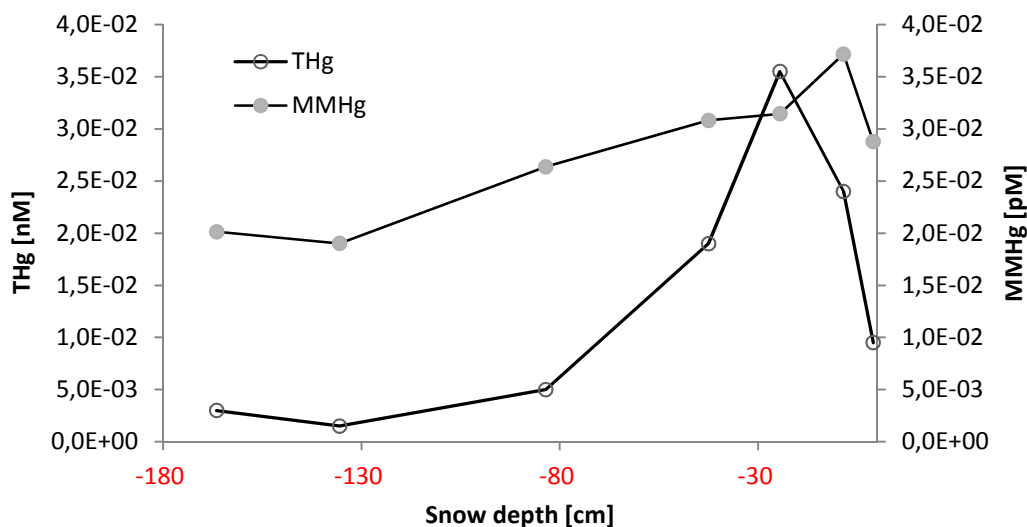


Figure 2. Depth profiles of THg and MMHg in the annual snowpack of the Kongsvegen glacier.

This depth profile can be divided in two distinct parts: 1) surface layers (3 upper layers), where THg and MMHg concentration do not vary the same way; 2) deeper layers, where THg and MMHg concentrations vary following the same trends. We suggest that the parallel decrease of MMHg and THg in deep layers is rather due to post-depositional processes. The commonly accepted mechanism for Hg^{II} degradation is photo-reduction by light, UV light being the most efficient. Light penetration is commonly described by the e-folding depth (depth over which the actinic flux is divided by e), which is in the order of 10-20 cm in snow (Simpson et al., 2002; Domine et al., 2008). Applied to our snow pit, this would mean that less than 0.005% of the actinic flux reaches depth down to 2 m. This percentage could be underestimated, as higher e-folding depth have been reported (Warren et al., 2006), and e-folding depth increases below 1 m depth in snow (Warren et al., 2006; Domine et al., 2008). The small amount of light radiations could reduce Hg^{II} , even at a much lower speed, but it is also possible that degradation of Hg species still occurs in dark areas of the snowpack, by non-photo-induced reduction. Recently, some small organics were shown to allow very slow Hg reduction in the dark (Figure 1A in He et al., 2012). As snow is porous, volatilized Hg^0 can evade to overlaying snow layers and finally be reemitted back to the atmosphere. This would explain the decrease of both MMHg and THg.

Condensations as well as re-oxidation processes (as described in Maron et al., 2008; Castro et al., 2009) and possible methylation processes can partially offset Hg^0 evasion. As a consequence, the concentration of Hg species in a given snow layer (below surface layers) could be depicted as the net yield of 1) degradation in this layer (as a removal process) and 2) re-condensation, re-oxidation and possibly methylation of Hg species degraded in the same layer and in deeper ones (as input processes). The yields and kinetic of such processes, as well as the speed of Hg^0 evasion are likely

influenced by numerous chemical and physical properties of the snow. For instance, surface specific area (SSA) is relevant when considering interfacial exchanges and reactions in snow, and could hence affect condensations and oxidations at the snow-air interface. Another example would be the porosity, which could affect Hg⁰ evasion. We measured density for every snow layer, but there is no sufficient knowledge of Hg dynamics in snowpack to discuss it.

3. Discussion on the acidity of snow

The pH of snow is usually measured after melting in open atmosphere by a regular pH-meter. However, as the snow melts, CO₂ solvation or evasion can occur to equilibrate the sample with the ambient air. The resulting variation of dissolved CO₂ (H₂CO₃) has an impact on the pH of the sample, as it equilibrates in solution with HCO₃⁻ (one deprotonation) and/or CO₃²⁻ (two deprotonations). Furthermore, all the samples did not melt at the same speed, the effects of the CO₂ equilibration with the ambient air are therefore suspected to vary from a sample to the next (as all the samples were not exposed to the ambient air for the same duration). In consequences, the pH measured in the melted sample can be only loosely related to the one in the original snow sample. In addition, the sample-to-sample heterogeneity of the equilibration effects – which is more problematic – prevents anyone to make inter-sample comparison. However, the acidity is a crucial chemical parameter, so we identify in the following pNH₄⁺ as a more accurate proxy for acidity than pH.

In order to assess the acidity of snow, we considered the Cl/Na ratio of our samples. Indeed, Cl in snow can be replaced by the conjugate base of stronger acids than HCl (HNO₃ or H₂SO₄). These acids are all present in the atmosphere and their reaction with sea-salt is known to lower the Cl/Na ratio in the aerosol as well as increasing their acidity (Legrand and Delmas, 1988; Toom-Saunty and Barrie, 2002). However, Cl/Na is not a concentration and can therefore only be related to other X/Na ratios and not to concentrations (which would take the dilution by snow into account).

We first attempted to use the displaced HCl (= HCl replaced by HNO₃ or H₂SO₄) as a proxy for acidity, as the displaced HCl is proportional to the atmospheric input to the aerosol. The displaced HCl is the Cl amount missing in the sample to reach the sea-salt ratio (1.18), and is calculated as follows:

$$[\text{Cl}]_d = (1.18 - [\text{Cl}]/[\text{Na}]) \times [\text{Na}]$$

However, we do not observe any correlation between $[\text{Cl}]_d$ and $[\text{SO}_4^{2-}]$, $[\text{NO}_3^-]$ or the pH, suggesting that $[\text{Cl}]_d$ is not a good proxy for acidity in our samples. This is certainly because small uncertainties in Cl/Na ratios induce large $[\text{Cl}]_d$ uncertainties for important Na concentrations (Figure 3).

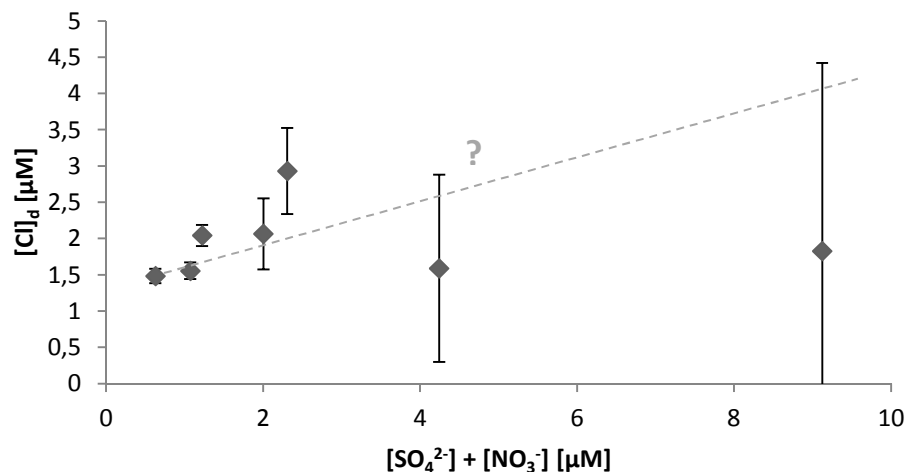


Figure 3. Correlation plot of $[\text{Cl}]_d$ versus $[\text{SO}_4^{2-}] + [\text{NO}_3^-]$. The uncertainty bars are calculated for a 0.01 uncertainty on both the sea-salt and the sample $[\text{Cl}]/[\text{Na}]$ ratio.

Our second approach was to investigate the correlations between Cl/Na and other X/Na ratios. We found that Cl/Na and NH_4^+/Na are negatively correlated ($\text{NH}_4^+/\text{Na} = -0.26[\text{Cl}/\text{Na}] + 0.32$, $r^2 = 0.94$, $n = 7$), suggesting a NH_4^+ enrichment during atmospheric acidification. In addition, $[\text{NH}_4^+]$ is strongly correlated with $[\text{SO}_4^{2-}] + [\text{NO}_3^-]$ (Figure 4a), the conjugate bases of atmospheric acids. This suggests that the acidification of aerosols causes an increase of the NH_4^+ concentration (probably by partial neutralization with gaseous NH_3), establishing a link between aerosol acidity and NH_4^+ concentration. Furthermore, by comparing pNH_4^+ and pH we obtain a cloudy positive correlation (Figure 4b), probably because of the clouding effect of CO_2 solvation on the pH of melted samples. Based on these observations, we consider in the following NH_4^+ as a proxy for the acidity in our samples.

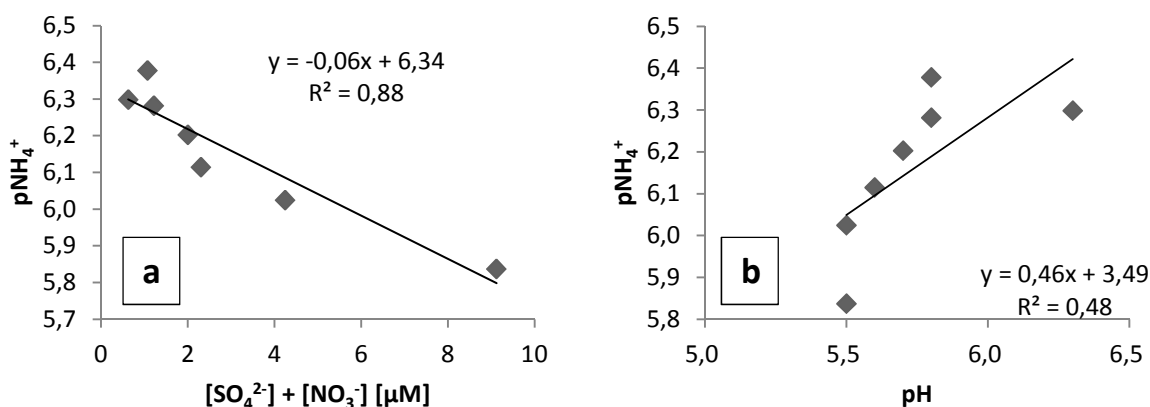


Figure 4. Correlation plot of pNH_4^+ with respect to $[\text{SO}_4^{2-}] + [\text{NO}_3^-]$ (a) and with respect to pH (b).

4. Evidences of *in situ* methylation

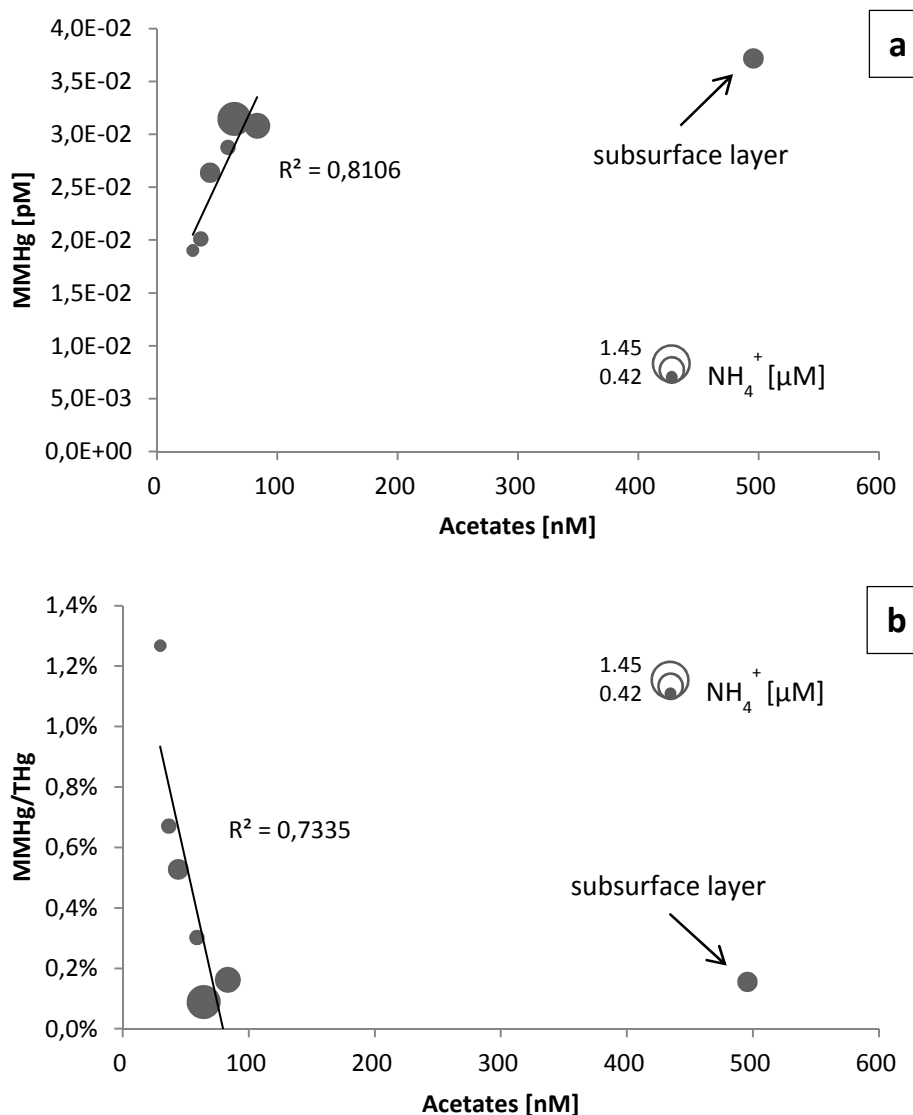


Figure 5. Correlations of acetates with respect to MMHg (a) and MMHg/THg (b). The dot size indicates the snow acidity (as ammonium concentration).

Figure 5 show a positive correlation between acetates and MMHg and a negative correlation between acetates and the MMHg/THg ratio in all snow layers, except the subsurface one. Both MMHg and THg in the snowpack can be reduced to Hg^0 which can be subsequently involved in a cycle of oxidations and reductions, Hg^{II} having the potential to be methylated in snow. Divalent Hg and acetates have been proven to form poly-acetate mercuric complexes $[\text{Hg}(\text{OAc})_n]^{2-n}$, which are required precursors to the reaction forming MMHg and CO_2 which is known to happen in synthetic aqueous media, even in the dark (Gårdfeldt et al., 2003). In our snowpack, reduction would be the major reaction taking place, lowering both THg and MMHg concentrations, but a small amount of

methylation could artificially compensate to some extent the net MMHg reduction rate with respect to THg. The link we outlined above between NH_4^+ and acidity suggests that the methylation process depends on the acidity of snow. It is consistent with the results from Gårdfeldt et al. who identified the pH-dependent formation $[\text{Hg}(\text{OAc})_n]^{2-n}$ as the critical step toward Hg^{II} methylation. As a result, in the deep layers of the snowpack both MMHg and THg concentrations decrease while MMHg/THg ratio increases with decreasing acidity of the snow layer. The less acidic the snow layer (or the less NH_4^+ it contains), the more efficient the methylation, as shown on Figure 6.

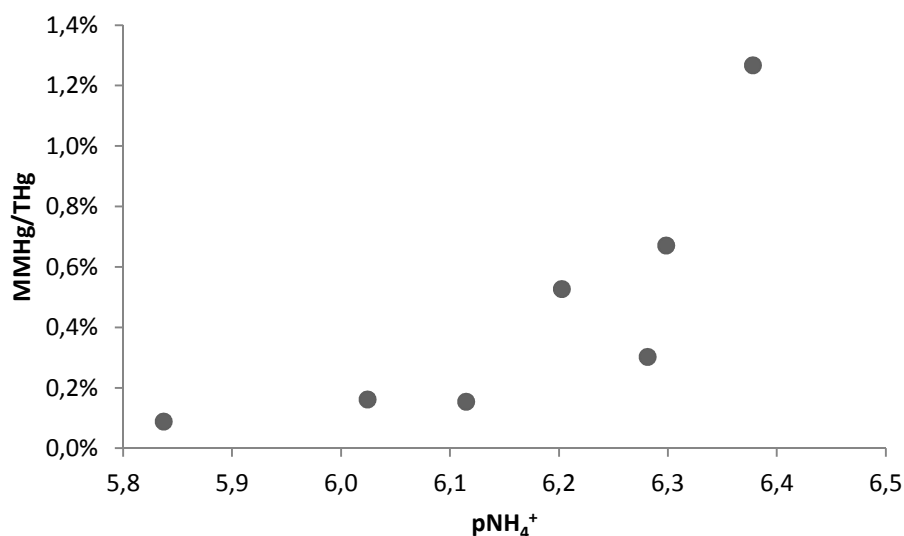


Figure 6. Relationship between pNH_4^+ and MMHg/THg.

This hypothesis is consistent with the correlations presented in Figure 5. On one hand, the more efficient re-methylation (depending on acidity), the higher MMHg/THg. On the other hand, the older (or deeper) snow, the lower THg and MMHg (due to degradation over time). Acetate concentration decreases with time (and with increasing MMHg/THg) as it is consumed by re-methylation (Figure 5b). The supposed mechanism is schematized in Figure 7.

The effect of snow acidity is primordial considering the mechanism in Figure 7. As mentioned above, the critical step is likely to be the formation of the $[\text{Hg}(\text{OAc})_n]^{2-n}$ complexes, particularly $[\text{Hg}(\text{OAc})_3]^-$ which is suspected to be the precursor of MMHg. For a given ligand L^- , the formation of $[\text{HgL}_n]^{2-n}$ complexes is thermodynamically favored if a) the acidity allows L^- to be the main form of the LH/L^- couple; b) $[\text{L}^-] \gg [\text{Hg}^{\text{II}}]$; c) the stability constant of $[\text{HgL}_n]^{2-n}$ is high; d) the number of competitive ligands is low. If conditions a) and b) are achieved in our snow samples for acetates ($\text{pK}_a \text{AcOH}/\text{AcO}^- = 4.75$; $[\text{AcO}^-] \gg 10000[\text{THg}]$), a lot of competitive ligands exist in snow. The DOC content of the snow pit in surface and depth snow ($n = 2$) is described in Table 1, highlighting that a large part of the DOC

is unknown. This unknown organic fraction contains chemical binding sites of high affinity for Hg^{II} (thiols, thioacids, carboxylic acids, alcohols, amines...etc).

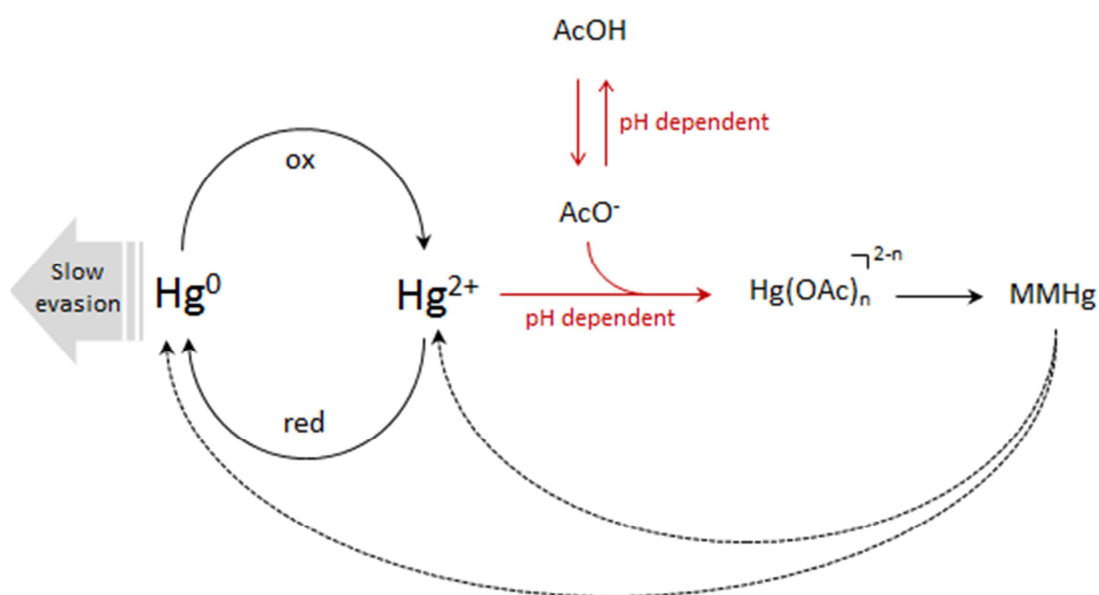


Figure 7. Qualitative mechanism of Hg dynamics in the snowpack, as hypothesized from our data.

Table 1. Overview of the DOC content and constitution (in weight percent) of snow from the Kongsvegen pit.

	Subsurface snow (n = 1)	Depth snow (n = 1)
DOC [ppb]	501,2	425,5
Acetates	5,8%	0,6%
Formates	0,4%	0,7%
Oxalates	0,7%	0,6%
Lactate	0,4%	0,2%
Propionate	0,7%	0,3%
Glutarates	-	-
Succinates	-	-
Identified DOC	8,0%	2,4%

Acetate has a low affinity for Hg^{II} compared to several usual organic molecules (Ravichandran, 2004; Dong et al., 2010, 2011), hence if the formation of [Hg(OAc)_n]²⁻ⁿ complexes is readily observed in synthetic aqueous media, it is less obvious in snow where lots of ligands with a high affinity for Hg^{II}

are present, among which some are probably better than acetates. Thus the optimal pH range for mercuric acetate complexes formation is likely very narrow compared to the one observed in Gårdfeldt et al., and even in this range $[\text{Hg}(\text{OAc})_n]^{2-n}$ complexes could be in minority among other Hg^{II} complexes. However, even in minority, such complexes would lead to the formation of MMHg. The rate of MMHg production would depend on the proportion of Hg^{II} bound as $[\text{Hg}(\text{OAc})_n]^{2-n}$, namely $R = [\text{Hg}(\text{OAc})_n]^{2-n}/\text{Hg}^{\text{II}}$. A qualitative trend of R with acidity is depicted in Figure 8.

A recent study identified $[\text{Hg}(\text{OAc})_n]^{2-n}$ complexes as a very minor part of Hg^{II} complexes in rain waters (Bittrich, 2011), thus assuming that MMHg in these waters is probably not due to Hg methylation via $[\text{Hg}(\text{OAc})_n]^{2-n}$ complexes. Contrastingly, another recent study assessed dissolved organic matter as the main ligand for Hg^{2+} and MMHg (Dong et al., 2010). Matching this theory, Hammerschmidt et al. (2007) proposed Hg^{II} methylation in rain waters as a MMHg source, based on equilibrium calculation. The yield of a chemical reaction does not depend on the formation rate of the reactive species (here $[\text{Hg}(\text{OAc})_n]^{2-n}$, R in Figure 8), but on its reactivity. This is the key concept of catalysis, where tiny amounts of catalytic species allow rapid and total reactions (note: this is an example, the reaction of Hg with acetates is not catalytic). Consequently, even if the active $[\text{Hg}(\text{OAc})_n]^{2-n}$ complexes are in extreme minority, it does not imply that MMHg formation from these complexes is negligible. Nevertheless, the formation rate of the $[\text{Hg}(\text{OAc})_n]^{2-n}$ is expected to affect the speed of the reaction.

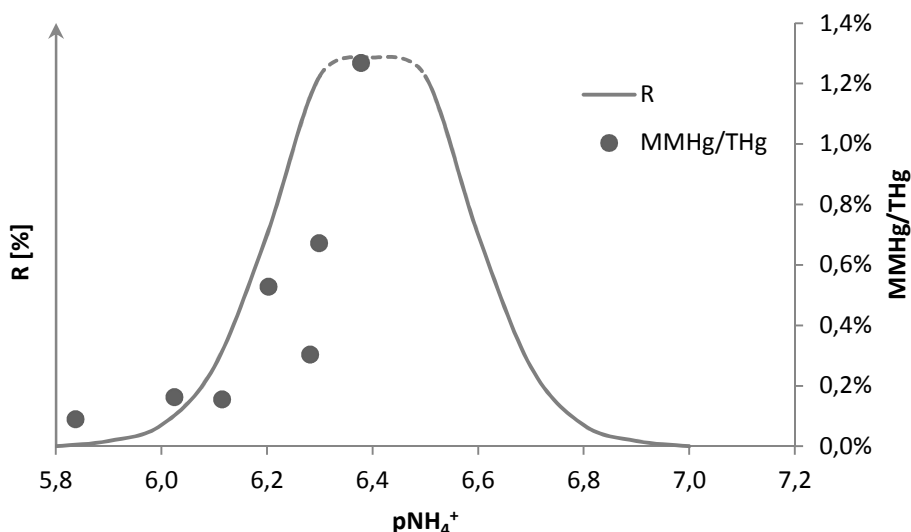


Figure 8. Qualitative relationship between the proportion of $[\text{Hg}(\text{OAc})_n]^{2-n}$ ($R = [\text{Hg}(\text{OAc})_n]^{2-n}/\text{Hg}^{\text{II}}$) and pNH_4^+ , compared with MMHg/THg (data from Figure 6).

As shown in the present chapter, methylation has a visible impact only on the very diluted (MMHg < 10 pg/L) and stable snow (overtime) from the Kongsvegen glacier, which does not undergo strong additional inputs and melts as snow from the coastal site. The small changes in MMHg/Ca induced by methylation are undetectable in our coastal snow, which experiences various inputs and meltings during the season, as highlighted in section II.ii. If changes in MMHg/Ca are significant and cannot be attributed to source fractionation, one could propose methylation processes such as the one described in Figure 7 to explain it. Such mechanism could contribute to the high concentrations previously observed in rain (Hall et al., 2005; Hammerschmidt et al., 2007), fresh snow (Rose et al., 2013) as well as the high MMHg/Ca enrichment observed in our fresh snow sample.

Interestingly, the correlations on which we base our reasoning are observable in each snow layer from the Kongsvegen pit including surface, suggesting that the process of methylation in snow initially starts either rapidly after deposition or even prior to its deposition. Indeed, the process considered in Figure 7 could take place in clouds first. Thus, despite methylation only has a minor effect on the post-depositional fate of MMHg in our snowpack, it could be a good candidate to explain both high amounts of MMHg and high MMHg/Ca enrichment in fresh snow. At the current state of knowledge of the MMHg cycle, this remains hypothetical and further investigation on the chemical composition of fresh snow or clouds are needed to assess the impact of methylation on the MMHg content of fresh snow.

5. Concluding remarks

The present chapter highlights the existence of an abiotic methylation pathway for Hg^{II} by acetates. This is the first time that an abiotic mechanism is observed in environmental samples, as well as the first evidences of an environmental Hg^{II} methylation mechanism in oxic conditions. As described in Gårdfeldt et al. this reaction involves the formation of mercuric acetates $[\text{Hg}(\text{OAc})_n]^{2-n}$ complexes, and is thus pH dependent. In addition, as soon as the $[\text{Hg}(\text{OAc})_n]^{2-n}$ complexes can be formed, even in low proportions, significant amounts of MMHg could be formed. These results imply that such mechanism can occur in numerous environmental media, as soon as chemical conditions are gathered to allow the formation of $[\text{Hg}(\text{OAc})_n]^{2-n}$ complexes, especially mild acidity. The chemistry of Hg and its particular deposition-reemission cycle allow its presence in all types of environmental media of the hydro-, cryo-, geo- and biospheres (Pirrone et al., 2010; Sprovieri et al., 2010; Mason et al., 2012). Natural and anthropogenic sources of acetates have been proposed but their nature and their respective importance are not established. Globally, acetates (or acetic acid) are the products of

the degradation of heavier organic molecules, such as sugars (fermentation)(Drake et al., 2006) or volatile organic molecules (volatile organic carbons, or VOCs) present in the atmosphere (Keene and Galloway, 1986; Seinfeld and Pandis, 1998). Mainly because acetic acid is present in the atmosphere and deposited in precipitations all over the globe, it is an omnipresent chemical species in the environment, such as Hg. It is therefore crucial to know that the abiotic Hg^{II} methylation by acetates is environmentally relevant, as suggested before (Gårdfeldt et al., 2003; Hammerschmidt et al., 2007) and as evidenced here. Indeed, among all the environmental matrices, a lot would be expected 1) to contain both Hg and acetates; and 2) to allow their complexation to $[\text{Hg}(\text{OAc})_n]^{2-n}$, hence the following reaction yielding MMHg. Here we emphasize that although this reaction is only responsible for ultra-trace amounts of MMHg in the present case of the Kongsvegen glacier, it could be a much greater contribution to the MMHg budget in other media where high amounts of MMHg remain unexplained, for example in precipitations.

References

- Bittrich, D.R., 2011. Speciation of Mercury (II) and Methylmercury in Cloud and Fog Water. *Aerosol and Air Quality Research*.
- Castro, L., Dommergue, A., Ferrari, C., Maron, L., 2009. A DFT study of the reactions of O₃ with Hg⁰ or Br⁻. *Atmospheric Environment* 43, 5708–5711.
- Domine, F., Albert, M., Huthwelker, T., Jacobi, H.-W., Kokhanovsky, A.A., Lehning, M., Picard, G., Simpson, W.R., 2008. Snow physics as relevant to snow photochemistry. *Atmospheric Chemistry and Physics* 8, 171–208.
- Dong, W., Bian, Y., Liang, L., Gu, B., 2011. Binding Constants of Mercury and Dissolved Organic Matter Determined by a Modified Ion Exchange Technique. *Environmental Science & Technology*.
- Dong, W., Liang, L., Brooks, S., Southworth, G., Gu, B., 2010. Roles of dissolved organic matter in the speciation of mercury and methylmercury in a contaminated ecosystem in Oak Ridge, Tennessee. *Environmental Chemistry* 7, 94.
- Drake, H.L., Küsel, K., Matthies, C., 2006. Acetogenic Prokaryotes. In: Dworkin, M., Falkow, S., Rosenberg, E., Schleifer, K.-H., Stackebrandt, E. (Eds.), *The Prokaryotes*. Springer New York, New York, NY, pp. 354–420.
- Gårdfeldt, K., Munthe, J., Strömberg, D., Lindqvist, O., 2003. A kinetic study on the abiotic methylation of divalent mercury in the aqueous phase. *The Science of the Total Environment* 304, 127–136.
- Hall, B., Manolopoulos, H., Hurley, J., Schauer, J., StLouis, V., Kenski, D., Graydon, J., Babiarz, C., Cleckner, L., Keeler, G., 2005. Methyl and total mercury in precipitation in the Great Lakes region. *Atmospheric Environment* 39, 7557–7569.
- Hammerschmidt, C.R., Lamborg, C.H., Fitzgerald, W.F., 2007. Aqueous phase methylation as a potential source of methylmercury in wet deposition. *Atmospheric Environment* 41, 1663–1668.
- He, F., Zheng, W., Liang, L., Gu, B., 2012. Mercury photolytic transformation affected by low-molecular-weight natural organics in water. *Science of The Total Environment*.
- Keene, W.C., Galloway, J.N., 1986. Considerations regarding sources for formic and acetic acids in the troposphere. *Journal of Geophysical Research* 91, 14466.
- Legrand, M., Delmas, R., 1988. Formation of HCl in the Antarctic atmosphere. *Journal of Geophysical Research-Atmospheres* 93, 7153–7168.
- Maron, L., Dommergue, A., Ferrari, C., Delacour-Larose, M., Faïn, X., 2008. How Elementary Mercury Reacts in the Presence of Halogen Radicals and/or Halogen Anions: A DFT Investigation. *Chemistry - A European Journal* 14, 8322–8329.

- Mason, R.P., Choi, A.L., Fitzgerald, W.F., Hammerschmidt, C.R., Lamborg, C.H., Soerensen, A.L., Sunderland, E.M., 2012. Mercury biogeochemical cycling in the ocean and policy implications. *Environmental Research*.
- Pirrone, N., Cinnirella, S., Feng, X., Finkelman, R.B., Friedli, H.R., Leaner, J., Mason, R., Mukherjee, A.B., Stracher, G.B., Streets, D.G., Telmer, K., 2010. Global mercury emissions to the atmosphere from anthropogenic and natural sources. *Atmospheric Chemistry and Physics* 10, 5951–5964.
- Ravichandran, M., 2004. Interactions between mercury and dissolved organic matter—a review. *Chemosphere* 55, 319–331.
- Rose, N.L., Munthe, J., McCartney, A., 2013. Winter peaks of methylmercury in deposition to a remote Scottish mountain lake. *Chemosphere* 90, 805–811.
- Seinfeld, J.H., Pandis, S.N., 1998. *Atmospheric chemistry and physics: from air pollution to climate change*. Wiley, New York.
- Simpson, W.R., King, M.D., Beine, H.J., Honrath, R.E., Zhou, X., 2002. Radiation-transfer modeling of snow-pack photochemical processes during ALERT 2000. *Atmospheric Environment* 36, 2663–2670.
- Sprovieri, F., Pirrone, N., Ebinghaus, R., Kock, H., Dommergue, A., 2010. A review of worldwide atmospheric mercury measurements. *Atmospheric Chemistry and Physics* 10, 8245–8265.
- Toom-Sauntry, D., Barrie, L.A., 2002. Chemical composition of snowfall in the high Arctic: 1990-1994. *Atmospheric environment* 36, 2683–2693.
- Warren, S.G., Brandt, R.E., Grenfell, T.C., 2006. Visible and near-ultraviolet absorption spectrum of ice from transmission of solar radiation into snow. *Applied Optics* 45, 5320.

ii. Elution of methylmercury from a melting snowpack

The snowmelt is a critical step toward MMHg entering the Arctic aquatic food chain, as it could deliver all the MMHg contained in snow to meltwater streams flowing directly to the fjord. It is therefore critical to follow the fate of MMHg simultaneously in snow and meltwater, in order to understand how it is delivered and how snowmelt affects its dynamics. A recent study from our team (field campaign in 2008) reported increasing concentrations of MMHg in melt water while decreasing in the snowpack (Larose et al., 2010). During our field campaign, a strong early melting occurred at the end of April before the final snowmelt in late May. We were not able to sample snowmelt water during the first melting event, but we sampled snowmelt water from a thicker snowpack (800 m away from the shore) during the late May snowmelt, using the equipment described in section II.ii (see reminder Figure 1).

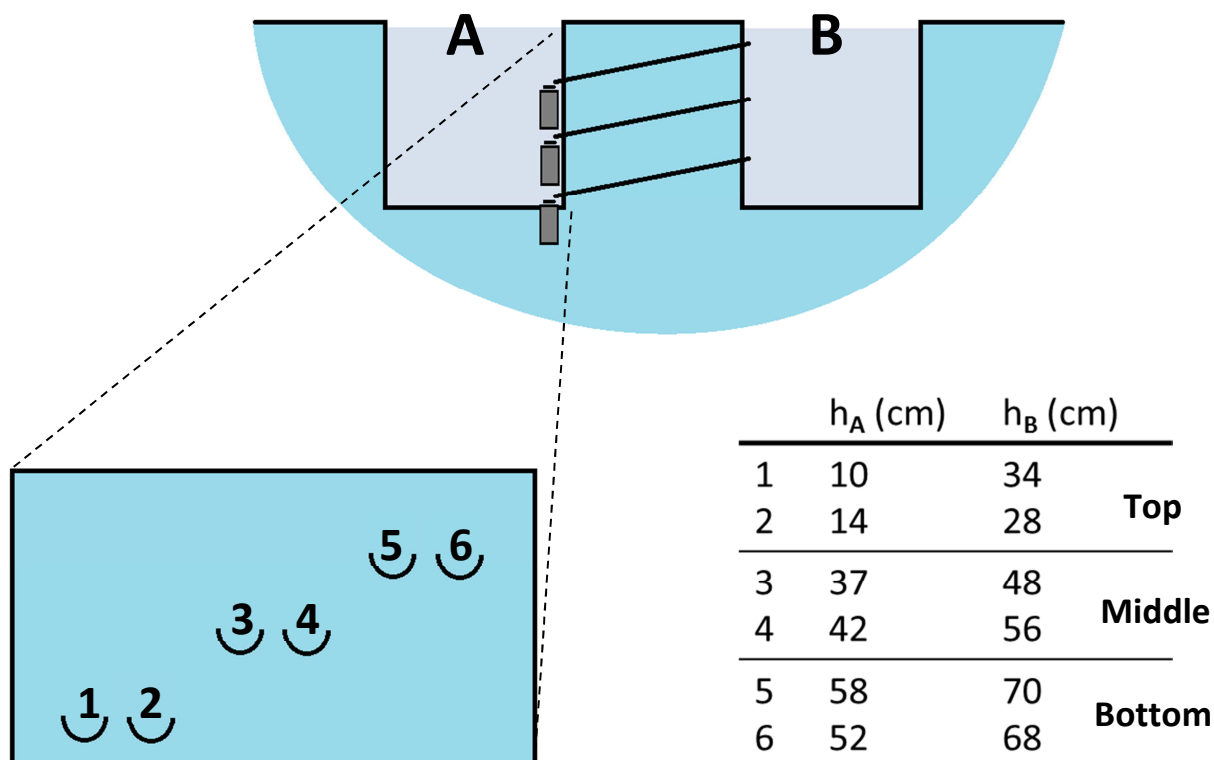


Figure 1. Scheme of the meltwater sampling system. The bottles are coated with aluminum sheet on their external side.

The elution profile of THg is presented in Figure 2a. Data suggest that the THg elution peak occurred earlier in the season (more about the snowmelt elution in the “Introduction” part), as we observe what seems to be a peak tail between the 25th and the 28th of May. All the major ions show the same “end-of-elution” profile (see Appendix). Data for MMHg is available from the 28th of May and do not allow the observation of the tail of an elution peak, if any (Figure 2b). However, MMHg concentration increases substantially in percolating water from the top and the middle of the snowpack from the last days of May, with a small delay (from the 29th for “top” samples, from the 2nd of June for “middle” samples). This MMHg concentration increase is not reflected in the “bottom” meltwater samples, where the MMHg concentration slightly decreases from 57.9 to 27.8 pg/L between the 28th of May and the 8th of June.

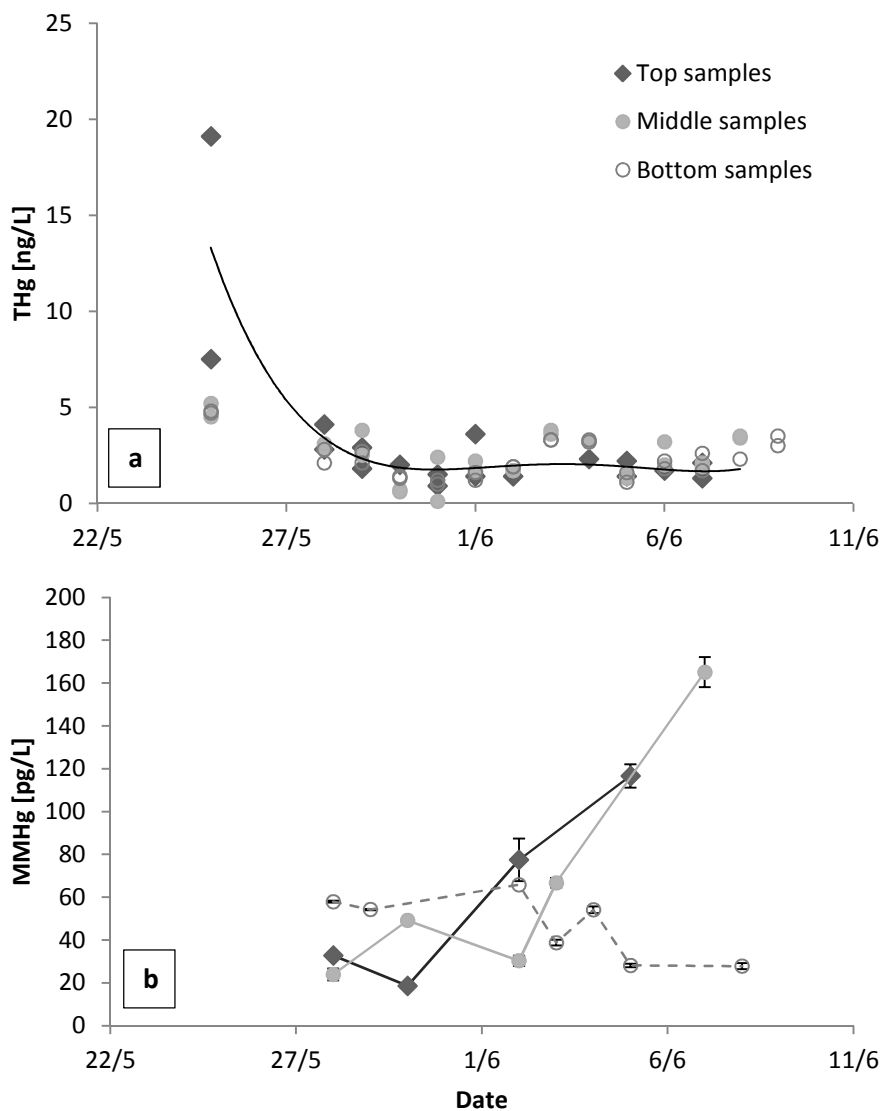


Figure 2. Elution profiles of THg (a) and MMHg (b) at different depth.

This increase of MMHg concentration delayed with depth suggests a slow elution process, although further meltwater collection would have been needed to confirm the existence of this MMHg elution peak as well as the percolation of MMHg-rich water to the bottom snow layer. Figure 3a presents the relationship between the MMHg concentration and the mean particle mass (in ng/unit) in snowmelt water. Interestingly, both seem to be positively correlated in “top” and “middle” samples (full circles in Figure 3a), the ones experiencing the MMHg elution. No correlation is observed in “bottom” samples, where no MMHg elution peak is observed (Figure 2b). The same observations are true for MMHg/Ca with respect to the mean particle mass, suggesting that the bigger the particles, the higher the MMHg enrichment (Figure 3b). Hence we suggest that MMHg in snow is bound to large particles, thus later eluted by percolating water than soluble species (major sea-salt ions) because particle coagulation and snow densification render the melting snowpack an efficient filter trapping the particles (Meyer et al., 2009). A minor soluble fraction of MMHg is probably eluted with other soluble species, which would explain the MMHg concentration in the “bottom” samples; however, MMHg data prior to the 28th of May would have been needed to verify this assessment. The MMHg concentrations measured in the “bottom” samples are between 57.9 and 27.8 pg/L and not negligible as the snow meltwater is enriched when percolating down through a thick snowlayer.

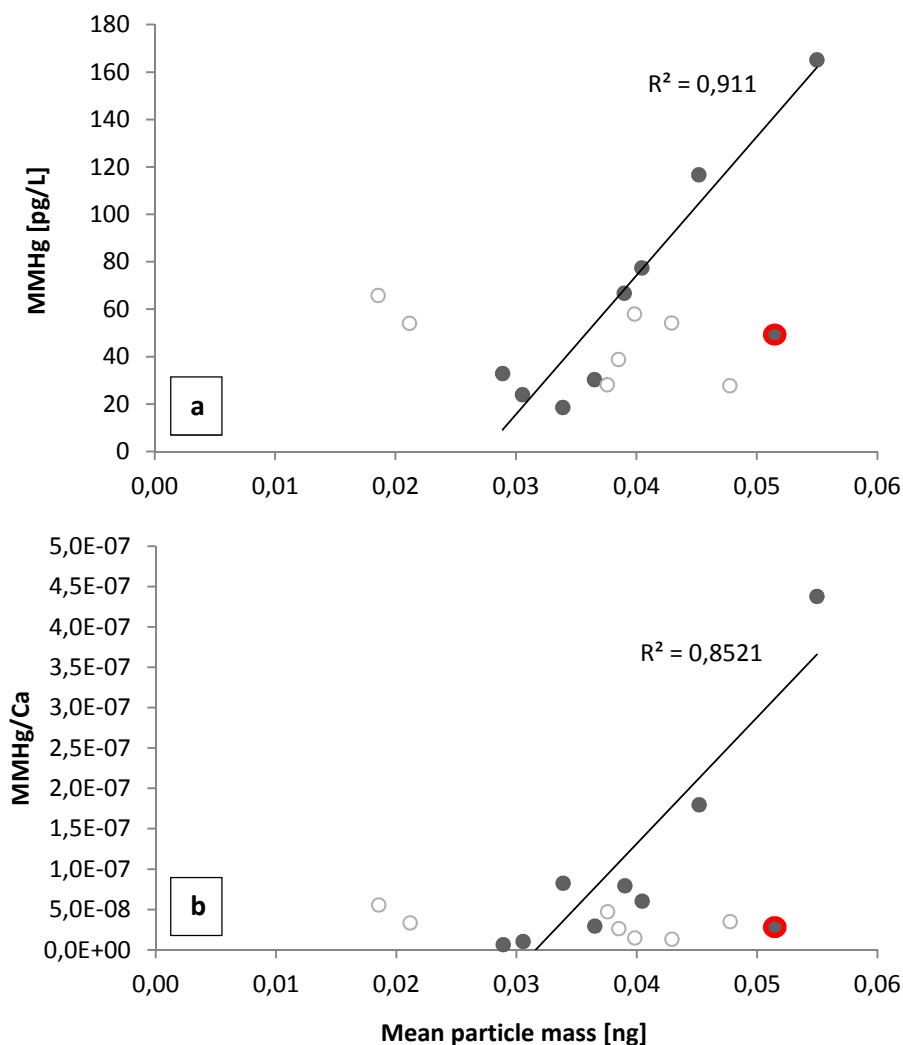


Figure 3. MMHg (a) and MMHg/Ca (b) with respect to the mean particle mass of the “top + middle” samples (full circles) and the “bottom” samples (open circles). An outlier sample (in red) contains abnormal low amounts of particles and is discarded for the linear regression.

The hypothesis of MMHg bound to large particles is consistent with our observations concerning the late spring particles observed in coastal surface snow. These particles are in the fraction of the bigger particles observed during the field campaign (see section III.ii) and that we believe to contain MMHg (see section III.iii). These particles have a common size signature (Figure 26 in section III.ii) but their mean size can vary between 4 and 8 μm . We did not find this size signature of late spring particles in our meltwater samples. It can be explained by the location of the snowmelt water sampling site which is 800 m away from the fjord while the coastal snow sampling site is only 10-20 m away. It is possible that the signature of the late spring particles is due to particles that deposit very rapidly, and that are therefore present only in locations very close to the fjord, their primary source (see section III.iii). Such particles could also fractionate into smaller ones and be deposited further from their original sea source, losing thereby their particular size signature. It is also possible that this particular

size signature is lost as these large late spring particles observed in coastal surface snow dissolve to some extent in meltwater.

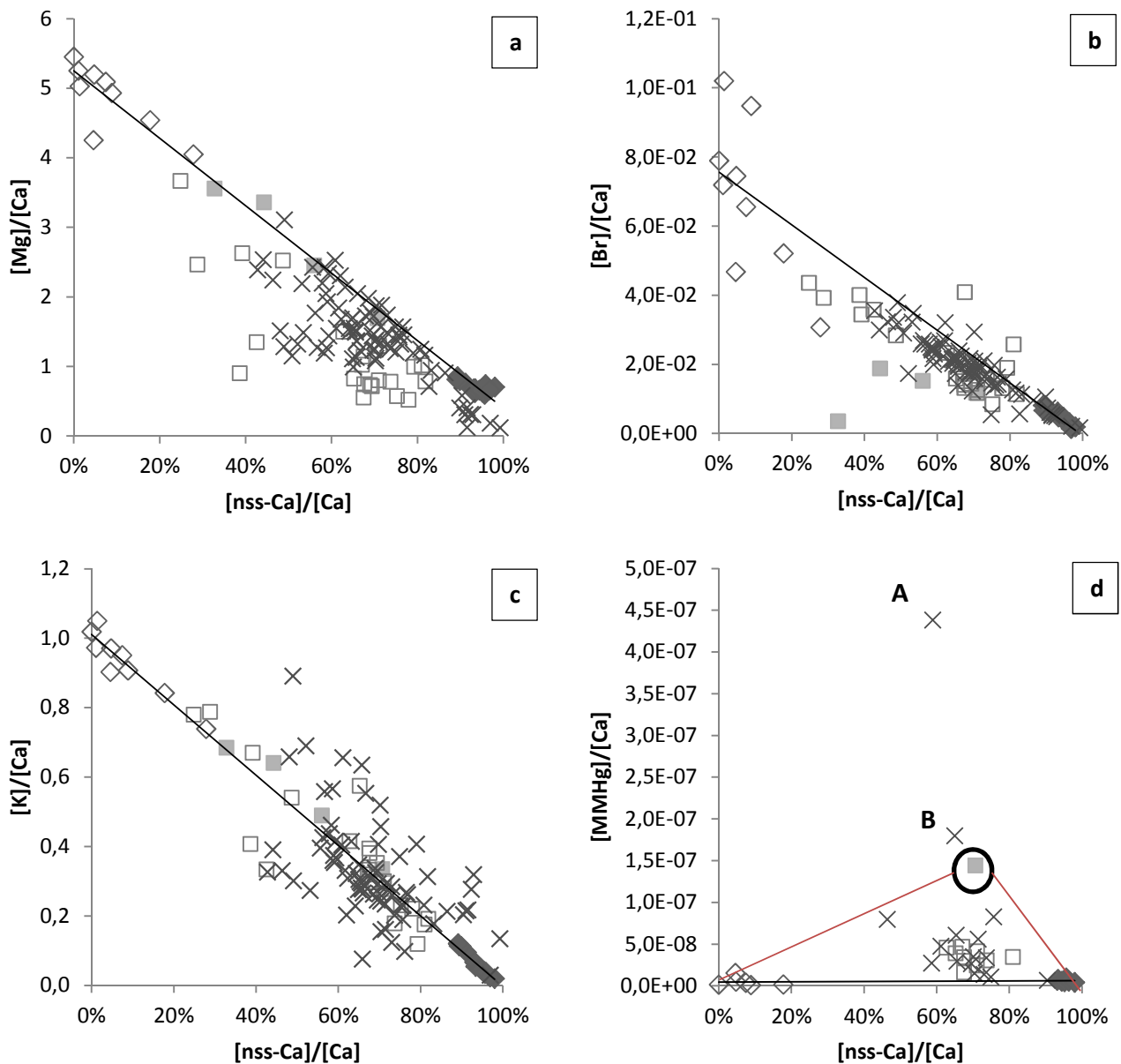


Figure 4. Meltwater samples (crosses) reported on the X/Ca ratio/ratio plots presented in section III.ii for Mg. The mixing line between the late spring particles and the sea-sprays is drawn in black; all other mixing lines are in red. Other signs stand for coastal snow samples: black diamonds represent the particle input event, open diamonds represent samples with strong sea-spray influence (including the strong storm event), grey squares represent fresh snow samples and open squares samples possibly chemically impacted by the snowmelt.

Furthermore, the data suggest that the chemical species (including MMHg) in our meltwater samples and MMHg in coastal snow (see part III) originate from the same sources. Indeed, the meltwater samples fit the “late spring particles/sea-sprays” mixing line on the ratio/ratio plots (presented in

section III.ii) or distribute around it the same way as snow samples do. The clearest examples are presented on Figure 4. Particularly, Figure 4d shows the repartition of meltwater samples on the ratio/ratio plot of MMHg/Ca with respect to nss-Ca/Ca. Almost all the samples fit the sources mixing triangle between late spring particles, sea-sprays, and fresh snow. The two outlier samples are probably due to the late elution of MMHg when all the other major ions (including Ca) are almost totally eluted from the snowpack, leading therefore to very high MMHg/Ca ratio. Our data confirm that for “top” and “middle” meltwater samples, MMHg/Ca increases as the melting season progresses (Figure 5), as all the major ions (including Ca) are almost totally eluted from snow (see Appendix).

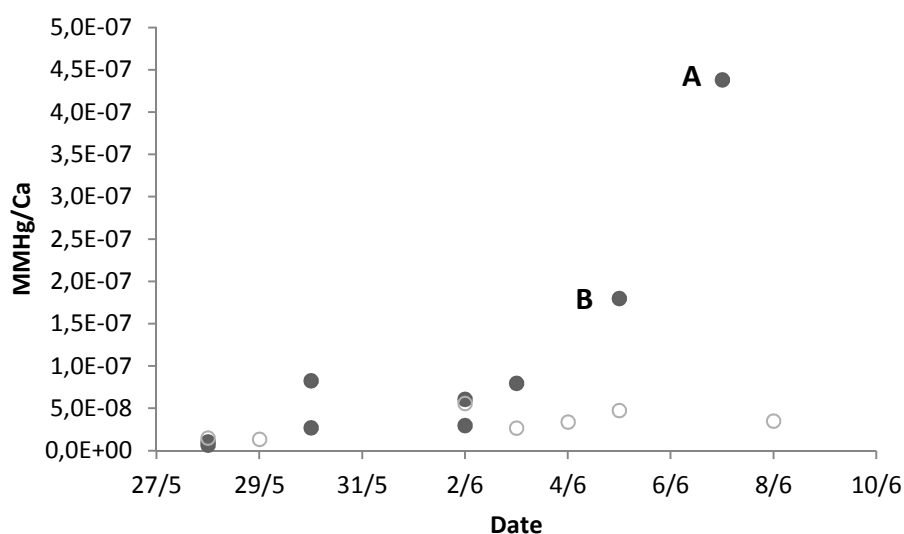


Figure 5. Evolution of MMHg/Ca in meltwater during the melting season. The samples with the highest MMHg/Ca (probable beginning of the MMHg elution peak) correspond to the outliers in Figure 1Figure 4d.

The present results suggest that MMHg is eluted lately from the snowpack compared to other ionic species (including THg). In addition, particles described as late spring particles in section III.ii are present in the meltwater samples and seem to be correlated with their MMHg content. Indeed, the chemical signature of the late spring particles is clearly recognizable here, although their physical one is not. We believe that the latter is due to the atmospheric ageing of these singular large marine particles into a fraction of smaller particles and of a much broader and equalized size range. This ageing would not have been noticeable on coastal snow sampled just next to the fjord (10-20 m away from it) showing a clear size signature (Figure 26 of section III.ii). This is consistent with our previous results concerning snow chemistry and the origins of MMHg in the coastal snowpack, discussed in section III.iii.

References

- Larose, C., Dommergue, A., De Angelis, M., Cossa, D., Averty, B., Maruszczak, N., Soumis, N., Schneider, D., Ferrari, C., 2010. Springtime changes in snow chemistry lead to new insights into mercury methylation in the Arctic. *Geochimica et Cosmochimica Acta* 74, 6263–6275.
- Meyer, T., Lei, Y.D., Muradi, I., Wania, F., 2009. Organic Contaminant Release from Melting Snow. 1. Influence of Chemical Partitioning. *Environmental Science & Technology* 43, 657–662.

V. Conclusion & perspectives

Version française

-

English version

Conclusion et perspectives

Grace à une politique volontaire dans les pays développés (Amérique du Nord, Union Européenne et Japon), les émissions atmosphériques de mercure sont en baisse depuis les années 70, bien que les émissions des pays en développement soient en forte augmentation (Arctic Monitoring and Assessment Programme, 2011). Les dernières estimations prévoient que les émissions globales de mercure pourraient augmenter à nouveau dans un futur proche si ces pays ne restreignent pas leurs émissions (UNEP, Global Mercury Assessment, 2013). Dans cette optique, des discussions en cours depuis plus de trois ans ont donné lieu à une convention devant être signée à l'automne 2013 (traité de Minamata), ayant pour but de réduire l'exposition de chacun au mercure, du mineur artisanal aux populations arctiques (source : site web de l'UNEP). Ce traité prévoit en outre des aides aux pays en voie de développement afin de limiter leurs émissions de mercure.

Contrairement aux émissions de Hg^{II} , qui induisent une pollution locale, les émissions de mercure atmosphérique (> 98% de Hg^0) peuvent affecter des zones très éloignées de leur lieu d'émission. En effet, Hg^0 est très stable dans l'atmosphère et peut donc y résider assez longtemps pour être transporté jusqu'aux régions les plus reculées du globe avant d'y être déposé (Arctic Monitoring and Assessment Programme, 2011; Ariya et al., 2004). Une fois déposé sous sa forme oxydée Hg^{II} , le mercure peut intégrer la chaîne alimentaire et s'y bioaccumuler en fonction du niveau trophique des espèces, principalement sous sa forme la plus neurotoxique, MMHg. Bien que les concentrations de MMHg dans les cryo- et hydrosphères soient au niveau picomolaire, la contamination en MMHg peut atteindre des niveaux critiques dans les poissons et mammifères du haut de la chaîne alimentaire, particulièrement en Arctique (Arctic Monitoring and Assessment Programme, 2011). Dans le monde entier, de nombreuses personnes sont de grands consommateurs de poisson, principalement pour raisons culturelles, et peuvent de ce fait être victimes d'empoisonnement au mercure. L'histoire de Richard L. Gelfond en est un exemple saisissant. Ce new-yorkais était autrefois adepte d'un régime à base de poissons de haut niveau trophique (thon, espadon...etc.) qui a causé chez lui un fort empoisonnement en MMHg, induisant des effets psychomoteurs irréversibles (Gelfond, ICMGP 2011, Halifax). Pour l'heure, la tendance à la baisse des émissions de mercure observée ces dernières années n'est pas suivie d'une baisse du niveau de mercure dans les populations animales arctiques (Arctic Monitoring and Assessment Programme, 2011). La présence de MMHg a été documentée dans tous les milieux de l'environnement arctique, depuis la neige jusqu'aux grands prédateurs (ours polaires, belugas), en passant par les eaux douce et marine. Pourtant, la présence de MMHg dans la

neige – un important réservoir de MMHg en Arctique – reste mal comprise et inexpliquée. Quelques études émettent des hypothèses afin d'expliquer la présence de MMHg dans le manteau neigeux, bien qu'aucune d'entre elles n'ait été démontrée à ce jour (Barkay and Poulain, 2007; Larose et al., 2010). De plus, l'existence d'un mécanisme de méthylation du mercure *in situ* (dans la neige) reste purement spéculative.

Dans ce contexte, cette thèse avait pour but d'explorer la dynamique du MMHg dans la neige arctique. Pour cela, nous avons étudié le manteau neigeux saisonnier dans la région de Ny-Ålesund, Svalbard (Kongsfjorden). La côte du Kongsfjorden est un site de choix pour l'étude de contaminants présents dans la neige et qui peuvent être transférés lors de la fonte aux écosystèmes aquatiques du fjord, comme le MMHg. L'utilisation d'une méthode de mesure du MMHg extrêmement sensible ainsi qu'une étude étendue de la chimie de la neige nous a permis d'établir un jeu de données extrêmement complet, couvrant quotidiennement une période de plus de deux mois. Grâce à une nouvelle approche analytique, nous avons eu l'opportunité de fournir une nouvelle lecture de la chimie de la neige et d'éclaircir les sources et la chimie du MMHg dans le manteau neigeux arctique.

Notre étude de la chimie de la neige de surface côtière a montré la contribution de deux sources principales de chimie dans la neige: 1) les sprays marins ; 2) des particules volumineuses non-corrélées au sel de mer. Les sprays marins ont logiquement la composition du sel de mer, avec très peu d'espèces organiques et de MMHg, et sont seulement responsables d'un modeste apport de MMHg dans la neige. Inversement les particules non-corrélées au sel de mer sont substantiellement enrichies en Ca, Mg, organiques et MMHg. Nous suggérons que ces particules ne sont pas d'origine terrigène – comme souvent pour des particules contenant Ca – mais plutôt d'origine marine: fragments de phytoplancton calcaire aggloméré à des gels organiques (formés de macromolécules organiques et de cations divalents, tels Ca^{2+} et Mg^{2+}). Cette hypothèse est cohérente avec la forte augmentation du nombre de ces particules dans la neige à la fin du printemps arctique, suivant le timing attendu du bloom planctonique du Kongsfjorden (aucune donnée disponible). En effet, un bloom planctonique augmenterait la production de gels bio-organiques, et la sénescence de ce bloom résulterait en l'accumulation de grandes quantités de fragments calcaires et bio-organiques. Il s'agit de conditions optimales pour la formation de volumineux aérosols contenant principalement Ca, Mg et des espèces organiques. Nous pensons que ces particules peuvent très probablement séquestrer le MMHg marin, de par leur nature organique, ce qui expliquerait l'augmentation de la concentration de MMHg dans la neige lorsque le nombre de ces particules augmente. Nos données d'eau de fonte, issue d'un site situé plus éloigné de la côte, ainsi que nos données du glacier Kongsvegen (reculé de toute influence marine directe) suggèrent que ces particules sont déposées principalement très proche du fjord, et sont dégradées petit-à-petit en sous-unités plus petites

lorsqu'elles résident dans l'atmosphère. De telles particules organiques contenant MMHg pourraient être émises de la surface du fjord même après la saison de neige, et donc contribuer à l'évasion de MMHg du fjord aux surfaces terrestres avoisinantes. Dans le cas particulier de la neige, une proportion substantielle de ces particules organiques marines pourrait être redélivrée aux eaux du fjord, compensant partiellement l'évasion du MMHg marin. Cette compensation pourrait être un facteur critique de la contamination en MMHg dans les écosystèmes aquatiques entourés de zones enneigées, qui sont très fréquents en Arctique.

En plus de ces résultats, les données du puits de neige au sommet du glacier Kongsvegen – reculé de toute influence marine – montrent les marques d'un processus chimique impliquant MMHg, NH_4^+ et acétates. Plus la neige est vieille, moins elle contient de MMHg (à cause de sa dégradation), mais plus le mercure est sous forme de MMHg (MMHg/THg augmente), en relation avec le contenu en acétates de la neige ainsi que son acidité. En nous basant sur ces données, et sur les résultats d'une précédente étude sur la méthylation abiotique de Hg^{II} par les acétates en milieu aqueux (Gårdfeldt et al., 2003), nous suggérons que Hg^{II} est méthylé par les acétates dans nos échantillons de neige de glacier. Cette méthylation est cependant très modeste et nous pensons qu'elle ne fait que compenser partiellement (donc ralentir artificiellement) la dégradation du MMHg déposé par la neige fraîche. Aucun processus chimique similaire n'a pu être observé dans la neige côtière. En effet, plusieurs fontes et de forts événements d'apport chimique (tempête, particules organiques...) – induisant une instabilité du manteau dans le temps et des concentrations en MMHg trop variables – cachent ce mécanisme de formation du MMHg, si toutefois il existe dans ce type de neige. Nous pensons que ce processus de méthylation ne peut vraisemblablement être identifié que dans un manteau neigeux très stable et éloigné de toute source directe de contaminants (dans une neige donc très "diluée"). En ce qui concerne l'impact de la méthylation *in situ* sur le cycle du MMHg en Arctique, nos données suggèrent que si cette réaction a lieu dans la neige, elle ne l'enrichit pas significativement en MMHg. La méthylation empêcherait plutôt la dégradation de la totalité du MMHg en maintenant par une très faible production une concentration minimum de MMHg dans la neige (quelques pg/L). De plus, il est possible que ce processus ait lieu avant même le dépôt de la neige fraîche, à la surface d'aérosols (dans le nuage) qui sont séquestrés par (ou adsorbés sur) la neige fraîche. Cela pourrait être dans ce cas à l'origine des enrichissements et hautes concentrations en MMHg observées dans la neige fraîche (Larose et al., 2010; Rose et al., 2013; cette thèse). Cependant dans notre cas MMHg semble être rapidement dégradé après son dépôt *via* la neige fraîche.

Sur la base de ces résultats, nous proposons un schéma du cycle détaillé du MMHg en Figure 1 (voir version anglaise ci-après), prenant en compte les connaissances établies sur le MMHg dans la neige

arctique enrichies de la contribution de cette thèse. Le rôle du manteau neigeux comme milieu de stockage du MMHg marin y est souligné, avant une diffusion dans la chaîne alimentaire lors de la fonte. Notre étude clarifie les sources de MMHg dans la neige arctique, approfondissant les hypothèses évoquées dans la littérature (et résumées dans Barkay and Poulain, 2007) et donne une vue d'ensemble des processus impliqués dans le cycle du MMHg en Arctique.

Les résultats de cette thèse sont issus d'études de terrain et requièrent de plus amples confirmations en laboratoire ou en expériences de terrain contrôlées. Le site de terrain doit être choisi avec soin selon les aspects du cycle du MMHg étudiés (sources ou processus). De plus, un dispositif flexible de mesure du MMHg serait une grande amélioration pour les études de terrain, en permettant des observations en temps réel donc plus de réactivité vis-à-vis d'événements particuliers. Nous avons effectué le premier pas dans cette direction en construisant un dispositif mobile de mesure du MMHg à des concentrations de l'ordre de la dizaine de pg/L dans des échantillons aqueux de 30-40 mL. Le produit de cette thèse – fut-il matériel ou connaissances scientifiques – procure des outils additionnels pour des études plus précises et plus focalisées sur le cycle biogéochimique du MMHg dans les environnements polaires. De futures recherches sont indispensables afin de détailler les processus responsables de la formation et de l'évasion d'aérosols marins organiques et leur impact sur la chimie de la neige, et particulièrement sur le cycle du MMHg. Les efforts à venir doivent aussi porter sur la compréhension de l'origine de la présence en si grande concentration de MMHg dans la neige fraîche (Larose et al., 2010; Rose et al., 2013; cette thèse). L'analyse isotopique, par l'identification de fractionnements isotopiques du mercure, serait un outil de choix pour 1) retracer l'origine géochimique du mercure ; ou 2) observer certaines réactions chimiques dont le mercure est substrat. En effet, le mercure peut avoir une signature isotopique particulière à son milieu d'origine (sédiments, biota...)(Bergquist and Blum, 2009) et qui évolue de façon particulière (fractionnement isotopique dépendant / indépendant de la masse) lors de certaines réactions, notamment lors de sa photo-réduction (Bergquist and Blum, 2007; Kritee et al., 2009, 2008; Malinovsky and Vanhaecke, 2011). Nous recommandons également l'utilisation à bon escient des diagrammes ratio/ratio pour observer les corrélations chimiques au-delà des corrélations directes "évidentes" (et souvent absentes) et d'identifier les sources de contaminants dans un milieu donné (Robinson et al., 2006). En effet, cette approche peut permettre l'observation de processus (Robinson et al., 2006) ce qui a permis dans notre cas de suspecter la méthylation abiotique de Hg^{II} par les acétates dans nos échantillons. Nous ne doutons pas qu'une telle méthodologie peut trouver un grand nombre d'applications dans l'étude de la réactivité du mercure environnemental.

Conclusion and perspectives

Thank to voluntary policies in the developed countries (North America and European Union), the global atmospheric emissions of mercury are decreasing since the 1970's, although emissions from the fast developing countries are sharply increasing (Arctic Monitoring and Assessment Programme, 2011; Fain et al., 2009). The latest forecasts claim that global mercury emissions could increase again in the future if these countries do not restrain their emissions (UNEP, Global Mercury Assessment, 2013). For this purpose, a convention is in debate for more than three years and expected to be ratified this autumn as the Minamata treaty, that aims to decrease the Hg exposure for everyone, from small-scale gold-miners to arctic populations (source: UNEP website). This treaty will also provide help to developing countries in order to limit their growing Hg emissions.

Unlike Hg^{II} emissions, which induce local and regional pollution, atmospheric mercury emissions (> 98% as Hg^0) are likely to show effects at a global scale, as Hg^0 is stable enough in the atmosphere to reach (and deposit) even in the most remote areas of the world (Arctic Monitoring and Assessment Programme, 2011; Ariya et al., 2004). Once deposited as Hg^{II} , mercury enters the aquatic food chains and biomagnifies with growing trophic level, mainly as its highly neurotoxic form MMHg. Although the MMHg levels in the cryo- and hydrosphere are fairly modest, MMHg contamination can reach critical levels in high trophic level fishes and mammals, particularly in the Arctic (Arctic Monitoring and Assessment Programme, 2011). Around the globe, many human populations are culturally avid fish consumers, and experience mercury poisoning because of this diet. A stunning example of how fish consumption can affect health is the story of Richard L. Gelfond, a Manhattanite who chose a diet rich in high trophic fishes (tuna, swordfish...etc.) inducing with time severe MMHg poisoning with irreversible psychomotor effects (Gelfond, ICMGP 2011, Halifax). So far, the decreasing trend of mercury emissions is not followed by a mercury decrease in the arctic wildlife (Arctic Monitoring and Assessment Programme, 2011). The presence of MMHg has been documented in all the compartment of the arctic environment from the snow, marine and freshwaters to the largest animals such as polar bears or belugas. Yet, there is a poor understanding on the presence of MMHg in snow which is one of the primary reservoirs of MMHg in the Arctic. Several studies raise hypotheses in order to explain the presence of MMHg in the snowpack, although none of them has ever been clearly identified and demonstrated (Barkay and Poulain, 2007; Larose et al., 2010). In addition, there are no clear evidences on pathways leading to MMHg formation.

In this context, the present thesis sights to explore the MMHg dynamics in arctic snow. The seasonal arctic snowpack was studied over two months at the Ny-Ålesund area (Kongsfjorden), Svalbard. The Kongsfjorden shore is of the greatest interest to investigate the cycling of contaminants present in snow, which can be transferred to the aquatic ecosystem of the fjord during snowmelt, such as MMHg. The use of an extremely sensitive MMHg measurement method as well as an extended study of the chemistry of snow provided us with a very complete dataset, with daily monitoring during more than two months. Thanks to a novel analytical approach of snow chemistry, we were able to provide a new insight into snow chemistry as well as a further understanding of MMHg dynamics in arctic snow.

Our study of the chemistry of coastal surface snow showed the contribution of two main sources to the chemical content of snow: 1) sea-sprays aerosols; and 2) sea-salt-unrelated large particles. As expected, sea-sprays have composition of sea-salt, with very low organics and MMHg and are responsible for a modest MMHg input in snow. Inversely, the sea-salt-unrelated particles are substantially enriched in Ca, Mg, organics and MMHg. We suggest that such particles were not of terrestrial origin – as often assessed for Ca containing particles – but rather of marine origin, as fragments of calcareous phytoplankton together with organic gels (formed with organic macromolecules and divalent cations such as Ca^{2+} and Mg^{2+}). This hypothesis is consistent with the steep increase of the number of these particles in snow at the end of the snow season, following the expected planktonic bloom of the Kongsfjorden (no data available). Indeed, a planktonic bloom would induce a substantial increase of bioorganic gels production, as well as the senescence of this bloom would lead to large amounts of calcareous and bioorganic fragments; these are the optimal conditions for the formation of large particles containing mainly Ca, Mg and organics. We believe that these particles are more likely to scavenge marine MMHg due to their intrinsic organic nature, which explains the increase of MMHg concentrations in snow with the increasing number of these particles. Our meltwater data, at a site located further from the shore, as well as our data from the Kongsvegen glacier (remote from sea influence) suggest that these particles deposit mainly very close to the fjord, and are gradually degraded to smaller particles with increasing atmospheric residence time. Such organic MMHg containing particles could be emitted from open sea even after the snow season, and thus contribute to the MMHg evasion of the fjord to the surrounding terrestrial surfaces. In the singular case of snow, a substantial fraction of the deposited marine particles could be delivered back to the fjord in meltwater streams, thus possibly offsetting the MMHg evasion from open sea waters. This offset could be a critical factor of MMHg contamination in aquatic ecosystems surrounded by snow, which are frequent in the Arctic.

In addition to these results, our data from the summit of the Kongsvegen glacier top – a study site remote from sea influence – highlighted evidences of a chemical process involving MMHg, NH_4^+ and acetates. The older the snow, the less MMHg it contains (because of degradation overtime), but the more mercury is in the MMHg form (MMHg/THg increases), in relationship with the acetate content and the acidity of snow. Based on this data and on a previous study on the abiotic methylation of Hg^{II} by acetates in synthetic rain waters (Gårdfeldt et al., 2003), we suggested that Hg^{II} is methylated by acetates in our glacier snow samples. This methylation is however very modest and we believe it to only partially compensate (hence artificially slower) the degradation of the MMHg deposited by fresh snow. Such chemical processes could not be identified in the coastal snow pack. Indeed, several thaws and strong chemical input events (storms, late spring particles...) – leading to unstable snowpack overtime and too high and varying MMHg concentrations – hide this mechanism (if existing) of MMHg formation. We believe that this process is likely to be identified only in very stable snowpacks overtime and remote from contaminant sources (hence very “diluted” compared to other sites). Concerning the impact on the MMHg cycling in the Arctic, our data suggest that if such methylation happens in snow, it does not significantly enrich the snowpack in MMHg. Methylation would rather prevent all the MMHg to be degraded in snow by maintaining a very low MMHg background level (a few pg/L). Moreover, it is possible that this methylating process takes place even prior to snow deposition, at the surface of aerosols (in cloud) that are scavenged by or adsorbed on fresh snow. It could be in this case responsible for the high MMHg enrichment observed in fresh snow, as well in this study as in recent ones (Larose et al., 2010; Rose et al., 2013). However, in our case, MMHg seems to be rapidly degraded after its deposition in fresh snow.

Based on these results, we propose a detailed MMHg cycle in Figure 1. It integrates the current knowledge on MMHg in arctic snow as well as the contribution of the present thesis. It also emphasizes the role of the snowpack as a storage medium for marine MMHg, which eventually returns to some extent MMHg back to the fjord at the melting season. The present study clarifies previous assumptions about the sources of MMHg in arctic snow (reviewed in Barkay and Poulain, 2007) and gives a global overview of the processes involved in the MMHg chemical cycling in the Arctic.

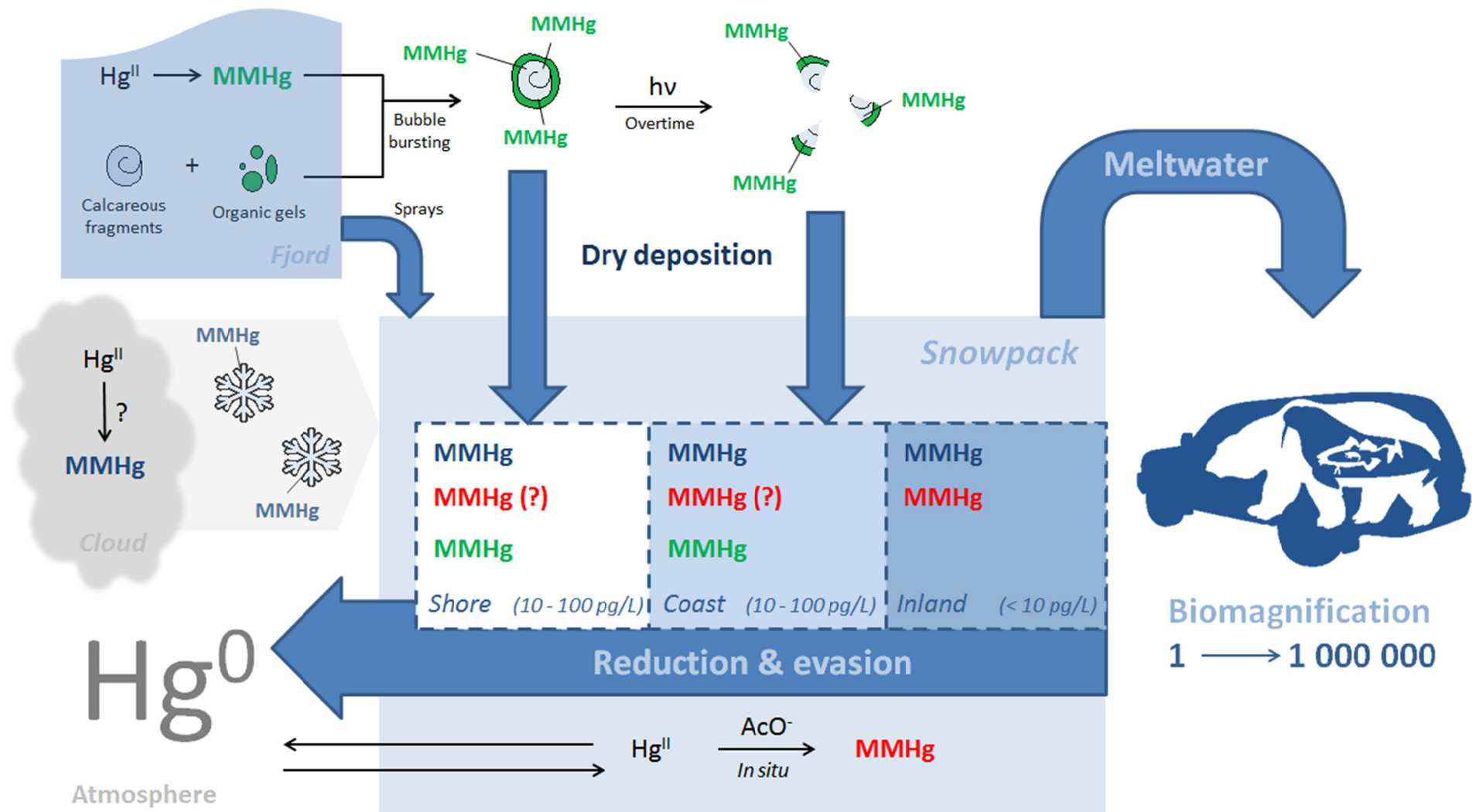


Figure 1. Description of the MMHg cycle in the Arctic detailed and updated with the results from the present study.

The results of this thesis are all derived from field studies, and need to be further confirmed by laboratory or controlled field experiments. The field campaign site shall be chosen with care according to the aspect of the MMHg cycling studied (biogeochemical sources or *in situ* processes). Moreover, a flexible MMHg measuring device would be a great improvement for field studies, as it would allow real-time observations and more reactivity to singular events. We did the first steps toward this direction by building a mobile assembly allowing the determination of MMHg at the tenth of pg/L level in 30-40 mL aqueous samples. Thus the product of this thesis – be it material or scientific knowledge – procures additional tools for more focused and accurate studies of the MMHg biogeochemical cycle in polar environments. Further research is needed to detail the processes responsible for the formation and evasion of organic marine aerosols and their impact on snow chemistry, and particularly on the MMHg cycle. Incoming efforts should also be put on a better understanding of the origin of MMHg in fresh snow, which has recently been showed to be highly enriched in MMHg (Larose et al., 2010; Rose et al., 2013; this thesis). Isotopic analysis, by identifying Hg isotopic fractionation, is a tool of choice for 1) investigating the geochemical origin of Hg; and 2) observing chemical reactions involving Hg as a substrate. Indeed, Hg can have a particular isotopic fractionation according to its origin medium (sediments, biota...)(Bergquist and Blum, 2009), which evolves by further Hg mass-dependent or mass-independent fractionation that occurs during chemical reactions, especially during Hg^{II} photo-mediated reduction (Bergquist and Blum, 2007; Kritee et al., 2009, 2008; Malinovsky and Vanhaecke, 2011). We would also like to promote the wittingly use of ratio/ratio plots to observe correlations between chemicals beyond the “obvious” direct one, as well as the source fractionation of chemicals in any medium (Robinson et al., 2006). Indeed, this approach can lead to the observation of processes (Robinson et al., 2006), which allowed in our case to suspect the abiotic methylation of Hg^{II} by acetates in our samples, and which can surely find new applications in investigating the reactivity of mercuric species in the environment.

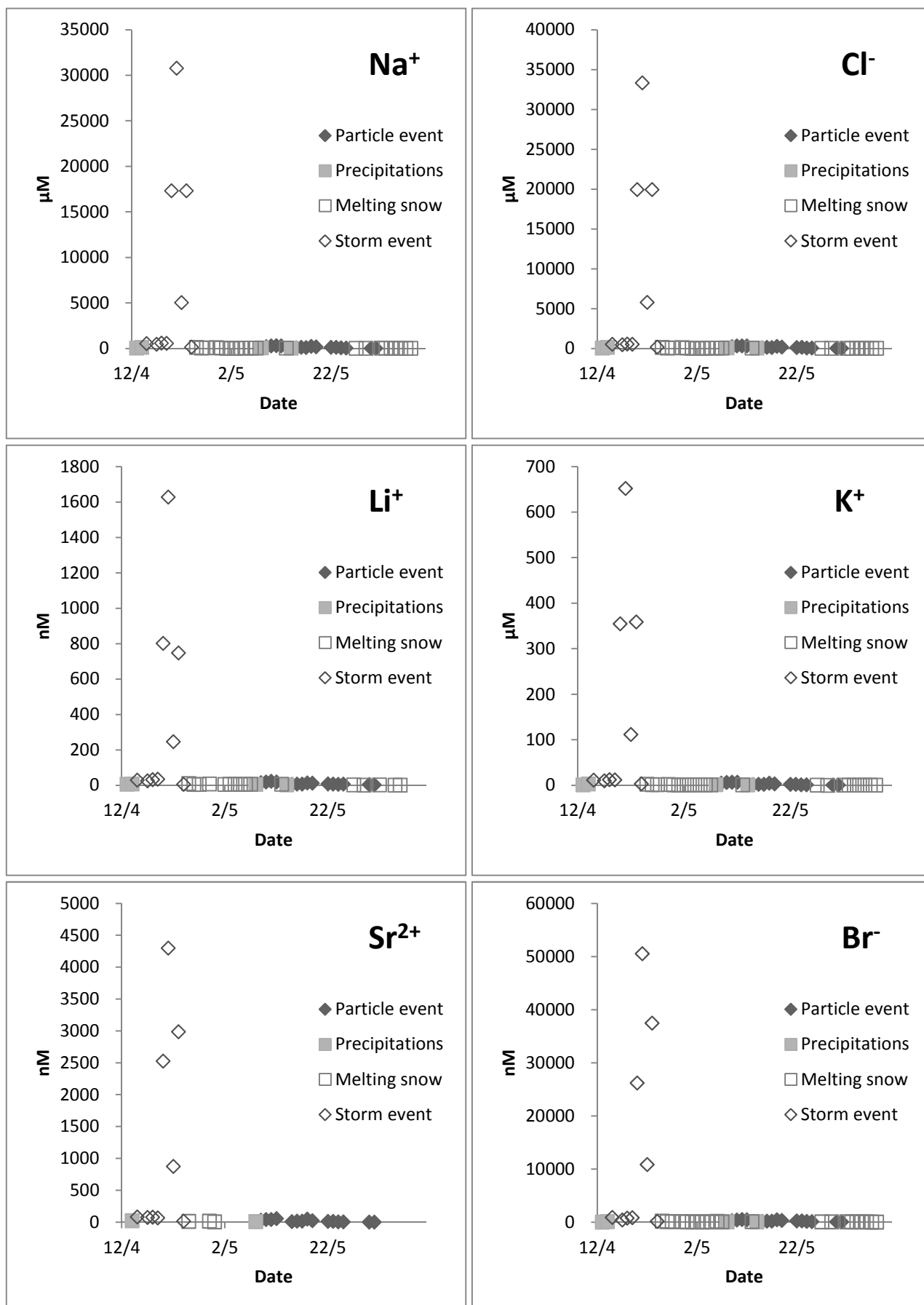
References

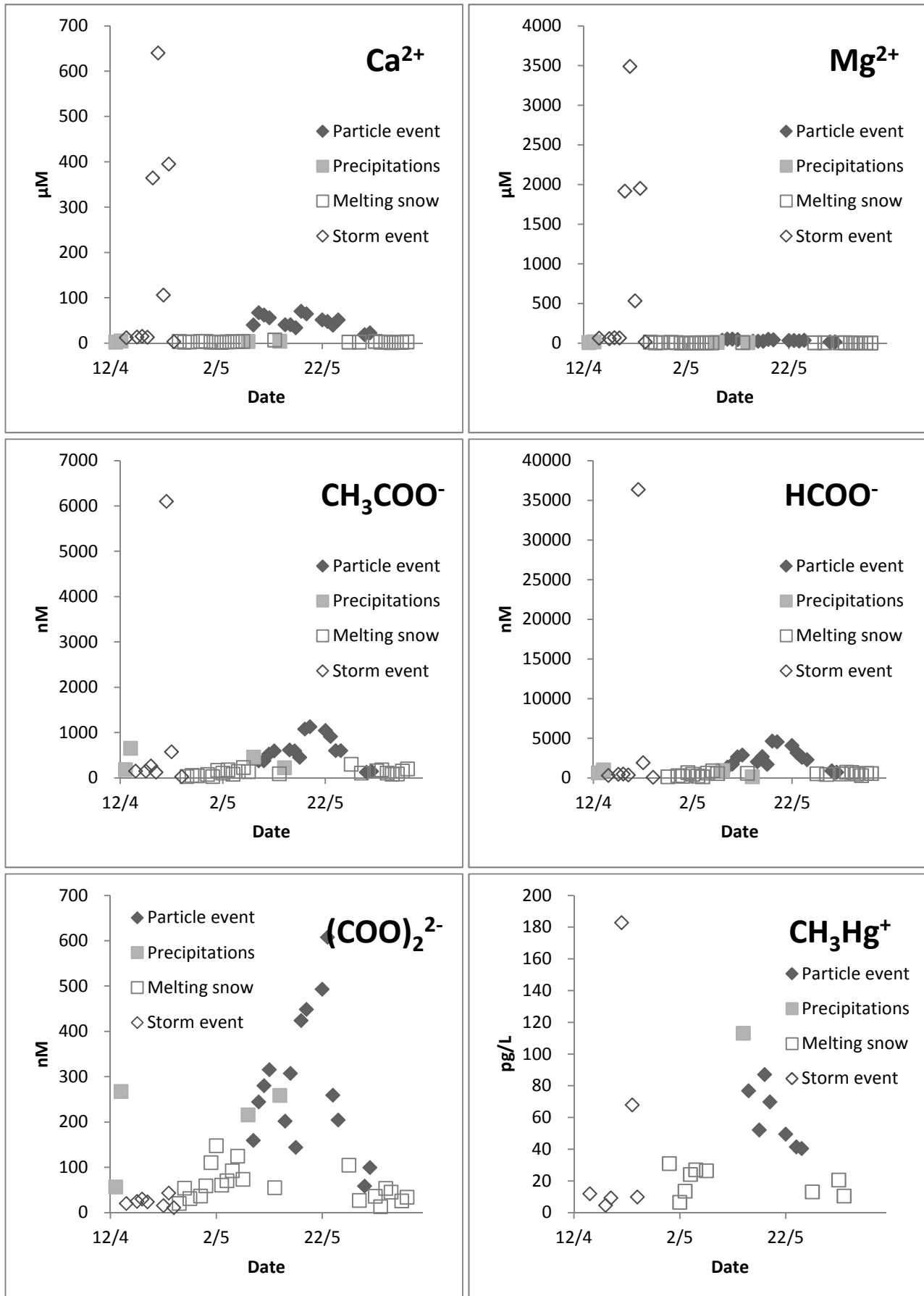
- Arctic Monitoring and Assessment Programme, 2011. AMAP assessment 2011. Arctic Monitoring and Assessment Programme, Oslo, Norway.
- Ariya, P.A., Dastoor, A.P., Amyot, M., Schroeder, W.H., Barrie, L., Anlauf, K., Raofie, F., Ryzhkov, A., Davignon, D., Lalonde, J., Steffen, A., 2004. The Arctic: a sink for mercury. *Tellus B* 56, 397–403.
- Barkay, T., Poulain, A.J., 2007. Mercury (micro)biogeochemistry in polar environments. *FEMS Microbiol. Ecol.* 59, 232–241.
- Bergquist, B.A., Blum, J.D., 2007. Mass-Dependent and -Independent Fractionation of Hg Isotopes by Photoreduction in Aquatic Systems. *Science* 318, 417–420.
- Bergquist, B.A., Blum, J.D., 2009. The Odds and Evens of Mercury Isotopes: Applications of Mass-Dependent and Mass-Independent Isotope Fractionation. *Elements* 5, 353–357.
- Fain, X., Ferrari, C.P., Dommergue, A., Albert, M.R., Battle, M., Severinghaus, J., Arnaud, L., Barnola, J.-M., Cairns, W., Barbante, C., Boutron, C., 2009. Polar firn air reveals large-scale impact of anthropogenic mercury emissions during the 1970s. *Proc. Natl. Acad. Sci.* 106, 16114–16119.
- Gårdfeldt, K., Munthe, J., Strömberg, D., Lindqvist, O., 2003. A kinetic study on the abiotic methylation of divalent mercury in the aqueous phase. *Sci. Total Environ.* 304, 127–136.
- Kritee, K., Barkay, T., Blum, J.D., 2009. Mass dependent stable isotope fractionation of mercury during mer mediated microbial degradation of monomethylmercury. *Geochim. Cosmochim. Acta* 73, 1285–1296.
- Kritee, K., Blum, J.D., Barkay, T., 2008. Mercury Stable Isotope Fractionation during Reduction of Hg(II) by Different Microbial Pathways. *Environ. Sci. Technol.* 42, 9171–9177.
- Larose, C., Dommergue, A., De Angelis, M., Cossa, D., Averty, B., Maruszczak, N., Soumis, N., Schneider, D., Ferrari, C., 2010. Springtime changes in snow chemistry lead to new insights into mercury methylation in the Arctic. *Geochim. Cosmochim. Acta* 74, 6263–6275.
- Malinovsky, D., Vanhaecke, F., 2011. Mercury isotope fractionation during abiotic transmethylation reactions. *Int. J. Mass Spectrom.*
- Robinson, A.L., Subramanian, R., Donahue, N.M., Rogge, W.F., 2006. Source Apportionment of Molecular Markers and Organic Aerosol¹. Polycyclic Aromatic Hydrocarbons and Methodology for Data Visualization. *Environ. Sci. Technol.* 40, 7803–7810.
- Rose, N.L., Munthe, J., McCartney, A., 2013. Winter peaks of methylmercury in deposition to a remote Scottish mountain lake. *Chemosphere* 90, 805–811.

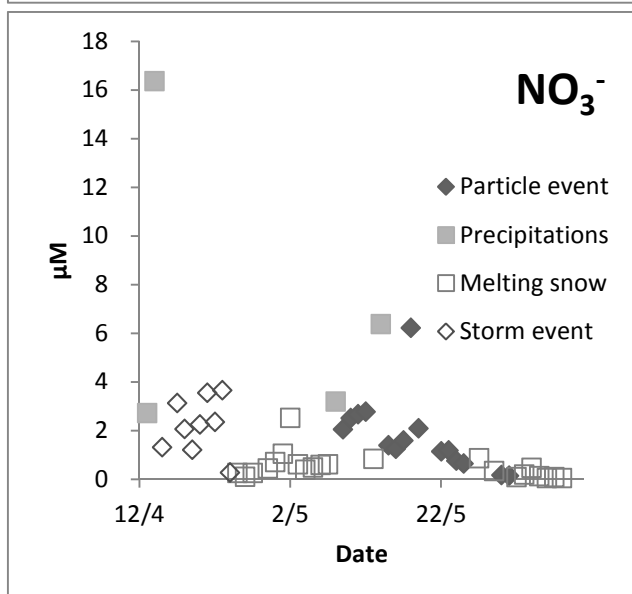
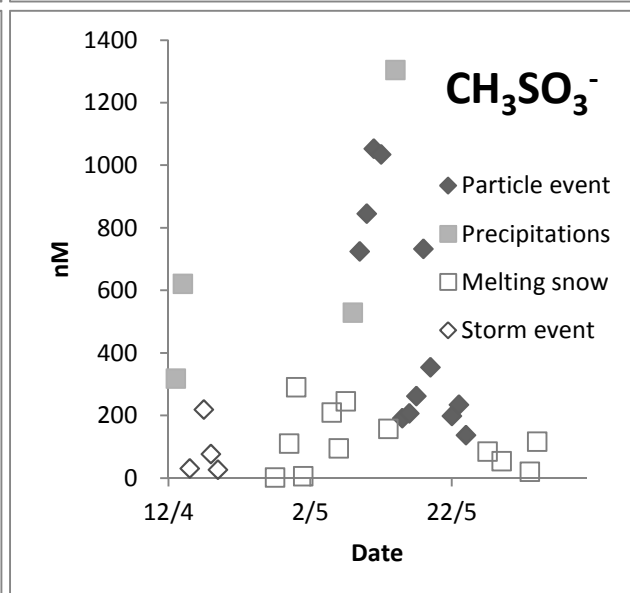
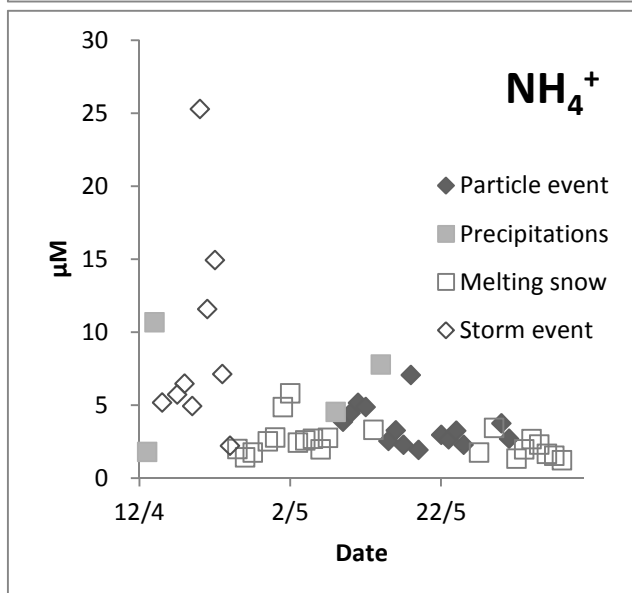
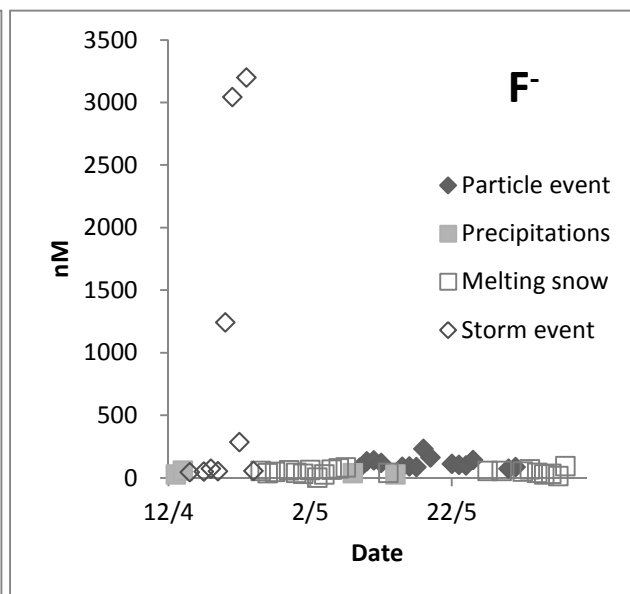
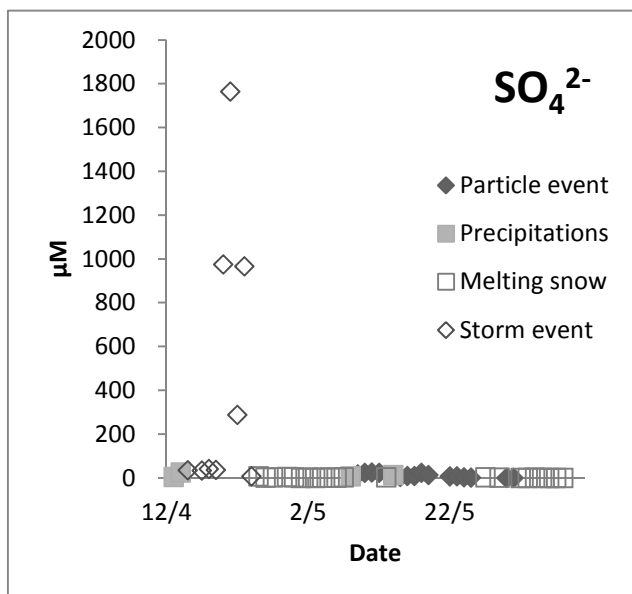
UNEP, Global Mercury Assessment, 2013. UNEP, 2013. Global Mercury Assessment 2013: Sources, Emissions, Releases and Environmental Transport. UNEP Chemicals Branch, Geneva, Switzerland.

VI. Appendix

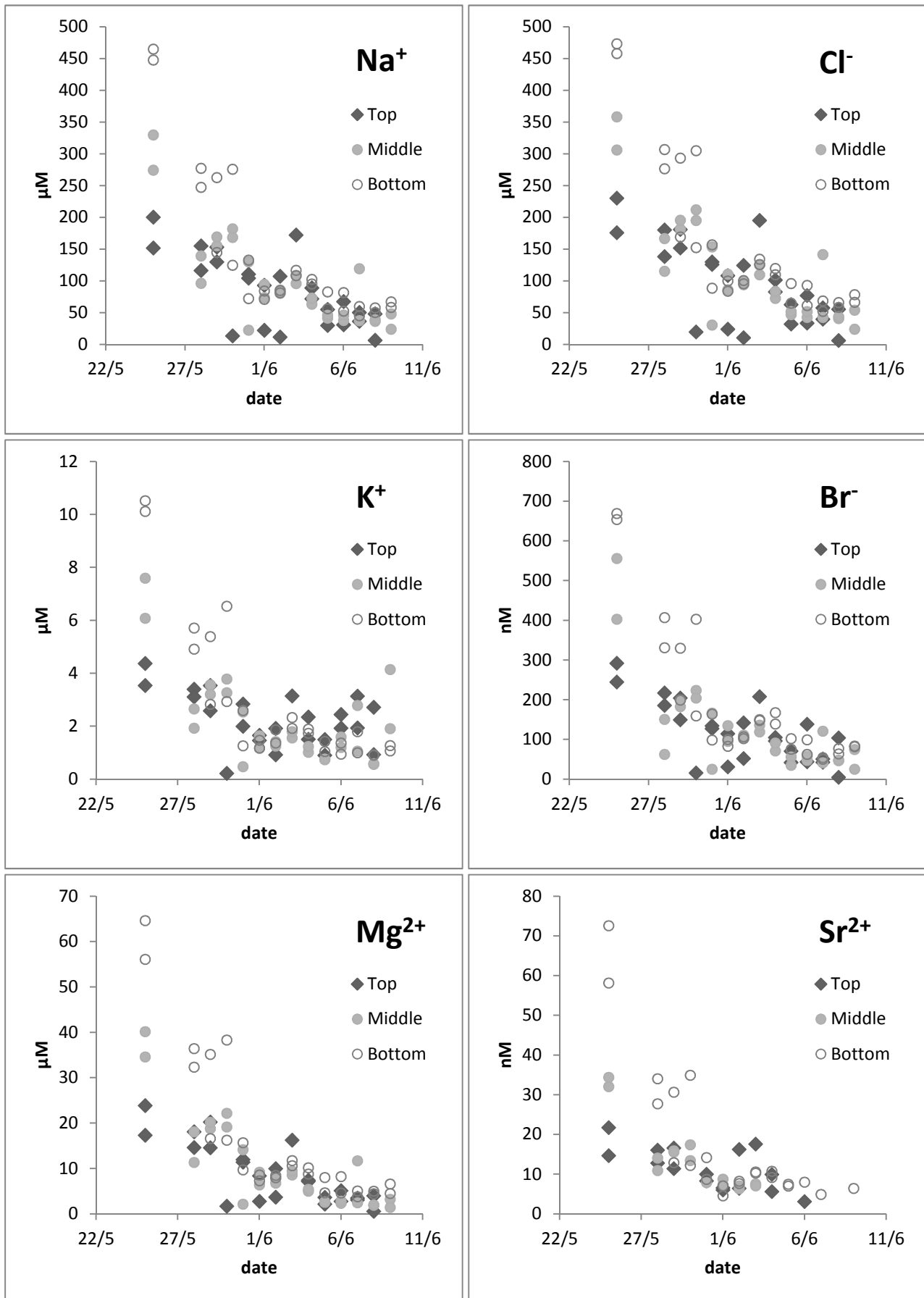
Coastal surface snow time series for major ions

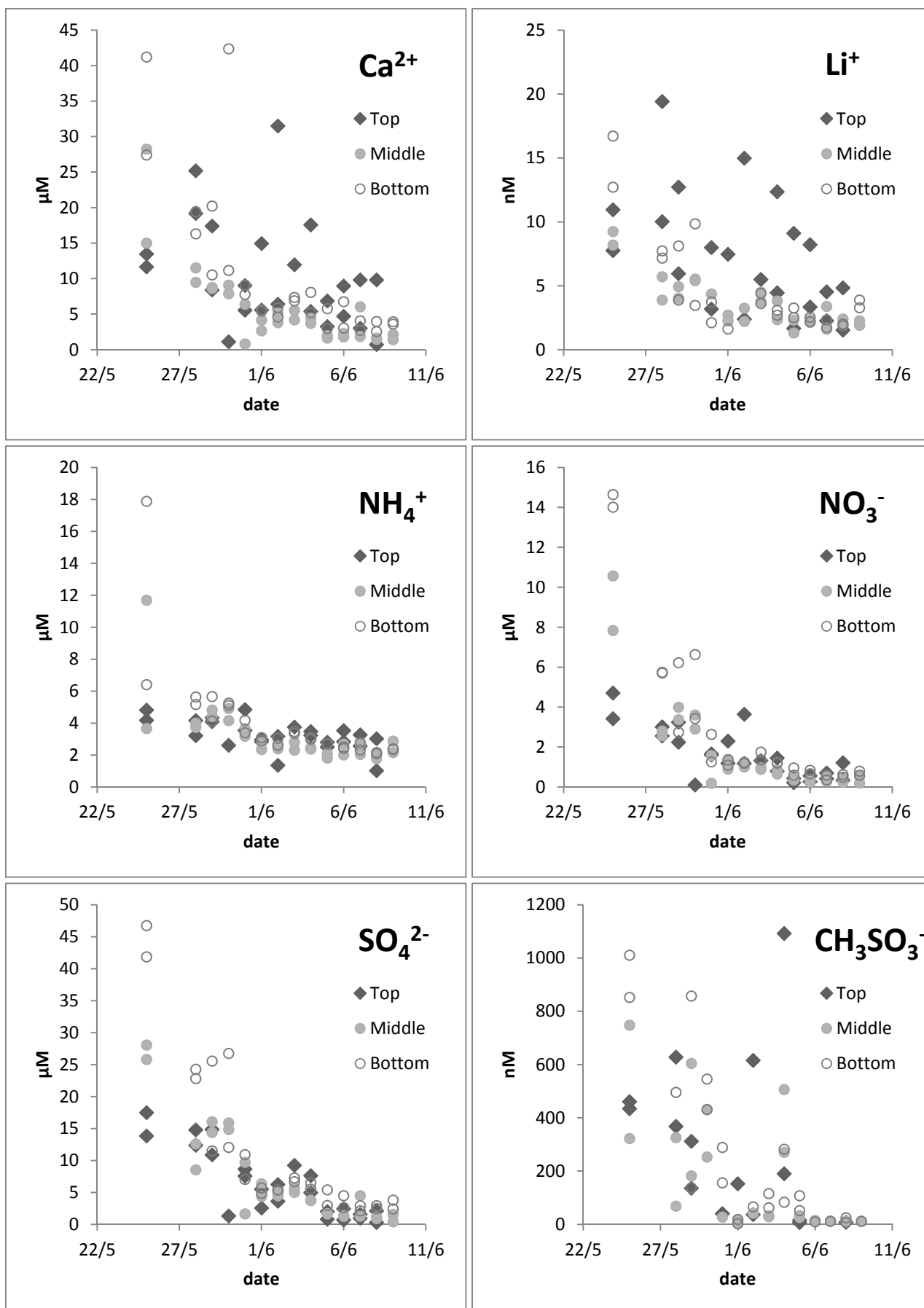


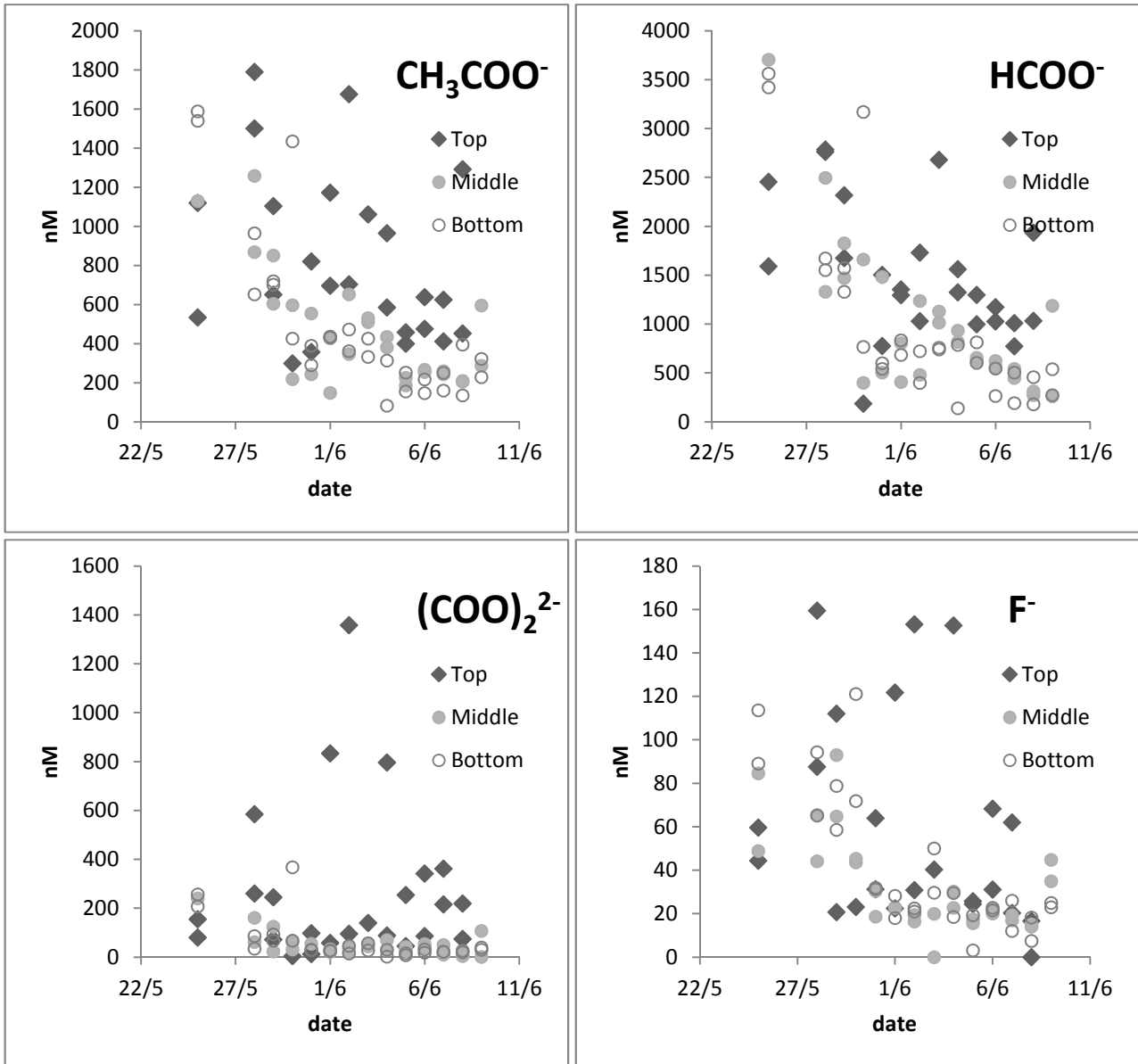




Meltwater data for major ions







Cite this: *Phys. Chem. Chem. Phys.*, 2011, **13**, 16772–16779

www.rsc.org/pccp

PAPER

Theoretical study of the solvation of HgCl_2 , HgClOH , $\text{Hg}(\text{OH})_2$ and HgCl_3^- : a density functional theory cluster approach†

Ludovic Castro,^a Aurélien Dommergue,^b Alexandre Renard,^b Christophe Ferrari,^b Alejandro Ramirez-Solis^c and Laurent Maron^{*a}

Received 1st July 2011, Accepted 3rd August 2011

DOI: 10.1039/c1cp22154j

The determination of the solvation shell of Hg(II)-containing molecules and especially the interaction between Hg(II) and water molecules is the first requirement to understand the transmembrane passage of Hg into the cell. We report a systematic DFT study by stepwise solvation of HgCl_2 including up to 24 water molecules. In order to include pH and salinity effects, the solvation patterns of HgClOH , $\text{Hg}(\text{OH})_2$ and HgCl_3^- were also studied using 24 water molecules. In all cases the hydrogen bond network is crucial to allow orbital-driven interactions between Hg(II) and the water molecules. DFT Born–Oppenheimer molecular dynamics simulations starting from the stable $\text{HgCl}_2-(\text{H}_2\text{O})_{24}$ structure revealed that an $\text{HgCl}_2-(\text{H}_2\text{O})_3$ trigonal bipyramid effective solute appears and then the remaining 21 water molecules build a complete first solvation shell, in the form of a water-clathrate. In the HgCl_2 , HgClOH , $\text{Hg}(\text{OH})_2-(\text{H}_2\text{O})_{24}$ optimized structures Hg also directly interacts with 3 water molecules from an orbital point of view (three Hg–O donor–acceptor type bonds). All the other interactions are through hydrogen bonding. The cluster-derived solvation energies of HgCl_2 , HgClOH and $\text{Hg}(\text{OH})_2$ are estimated to be -34.4 , -40.1 and -47.2 kcal mol⁻¹, respectively.

I. Introduction

Mercury (Hg), one of the most toxic substances on Earth, exists naturally in small amounts in the environment. However, human activities including fossil fuel combustions, metallurgy, manufacturing industries have contributed to increase Hg levels in soil, sediments and aquatic ecosystems worldwide.¹ Even in remote and pristine areas high Hg levels have been detected in biota such as in fish, birds, mammals and humans.^{2,3} These elevated levels of Hg are driven, in large part, by the long range transport of mercury in the atmosphere and its bioaccumulation and biomagnifications along the food chains. In spite that environmental concentrations are generally lower than levels encountered around contaminated sites they may have significant adverse effects on humans and the ecosystems. Some large-scale epidemiologic studies on a large cohort of populations consuming sea fishes and sea mammals showed the evidence of fetal neurotoxicity of mercury, even at

low concentrations of exposure to Hg-containing molecules.^{4–7} Mercury reaches remote ecosystems mainly as elemental gaseous mercury ($\text{Hg}(0)$). Once oxidized to more water soluble forms, Hg can be deposited after atmospheric scavenging by wet and dry deposition. The deposition velocity is readily enhanced in polar regions during springtime due to the episodic existence of Atmospheric Mercury Depletion Events (AMDEs) that oxidize $\text{Hg}(0)$ and deposit $\text{Hg}(\text{II})$ species onto polar environmental surfaces more rapidly than anywhere else.^{8,9} In order to understand the mechanisms of food chain contaminations in remote areas, the question of the chemical and biological fate of deposited Hg species is of utmost importance. As can be expected, the Hg^{2+} ion is not inert once deposited. Hg^{2+} complexes can be easily photo-degraded or reduced by compounds produced *via* photochemical reactions¹⁰ and reemitted back to the atmosphere as $\text{Hg}(0)$ from various environmental matrices including soil,¹¹ fresh water,¹² sea water¹³ and snow.¹⁴ The bioavailability of deposited Hg is followed by an important biochemical step in which Hg will cross a cell membrane by passive or active diffusion. The bioavailability is a critical issue in determining Hg toxicity, the potential for Hg accumulation and for the production of organo-mercurial species such as monomethylmercury. The bioavailability of Hg can be assessed in environmental samples by using biochemical tools such as biosensors.^{15–17} However, measurements of Hg bioavailability are to be carefully discussed due to the complex nature of environmental samples. Hg bioavailability will depend on pH

^a Université de Toulouse, INSA, UPS, LPCNO, 135 Avenue de Rangueil, F-31077 Toulouse, France.

E-mail: laurent.maron@irsamc.ups-tlse.fr

^b Laboratoire de Glaciologie et Géophysique de l'Environnement, CNRS/Université Joseph Fourier Grenoble I, 54 rue Molière, 38402 Saint Martin d'Hères, France

^c Depto. de Física, Facultad de Ciencias, Universidad Autónoma del Estado de Morelos Cuernavaca, Morelos 62290, Mexico

† Electronic supplementary information (ESI) available. See DOI: 10.1039/c1cp22154j

variations that facilitate Hg uptake, changes in the proportion of ligands, and changes in the concentration of other metal ions that compete with Hg.¹⁸

Among the many possibilities of Hg-complexes, the neutral closed-shell HgCl₂ molecule together with hydroxo complexes appears to be one of the most abundant species in oxic environments if organic complexation is not considered.^{19,20} Using laboratory-synthesized lipid bilayer membranes (lecithin–cholesterol–tetradecane), Gutknecht²¹ studied the permeability of HgCl₂, HgCl₃[−], HgCl₄^{2−}, HgOHCl and Hg(OH)₂, of which three are non-ionic species and, therefore, more likely to pass across lipid bilayers and biological membranes. Based on the results of this study, lipid membranes are highly permeable to HgCl₂ with a permeability about 20 times higher than the permeability to water and more than a million times higher than the permeabilities to Na⁺, K⁺ and Cl[−]. Barkay *et al.*²² obtained similar results with uncharged HgCl₂ being more bioavailable than anionic forms of mercuric chloride. However, they also reported permeability at significant rates for other non-ionic forms of Hg, such as Hg(OH)₂ and HgClOH, in contrast with the findings of Gutknecht.²¹

In spite of a large body of quantitative information, the understanding of the mechanisms is limited due to a large number of uncontrolled environmental parameters, the use of inadequate analytical tools and the lack of detailed theoretical information to elucidate the molecular processes at work. From the biochemical and biophysical points of view, new studies are aimed at tackling both, the relative stability of Hg-containing (neutral and charged) molecular species and the molecular processes involved in the trans-membrane passage of Hg-containing molecules into the cell.^{21–23} We shall concentrate here on specific questions related to the last issue from the molecular perspective of abundant Hg-containing species in aqueous environments. Therefore, several questions appear and are related to the bioavailability of HgCl₂ molecules: (a) how is this stable species solvated? (b) how many water molecules can it hold in its first solvation shell and what is the interaction energy with its water environment? (c) can this species be considered as a water-dressed molecule for trans-membrane transport making it available to the cell interior? For the latter question, it should be noticed that this is an open issue, especially important for microorganisms that have not developed any resistance mechanism to Hg(II) contamination. Answering these questions would represent a crucial step forward, because this knowledge will allow us to propose new molecular-based models to explain the passage of this very common Hg-species through the cell membrane. Here we emphasize that a recent study on the solvation pattern of arsenious acid, As(OH)₃, has allowed us to better understand how this neutral molecule can go through the cell membrane *via* aquaglyceroporines due to its singular amphipathic solvation pattern.²⁴ In particular, detailed information about its specific solvation pattern (tight or soft, with few or many water molecules in the first solvation shell) as occurs for other toxic metalloids such as As(III) can be used by experimentalists to provide new insights into the type of trans-membrane protein channels used for cellular uptake of this abundant Hg species.

We report here the first step of our research program, as in the case of As(III), which is the study of the aqueous solvation of abundant Hg(II)-containing molecules through cluster models.

II. Computational details

Mercury²⁵ and chlorine atoms²⁶ were treated with the Stuttgart–Dresden relativistic effective core potentials (RECP) in combination with their adapted valence basis sets, augmented by a set of polarization functions (f for Hg and d for chlorine).^{27,28} Oxygen and hydrogen atoms have been described with a 6-31G(d,p) double- ζ basis set.²⁹ The DFT calculations were carried out using the restricted Kohn–Sham scheme with the hybrid B3PW91 functional.^{30,31} Geometry optimizations were carried out without any symmetry restrictions and the nature of the minima was verified with analytical frequency calculations. Gibbs free energies were obtained at $T = 298.15$ K within the harmonic approximation. DFT calculations were carried out with the Gaussian03 program.³² Finally, the electronic density (at the DFT level) of selected structures has been analyzed using the Natural Population Analysis (NPA) and the Natural Bond Orbital (NBO) schemes.³³

The interaction of HgCl₂ with water was studied *via* step-wise solvation by adding a number (n) of water molecules to the system, with $n = 1, 2, 3, \dots, 24$. Special care was taken in order to insure that the O–Hg–O–O dihedral angles were properly sampled. The stability of the optimized structures with the largest number of water molecules was then verified using Born–Oppenheimer (BO) molecular dynamics at the DFT level (B3PW91). The BO DFT molecular dynamics simulations (BO-DFT-MD) were carried out with the Geraldyn2.1 code,³⁴ which has been coupled to the electronic structure modules of the Gaussian03 code.³² The BO-DFT-MD algorithm in Geraldyn uses the velocity-Verlet integration scheme.³⁵ The simulation time was 15 ps with a time step of 0.5 fs. A Nosé–Hoover chain of thermostats^{36,37} was used to control the temperature at 1000 K. Electronic structure as well as the energy gradient calculations were performed at the same level of theory (B3PW91, RECPs and basis sets) as that used in the static approach. The trajectory was simulated starting from the optimized equilibrium structure of HgCl₂–(H₂O)₂₄ without any preferred velocity vector other than the thermal energy. The 15 ps simulation took 70 days on a QuadCore dual-processor@2.8GHz running the Linux versions of Geraldyn2.1-G03. The production run was started following an initial thermalization period which was achieved after 5 ps of simulation, so that the Hg–O radial distribution function was extracted from the last 10 ps of the simulation.

III. Results and discussion

1. Solvation of HgCl₂

Bare HgCl₂ is a quasi-linear molecule (178.2°) with a Hg–Cl bond distance of 2.30 Å. The NPA charges are +1.10 for Hg and −0.55 for both chlorine atoms. From the NBO analysis, Hg–Cl bonds show a slight ionic character (26% participation

of the 6s orbital of Hg and 74% participation of sp^3 orbitals of Cl), in agreement with the high electronegativity of chlorine. This shows that, although the Hg–Cl bonds are somewhat ionic, the quasi linear geometry leads to practically zero dipole moment, therefore making it hard for the molecule to interact with the dipole moments of the surrounding water molecules through non-bonded interactions.

The solvation of $HgCl_2$ was studied by incremental additions of water molecules in the $HgCl_2$ environment. The main optimized geometrical parameters and NPA charges are given in Tables 1 and 2, respectively. Gibbs free energies of solvation are given in Table 3.

When a single water molecule is added around the $HgCl_2$ optimized structure (see Fig. 1) the geometry looks like the one computed by Shepler *et al.*³⁸ at the MP2/aVDZ level of theory. An interaction is found between Hg and the oxygen (2.62 Å), inducing a T-shape geometry around mercury. The Cl–Hg–Cl

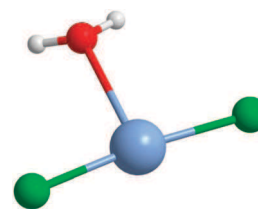


Fig. 1 Optimized geometry of $HgCl_2-H_2O$.

angle decreases by 4.6 degrees compared to $HgCl_2$ in the gas phase, mainly because of electrostatic repulsions between the charged oxygen (–0.99) and both chlorine atoms (–0.60 and –0.58). The Hg–Cl bond lengths slightly increase but Hg–Cl dissociation is not reached (and will not be reached, even with 24 water molecules, see afterwards) because of the covalent nature of the Hg–Cl bond. Thus, $HgCl_2$ is not a real salt like NaCl or $CaCl_2$. Since Hg–Cl bonds are longer, their polarity increases as well. The nature of the Hg–O interaction is found to be merely electrostatic, although an oxygen lone pair points toward mercury. The interaction energy is only -2.7 kcal mol⁻¹, which compares well with the MP2 results of Shepler *et al.*³⁸ A second water molecule is then added in such a way that two Hg–OH₂ interactions are formed at the beginning but the optimization does not maintain this structure (Fig. 2, left). The structure resembles again the one computed by Shepler *et al.*³⁸ at the MP2/aVDZ level of theory. The new H₂O molecule is stabilized by two hydrogen bonds, one between its hydrogen and a chlorine atom and one with the first water molecule. The solvation energy is -4.0 kcal mol⁻¹.

Addition of a third water molecule, in such a way that three Hg–OH₂ interactions are formed at the beginning, leads to the growth of the hydrogen bond network (Fig. 2, right). This structure does not look like the one calculated by Shepler *et al.*³⁸ at the MP2/aVDZ level of theory. A second optimization was thus realized starting with the optimized geometry of Shepler *et al.*³⁸ but this leads to a less stable structure (by only 0.9 kcal mol⁻¹), very close to the starting geometry. This is consistent with the fact that Shepler *et al.*³⁸ also obtained another geometry very close to the one shown in Fig. 2, less stable than their most stable one by only 0.7 kcal mol⁻¹.

These results (involving such small energetic differences) show that the use of different theoretical methods can reverse the stability of these two geometries. The alternate structure is given in the ESI.† When a fourth water molecule is then added in such a way that four Hg–OH₂ interactions are formed at the beginning, a second Hg–O orbital interaction is maintained (Fig. 3, left) in the optimized cluster.

Table 1 Optimized geometrical parameters of gaseous and solvated $HgCl_2$ systems. The oxygen atoms are those directly linked to Hg

Water molecules	Hg–Cl d1/Å	Hg–Cl d2/Å	Cl–Hg–Cl angle/°	Hg–O d1/Å	Hg–O d2/Å	Hg–O d3/Å
0	2.30	2.30	178.2	—	—	—
1	2.32	2.32	173.6	2.62	—	—
2	2.35	2.32	167.7	2.50	—	—
3	2.36	2.34	164.3	2.47	—	—
4	2.38	2.35	163.6	2.48	2.48	—
6	2.45	2.40	144.3	2.35	2.52	—
8	2.45	2.41	151.8	2.52	2.53	2.62
12	2.45	2.45	142.0	2.44	2.48	2.66
24 (equatorial)	2.60	2.51	125.1	2.27	2.45	2.51
24 (apical)	2.52	2.47	176.2	2.36	2.42	2.65

Table 2 Calculated NPA charges of Hg, Cl and O (directly linked to Hg) atoms in gaseous and solvated $HgCl_2$ systems. Tag numbers for Cl and O correspond to those in Table 1

Water molecules	Hg	Cl 1	Cl 2	O 1	O 2	O 3
0	+1.10	–0.55	–0.55	—	—	—
1	+1.15	–0.60	–0.58	–0.99	—	—
2	+1.17	–0.62	–0.59	–1.03	—	—
3	+1.17	–0.62	–0.61	–1.03	—	—
4	+1.19	–0.65	–0.63	–1.03	–1.03	—
6	+1.24	–0.70	–0.66	–1.06	–1.07	—
8	+1.22	–0.69	–0.69	–1.06	–1.07	–1.00
12	+1.24	–0.72	–0.70	–1.07	–1.11	–1.00
24 (equatorial)	+1.31	–0.77	–0.75	–1.07	–1.07	–1.05
24 (apical)	+1.27	–0.71	–0.67	–1.08	–1.09	–1.09

Table 3 Solvation energies, calculated as: $\Delta G_{\text{solv}}^{\circ} = [G^{\circ} n \text{ water molecules}] - nG^{\circ}(\text{H}_2\text{O}) - G^{\circ}(\text{HgCl}_2)$

Water molecules	$\Delta G_{\text{solv}}^{\circ}/\text{kcal mol}^{-1}$
1	–2.7
2	–4.0
3	–6.1
4	–8.6
6	–12.4
8	–14.3
12	–14.9
24 (equatorial)	–31.3
24 (apical)	–34.4

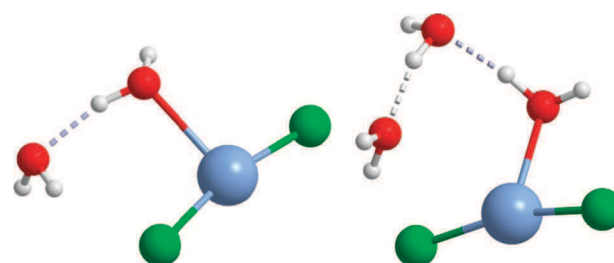


Fig. 2 Optimized geometries of $HgCl_2$ solvated by 2 (left) and 3 (right) water molecules.

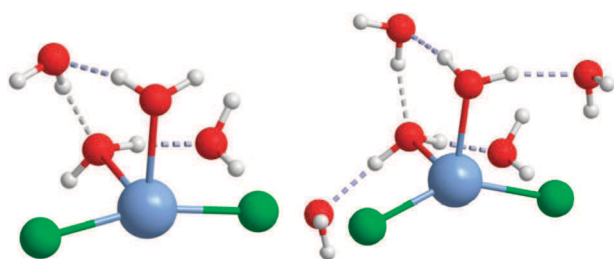


Fig. 3 Optimized geometries of HgCl_2 solvated by 4 (left) and 6 (right) water molecules.

The $\text{H}_2\text{O}-\text{Hg}-\text{OH}_2$ angle is 89.2° . It is a rather small angle which allows the participation of every water molecule into a small hydrogen bond network. The formation of this network seems more favorable than the $\text{Hg}-\text{O}$ interactions, since only one interaction was found in the $\text{HgCl}_2-(\text{H}_2\text{O})_2$ system, while two $\text{Hg}-\text{O}$ interactions could have been built at least. With six water molecules (Fig. 3, right), the water network expands but no other $\text{Hg}-\text{O}$ interaction is found. The trends are the same as previously: the $\text{Cl}-\text{Hg}-\text{Cl}$ angle decreases (144.3° with six H_2O molecules) due to a shorter $\text{Hg}-\text{O}$ distance (2.35 \AA), the $\text{Hg}-\text{Cl}$ bond lengths increase (up to 2.45 \AA) as well as the Hg ($+1.24$) and Cl charges (up to -0.70). The solvation energies are calculated to be $-8.6 \text{ kcal mol}^{-1}$ and $-12.4 \text{ kcal mol}^{-1}$ with four and six water molecules, respectively.

The system of HgCl_2 with 8 water molecules was then optimized in such a way that four $\text{Hg}-\text{OH}_2$ interactions are formed at the beginning (Fig. 4, left). In this case a third water molecule directly interacts with Hg (64.3° with the closest water molecule) and participates in the hydrogen bond network. This third molecule brings electronic density to mercury. It is the reason why the shortest $\text{Hg}-\text{O}$ bond distance of the previous system (2.35 \AA) relaxes and extends (2.52 \AA). As a consequence, the $\text{Cl}-\text{Hg}-\text{Cl}$ angle increases (151.8°) and the free energy of solvation is now $-14.3 \text{ kcal mol}^{-1}$. Then, the system of HgCl_2 with 12 water molecules was optimized (Fig. 4, right). The four new water molecules simply extend the hydrogen bond network, and this happens irrespective of their initial positions relative to the previously optimized cluster. The distance and charge trends are the same as previously. The free energy of solvation is nearly unchanged, $-14.9 \text{ kcal mol}^{-1}$. The four new water molecules do not bring any supplementary stability to the system, because of their peripheral positions.

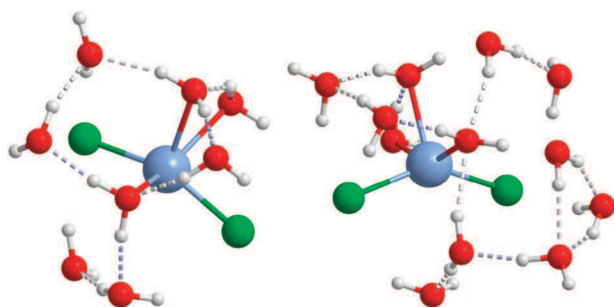


Fig. 4 Optimized geometries of HgCl_2 solvated by 8 (left) and 12 (right) water molecules.

Finally, the HgCl_2 system with 24 water molecules was computed in order to form a complete first solvation shell around HgCl_2 . Two different stable geometries were found. Both of them exhibit a trigonal bipyramid pattern around mercury, but they differ by the position of chlorine atoms. It is noteworthy that this structured geometry appears exclusively once the full surrounding hydrogen bond network is achieved. To summarize, water molecules have created their own network (which provides the highest gain of stability to the system) and then the favorable interactions between water and mercury appear.

In the first orientation, which we shall call “equatorial” (Fig. 5), chlorine atoms form a part of the triangular base. $\text{Hg}-\text{Cl}$ distances are rather long (2.60 and 2.51 \AA). Hg and Cl charges are higher too ($+1.24$ for Hg , -0.77 and -0.75 for Cl). From the second-order NBO analysis, it is noteworthy that oxygen atoms directly linked to Hg bring electronic density to $\text{Hg}-\text{Cl}$ antibonding orbitals (27 , 17 and 13 kcal mol^{-1} for oxygen atoms 1, 2 and 3 respectively). Thus, the formation of a triangular bipyramid around mercury allows orbital interactions between mercury and oxygen atoms, whereas the interactions were mostly electrostatic in the previous cases. The solvation energy of this structure is $-31.3 \text{ kcal mol}^{-1}$ (with respect to $\text{HgCl}_2 + 24\text{H}_2\text{O}$), which shows the importance of the formation of the complete hydrogen bond network and of the orbital interactions between Hg and three water molecules.

In the second orientation (labelled “apical” in the tables; Fig. 6), chlorine atoms are in apical positions of the triangular bipyramid pattern ($\text{Cl}-\text{Hg}-\text{Cl}$ angle of 176.2°). From the second order NBO analysis, oxygen atoms bring electronic density to $\text{Hg}-\text{Cl}$ antibonding orbitals (7 , 17 and 21 kcal mol^{-1} for oxygen atoms 1, 2 and 3 respectively) and the solvation energy is found to be $-34.4 \text{ kcal mol}^{-1}$. An estimate of the solvation energy with a continuum model is $-44.9 \text{ kcal mol}^{-1}$, where no orbital interactions are taken into account, showing that the cluster model which considers only the first solvation shell yields 78% of that value. The difference of solvation energies between both orientations is only $3.1 \text{ kcal mol}^{-1}$, thus, the formation of both structures are nearly equally favorable. This fact allows us to think that HgCl_2 may have a non-negligible dipole moment in water due to the presence of

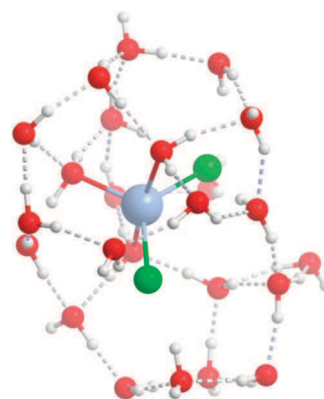


Fig. 5 Optimized geometry of HgCl_2 solvated by 24 water molecules, “equatorial” structure.

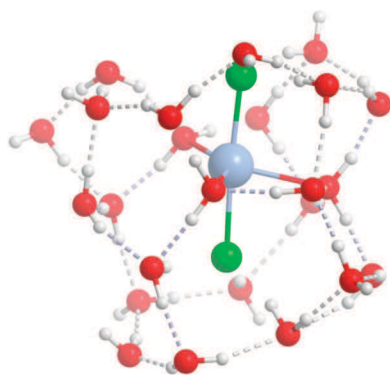


Fig. 6 Optimized "apical" structure of HgCl_2 solvated by 24 water molecules.

the first geometry possessing a Cl-Hg-Cl angle of 125.1° . In this view one can think of an effective $\text{Sol-(H}_2\text{O)}_{21}$ structure where Sol is the $\text{HgCl}_2\text{-(H}_2\text{O)}_3$ moiety (as we shall see below, this model is supported also by molecular dynamics results at finite temperature). Dipole moments were thus computed by single point calculations for both $\text{HgCl}_2\text{-(H}_2\text{O)}_3$ structures (with only the three directly interacting water molecules frozen at the equatorial and apical optimized configurations). As expected, the dipole moments of the nearly isoenergetic $\text{HgCl}_2\text{-(H}_2\text{O)}_3$ structures are quite different, 7.68 D and 1.03 D for the equatorial and the apical orientations, respectively.

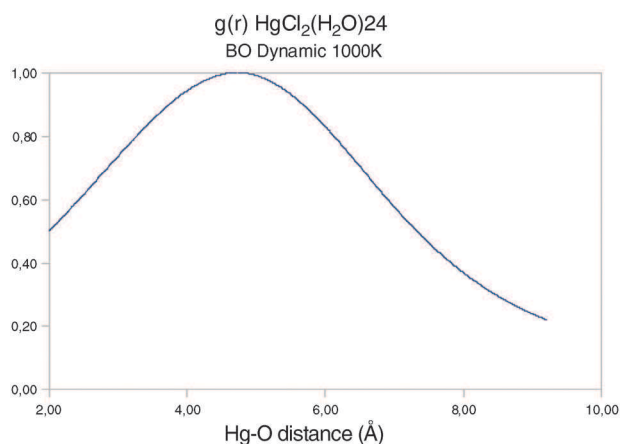


Fig. 7 Hg–O radial distribution function for $\text{HgCl}_2\text{-(H}_2\text{O)}_{24}$ at 1000 K.

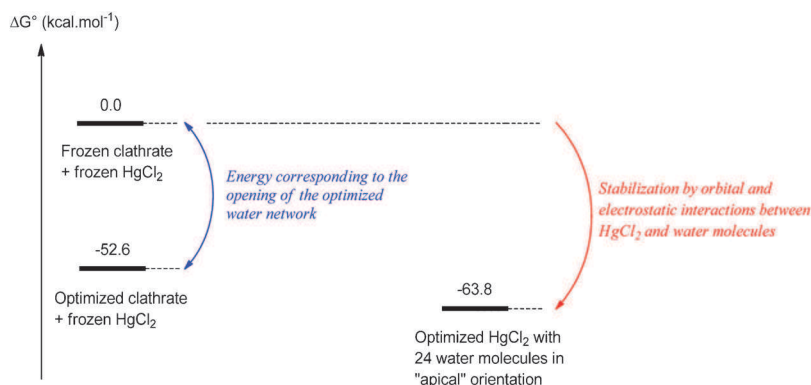


Fig. 8 Diagram of energy levels of different molecular systems.

This could account for the ability of HgCl_2 to easily cross membranes, as reported for As(OH)_3 by Hernández-Cobos *et al.*²⁴

In order to check the validity of this cluster approach, a Born–Oppenheimer molecular dynamics simulation was carried out at the DFT level (B3PW91) starting from the most stable $\text{HgCl}_2\text{-(H}_2\text{O)}_{24}$ structure imposing a rather high temperature of 1000 K to check for the thermodynamic stability of this solvated structure in the gas phase. After 5 ps of thermalization, a 10 ps trajectory has been computed with the Geraldyn code to obtain the radial distribution function ($g(r)$) (Fig. 7).

First of all, analysing the trajectory, we found that the three direct Hg–OH₂ interactions remain during the entire trajectory. However, it is noteworthy that exchanges occur between water molecules in the network and the water molecules directly interacting with Hg (during the 10 ps simulation, 54 exchanges were observed). This phenomenon explains the shape of the $g(r)$ curve. Indeed, the mean Hg–O distance (4.50 Å) is longer than the shortest Hg–O distances found with the cluster approach (2.52 Å), in line with the aforementioned exchanges. Moreover, the shape of the ensuing Hg–O radial distribution function also shows the relatively low structuration around Hg, and this result is in excellent agreement with the EXAFS experiment reported by Akesson *et al.* (Fig. 8).³⁹

It is possible to estimate the energy gain supplied by the interactions between HgCl_2 and 24 water molecules, for instance, in the apical optimized structure. For that purpose, three other calculations were done: (i) a frequency calculation of a frozen geometry of the 24 water molecules cluster (also called clathrate). The frozen clathrate geometry is the same as in the optimized geometry of HgCl_2 solvated by 24 water molecules in apical orientation. HgCl_2 has just been removed from the entire system. This new system is called the "frozen clathrate". (ii) The optimization of this 24 water molecules clathrate (Fig. 1 in ESI†). (iii) A frequency calculation of a frozen geometry of HgCl_2 . This frozen geometry is the same as in the optimized geometry of HgCl_2 solvated by 24 water molecules in the apical orientation.

One can estimate the energy cost of the opening of the optimized clathrate in order to create the required cavity to host the HgCl_2 molecule by eqn (1). This energy cost is calculated to be $52.6 \text{ kcal mol}^{-1}$. It is also possible to estimate

the energy gain supplied by the orbital and electrostatic (including hydrogen bonds with chlorine atoms) interactions between HgCl_2 and the surrounding water molecules using eqn (2). This stabilization is equal to $-63.8 \text{ kcal mol}^{-1}$.

$$\text{Energy cost} = G^\circ(\text{frozen clathrate}) - G^\circ(\text{optimized clathrate}) \quad (1)$$

$$\Delta G_{\text{stabilization}}^\circ = G^\circ(\text{optimized HgCl}_2 \text{ with 24 water molecules}) - G^\circ(\text{frozen clathrate}) - G^\circ(\text{frozen HgCl}_2) \quad (2)$$

The interactions between HgCl_2 and water molecules compensate the energy lost due to the opening of the water network and give additional stability to the system (around 11 kcal mol^{-1}).

2. Influence of pH

When pH increases, an equilibrium takes place between HgCl_2 , HgClOH and Hg(OH)_2 . Solvations of HgClOH and Hg(OH)_2 were thus taken into account too. HgClOH and Hg(OH)_2 were solvated directly with 24 water molecules. Both the equatorial and apical orientations previously observed for HgCl_2 were found as stable structures for the two molecules.

Globally, structural and energetic differences between $\text{HgCl}_2\text{-(H}_2\text{O)}_{24}$ and $\text{HgClOH-(H}_2\text{O)}_{24}$ are small. The Hg-OH bond is found to be mainly covalent in HgClOH in the gas phase, as the Hg-Cl one, and same trends appear during the solvation (*i.e.*, bond elongations). The solvation energies are $-38.6 \text{ kcal mol}^{-1}$ and $-40.1 \text{ kcal mol}^{-1}$ for the equatorial and the apical orientations, respectively, thus slightly larger than for HgCl_2 . This better solvation is due to the presence of the OH group which forms hydrogen bonds by two different ways (through the O and the H atoms) whereas the Cl group can only establish $\text{Cl}\cdots\text{H}$ bonds with the surrounding waters. For the apical system, the energy of opening of the water clathrate is $52.1 \text{ kcal mol}^{-1}$ and the stabilization brought in by the interaction between HgClOH and the water molecules is $-67.0 \text{ kcal mol}^{-1}$. For Hg(OH)_2 , same trends are found again; as expected, the energies of solvation are larger due to the presence of two OH groups ($-42.5 \text{ kcal mol}^{-1}$ and $-47.2 \text{ kcal mol}^{-1}$ for the equatorial and the apical orientations, respectively). The energy of opening of the water clathrate is $51.1 \text{ kcal mol}^{-1}$ and the stabilization brought in by the interaction between Hg(OH)_2 and the water molecules is $-69.6 \text{ kcal mol}^{-1}$.

In conclusion, there are no relevant structural differences between the solvation patterns of HgCl_2 , HgClOH and Hg(OH)_2 . However, from the energetic point of view, solvation is more favorable when the number of OH groups linked to Hg increases, because of their ability to build hydrogen bonds by two different ways.

3. Influence of salinity

The salinity of an aqueous solution of HgCl_2 exerts an influence on the relative amount of different inorganic mercury species (Hg^{2+} , HgCl^+ , HgCl_2 , HgCl_3^- , $[\text{HgCl}_4]^{2-}$). Since different levels of salinity exist in aqueous environments, it was interesting to take it into account and we focused on HgCl_3^- . The solvation of HgCl_3^- was again simulated by incremental additions of water molecules in its environment.

Table 4 Calculated geometrical parameters in gaseous and solvated HgCl_3^- systems. The oxygen atoms are those directly linked to Hg

Water molecules	Hg-Cl d1/Å	Hg-Cl d2/Å	Hg-Cl d3/Å	Hg-O d1/Å	Hg-O d2/Å
0	2.46	2.46	2.46	—	—
3	2.46	2.47	2.54	—	—
6	2.51	2.55	2.59	2.53	2.56
9	2.50	2.58	2.61	2.47	2.65
12	2.50	2.58	2.64	2.50	2.54

Table 5 Solvation energies, calculated as: $\Delta G_{\text{solv}}^\circ = [G^\circ(\text{system with } n \text{ water molecules}) - nG^\circ(\text{H}_2\text{O}) - G^\circ(\text{HgCl}_3^-)]$

Water molecules	$\Delta G_{\text{solv}}^\circ/\text{kcal mol}^{-1}$
3	-0.9
6	-10.4
9	-20.1
12	-29.0

As shown below, the geometry of this molecule leads to a smaller number of water molecules (12) needed to build the first solvation shell as compared to the previous cases. Calculated geometrical parameters and Gibbs free energies of solvation are introduced in Tables 4 and 5 respectively.

First, HgCl_3^- was optimized in the gas phase. It is a triangular molecule with a Hg-Cl bond distance of 2.46 \AA . From the NBO analysis, Hg-Cl bonds are covalent, with a slight ionic character (15% participation of sp^2 orbitals of Hg and 85% participation of sp^3 orbitals of Cl), in agreement with the high electronegativity of chlorine. Then three water molecules were added and the structure was optimized (Fig. 9, left). The three molecules are positioned in order to make hydrogen bonds with the chlorine atoms, but no network is built between them. With six water molecules, two of them interact with mercury in apical positions. These interactions form the same triangular bipyramid pattern that is found for HgCl_2 with 24 water molecules. This pattern is already achieved with only six water molecules in the case of HgCl_3^- because of its triangular geometry and the lack of space around mercury. Water molecules can only interact through both apical positions. Moreover, the hydrogen bond network is preserved, thanks to the presence of three chlorine atoms.

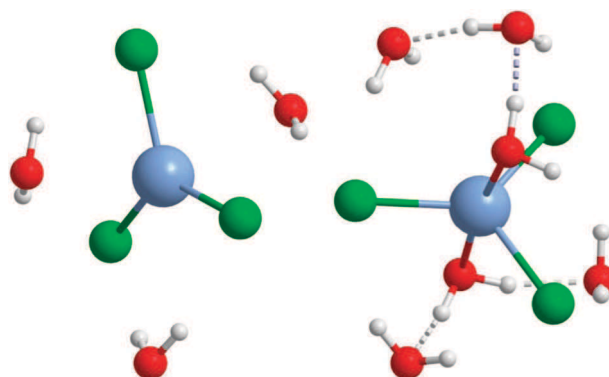


Fig. 9 Optimized geometries of HgCl_3^- solvated by 3 (left) and 6 (right) water molecules.

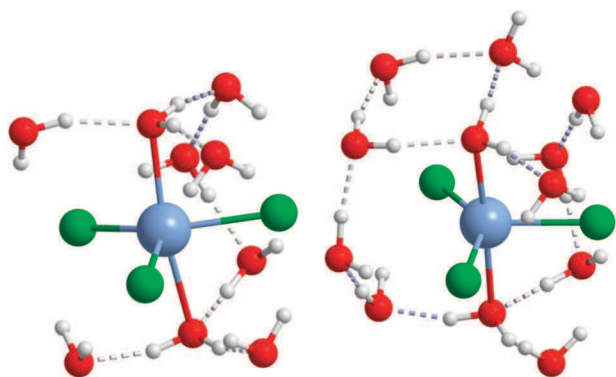


Fig. 10 Optimized geometries of HgCl_3^- solvated by 9 (left) and 12 (right) water molecules.

From this system, additional water molecules only contribute to the hydrogen bond network since the definitive geometrical pattern around mercury is already established. This has been confirmed by studying the systems with 9 and 12 water molecules (Fig. 10).

IV. Conclusions

This study is only the first step of a long-term research program, which aims at identifying the molecular processes involved in the cellular uptake of Hg-containing molecules. As already mentioned, the determination of the solvation patterns of Hg(II)-containing molecules and, more specifically, achieving a detailed understanding of the interaction between Hg(II)-containing species and the surrounding water molecules is the first requirement to build molecular models that explain the transmembrane passage of Hg into the cell. In this work we report a systematic study by stepwise solvation of HgCl_2 including up to 24 water molecules. In order to include pH effects, the solvation patterns of HgClOH and Hg(OH)_2 were also studied using 24 water molecules. In all cases the cohesion of the hydrogen bond network is important to allow orbital-driven interactions between Hg(II) and the water molecules. One has to include at least 20 water molecules to have a reasonable view of the first solvation shell, which is found to derive from a water-clathrate. In both $\text{HgCl}_2-(\text{H}_2\text{O})_{24}$ optimized structures Hg directly interacts with 3 water molecules from an orbital point of view (three Hg–O donor–acceptor type bonds). All the other interactions (either between the ligand coordinated to Hg(II) and the water molecules or in between the water molecules) are mainly electrostatic (hydrogen bonding). The cluster-derived solvation energies of HgCl_2 , HgClOH and Hg(OH)_2 are estimated to be around -34.4 , -40.1 and -47.2 kcal mol $^{-1}$, respectively. We have also shown, through DFT Born–Oppenheimer molecular dynamics simulations, that the optimal $\text{HgCl}_2-(\text{H}_2\text{O})_{24}$ clusters are stable in the gas phase at temperatures even as high as 1000 K. Perhaps even more important, these simulations starting from the stable $\text{HgCl}_2-(\text{H}_2\text{O})_{24}$ structure revealed that an $\text{HgCl}_2-(\text{H}_2\text{O})_3$ trigonal bipyramid effective solute appears and then the remaining 21 water molecules build a complete first solvation shell, in the form of a water-clathrate. These simulations allow us to estimate a high exchange rate of 5.4×10^{10} exchanges

per second at $T = 1000$ K between the water molecules directly bonded with Hg and those of the immediate environment, although this rate could be significantly lower in solution due to competition of exchange between the first–second and the second–third solvation shells in the liquid phase.

The next step in our research program involves the solvation of these Hg-containing molecules in the condensed phase. However, as for the toxic As(OH)_3 molecule, the understanding of the solvation of HgCl_2 in the condensed aqueous phase requires the use of sophisticated classical Hg(II)–water, Cl–water and HgCl_2 –water–water non-additive interaction potentials in conjunction with Monte Carlo or molecular dynamics simulations for the solution. Work is already in progress in that direction.

Acknowledgements

We thank the Institut Universitaire de France, CALMIP and CINES for grant of computing time. CNRS and UPS for financial support of this work. AD thanks EC2CO (CNRS/INSU) for its financial support. LC, LM and ARS wish to thank support from the ECOS-ANUIES/CONACYT Mexican–French cooperation program. ARS also thanks support from CONACYT basic science project No. 130931.

References

- 1 J. E. Gray and M. E. Hines, *Appl. Geochem.*, 2006, **21**, 1819–1820.
- 2 AMAP, Arctic Pollution 2011, Arctic Monitoring and Assessment Programme (AMAP), Oslo, 2011.
- 3 B. M. Braune, P. M. Outridge, A. T. Fisk, D. C. G. Muir, P. A. Helm, K. Hobbs, P. F. Hoekstra, Z. A. Kuzyk, M. Kwan, R. J. Letcher, W. L. Lockhart, R. J. Norstrom, G. A. Stern and I. Stirling, *Sci. Total Environ.*, 2005, **351**, 4–56.
- 4 P. Grandjean, P. Weihe, R. F. White, F. Debes, S. Araki, K. Yokoyama, K. Murata, N. Sorensen, R. Dahl and P. J. Jorgensen, *Neurotoxicol. Teratol.*, 1997, **19**, 417–428.
- 5 G. J. Myers, P. W. Davidson, C. Cox, C. Shamlaye, E. Cernichiari and T. W. Clarkson, *Environ. Res.*, 2000, **83**, 275–285.
- 6 G. J. Myers, P. W. Davidson, C. Cox, C. F. Shamlaye, D. Palumbo, E. Cernichiari, J. Sloane-Reeves, G. E. Wilding, J. Kost, L. S. Huang and T. W. Clarkson, *Lancet*, 2003, **361**, 1686–1692.
- 7 T. Kjellstrom, P. Kennedy, S. Wallis, A. Stewart, L. Friberg and B. Lind, *Physical and Mental Development of Children with Prenatal Exposure to Mercury from Fish. Stage II: Interviews and Psychological Tests at Age 6*, National Swedish Environmental Protection Board, Solna, Sweden, 1989.
- 8 W. H. Schroeder, K. G. Anlauf, L. A. Barrie, J. Y. Lu, A. Steffen, D. R. Schneeberger and T. Berg, *Nature*, 1998, **394**, 331–332.
- 9 S. E. Lindberg, S. Brooks, C. J. Lin, K. J. Scott, M. S. Landis, R. K. Stevens, M. Goodsite and A. Richter, *Environ. Sci. Technol.*, 2002, **36**, 1245–1256.
- 10 H. Zhang, in *Structure and Bonding—Recent Developments in Mercury Science*, ed. D. A. Atwood, Springer, Berlin/Heidelberg, 2006, vol. 120, pp. 37–79.
- 11 E. Bahlmann, R. Ebinghaus and W. Ruck, *J. Environ. Manage.*, 2006, **81**, 114–125.
- 12 M. Amyot, G. Mierle, D. R. S. Lean and D. J. McQueen, *Environ. Sci. Technol.*, 1994, **28**, 2366–2371.
- 13 M. Amyot, G. A. Gill and F. M. M. Morel, *Environ. Sci. Technol.*, 1997, **31**, 3606–3611.
- 14 A. Dommergue, E. Bahlmann, R. Ebinghaus, C. Ferrari and C. Boutron, *Anal. Bioanal. Chem.*, 2007, **388**, 319–327.
- 15 O. Selifonova, R. Burlage and T. Barkay, *Appl. Environ. Microbiol.*, 1993, **59**, 3083–3090.

- 16 T. Barkay, R. R. Turner, L. D. Rasmussen, C. A. Kelly and J. W. Rudd, in *Bioluminescence Methods and Protocols 102*, ed. A. Robert and LaRossa, Humana Press Inc., NJ, 1998, pp. 231–246.
- 17 C. Larose, A. Dommergue, N. Maruszczak, J. Coves, C. P. Ferrari and D. Schneider, *Environ. Sci. Technol.*, 2011, **45**, 2150–2156.
- 18 I. Worms, D. F. Simon, C. S. Hassler and K. J. Wilkinson, *Biochimie*, 2006, **88**, 1721–1731.
- 19 F. M. M. Morel, A.M. L. Kraepiel and M. Amyot, *Annu. Rev. Ecol. Syst.*, 1998, **29**, 543–566.
- 20 C. Larose, A. Dommergue, M. De Angelis, D. Cossa, B. Averty, N. Maruszczak, N. Soumis, D. Schneider and C. Ferrari, *Geochim. Cosmochim. Acta*, 2010, **74**, 6263–6275.
- 21 J. Gutknecht, *J. Membr. Biol.*, 1981, **61**, 61–66.
- 22 T. Barkay, M. Gillman and R. R. Turner, *Appl. Environ. Microbiol.*, 1997, **63**, 4267–4271.
- 23 G. R. Golding, C. A. Kelly, R. Sparling, P. C. Loewen and T. Barkay, *Environ. Sci. Technol.*, 2007, **41**, 5685–5692.
- 24 J. Hernández-Cobos, M. C. Vargas, A. Ramirez-Solís and I. Ortega-Blake, *J. Chem. Phys.*, 2010, **133**, 114501.
- 25 W. Kuechle, M. Dolg, H. Stoll and H. Preuss, *Mol. Phys.*, 1991, **74**, 1245–1263.
- 26 A. Bergner, M. Dolg, W. Kuechle, H. Stoll and H. Preuss, *Mol. Phys.*, 1993, **80**, 1431–1441.
- 27 A. W. Ehlers, M. Bohme, S. Dapprich, A. Gobbi, A. Hollwarth, V. Jonas, K. F. Kohler, R. Stegmann, A. Veldkamp and G. Frenking, *Chem. Phys. Lett.*, 1993, **208**, 111–114.
- 28 L. Maron and C. Teichteil, *Chem. Phys.*, 1998, **237**, 105–122.
- 29 W. J. Hehre, R. Ditchfield and J. A. Pople, *J. Chem. Phys.*, 1972, **56**, 2257–2261.
- 30 J. P. Perdew and Y. Wang, *Phys. Rev. B: Condens. Matter*, 1992, **45**, 13244–13249.
- 31 A. D. Becke, *J. Chem. Phys.*, 1993, **98**, 1372–1377.
- 32 M. J. Frisch, G. W. Trucks, H. B. Schlegel, G. E. Scuseria, M. A. Robb, J. R. Cheeseman, J. J. A. Montgomery, T. Vreven, K. N. Kudin, J. C. Burant, J. M. Millam, S. S. Iyengar, J. Tomasi, V. Barone, B. Mennucci, M. Cossi, G. Scalmani, N. Rega, G. A. Petersson, H. Nakatsuji, M. Hada, M. Ehara, K. Toyota, R. Fukuda, J. Hasegawa, M. Ishida, T. Nakajima, Y. Honda, O. Kitao, H. Nakai, M. Klene, X. Li, J. E. Knox, H. P. Hratchian, J. B. Cross, V. Bakken, C. Adamo, J. Jaramillo, R. Gomperts, R. E. Stratmann, O. Yazyev, A. J. Austin, R. Cammi, C. Pomelli, J. W. Ochterski, P. Y. Ayala, K. Morokuma, G. A. Voth, P. Salvador, J. J. Dannenberg, V. G. Zakrzewski, S. Dapprich, A. D. Daniels, M. C. Strain, O. Farkas, D. K. Malick, A. D. Rabuck, K. Raghavachari, J. B. Foresman, J. V. Ortiz, Q. Cui, A. G. Baboul, S. Clifford, J. Cioslowski, B. B. Stefanov, G. Liu, A. Liashenko, P. Piskorz, I. Komaromi, R. L. Martin, D. J. Fox, T. Keith, M. A. Al-Laham, C. Y. Peng, A. Nanayakkara, M. Challacombe, P. M. W. Gill, B. Johnson, W. Chen, M. W. Wong, C. Gonzalez and J. A. Pople, *Gaussian 03 Revision D.02*, Gaussian, Inc., Wallingford, CT, 2004.
- 33 A. E. Reed, L. A. Curtiss and F. Weinhold, *Chem. Rev.*, 1988, **88**, 899–926.
- 34 C. Raynaud, L. Maron, J. P. Daudey and F. Jolibois, *Phys. Chem. Chem. Phys.*, 2004, **6**, 4226–4232.
- 35 L. Verlet, *Phys. Rev.*, 1967, **159**, 98.
- 36 S. Nosé, *J. Chem. Phys.*, 1984, **81**, 511–519.
- 37 W. G. Hoover, *Phys. Rev. A: At., Mol., Opt. Phys.*, 1985, **31**, 1695–1697.
- 38 B. C. Shepler, A. D. Wright, N. B. Balabanov and K. A. Peterson, *J. Phys. Chem.*, 2007, **111**, 11342–11349.
- 39 R. Akesson, I. Persson, M. Sandstrom and U. Wahlgren, *Inorg. Chem.*, 1994, **33**, 3715–3723.